

**VIRTUAL
CONFERENCE**

american society for precision engineering and nanotechnology

Conference Proceedings

Special interest Group:

**Advancing Precision in
Additive Manufacturing**

21st - 23rd September 2021

Proceedings of the Special Interest Group meeting on
Advancing Precision in Additive Manufacturing

September 21-23, 2021
Virtual

Editors:

R.K. Leach

J.S. Taylor

Proceedings Compilation:

C. Nisbet



Proceedings of the Special Interest Group meeting on
Advancing Precision in Additive Manufacturing

The local hosts and organising committee for the joint Special Interest Group meeting between euspen and ASPE on Advancing Precision in Additive Manufacturing.

Dr Anke Günther, Reishauer AG and ETH Zurich/ IWF
Prof. Richard Leach, University of Nottingham
Prof. Geoff McFarland, Renishaw
Dr Adriaan Spierings, inspire AG
Dr John Taylor, University of North Carolina at Charlotte

Published by **euspen**
ISBN: 978-1-9989991-0-1

Printed in the UK, September 2021
twenty10
33 Rothersthorpe Crescent Mews
Northampton
NN4 8JD
UK

© **euspen** Headquarters
Cranfield University Campus
Building 90, College Road
Bedford
MK43 0AL
UK
Tel: 0044 (0) 1234 754023
Website: www.euspen.eu

Information correct at time of printing and may become subject to change

Welcome to the 8th meeting of *Advancing Precision in Additive Manufacturing*. We are a jointly sponsored **euspen** Special Interest Group and ASPE Topical Meeting, alternating annually across the Atlantic – in normal times. This year, we are again meeting virtually due to COVID-19, and like last year, we have an excellent program of keynote talks, state-of-the-art reviews, and technical papers and tutorials.

Advancing Precision in Additive Manufacturing has a unique perspective that differentiates our topics and philosophical approach from the plethora of other meetings on additive manufacturing (AM). We demonstrate a proactive and conscious commitment to *determinism* and expertise in *precision engineering*. We might summarise our creed of determinism as the commitment to *ensuring results with high certainty* by 1) a first-principles understanding of performance and error sources; 2) pursuit of repeatability; 3) expressing performance using quantifiable metrics; and 4) the ability to measure and often control these quantifiable metrics. Our precision engineering expertise embodies many tools including design for precision/metrology, error budgets, evaluation of uncertainty, standards, controls, and other related topics to meet the demands of determinism.

Our span of papers addresses key elements of achieving determinism in AM. We have papers on the dependence of errors on process variables and how to incorporate AM into a holistic manufacturing process. New focus areas include lattice structures and AM on micro-nano length scales. We examine the in-process controls and sensor data needed to achieve predictable and repeatable results. We strive to relate quality with specifiable and measurable quantities. New approaches are presented for extracting actionable information from diverse measurement modalities, and we develop measurement tools for characterising volumes and surfaces with the unique challenges of AM.

We ask all of the listeners and speakers to consider how their topics and presentations contribute to determinism. Please take the explicit and proactive step in answering ‘how does this work push additive manufacturing forward as a deterministic manufacturing process?’ Are we specifying and measuring the right properties? Are we using the most appropriate measurement tools? Can we extract more information from the data that we collect? Are we rigorous about our treatment of uncertainties?

Above all, let's work together to make this meeting useful. The virtual environment offers an expanded capability to clearly view presentations and ask questions for our speakers and other participants. And, of course, let's share our comradeship in precision engineering!

The Organising Committee

September 2021

Keynotes

- K1** **Next generation design for additive manufacturing and how the technologies need to adapt** **11**
Dr.-Ing. Bernhard Mueller
Fraunhofer IWU, DE
- K2** **Transforming the supply chain of metal components for industrial gas turbines through the new possibilities of additive manufacturing** **12**
Marco Salvisberg
GF Casting Solutions, CH
- K3** **Evaluation of hybrid AM technology chains considering process accuracies for the integration into industrial production** **13**
Martin Schaefer
Siemens AG, DE

State-of-the-art reviews

- S1** **A review of the state-of-the-art and precision engineering challenges in micro/nanoscale additive manufacturing** **15**
Michael A. Cullinan
University of Texas at Austin, US
- S2** **In-process measurement methods for defect identification in metal powder bed fusion** **16**
Afaf Remani
University of Nottingham, UK
- S3** **Machine learning for precision engineering** **17**
Joe Eastwood
University of Nottingham, UK

Session 1: Industrial application & process optimization

- O1.01** **Printing miniature valves by micro-SLA for soft robotics** **19**
F. Boudoire¹, H. A. Sonar², S. Unterhofer¹, D. Bayat¹, S. Lani¹, J. Paik²
¹CSEM, Micro & Nano Systems Division, 2002 Neuchâtel, Switzerland
²EPFL, Reconfigurable Robotics Laboratory, 1015 Lausanne, Switzerland
- O1.02** **Influence of the CNC behaviour on the laser spot trajectory in LPBF process** **22**
Kevin. Godineau¹, Sylvain. Lavernhe¹, Christophe. Tournier¹
¹Université Paris-Saclay, ENS Paris-Saclay, Institut Farman FR3311, LURPA, France
- O1.03** **Toward specification of complex additive manufactured metal surfaces for optimum heat transfer** **26**
Kuldeep Mandloi ¹, Chris Evans ², Jason C. Fox ², Harish Cherukuri ¹, Jimmie Miller ¹, Angela Allen ¹, David C. Diesenroth ², Alkan Donmez ²
¹University of North Carolina at Charlotte, USA
²National Institute of Standards and Technology, Gaithersburg, USA
- O1.04** **Surface topography process signatures in nickel superalloy 625 additive manufacturing** **30**
J.C. Fox², A. Allen¹, B. Mullany¹, E. Morse¹, R.A. Isaacs³, M. Lata¹, A. Sood¹, and C. Evans^{1,2}
¹University of North Carolina at Charlotte
² National Institute of Standards and Technology
³ Zeiss

Session 2: Integration of AM into a holistic manufacturing process

- O2.01 Improving additive manufactured surfaces properties with post processing techniques 35**
Matthieu Rauch^{1,2}, Jean-Yves Hascoet^{1,2}
¹Centrale Nantes / GeM - UMR CNRS 6183, equipe PMM, 1 rue de la Noe, 44321 Nantes - FRANCE
²Joint Laboratory of Marine Technology (JLMT) Centrale Nantes - Naval Group - FRANCE
- O2.02 Computer vision based zero point estimation for hybrid builds in metal additive manufacturing 39**
Jakob Wilm¹, Eythor R. Eiriksson², Sven D. Sørensen³, Lasse Haahr-Lillevang⁴, Nikolaj K Vedel-Smith⁴, Venkata K. Nadimpalli⁵, Gisli Hjalmysson⁶ and David B. Pedersen⁵
¹SDU Robotics, University of Southern Denmark
²Euler ehf – euler3d.com
³LEGO Group A/S, Denmark
⁴Danish Technological Institute
⁵Dept. Mechanical Engineering, Technical University of Denmark
⁶Reykjavik University, Iceland
- O2.03 Accuracy and microstructure of additively manufactured and post-machined parts 42**
Hans-Christian Möhring, Dina Becker
Institute for Machine Tools - University of Stuttgart

Session 3: Focus on micro-nano

- O3.01 Insights into challenges and potentials of two-photon lithography 47**
S. Kühne¹, M. Malcher¹, V. Juzumas², E. Bosler¹, D. Oberschmidt¹
¹Technische Universität Berlin, Department Micro and Precision devices MFG, Germany
²Altechna R&D | Workshop of Photonics, Lithuania
- O3.02 Characterizing shrinkage and quality of ceramic two-photon printed microstructures 51**
John Cortes¹, Magi Mettry¹, Matthew Worthington¹, Swetha Chandrasekaran¹, Robert Panas¹
¹Lawrence Livermore National Laboratory, Livermore, CA, USA

Session 4: Focus on lattice structures

- O4.01 Direct additive manufactured beam shape defect identification from computed tomography and modal decomposition 56**
Marc-Antoine de Pastre¹, Yann Quinsat¹, Claire Lartigue¹
¹LURPA, ENS Paris-Saclay, Université Paris-Saclay, 91190 Gif-sur-Yvette, France
- O4.02 A two step modelling approach to limit the exploitable AM parameter space and optimized parameter selection for finest lattice structures using LPBF 60**
H. Korn¹, P. Koch², S. Holtzhausen², J. Thielsch¹, A. Seidler², B. Müller¹, W.-G. Drossel¹
¹Fraunhofer Institute for Machine Tools and Forming Technology IWU, Germany
²Technische Universität Dresden, Institute of Machine Elements and Machine Design, Germany

O4.03	Influence of the processing parameters on the dimensional accuracy of In625 lattice structures made by laser powder bed fusion Lucas Fournet-Fayard ^{1,2} , Charles Cayron ¹ , Imade Koutiri ² , Valérie Gunenthiram ³ , Pierrick Sanchez ⁴ , AnneFrançoise Obaton ¹ ¹ Laboratoire Commun de Métrologie (LCM), Laboratoire National de Métrologie et d'Essais (LNE), 75015 Paris, France ² Laboratoire PIMM, Arts Et Métiers Institute of Technology, CNRS, Cnam, HESAM University 75013 Paris, France ³ CETIM – Additive Factory Hub (AFH), 91191 Gif-Sur-Yvette, France ⁴ Carl Zeiss Services, 95000 Neuville-sur-Oise, France	64
O4.04	Design and measurement strategy of additive manufacturing lattice benchmark artefact Younes Chahid ¹ , Radu Racasan ¹ , Paul Bills ¹ , Liam Blunt ¹ ¹ EPSRC Future Metrology Hub, School of Computing and Engineering, University of Huddersfield, HD1 3DH Huddersfield, UK	68
O4.05	Testing the similarity conditions in the CT measurement of additively manufactured lattice structures M. Pranievicz ¹ , M. Ferrucci ¹ , J. Fox ¹ , C. Saldana ² ¹ National Institute of Standards and Technology ¹ , USA ² Georgia Institute of Technology, USA	70
Session 5: In-process metrology and data fusion		
O5.01	Smart machines for fused filament fabrication based on multi-sensor data fusion, digital twins and machine learning A. Rossi ¹ , M. Moretti ¹ , N. Senin ¹ ¹ University of Perugia, Italy	75
O5.02	Fast measurement of metal laser powder bed fusion layer surfaces using light scattering and principal component analysis Mingyu Liu ¹ , Nicola Senin ^{1,2} , Richard Leach ¹ ¹ Manufacturing Metrology Team, Faculty of Engineering, University of Nottingham, Nottingham, UK ² Department of Engineering, University of Perugia, Italy	79
O5.03	Stereo camera based in-situ monitoring of L-PBF process stability by spatter detection Daniel Brummerloh ^{1,2} , Dennis Jutkuhn ^{1,3} , Zheng Yang ⁴ , Alexander Penn ² , Claus Emmelmann ³ ¹ Fraunhofer Research Institution for Additive Manufacturing Technologies IAPT, Germany ² Institute of Process Imaging, Hamburg University of Technology, Germany ³ Institute of Laser and System Technologies, Hamburg University of Technology, Germany ⁴ Hexagon Technology Center GmbH, Switzerland	82
O5.04	Design of a multi-sensor measurement system for in-situ defect identification in metal additive manufacturing Afaf Remani ¹ , Richard Williams ² , Adam Thompson ¹ , John Dardis ³ , Nick Jones ³ , Paul Hooper ² , Richard Leach ¹ ¹ Manufacturing Metrology Team, Faculty of Engineering, University of Nottingham, Nottingham, NG8 1BB, UK ² Department of Mechanical Engineering, Imperial College London, SW7 2AZ, UK ³ Renishaw Plc, New Mills, Kingswood, Wotton-under-Edge, GL12 8JR, UK	86

Session 6: Metrology

- 06.01 Direct part density inspection in laser powder bed fusion using eddy current testing** 91
Adriaan B. Spierings¹, Marvin A. Spurek^{1,2}, Marc Lany³, Gilles Santi³, Bernard Revaz³, Konrad Wegener²
¹*inspire AG, Innovation Center for Additive Manufacturing (icams), CH-9014 St.Gallen, Fürstenlandstrasse 122, Switzerland*
²*Swiss Federal Institute of Technology, ETH Zurich, Institute of Machine Tools and Manufacturing, CH-8092 Zurich, Leonhardstrasse 21, Switzerland*
³*Sensima Inspection SARL, 1196 Gland, 2 Route Cite Ouest, Switzerland*
- 06.02 Analysis of metal powder geometrical characteristics influencing the quality of additively manufactured parts** 95
Filippo Zanini¹, Nicola Buzzacchera¹, Simone Carmignato¹
¹*Department of Management and Engineering, University of Padova, Vicenza, Italy*
- 06.03 Comparison of dimensional measurements from images acquired by synchrotron tomography with VGSTUDIO MAX and ImageJ** 98
C. Cayron¹, A. De Soete¹, Y. Gaillard², C. Yardin¹, N. Coutant³, R. Nanjareddy³, P. Bouvet², A.-F. Obaton¹
¹*Laboratoire Commun de Métrologie (LCM), Laboratoire National de Métrologie et d'Essais (LNE), 75015 Paris, France*
²*Centre Technique des Industries de la Fonderie (CTIF), 92318 Sèvres, France*
³*Volume Graphics (VG) GmbH, 69115 Heidelberg, Germany*
- 06.04 Quantifying the influence of local porosity on the colour differences of dyed laser sintered polyamide-12 with X-ray CT** 102
S. Bellens¹, M. Janssens¹, T. Craeghs¹, P. Vandewalle², W. Dewulf³
¹*Materialise NV, Technologielaan 15, Leuven, Belgium*
²*EAVISE, PSI, Dept. Of Electrical Engineering (ESAT), KU Leuven, Jan Pieter de Nayerlaan 5, Sint-Katelijne-Waver, Belgium*
³*Dept. Of Mechanical Engineering, KU Leuven, Celestijnenlaan 300, Heverlee, Belgium*
- 06.05 Characterisation of high speed sintering surface topography with re-entrant open surface pores using 3D surface texture parameters and material ratio curve** 106
S. Lou¹, Z. Zhu², W. Zeng¹, C. Majewski³, P. J. Scott¹, X. Jiang¹
¹*EPSRC Future Metrology Hub, University of Huddersfield, Queensgate, Huddersfield, HD1 3DH, UK*
²*Advanced Forming Research Centre, National Manufacturing Institute Scotland, Renfrewshire, PA4 9LJ, UK*
³*EPSRC MAPP Future Manufacturing Hub, University of Sheffield, Sheffield, S10 2TN, UK*
- 06.06 Exploratory research on the correlation of probability of detection and image quality during the tomographic characterisation of additive manufacturing defects** 110
M. Sinico^{1,2}, S. Bellens^{1,2,3}, T. van Herreweghen¹, G.M. Probst^{1,2}, W. Dewulf¹
¹*Department of Mechanical Engineering, KU Leuven, 3001 Leuven, Belgium*
²*Member of Flanders Make - Core Lab MaPS, KU Leuven, 3001 Leuven, Belgium*
³*Materialise NV, 3001 Leuven, Belgium*

Poster Session

- P1.01 Surface irregularities of metal SLM Part with different surface inclinations and their impact on surface texture characterization 115**
S. Ramadurga Narasimharaju¹, W. Liu¹, W. Zeng¹, T. L. See², P. J. Scott¹, X. Jiang¹, S. Lou¹
¹EPSRC Future Metrology Hub, University of Huddersfield, Queensgate, Huddersfield, UK
²Laser Processing Group, Manufacturing Technology Centre, Ansty Park, Coventry, UK
- P1.02 Topology optimization for additive manufacturing 119**
Kazybek Kassym¹, Konstantinos Kostas¹, Didier Talamona¹
¹Nazarbayev University, MAE – School of Engineering and Digital Sciences, Nur-Sultan, Kazakhstan¹
- P1.03 Prediction of dimensional accuracy and warpage of additive manufactured parts using finite element model 123**
D. Syrlybayev¹, A. Seisekulova¹, M. Akhmetov¹, A. Perveen¹, D. Talamona¹
¹Department of Mechanical & Aerospace Engineering, School of Engineering and Digital Sciences, Nazarbayev University, Kabanbay Batyr Ave. 53, Nur-Sultan 010000 Kazakhstan
- P1.04 Micro-replication of high precision optically enhanced moulds fabricated by multiphoton polymerization 127**
Sara Vidal¹, Félix Ares¹, Ivette Coto¹, Francisco Gontad¹, Tamara Delgado¹, Pablo Romero¹, Nerea Otero¹
¹AIMEN Technology Centre, Spain
- P1.05 High-resolution X-ray computed tomography for additive manufacturing: Towards traceable porosity defect measurements using digital twins 130**
B. A. Bircher¹, S. Wyss¹, D. Gage², A. Küng¹, C. Körner², F. Meli¹
¹Laboratory for Length, Nano- and Microtechnology, Federal Institute of Metrology METAS, Bern-Wabern, Switzerland
²Chair of Materials Science and Engineering for Metals, Friedrich-Alexander University Erlangen-Nürnberg, Erlangen, Germany
- P1.06 Impulse excitation technique for improved inspection in additive manufacturing 134**
Juan Jose Bustos¹, Alex Van den Bossche¹
¹GrindoSonic bvba, Esperantolaan 4, Leuven 3001, Belgium
- P1.07 Dimensional accuracy of an artifact for rapid casting 138**
Muslim Mukhtarkhanov¹, Didier Talamona¹, Asma Perveen¹
¹Department of Mechanical and Aerospace Engineering, Nazarbayev University, Nur-Sultan 010000, Kazakhstan
- P1.08 Enhancing surface finish consistency by novel ECM process on SLM AM components 142**
Ahmed Tawfik¹, Aaron Holt², Paul Bills¹, Neil Dickinson², Liam Blunt¹
¹Huddersfield University, UK
²Holtex group Ltd, UK
- P1.09 Application of metal additive manufacturing material extrusion in the production of tool inserts for polymer profile extrusion die surface roughness investigation 143**
M. Kain¹, P. Parenti², M. Calao¹, D. B. Pedersen¹, M. Annoni², G. Tosello¹
¹Department of Mechanical Engineering, Technical University of Denmark, Building 427A, Produktionstorvet, 2800 Kgs. Lyngby, Denmark
²Dipartimento di Meccanica, Politecnico di Milano, Via La Masa 1, Milan, Italy

Keynotes

Next generation design for additive manufacturing and how the technologies need to adapt

Bernhard Mueller

Fraunhofer IWU, Dresden, DE

Abstract

Design for Additive Manufacturing (D4AM) has become popular, raising awareness that, for an industrial breakthrough it is crucial to make use of the design freedom that AM potentially provides to a maximum extent. Transformation and evolution of existing designs for conventional manufacturing to AM are bound to fail in providing economically viable success stories on the road towards AM industrialization. As of today, D4AM incorporates design strategies and software solutions like topology optimization, bionics/biomimicry and generative design, lightweight engineering and lattice structures. D4AM constantly pushes the envelope of AM process limitations. To go beyond the aforementioned D4AM strategies for a true next generation D4AM, design/process interaction is necessary. Digital workflows have to be adapted or even set up in a completely new manner, e.g. to achieve extra delicate, homogeneous and reliable lattice structures or extra thin, stable and pressure-tight wall features with smooth surfaces. Functional materials have to be qualified for AM to achieve smart or programmable materials implemented in AM made parts and products. Material and process combinations can be designed for hybrid components and an AM process development has to be undertaken to support these hybrid designs. The potential for smart AM parts is vast with next generation D4AM: extreme lightweight parts can incorporate delicate and reliable lattice structures and mechanical properties like stiffness of parts can be designed and varied – components can even show a varying stiffness during deformation. Miniature heat exchangers can be automatically designed using fractal design principles and can be adapted to any given build space and performance requirements. Sensoric functions can be printed right into AM parts like molds and dies, robotic grippers or structural parts for monitoring purposes. Very different materials like metals and ceramics can be combined in one part via AM, and mass production technologies like die casting can be flexibilized via AM hybridization. The road to successful, wide spread industrial application of AM is long and winding, but next generation Design for Additive Manufacturing is about to accelerate this journey.

Transforming the supply chain of metal components for industrial gas turbines through the new possibilities of additive manufacturing

Marco Salvisberg

GF Casting Solutions, CH

Abstract

The world of manufacturing technology is changing rapidly, and GF Casting Solutions, one of the world's leading suppliers of cast components for the automotive, aerospace and power generation industries, is responding to this challenge by offering its customers solutions that can react faster and more flexibly to constantly changing market conditions, than would have been possible in the past. In general, developments have to be successfully completed much faster, and components are no longer purchased from stock but ordered directly from the supplier on demand.

This keynote will show how additive manufacturing has changed and will continue to change the supply chain for nickel-based alloy components for the energy sector. Thanks to the possibilities of additive manufacturing, components can be developed faster, functions can be integrated and total cost of ownership can be drastically reduced. Thanks to the improved process stability compared to traditional manufacturing methods, even more precise components can be produced, which leads to a reduction in post-processes such as machining. A major task still to be solved is the surface roughness of components. Particularly in the down skin areas or where supports are required, the surface quality is far from reaching the surface tolerances known from precision casting.

In addition to the challenge regarding surface roughness, there is still a lot of untapped potential to make the AM process and especially the downstream processes leaner and more cost effective, in order to be able to substitute even more components that are still produced with traditional manufacturing methods.

To tap this potential, the industry needs the support of research and development to jointly find solutions for the existing challenges, so that additive manufacturing can become an established standard manufacturing process.

Evaluation of hybrid AM technology chains considering the process accuracies for integration into industrial production

Martin Schäfer

Siemens AG, DE

Abstract

To integrate additive manufacturing (AM) into industrial production and to expand its range of application, the linking of these still new manufacturing processes with conventional technologies is necessary and is one of the important key developments, along with other developments such as “adaptive design”, to make additive manufacturing processes usable for large parts of the industrial sectors.

The presentation shows the planning of hybrid process chains and which requirements exist and still must be solved.

It is necessary to combine the different processes with each other in a sensible way and to adapt each other if needed. The underlying characteristic of AM processes, that basic materials are changed during the manufacturing of the products, requires a special approach for the production integration of these technologies besides the persisting challenges of anisotropy or the reproducibility of the processes.

“Coordination” is an essential part of hybrid manufacturing, especially regarding geometric alignment and material transitions. Accuracy and alignment aspects in particular must be taken into account here. Possibilities and challenges are highlighted.

Furthermore, there is a need to plan and evaluate technology chains. This also requires a broad technology knowledge and corresponding databases. There is still a lot of groundwork to be done here. However, this planning is one of the building blocks to successfully implement the major future targets of the society such as resilient production or the circular economy.

The merging of technologies requires knowledge of the technical possibilities of the various AM processes, whose part sizes range from the sub-millimeter to the meter with accuracies from micrometers to millimeters (stereo lithography and 2-photon polymerization; “concrete extrusion”). Using these possibilities and combining them with traditional processes to form process chains is one of the working areas of hybrid manufacturing. With adapted interface execution it is possible to use the advantages of the different processes and to optimize the production in terms of product designs and material properties.

State-of-the-art reviews

A review of the state-of-the-art and precision engineering challenges in micro/nanoscale additive manufacturing

Michael A. Cullinan

University of Texas at Austin, US

Abstract

Microscale additive manufacturing is one of the fastest growing areas of research within the additive manufacturing community. However, there are still significant challenges that exist in terms of available materials, resolution, throughput, and ability to fabricate true three-dimensional geometries. These challenges render commercialization of currently available microscale additive manufacturing processes difficult. This talk will review the current state-of-the-art of microscale additive manufacturing technologies and investigate the factors that currently limit each microscale additive manufacturing technology in terms of materials, resolution, throughput, and ability to fabricate complex geometries. This talk will offer prognosis about the future viability and applications of each technology along with suggested future research directions that could be used to bring each process technology in line with its fundamental, physics-based limitations. This talk will also bring together the general design guidelines that must be followed while designing scalable microscale AM processes. Finally, this talk will conclude with an analysis of the role of precision engineering in the future advancement of microscale additive manufacturing technologies.

In-process measurement methods for defect identification in metal powder bed fusion

Afaf Remani

University of Nottingham, UK

Abstract

The possibility of using a variety of sensor signals acquired during metal powder bed fusion processes, to support part and process qualification, has been constantly attracting a great interest. The number of research studies in this field has been characterised by significant growth in the last few years, with several advances and new solutions compared with initial studies. Moreover, industrial powder bed fusion systems are increasingly equipped with sensors and toolkits for data collection, visualisation and, in some cases, embedded in-process analysis. Many new methods have been proposed and defect detection capabilities have been demonstrated. Nevertheless, several challenges and open issues still need to be tackled to bridge the gap between methods proposed in the literature and actual industrial implementation. We present a state-of-the-art of in-situ sensing, measurement, and monitoring for metal powder bed fusion processes, with a classification of the defects that are practically detectable while the part is being produced. The research areas where additional technological advances are currently needed will also be highlighted.

Machine learning for precision engineering

Joe Eastwood

University of Nottingham, UK

Abstract

Advances in high performance computing combined with access to rich and massive datasets have led to a revolution in machine intelligence. The growing ubiquity of machine learning across all sectors presents many opportunities, and the precision engineering world has not been slow in leveraging this new tool. While initially confined to the world of academia, the technologies have matured enough to be seen in many industrial settings. From post-process surface metrology, to in-situ monitoring and process control – machine learning is now contributing to many applications at the cutting edge of our field. This talk will cover, at a high level, the current state of the art in machine learning as it applies to precision engineering.

Session 1: Industrial application & process optimization

Printing miniature valves by micro-SLA for soft robotics

F. Boudoire¹, H. A. Sonar², S. Unterhofer¹, D. Bayat¹, S. Lani¹, J. Paik²

¹CSEM, Micro & Nano Systems Division, 2002 Neuchâtel, Switzerland

²EPFL, Reconfigurable Robotics Laboratory, 1015 Lausanne, Switzerland

florent.boudoire@csem.ch

Abstract

Solenoid valves are characterized by high actuation frequencies desirable in many fields and in particular in robotics. Manufacturing such valves by UV-stereolithography would grant high resolution, miniaturization, and design flexibility. Using this fabrication technique, we developed miniature solenoid valves with a lifetime of more than 5 million cycles. To achieve this long lifetime, we optimized in particular the surface microstructure of the valve, to achieve low friction coefficients, by studying the effect of the print layer height.

UV-stereolithography, polymer, valve, tribology

1. Introduction

The field of soft robotics is gaining traction in recent years due to its high compliance capabilities. Soft robots typically rely on pneumatic actuation to interact with their environment. This actuation is performed by solenoid valves that control the pressurization with a response time on the millisecond scale. Miniature pneumatic valves with dimensions below 20 mm are interesting in this field for streamlined integration, in particular for wearable devices.[1] Additive manufacturing provides unique opportunities to miniaturize such valves while providing design flexibility for improved integration.[2] We present the development of polymer-based miniature valves produced by UV-stereolithography (SLA). In a first part we describe the valve design and fabrication. In a second part we present the protocol we followed to optimize two important parameters of the stereolithography process, the exposition time and layer height, for optimal dimensional fidelity and surface microstructure. And in a third part we present the actuation performance and lifetime of the optimized valve.

2. Results and discussion

2.1. Valve design and fabrication

The valves are composed of a solenoid assembly mounted on a polymer-based valve body featuring an embedded permanent magnet plunger (Figure 1). The solenoid assembly is composed of a copper solenoid (wire diameter 0.112 mm, 868 turns) and an aluminium heat sink with a gyroid morphology fabricated by selective laser melting. A steel core, also fabricated by selective laser melting, is inserted between the polymer valve and the copper solenoid to strengthen the magnetic field during operation.

We fabricated the polymer-based valve body by UV-stereolithography. We used the HiTemp resin from Formlabs to produce this valve since the polymer resulting from this resin can withstand the temperature of 80°C reached by the solenoid under operation. We printed the valve using a custom high-resolution SLA 3d printer based on a digital light processing (DLP)

projector (Visitech, wavelength of 385 nm) with a projected pixel size of 15 μm . We programmed a custom Python software to control the DLP-SLA 3d printer that allows full control of the system hardware. A feature implemented in this software allows us to insert a $\text{Sm}_2\text{Co}_{17}$ magnet plunger inside the valve during printing. We can indeed pre-program a layer at which the print will stop, allowing for manual insertion of the magnet inside the valve. The magnet is secured inside the valve thanks to a ferromagnetic plate fixed to the print platform. After insertion we can resume the fabrication process. This strategy results in a monolithic valve body with an embed magnetic plunger as described in the rendering presented in Figure 1.

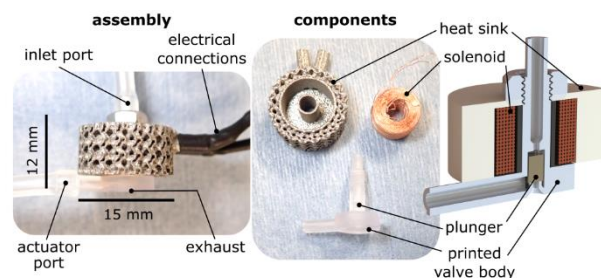


Figure 1. 3D printed miniature valve assembly and components

2.2. Optimisation of the print parameters and tribological surface analyses

To guide the embedded magnetic plunger inside the polymer-based valve body-controlled tolerances need to be achieved. Therefore, we optimized the exposition dose for the Formlabs HiTemp resin for different layer heights. This optimisation was performed using a similar strategy to generate working curves as what was presented by Luongo et al.[3], generating a set of defined exposition intensities using different greyscale levels in projected images. We printed parts featuring lines of 300 μm width and 300 μm height printed with 26 different exposition doses. The lines height and width were then measured using a Bruker interferometer. The dose yielding the dimensions closest to the set dimensions was then used for printing at the

corresponding layer height. This process was repeated for each layer height presented in Figure 2 and 3.

Once we calibrated the optimal dose for accurate printing, we performed a tribological study of surfaces printed at different layer heights. The goal was to obtain the lowest coefficient of friction (COF) for the surfaces guiding the magnet plunger inside the valve body. We printed parallelograms at different layer heights with the optimised exposition doses and measured the coefficient of friction, in the direction that the magnet plunger follows during actuation, using an Aton-Paar tribometer. Three measurements were performed for each sample, using a ruby static counter parts, a normal force of 50 mN, a total measurement distance of 20 m and a linear speed of 1 cm/s. The measured coefficient of friction was averaged for each of the three measurements. The average and standard deviation of the three obtained values for each layer height are presented in Figure 2.

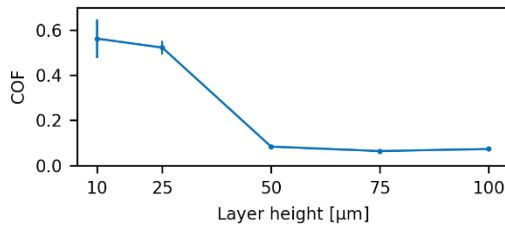


Figure 2. Coefficient of friction measured orthogonally to the printed layers as a function of the layer heights

A sharp decrease in coefficient of friction is observed for layer heights starting from 50 μm and above. This change in coefficient of friction can be explained by looking at the surface morphology for these different layer heights (Figure 3).

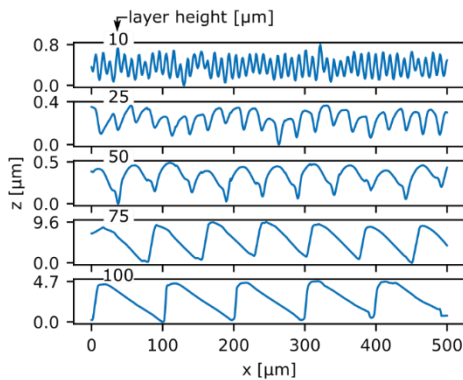


Figure 3. Surface profiles measured by interferometry for different layer heights

A sharp decrease in coefficient of friction is observed for layer heights starting from 50 μm and above. This change in coefficient of friction can be explained by looking at the surface morphology for these different layer heights (Figure 3). The scalloping observed for each layer is due to the resin absorption giving rise to an exponentially decaying exposition dose profile during printing[4]. We postulate that the increased frequency of this scalloping structures with decreased layer height leads to a larger area of contact for parts sliding against this surface, explaining the higher coefficient of friction at lower layer height. Hence, we decided to print the valve with a layer height of 50 μm, keeping the coefficient of friction at only 0.1 while keeping an acceptable resolution in the vertical print direction.

2.3. Valve performance and lifetime assessment

To assess the valve performance, we provided a constant pneumatic pressure at the valve inlet while measuring the pressure at the valve outlet. We actuated the valve at 10 Hz by switching the polarity at this frequency on the solenoid, using 0.2A of current. We measured a proper actuation at this frequency with up to 30 kPa inlet pressure (Figure 4)

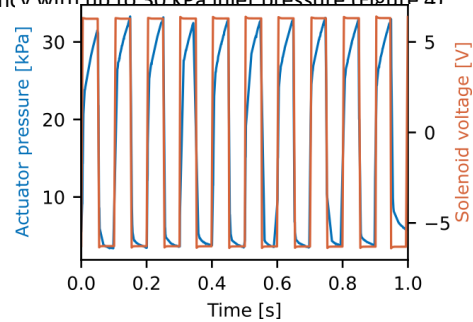


Figure 4. Characterization of the valve actuation at 10 Hz under 30 kPa

To benchmark the lifetime of the valve, printed with the optimised parameters leading to a surface coefficient of friction of only 0.1, we performed long term measurements at the 10 Hz actuation frequency. For three different valves we measured a lifetime of over 5 millions cycles (Figure 5), proving that the valves wear is mitigated by their low surface friction.

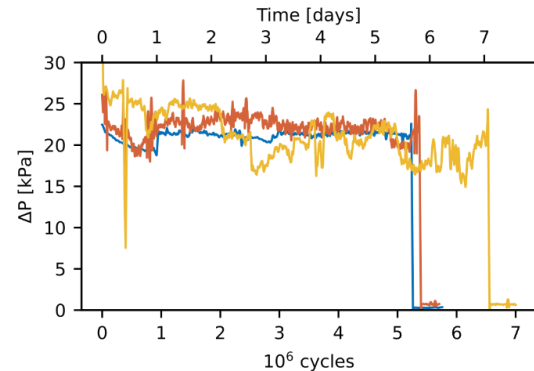


Figure 5. Measured pressure variation over the number of actuation cycles for three different valves, at an actuation of 10 Hz

3. Conclusions

We optimized a custom high resolution SLA printing process, based on a digital light processing UV projector, to 3d print miniature valves with an embed magnet plunger. Using a combination of microstructure analysis by interferometry and tribological characterisations we optimized the fabrication parameters to obtain accurate prints with low friction surfaces. This control allows an accurate guidance of the plunger inside the valve body, resulting in an actuation at high frequency with a lifetime of more than 5 million cycles under operation. The valves can be easily adapted and integrated to a wealth of applications thanks to their straightforward monolithic design and the adaptability granted by additive manufacturing. In conclusion, we have proved through optimization of tolerances and surface quality that SLA is suited to the production of miniaturized valves fitting the requirements of soft robotics actuation.

References

- [1] H. A. Sonar and J. Paik, 2016, *Front. Robot. AI*, vol. 2
- [2] H. Gong, A. T. Woolley, and G. P. Nordin, 2016, *Lab. Chip*, vol. 16, no. 13, pp. 2450–2458

- [3] A. Luongo *et al.*, 2020, *Comput. Graph. Forum*, vol. 39, no. 1, pp. 347–359
- [4] H. Gong, M. Beauchamp, S. Perry, A. T. Woolley, and G. P. Nordin, 2015, *RSC Adv.*, vol. 5, no. 129, pp. 106621–106632

Influence of the CNC behaviour on the laser spot trajectory in LPBF process

Kevin. Godineau¹, Sylvain. Lavernhe¹, Christophe. Tournier¹

¹Université Paris-Saclay, ENS Paris-Saclay, Institut Farman FR3311, LURPA, France

kevin.godineau@ens-paris-saclay.fr

Abstract

The quality of the parts produced in additive manufacturing by laser powder bed fusion (LPBF) depends on the understanding of all the physics involved in the process. In LPBF, the effective path of the laser spot is rarely studied and existing works are mainly focused on the choice of the scanning strategy and its parameters. However, the programmed scanning path during the CAM stage is adapted by the numerical control (NC) unit of the manufacturing machine in order to generate admissible setpoints for the actuators (galvanometers). This modification locally generates deviations on the scanning path and significant decrease of the laser spot velocity. In order to identify the NC unit behaviour, a test bench that replicates an industrial machine has been developed. This test bench allows the acquisition of the setpoints sent to the actuators and their real positions at a frequency of 100 kHz, as well as the energy deposited by the laser spot in the work plane. An analysis of those data shows that the processing done by the NC is based on a filtering method which in some cases can generate a deviation of the scanning path of more than 100 μm for a programmed speed of 2 m/s. Finally, in order to correctly estimate the amount of energy brought by the laser on the powder, a dedicated model has been developed. This model takes into account the dynamics of the actuators, the behaviour of the NC unit and the optical chain of the system. Experimental tests have been conducted to validate the simulations produced by the proposed model.

Accuracy, Computer numerical control (CNC), Identification, Monitoring

1. Introduction

The control of the effective path of the laser spot plays an essential role in LPBF process. Indeed, the movement of the laser spot on the powder bed allows distributing the energy necessary for the fusion. The work described in this paper highlights the impact of the numerical control unit behaviour on the effective path of the laser spot. The numerical control unit performs the following operations (also shown in figure 1):

1. Sampling - interpolate the paths generated by the slicer X^{cons} into a set of laser spot positions X^{inter} .
2. Inverse Kinematic Transformation (IKT) - convert laser spot positions X^{inter} into actuator positions Q^{inter} .
3. Geometric and Time Interpolation - locally modify the positions Q^{inter} to produce setpoints Q^{filt2} that respect the kinematic constraints of the actuators.

Step 3 is required because the paths generated by the slicer are not physically achievable, as they assume infinite accelerations of the actuators.

These 3 steps generate local modifications of the velocity and the effective path. This aspect is never taken into account in thermal simulations and is nevertheless critical, as it leads to greater energy deposition locally on the part. In machining and robotics, the operations carried out by the numerical control unit are well known and are the subject of many works. Those works are focused on the optimization of the instructions sent to the actuators to control the effective path of the system with respect to the kinematic constraints of the actuators [1].

In LPBF additive manufacturing, very few works deal with time interpolation of laser spot path. Wienken et al highlight the

developments of the SCANLAB company and succinctly describe the operation of the actuator control structure [2]. Trajectories that are initially speed-limited are processed to be transformed into acceleration-limited trajectories.

A research team at the National Institute of Standards and Technology (NIST) is also working on these aspects. For this purpose, they have developed a replica of a LPBF additive manufacturing machine [3]. Using this platform, they are able to analyse the control laws used by the industrial controller (velocity-limited laws) and implemented acceleration-limited [4] and jerk-limited [5] motion laws. The integration of these laws makes it possible to obtain setpoints that are less demanding on the actuators and are therefore better respected by the system.

The work carried out in this paper concerns the study and characterization of an existing industrial CNC. The analysis of this system allows us to highlight its limits and thus to underline the possible improvements.

This paper is organized as follows: section 2 is dedicated to the design of the test bench. The analysis of the different signals allows in section 3 to identify the behaviour of the CNC system and its impact on the effective path. This knowledge is used to set up a simulator of the energy supplied to the powder bed. This model is briefly presented and experimentally validated in section 4 before concluding remarks.

2. Design of the test bench

In this section, the developed test bench is presented and different signals are analysed to identify the control solutions implemented in the industrial numerical controller.

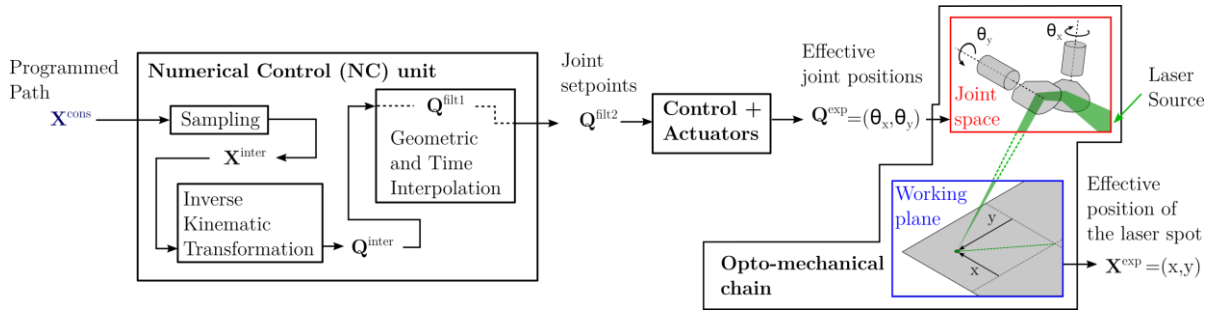


Figure 1. Architecture of the industrial numerical controller and the test bench developed.

2.1. Description of the test bench architecture

The architecture of the developed platform is shown in Figure 1. This platform integrates an industrial chain currently used in several LPBF additive manufacturing machines. The different signals used in this paper are presented in Figure 1. Signals that have not already been described are explained in the following list:

- Q^{filt1} refers to the internal setpoints of the time and geometry interpolation step.
- Q^{filt2} represents the joint position setpoints sent to the control system.
- Q^{exp} and X^{exp} represent respectively the joint positions of the actuators and the real positions of the laser spot in the working plane.

The test bench is completed with a camera in order to measure the energy deposited on the surface of the working plane. To simplify the measurements and minimize sources of error, the laser beam is fired directly on to the CCD matrix. This allows the trace of the laser spot to be observed. The technological solution used is detailed in [6].

2.2. Data analysis

To better understand the operations performed in the CNC, the joint signals Q^{inter} , Q^{filt1} and Q^{filt2} are derived to observe the angular velocities as well as the angular accelerations.

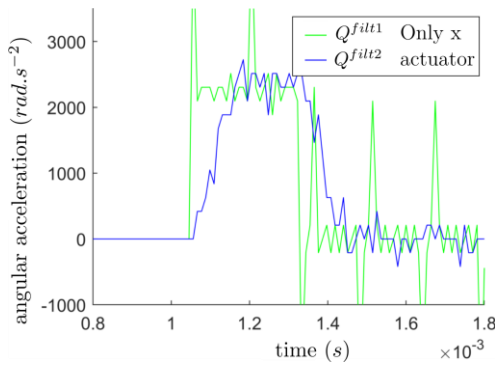


Figure 2. Angular acceleration measurement of the actuator x .

Figure 2 shows the angular accelerations of the different signals. For readability consideration, the signal Q^{inter} and Q^{exp} are not displayed. The input setpoints correspond to a velocity jump of the x -axis. The signal Q^{filt1} represents an acceleration pulse of duration $T_1 = 260 \mu s$. The signal Q^{filt2} represents an acceleration trapezoid whose rising and falling phase duration is identical and equal to $T_2 = 125 \mu s$. The Q^{filt2} signal therefore corresponds to a jerk-limited signal (acceleration trapezoid).

Observations made on this test were repeated for other setpoints on both actuators. The conclusions on the duration of the jerk and acceleration phases are identical. The same applies to the deceleration phases. The study of the literature shows

that the processing carried out by the numerical control unit is based on a finite impulse response (FIR) gate filtering approach [7]. The solution used consists of two successive gate filters of characteristic times T_1 and T_2 . These two filters of fixed duration make it possible to limit the maximum acceleration and jerk.

A velocity saturation is also performed between Q^{filt1} and Q^{filt2} when the setpoint exceeds the maximum velocity value of 25 rad.s^{-1} . In this work, such angular velocities are never requested from the actuators. Indeed, to request a single actuator (galvanometer) for this angular velocity would be tantamount to requesting for a laser spot velocity in the work plane of approximately 35 m.s^{-1} .

3. Analysis of the NC behaviour

In this section the influence of filtering on the velocity and the contour error is highlighted. An analysis of the system dynamics is also performed. Finally, all these developments are experimentally validated.

3.1. Assumptions and parameterization

To simplify the understanding, we will consider in the following work that the filters are applied on the X^{inter} setpoints in the working plane. The impact of the inverse kinematic transformation (IKT) on the filtering operation is therefore considered negligible. This assumption is validated through simulations. Over the whole angular range of the actuators and for velocity lower than 10 m.s^{-1} this assumption generates deviations that do not exceed 10^{-8} rad . This error transcribed on the working plane is therefore negligible because less than $0.1 \mu m$.

Finally, to simplify the study we are interested in the realization of a path composed of two successive segments represented in Figure 3. The programmed path is shown in black and the filtered one in blue.

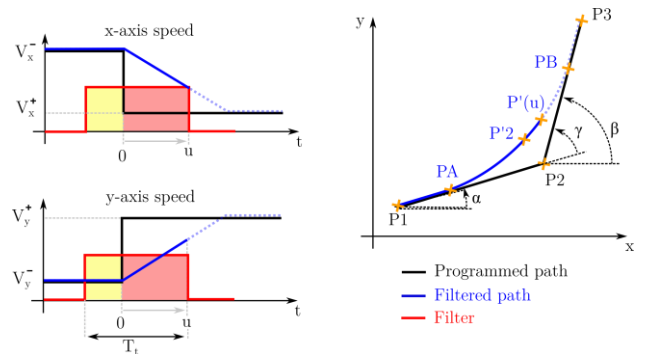


Figure 3. Parameterization of a filtering operation. Example with a gate filter.

1. The programmed velocity of the path is called V_{eff} .

2. The velocity of the x-axis is noted V_x^- on the segment $(P1, P2)$ and V_x^+ on $(P2, P3)$ (same for y-axis).
3. The oriented angle between the two segments is noted γ
4. The interaction time between the filter and the second segment of the path is noted u .
5. The function $a(u)$ corresponds to the algebraic area of the filter during the time u (red area on Figure 3).
6. The time of the filter, noted T_t , is symmetric and has a unit area $a(T_t) = 1$.
7. The function $A(u)$ corresponds to the integral of the algebraic area of the filter during time u .
8. When $u = 0$ the filter has no impact on the geometry of the path. The current point $P'(u)$ is located in PA .
9. When $u = T_t$ the filter has no longer impact on the path. The current point $P'(u)$ is located in PB .

3.2. Influence of filtering on path velocity

Firstly, the velocity of the filtered path is studied. The knowledge of this velocity is important, because a decrease of it leads to an increase of the deposited energy if the laser power is constant. The velocity of the x-axis is expressed in equation (1) (same for the y-axis).

$$Vf_x(u) = (1 - a(u))V_x^- + a(u)V_x^+ \quad (1)$$

The norm of the velocities $Vf_x(u)$ and $Vf_y(u)$ is used to calculate the tangential velocity of the filtered path. This velocity is written in equation (2).

$$Vf(u) = V_{eff} \sqrt{1 + 2 \cdot a(u)(1 - a(u))(\cos(\gamma) - 1)} \quad (2)$$

For a symmetric filter of unit area, the minimum of this function is obtained in $u = T_t/2$. The minimum velocity of the filtered path is expressed in equation (3).

$$Vf\left(u = \frac{T_t}{2}\right) = Vf_{min} = V_{eff} \left| \cos\left(\frac{\gamma}{2}\right) \right| \quad (3)$$

As shown in equation (3) the minimum velocity of the filtered path is independent of the filter used. This minimum velocity depends only on the tangential velocity and the angle between the two consecutive segments. $Vf_{min} = V_{eff}$ for $\gamma = 0$ and $Vf_{min} = 0$ for $\gamma = 180 \text{ deg}$. This equation is verified experimentally in section 3.5.

3.3. Influence of filtering on the contour error

It is also important to study the geometry of the filtered path. Indeed, this geometry has an impact on the effective path and therefore on the geometry of the built part. To study this, the contour deviation criterion e_c is used. This criterion defines for each point of the theoretical path the minimum distance between the whole filtered path and this point.

The filtered path $P'(u)$ shown in Figure 3 is calculated by starting from the position of the point PA and integrating the filtered velocity obtained in equation (1). After simplification, the equation (4) is obtained which gives the distance between the filtered path $P'(u)$ and the point $P2$.

$$\|P'(u) - P2\| = V_{eff} \left[\left(u - \frac{T_t}{2}\right)^2 + 2A(u) \left(u - \frac{T_t}{2} - A(u)\right) (\cos(\gamma) - 1) \right]^{1/2} \quad (4)$$

If the filter is positive then the functions $a(u)$ and $A(u)$ are monotone (increasing) and positive. Under this condition, the maximum contour deviation is obtained in $u = T_t/2$. The

contour deviation then corresponds to the distance between $P'2$ and $P2$. The point $P'2$ is then located on the bisector between the two consecutive segments. The previous equation can thus be simplified to obtain equation (5).

$$e_c = 2 \cdot V_{eff} A\left(\frac{T_t}{2}\right) \left| \sin\left(\frac{\gamma}{2}\right) \right| \quad (5)$$

This equation describes the deviation from the contour as a function of the integral of the filter area, the velocity of the programmed path and the oriented angle between the two consecutive segments. This equation is valid for all positive symmetric filters of unit area.

When applying equation (5) to a trapezoidal filter (combination of two gate filters of durations T_1 and T_2 with $T_1 > T_2$) equation (5) becomes:

$$e_c = V_{eff} \frac{T_2^2 + 3T_1^2}{12T_1} \left| \sin\left(\frac{\gamma}{2}\right) \right| \quad (6)$$

Equation (6) is verified experimentally in section 3.5.

3.4. Identification of the dynamic behaviour of the system

Now that the architecture is known, it is possible to identify the dynamic behaviour of the control system and the actuators. To do this, sinusoidal setpoints are sent to each axis.

Figure 4 shows the ratio between the amplitudes of Q^{exp} and Q^{filter} signals at different frequencies. This figure shows the behaviour of the actuators and their control structures. The assembly associated with the y actuator is less dynamic, this is due to the fact that the mirror has a greater inertia.

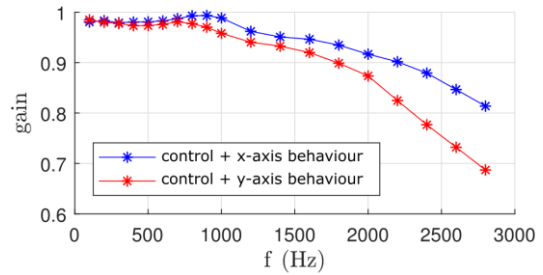


Figure 4. Bode diagram of the behaviour of the assembly (Control + Galvanometer).

3.5. Experimental validation

In order to confirm the developments made in sections 3.3 and 3.4, several paths with different velocity and angles were performed. Figure 5(a) shows the set path, the filtered path and the actual path. Figures 5(b) and 5(c) show respectively the tangential velocity and contour error profiles

For angle 1 ($\gamma = 53,13 \text{ deg}$) equations (3) and (6) predict a minimum velocity of $1789 \text{ m} \cdot \text{s}^{-1}$ and a contour error of $62 \mu\text{m}$. The experimental results show that the minimum velocity of the filtered set points is $1708 \text{ m} \cdot \text{s}^{-1}$ and the contour error is $62 \mu\text{m}$. For angle 2 ($\gamma = 108,43 \text{ deg}$) the theoretical velocity is $1170 \text{ m} \cdot \text{s}^{-1}$ and the contour error is $114 \mu\text{m}$. The measurements show a minimum velocity of $1101 \text{ m} \cdot \text{s}^{-1}$ and a contour error of $109 \mu\text{m}$. The deviations between theory and measurement in velocity are mostly due to errors in sampling of the setpoints made in the numerical control unit.

The effective path is very similar to the filtered path. This is due to the actuator servo control, which is very efficient, and to the filtering, which allows the generation of achievable setpoints.

By studying the filtering further, the limits of the employed solution can be shown. For example, the acceleration and deceleration duration is always constant, regardless of the value of the requested velocity. The actuators are therefore not used to their full capabilities. It is thus possible to improve this solution by adapting the filter duration to the solicitation. This would save time without necessarily losing quality.

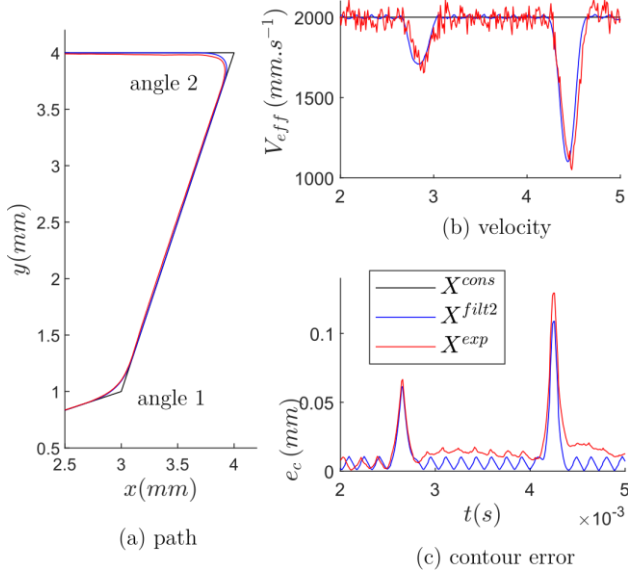


Figure 5. Path performed at a programmed velocity $V_{eff} = 2 \text{ m.s}^{-1}$.

4. Impact on the energy provided to the powder

Now that the impact of the system dynamics on the path has been quantified, it remains to add the energetic behaviour of the laser source in order to establish a model in order to simulate the energy deposition on the powder bed.

The modelling of the laser source and the measurement protocol of the deposited energy are described in [6]. The developed simulator takes into account:

1. the behaviour of the CNC identified in section 2.2, 3.2 and 3.3;
2. the dynamics of the actuators as well as the servo control identified in section 3.4;
3. the energy distribution of the laser source which is in this paper considered as Gaussian;
4. the influence of the opto-mechanical chain on the energy delivered by the laser spot on the powder bed [6].

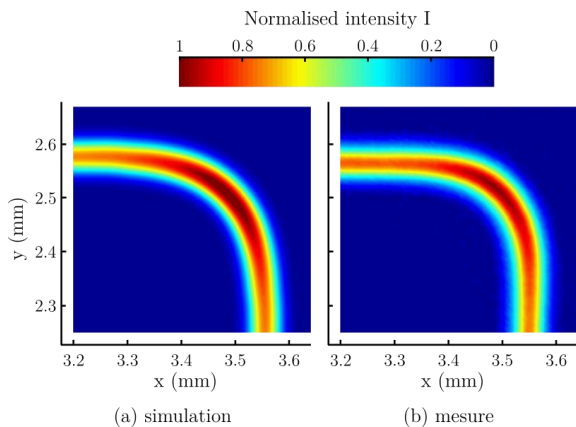


Figure 6. Influence of interpolation on a path composed of two right-angled segments for a programmed velocity $V_{eff} = 1,5 \text{ m.s}^{-1}$.

Figure 6 shows the energy delivered to the powder bed in the case of a right-angle path of programmed velocity $V_{eff} = 1,5 \text{ m.s}^{-1}$. The laser beam used on the test bench is of very low power (1 mW) in order not to damage the CCD matrix. Thus, for readability purposes, the intensity is normalised.

The geometrical deviations from the target path are in good agreement with equation (6). The decrease in velocity observed in the corner generates an accumulation of energy. The simulator is accurate and allows the energy provided to the material to be quantified. The deviations on the maximum amplitude are about 5% and the differences between the model and the measurement are mainly due to the energy distribution of the laser source at the entrance of the opto-mechanical chain. The experimental energy distribution of the laser source is not perfectly a gaussian distribution which is an assumption made here.

5. Conclusion and perspectives

A test bench has been developed in order to study the impact of the CNC processing on the laser spot path. Filtering solutions have been highlighted. These solutions lead to velocity decreases as well as significant deviations from the CAM path. The identification of the machine's behaviour has allowed the development of a simulator to study the energy provided to the powder bed.

This work can greatly improve thermal simulations by taking into account the effective path and tangential velocity of the laser spot. This study also highlights numerous perspectives related to the development of new control strategies. For example, it seems relevant to couple the power of the laser beam and the kinematics of the trajectories in order to homogenize the energy deposition.

Acknowledgements

This work is supported by the SOFIA project and funded by Bpifrance.

References

- [1] Tajima S, Sencer B and Shamoto E, "Accurate interpolation of machining tool-paths based on FIR filtering" *Precision Engineering*, vol. **52**, pp. 332-344, 2018
- [2] Wienken C. J., Unterholzner A and Breit M, "Advanced galvo control enables efficient laser micro processing" *9th International Conference on Photonic Technologies*, LANE 2016
- [3] Lane B and al., "Design, Developments, and Results from the NIST Additive Manufacturing Metrology Testbed (AMMT)" *Proceedings of the 26th Annual International Solid Freeform Fabrication Symposium--An Additive Manufacturing Conference*, pp. 1145-1160, 2016
- [4] Yeung H, Neira J, Lane B, Fox J and Lopez F, "Laser Path Planning and Power Control Strategies for Powder Bed Fusion Systems" *Solid Freeform Fabrication Symposium*, 2016
- [5] Yeung H, Lane B, Donmez M, Fox J and Neira J, "Implementation of Advanced Laser Control Strategies for Powder Bed Fusion Systems" *Procedia Manufacturing*, vol. **26**, pp. 871-879, 2018
- [6] Godineau K, Lavernhe S and Tournier C, "Influence of the opto-mechanical chain on the energy provided by the laser spot to the material in laser powder bed fusion processes" *EUSPEN Special Interest Group Meeting*, 2019
- [7] Biagiotti L and Melchiorri C, "FIR filters for online trajectory planning with time- and frequency-domain specifications" *Control Engineering Practice*, vol. **20**, pp. 1385-1399, 2012

Toward specification of complex additive manufactured metal surfaces for optimum heat transfer.

Kuldeep Mandloi¹, Chris Evans², Jason C. Fox², Harish Cherukuri¹, Jimmie Miller¹, Angela Allen¹, David C. Deisenroth², Alkan Donmez².

¹University of North Carolina at Charlotte, USA

²National Institute of Standards and Technology, Gaithersburg, USA

kmandloi@uncc.edu

Abstract

Metal additive manufacturing (AM) offers the possibility of incorporating cooling channel geometry into components in high-temperature applications. Additionally, it has the prospect of optimizing cooling channel geometry unconstrained by geometric limitations of conventional machining processes. Such channels will necessarily have surfaces manufactured at various orientations resulting in different topographies that may influence heat transfer. Numerous studies have shown that conventional (amplitude) roughness parameters do not discriminate between topographies produced under different build conditions – but such descriptions have been used in studies of micro-channel, heat exchanger performance. The motivation behind this study is to explore the correlation between AM roughness characteristics (weld tracks amplitudes/wavelengths and their orientation, spatter, etc) and the resulting effect on heat transfer and pressure drop in fabricated microchannels. Computational Fluid Dynamics (CFD) models for mini-channels using StarCCM+ (a CFD code) were developed by acquiring the roughness data from the real AM surfaces with various roughness parameters such as different wavy patterns and the part orientation during the build. Simplified versions of measured surface topographies reduce the computational overhead. The pressure drops across the mini-channels and Nusselt (Nu) numbers were computed and analyzed for these cases under both laminar- and turbulent-flow conditions. Significant differences in the Nu numbers and pressure drops were observed across the different AM surfaces considered. Further CFD modeling of mini-channels with different wavy surfaces helped in exploring the suitable dimensions for the mini-channel experimental set-up and also enabled exploration of the Reynolds number range to consider experimentally. Heat-balance considerations have been used to validate the current findings. An experimental set-up is under development to compare models in an idealized set-up. Initial results from the experiments are also described.

Cooling, Experimentation, Fluid, Modeling, Surface Roughness

1. Overview

The aerospace community has a great interest in additive manufacturing (AM), particularly laser powder bed fusion (LPBF), since it can be used to manufacture parts from high-temperature nickel alloys. However, the uncertainty in material properties makes LPBF questionable for use in high stress turbine parts, though interest for high temperature parts with complex cooling channels is growing [1]. The complexity of these cooling designs is limited in conventional manufacturing methods. Using AM, designers have the opportunity to create cooling geometries that would be impossible to achieve with other methods. While roughness of external surfaces may be reduced through conventional machining, most surface treatment processes cannot be applied to internal channels especially when the dimensions are a millimeter or sub-millimeter scale [6].

For adoption of AM for parts requiring complex cooling channels to continue, an understanding of the relationship between the as-built surface finish and heat transfer must be developed. In LPBF, there are numerous build parameters, such as part orientation during the build, that affect the final part-surface topography and hence heat transfer. There is already a substantial literature in the measurement of surfaces produced

by metal additive manufacturing and by powder bed fusion techniques, in particular [2]. It is generally recognized that complex, textured surfaces are poorly characterized or specified by conventional statistical parameters (see for example [3]). The classic literature on the impact of surface roughness on heat transfer (Moody's diagram) uses a simplified treatment of surface roughness, while powder bed fusion processes generate complex surfaces with a mixture of strongly anisotropic, periodic components and a population of individual features (pores and particles, for example), all of which may affect heat transfer and fluid flow. Simonelli et al. [4] have investigated the effect of build direction on mechanical properties of Selective Laser Melting (SLM) and Direct Metal Laser Sintering (DMLS) parts. However, no build-direction studies have examined the effects on internal channel geometry with spatter and their effects on heat transfer at different Reynolds number conditions.

The focus of this study is the dependence of fluid-flow and heat transfer characteristics on the surfaces based on build-orientation and spatter. Our goal is to relate appropriate surface specification to heat transfer. Various Computational Fluid Dynamics (CFD) models for mini channels using Star CCM+ were developed by acquiring the roughness data from the real AM surfaces with varying surface characteristics such as different wavy patterns and build direction variation. Simplified geometric models of AM surfaces based on the measured

surface topographies were developed to reduce the computational overhead (see Figs 3 and 4). The pressure drops across the mini-channels and Nusselt numbers (Nu) are computed and analyzed for a variety of surface topographies under both laminar and turbulent flow conditions. The CFD results show a significant difference in Nu numbers and pressure drop with AM surfaces and different part orientation during the builds. Further CFD modeling of mini-channels with different wavy surfaces facilitated exploration of suitable dimensions for the mini-channel experimental set-up and also enabled identification of the Reynolds number range for the experiments. Heat balance considerations and results from equipment experimental setup have been used to validate the current findings.

2. Methodology to Model AM surfaces

In this work, simplified AM surfaces were modeled. Prior work on characterization of topography with changes in part orientation during the build is published in CIRP Annals [5]. In that work, several characterization techniques analyzed surface data captured using a focus-variation microscope to better understand the effect of part orientation during the build on surface features. Investigations of the area scale (Figure 1), amplitude-wavelength content, and positions of partially-melted powder particles on the surface showed the large dynamic range of surface-structure wavelengths and amplitudes. Initial attempts at modeling heat transfer with real AM surfaces were unreasonable due to long computational time as a result of the required mesh sizes.

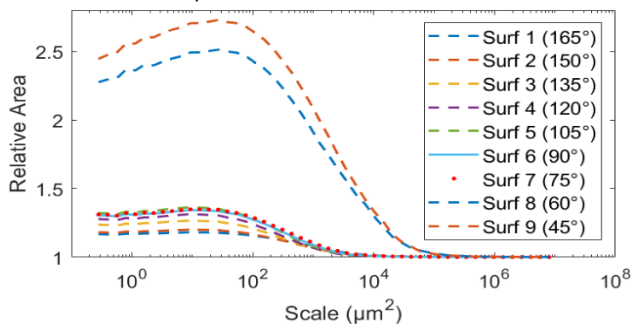
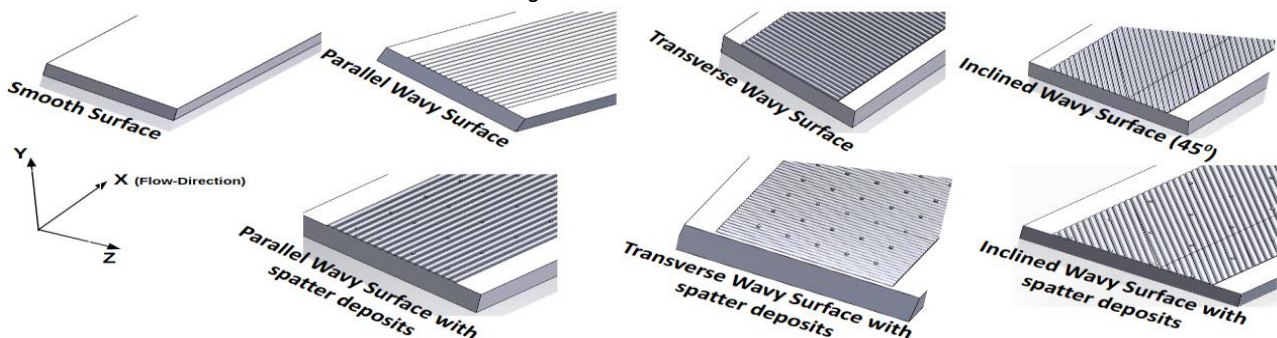


Figure 1. Relative Area analysis of AM different surfaces [5].

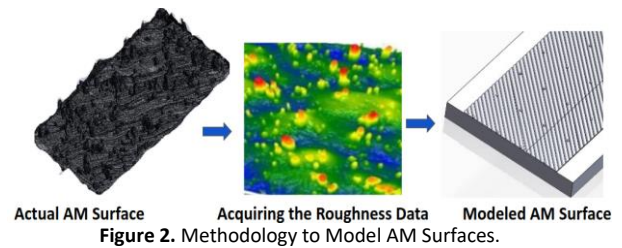
The methodology to model AM surfaces is shown in Fig. 2. To model the wavy surfaces, the root mean square (RMS) dimensions of actual surfaces (e.g., wavelength of 150 μm and amplitude of 30 μm) have been used. The wavy surface is idealized by using the absolute value sine function with a period and amplitude consistent with these RMS values.

Figure 4. Modeled AM Surfaces



3.2. Model Assumptions

Steady-state conditions were assumed for the fluid flow and heat transfer through conduction and convection. Mass flow inlet and pressure outlet boundary conditions were applied at



To test variation due to part orientation during the build, three surface patterns have been modeled. These surfaces include bead orientations (track/scan directions) parallel to the flow, transverse to the flow, and at a 45° angle to the flow. For the comparison of CFD results, a smooth surface has also been modeled as a reference. According to Figures 3 and 5 in [5], the relative area of AM surfaces is significantly affected by protrusions (spatter deposits). To identify the effect of those spatter deposits on the heat transfer, hemispherical protrusions on the top of wavy surfaces were added. The size of the protrusions (i.e., spatter) is the mean radius (29 μm) of the powder particles used. Modeled AM surfaces with different part orientations during the builds, with and without spatter, are shown in Fig.4.

3. Methodology for Numerical Investigation

3.1. CFD Models

The CFD models and planned test channels have a thermoplastic resin (i.e., Polyoxymethylene, POM) side and upper walls while the bottom part of the channel was made of nickel superalloy 625 (IN625) (Fig 3). The POM thermoplastic resin was chosen as the material for side and upper walls as preparations for experimental analysis showed this material could be fabricated to the required designs while isolating the effects of AM surfaces and reducing the conduction loss from side and upper walls.

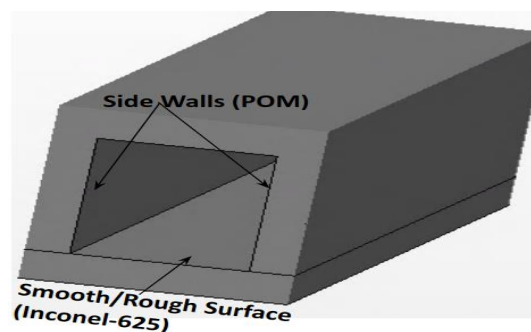


Figure 3. CFD Model with artificial AM surfaces

the entry and exit of the channel, respectively. All sidewalls of the channel were assumed to be insulated and constant heat flux was provided at the bottom of the channel. In-built laminar and turbulent flow models ($k-\epsilon$ model) in StarCCM+ were used during the simulations.

4. Grid Independence Study

For the grid independence analysis, the average surface-output temperature was plotted against the number of cells (shown in Fig.5) and various trades were run to optimize the mesh size, ranging from 85000 to 5 million cells. The optimum number of cells was approximately 3 million. For the meshing, the prismatic, boundary-layer cells were used to resolve the boundary layers at fluid-solid interfaces. In order to capture the circulation near the wavy surfaces, the growth size of prismatic layers was kept at 15 percent of the base size.

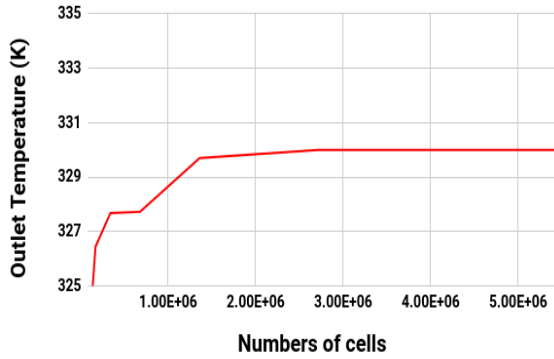


Figure 5. Grid Independence Analysis.

5. CFD Results and Discussion

The effects of surface roughness on heat transfer were analysed in terms of the Nusselt Number (Nu), the Pressure Drop (ΔP) across the channel, and a Performance Factor (PF). Here, the performance factor has been defined as the ratio of Nu to (ΔP).

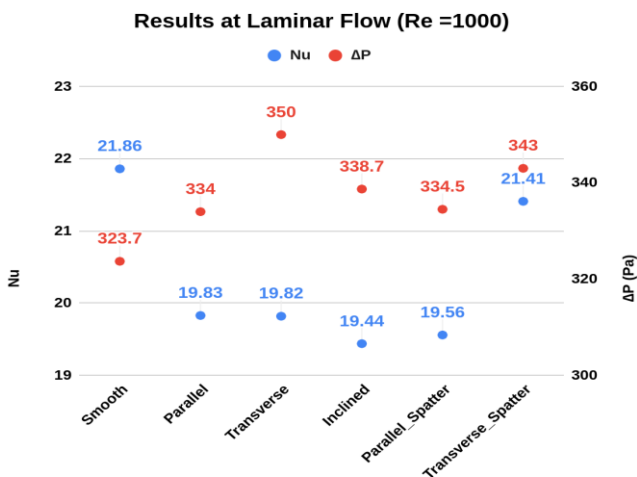


Figure 6. Nusselt Number (Nu) and Pressure Drop (ΔP) for various channels for the laminar flow case.

The laminar flow ($Re = 1000$) results for Nusselt Number (Nu) and Pressure drop (ΔP) for various channels containing different artificial rough surfaces are shown in Fig 6. The corresponding results for turbulent flow with $Re = 4000$ are shown in Fig 7. As the figures indicate, smooth surfaces perform (thermally) the best (higher Nu and lower ΔP values) under laminar flow conditions. However, under turbulent flow conditions, the Nu number for smooth surface case decreases significantly. Another interesting observation is that the channel with transverse AM surface and spatter deposits performs as well as the smooth surface case under laminar flow conditions. However, when turbulent flow conditions are present, it performs better than the smooth surface case. This is also confirmed by the performance factor calculations shown in

Fig 8. From Fig 7, it is clear that, for the turbulent flow case, the thermal performance of the channels with transverse AM surfaces is much higher than the channel with smooth surfaces.

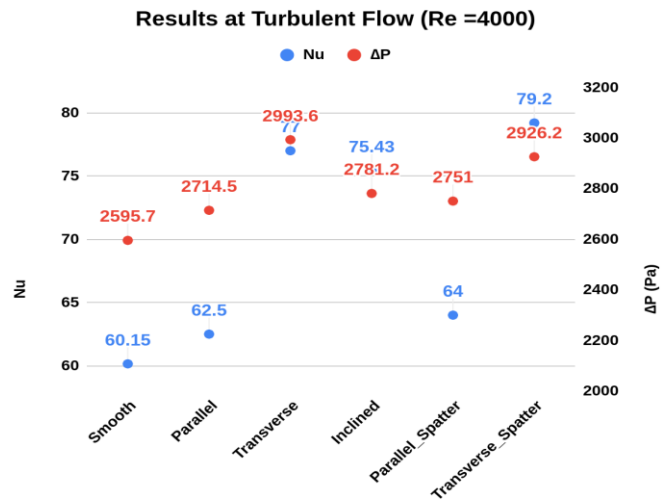


Figure 7. Nusselt Number (Nu) and Pressure Drop (ΔP) for various channels for the turbulent flow case.

Performance Factor (PF) for both Laminar and Turbulent Flow

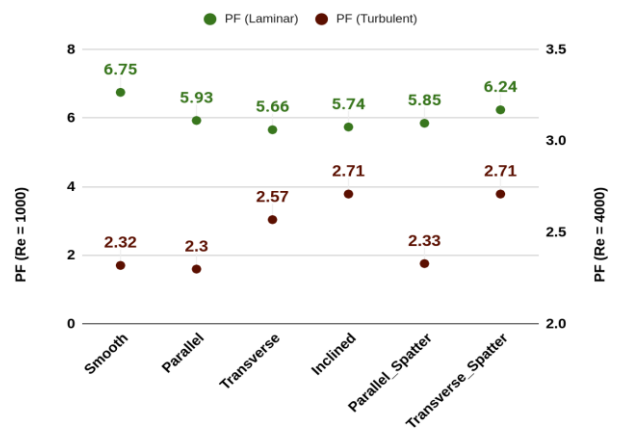


Figure 8. Performance Factor (PF) x 100 for various channels for the laminar and turbulent flow cases considered.

6. Validation of CFD Modeling

To validate the CFD modeling and to test the experimental equipment, an initial experimental setup was designed with aluminium alloy 6061(having smooth internal surface) and tested with different mass flow rates and amount of heat supply. The test setup contains four holes (on the upper side of the channel) with different sizes to accommodate two cylindrical heaters and temperature probes. Figures 9 and 10 show the CFD model and the setup for equipment testing. The experimental results from this test setup were used to validate the steady-state CFD simulation. Preliminary results from the experiment are shown in Fig.11 and the CFD and experimental results are shown in Table 1 for comparison.

From Table 1, it can be observed that the CFD and the experimental results are quite similar. The slight difference in the outlet temperature is due to the varying environmental conditions and distance from the actual outlet of the channel to the outlet water temperature probe (as shown in Fig. 9). Similarity between the results, however, validates the CFD models.

Table 1: Comparison of CFD and Experimental results (Laminar-Flow)

Parameters	CFD Results	Experimental Results (mean)	Uncertainty in Experimental Results
\dot{m}	0.0053 kg/s	0.0053 kg/s	-
Q_{in}	28 W	28 W	-
T_{in}	26.85°C	26.85°C	-
T_{room}	22.20°C	22.20°C	-
T_{out}	29.10°C	28.15°C	0.01°C
T_{Probe1}	35.30°C	33.12°C	0.03°C
T_{Probe2}	37.20°C	35.35°C	0.06°C
T_{Probe5}	35.40°C	33.23°C	0.05°C
Time Constant	32.01 s	32.6 s	

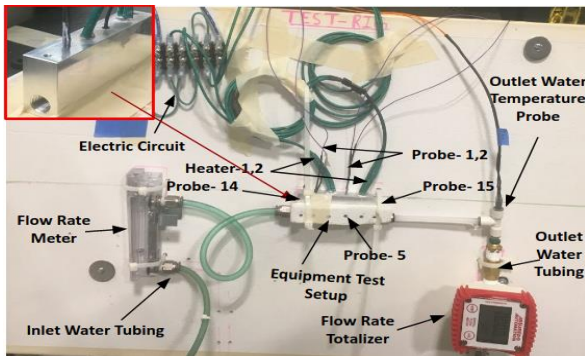


Figure 9. Experimental Setup.

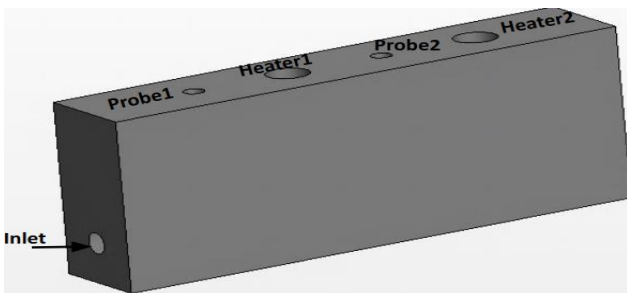


Figure 10. CFD Setup.

7. Conclusion

In this paper, the fluid-flow and heat-transfer characteristics of various mini-channels with different AM surfaces were studied computationally. Both laminar- and turbulent-flow conditions were considered in the CFD simulations. The computational studies show that smooth surfaces provide the best thermal performance under laminar-flow conditions. However, under turbulent-flow conditions, smooth surfaces along with parallel wavy surfaces appear to perform the poorest. Interestingly, the transverse AM surface with spatter deposits performs almost as well as the smooth surface case in laminar-flow studies and significantly better in turbulent-flow studies. This observation is further confirmed by the performance factor calculations. Preliminary results on validating CFD results with

experiments have been encouraging. Further experimental work to validate the CFD results for various AM surfaces is currently under development.

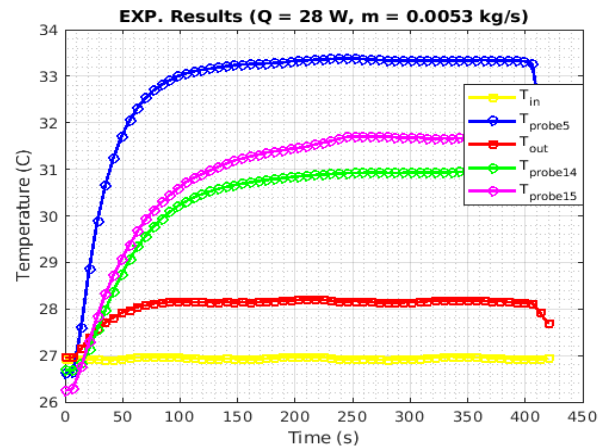


Figure 11. Preliminary Results from Experiments.

Acknowledgements

We would like to extend gratitude to the Affiliates of Center for Precision and Metrology (CPM) at UNC Charlotte for providing the financial support to this project. We also extend our heartiest thanks to the CPM and the MEES Department at UNC Charlotte for providing access to their research facilities such as high-performance computing (HPC) clusters for CFD simulations and CPM laboratories for conducting experiments.

References

- [1] Jacob C. Snyder, Curtis K. Stimpson, Karen A. Thole and Dominic Mongillo Y 2016 Build Direction Effects on Additively Manufactured Channels J. Turbomach. **TURBO-15-1262**.
- [2] R.K. Leach, D. Bourell, S. Carmignato, A. Donmez, N. Senin, W. Dewulf, Geometrical metrology of metal additive manufacturing, CIRP Ann. 68 (2019) 677–700.
- [3] X.Jiang, N. Senin, P.J. Scott, Francois Blateyron Feature based characterization of surface topography and its application, CIRP Ann 70,2(2021) in press
- [4] M. Simonelli, Y.Y. Tse and C. Tuck Y 2014 J. Materials Science and Engineering. **616** 1-11.
- [5] Jason Fox, Chris Evans and Kuldeep Mandloi Y 2021 Characterization of laser powder bed fusion surfaces for heat transfer applications CIRP Annals Manufacturing Technology.
- [6] Pyka G., Burakowski A., Kerckhofs G., Moesen M., Van Bael S., Schrooten J. and Wevers M. Y 2012 Surface modification of Ti6Al4V open porous structures produced by additive manufacturing. Adv. Eng. Mater. 14(6) pp. 363–370.

Disclaimer

Certain commercial entities, equipment, or materials may be identified in this document in order to describe an experimental procedure or concept adequately. Such identification is not intended to imply recommendation or endorsement by the National Institute of Standards and Technology, nor is it intended to imply that the entities, materials, or equipment are necessarily the best available for the purpose.

Surface topography process signatures in nickel superalloy 625 additive manufacturing

J.C. Fox(2), A. Allen(1), B. Mullany (1), E. Morse(1), R.A. Isaacs (3), M. Lata(1), A. Sood (1), and C. Evans (1,2)

¹ University of North Carolina at Charlotte, ² National Institute of Standards and Technology, ³ Zeiss
cevas52@uncc.edu

Abstract

Prior analyses of surface measurements performed – by several groups – on laser powder bed fused metals have tended to use ISO standard short wavelength filters and focus on weld tracks, “chevrons” (melt pool wake), and particles. This work, utilizing two sets of nickel superalloy 625 samples fabricated in an EOS M290 three years apart, extends the palette of features analyzed. In addition to the previously identified features, coherence scanning interferometer measurements reveal fine dendritic structures with a base periodicity of order 1 μm and long-range order up to 100 μm . Localized areas of radial primary dendrites with orthogonal secondary dendrites are also observed. Additional observations include areas of disordered fine structure, fine particles, and localized thin films, presumably from the plume of condensing metal. The composition of these features is varied, both locally and across the extent of the samples.

Laser Powder Bed Fusion, Nickel Superalloy, Surface structure, Microstructure

1. Introduction

Laser powder bed fusion (LPBF) is one popular process for additive manufacturing (AM) of a range of metals, including superalloys such as nickel superalloy 625 (IN625) discussed here. Surface topography is widely used as one acceptance criterion in conventional manufacturing and as a process signature for process optimization and control. Top surfaces in LPBF have surface topographic features with amplitudes and spatial wavelengths greater and more diverse than in conventional machining that challenge conventional geometric metrology [1] and are poorly described by commonly used surface measurement parameters.

Prior analyses of surface measurements – performed by several groups – on laser powder bed fused metals have tended to focus on weld tracks, “chevrons” (melt pool wake), particles, undercuts, and cracks, as reviewed in [2] and cited references [1,3,4]. Here we report on additional textures and features with lateral scales varying from a 100 μm scale down to tens of nm on LPBF IN625.

2. Experimental methods

Two sets of samples were built in the progression of this study. The first is described in detail in Reese *et al.* [5]. The second set (12 samples) was fabricated in 2020 with integrated coordinate systems that allow the location of features measured with a variety of tools. The samples were built in IN625 using a commercially available EOS M290 system. Vendor recommended process parameters were used for the part, except the upskin (e.g., region near the upward facing surfaces) where parameters are varied to improve surface finish was turned off, maintaining interior characteristics of the build at the top surface for examination.

The data from sample 9 in the 2020 build is analyzed in this work (see Figure 1 for details). Sample 9 is a block (20 mm x

25 mm) whose base height is approximately 10.57 mm above a sub-plate with sub-regions 9B to 9E each increasing in height by one layer (40 μm). An integrated coordinate system is ‘burned’ on the sample using the laser (no additional powder) to enable the location of specific regions on the different measurement systems. The build was performed on a 127 mm x 127 mm x 12.5 mm sub-plate, which was bolted to the center of the LPBF machine’s build plate. Figure 1 also indicates the locations of the sample and sub regions with respect to the sub-plate and machine argon gas delivery source.

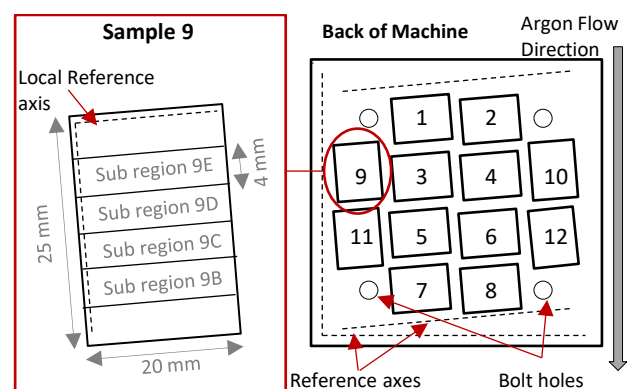


Figure 1. Schematic (top-down view) of sample 9 (left) and build layout of the 127 mm x 127 mm subplate (right).

Measurements of the first set of samples showed unexpected films and particulates, which might have been a by-product of the wire electrical discharge machining (EDM) removal of samples from the build plate, or handling protocols [5]. Thus, for the second set, loose powder was removed with care to minimize interaction with the sample surfaces and the entire sub-plate was double bagged until cleaning.

Cleaning was performed with the sub-plate face down in two room temperature ultrasonic baths, first in acetone and then in high purity ethanol. Initial coherence scanning interferometer

(CSI) measurements were performed before any machining to remove samples from the build plate.

The surface metrology results presented here were obtained using a Zygo NexView CSI with a 50x (0.55 NA) Mirau objective (spatial sampling 0.17 $\mu\text{m}/\text{pixel}$ with 4x oversampling to minimize data drop-out) [6]. Features of interest (Fol) have lateral scales from hundreds of micrometers to below the diffraction limit. The Sparrow criterion indicates a limiting lateral resolution of 0.52 μm . Smaller discrete features may be identified [7] although the amplitude reported is not reliable. To reach the longer spatial wavelength of interest, stitching algorithms native to the Zygo MX software are used [8].

Intensity images in the CSI are in focus at every pixel on rough surfaces. The modulation intensity mode provides high contrast surface images that facilitate identification of Fol for detailed evaluations of height maps and, using the developed coordinate systems, locating Fol in other measurement tools.

Scanning electron microscope (SEM) images were acquired on a ZEISS GEMINI SEM 450, Secondary Electron (SE) and In-lens SE-detectors. Energy Dispersive Spectroscopy (EDS) was performed at 5kV with an Oxford UltimMax 100 mm² large area Analytical Silicon Drift Detector (SDD). To facilitate these measurements, the sub-plate was sectioned using a bandsaw with no cooling fluids to prevent contamination. To prevent damage to the sample, sectioning was performed through the sub-plate to separate sample 9 from the rest of the build. Sample 9 was then re-cleaned ultrasonically using ethanol for 8 minutes before packaging and shipping to the Zeiss facility for measurement.

3. Results

In investigating the height and intensity data from the CSI system, the expected chevron patterns are more subtle in this sample because build conditions led to large length-to-width melt pool ratios such as those seen in [4]. Several other textures and fine scale features were present in addition to flow lines and chevron patterns. This section will detail the various structures found on the sample surface and Figure 2 depicts the relevant size scales observed.

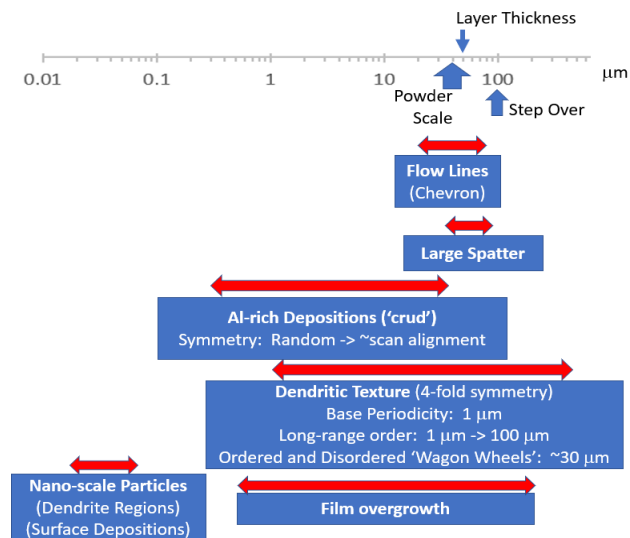


Figure 2. Graphical representation of size scales observed for features of interest.

An intensity image from the Zygo system, which captures many of the Fols, and an SEM image of the same area are shown in Figure 3 and Figure 4, respectively.

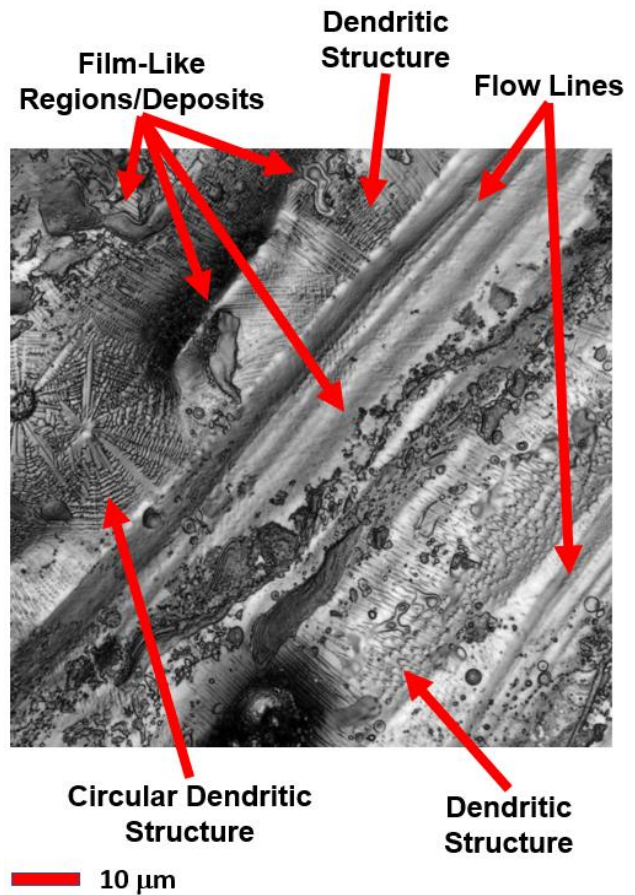


Figure 3. Intensity image from the Zygo Nexview CSI with various structures identified. Direction of laser path is $\approx 45^\circ$ through the image.

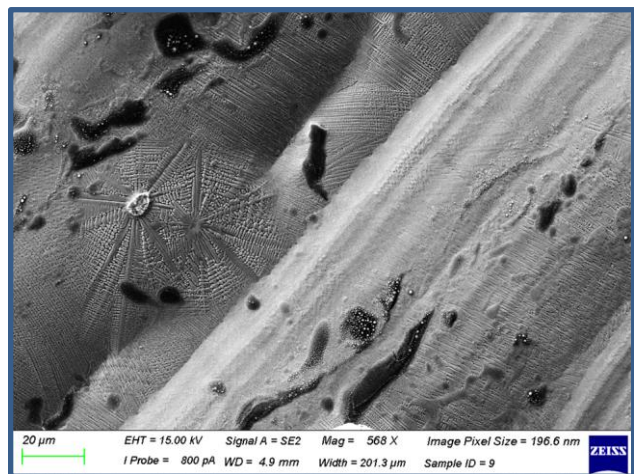


Figure 4. SEM image of approximately the same region as Figure 3.

3.1. Film-like Regions and Deposits

Across the surface there are regions of a film-like structure that appear to obscure other features. These structures were previously thought to be contamination from the wire electrical discharge machining (EDM) but are present without subjecting the part to that process thus nullifying that hypothesis. Size scales of these regions are on the order of below 1 μm to tens of micrometers. They are irregular in shape but tend to cluster somewhat parallel to the direction of the laser path. These are seen labeled in Figure 3 and as dark regions in Figure 4. Figure 5 presents results of an elemental analysis of a similar region via EDS. From the elemental analysis, the deposit has very high aluminum and oxygen content. For reference, the material

specification for IN625 requires aluminum to be less than 0.4% with no oxygen specified. Additionally, the LPBF process is performed in an inert argon environment. It is hypothesized that the aluminum content is vaporized in the fusion process and subsequently re-deposited on the surface, with oxygen being a contamination pickup from powder recycling/storage/reuse [9] or atmospheric oxidation of an aluminum film. Additional analysis is ongoing.

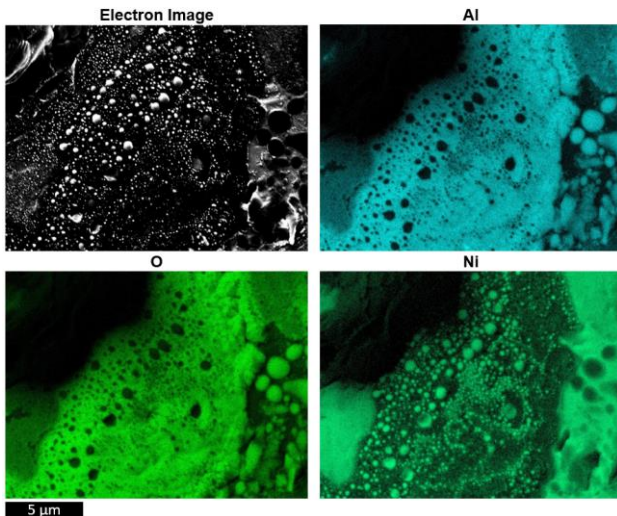


Figure 5. Elemental window integral maps from EDS of a film-like region. Only aluminum, oxygen, and nickel maps are shown for brevity.

3.2. Dendritic Structures

Dendritic structures are another common feature seen on the surface and have varying characteristics. Dendritic structures are expected for IN625 [10]. Common among all the dendritic structures is a base periodicity of $\approx 1 \mu\text{m}$ and long-range order from $1 \mu\text{m}$ to $\approx 100 \mu\text{m}$. Some of the dendritic structures appear in a near circular shape with rotational symmetry and primary dendrites forming a line between the edge and the center of the structure with orthogonal secondary dendrites. The pattern resembles a “wagon wheel” and is observed to have diameters in the tens of micrometers range with either a small depression (100's nm scale) or particle ($10\text{'s } \mu\text{m}$ scale) at the center, suggesting these structures are related to particle impacts on the surface (i.e., either ejecta remelting part of the surface or particles solidifying a portion of the melt pool on contact). An example, seen in an SEM image, is shown in Figure 6.

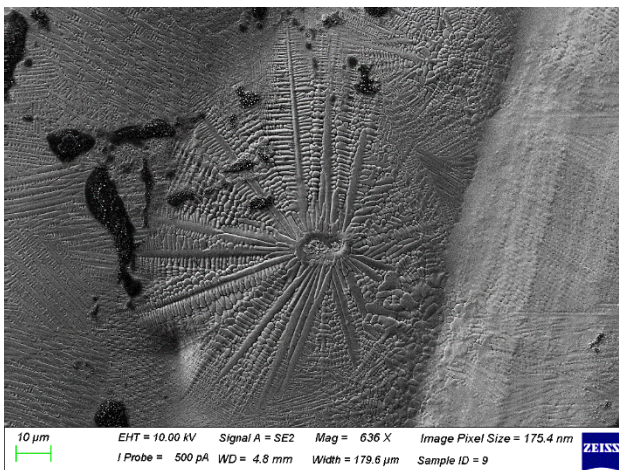


Figure 6. A circular dendritic microstructure.

Height measurement of one such structure, with a cylinder form removal and digital Gaussian high-pass filter of $30 \mu\text{m}$,

shows a peak to valley height profile of approximately $1 \mu\text{m}$ and width between $10 \mu\text{m}$ and $20 \mu\text{m}$.

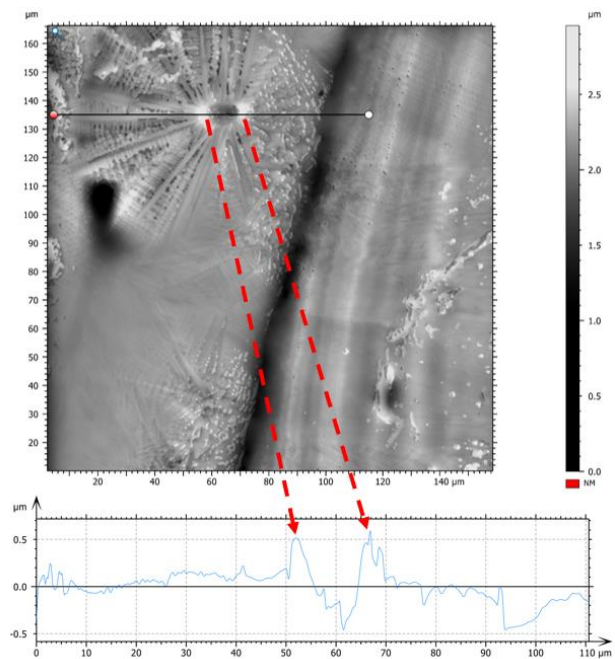


Figure 7. Height map of circular dendritic structure

In some instances, circular or near circular dendritic structures were found with a disordered appearance (i.e., no clear center to boundary line for primary dendrites) as shown in Figure 8. Currently, it is not clear what conditions would be necessary to create such a structure.

Much more common than the “wagon wheel” and “disordered” dendritic structures, however, are the dendritic structures without the rotational symmetry. These regions can be seen labeled in Figure 3 and cover large length scales (i.e., tens to hundreds of micrometers) and, as previously shown, are an expected condition of as-built AM IN625 [10].

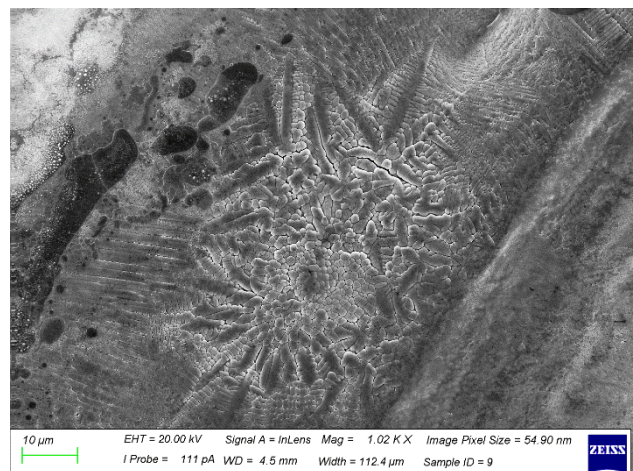


Figure 8. SEM image of the “disordered” dendritic structure.

3.3. Nanoscale “Particles”

Closer inspection of the surface has shown nanoscale features in both the aluminum rich deposits and across dendritic structures (e.g., Figure 9). It is hypothesized that these are Laves phase structures, though additional analysis is required to confirm.

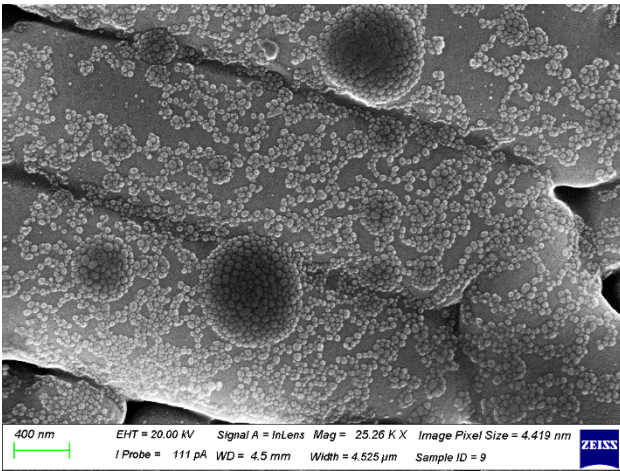


Figure 9. SEM image of nanoscale “particles” seen on a dendritic structure

4. Conclusions and further work

Often, AM literature focuses on surface structures in the 1 μm and greater regime, as smaller features challenge the capabilities of conventional geometrical metrology equipment. However, this study has found several features of interest down to even tens of nanometers. These features, which are well summarized in Figure 2, are more prevalent than the expected flow lines and chevron patterns commonly seen. In this work, height data and intensity images from CSI measurements along with SEM and EDS measurements were used to investigate and identify these features. Measurements were carefully aligned using part coordinate systems printed in the LPBF machine during builds, allowing for detailed analysis of multiple forms of data simultaneously.

Film-like structures on the surface were identified to have high concentrations of aluminum and oxygen. These are hypothesized to be vaporized aluminum from the fusion process and oxygen exposure from powder storage in an air environment prior to reuse. Regardless, these indicate local chemistry deviation from required material specifications.

Dendritic microstructure with a base short-range order of $\approx 1 \mu\text{m}$ were seen in SEM images, and careful alignment of data sources allowed for confirmation of their signature in CSI intensity images. Ordered dendritic structures are most common, which are expected for as-built AM IN625. “Wagon wheel” like structures with radial primary dendrites and orthogonal secondary dendrites are present and hypothesized to nucleate from particle or ejecta impacts. Some of the dendritic structures are disordered and lack the radial primary dendrites. Finally, nanometer-scale particles are present on the surface over dendritic structures and the film-like regions. We suspect these are Laves phase structures, but additional testing is required to confirm.

Future work will include determining the quantity of various structures. This will give insight into situations that create greater or fewer instances of the various structures. Powder characterization is being performed to help determine the source of the oxygen and aluminum concentrations, and further metallurgical testing is planned. These investigations will help relate the surface structures to the aspects of the process that created them and aid in the development of process-structure-property relationships.

Acknowledgements

This work was supported in part by Zeiss and in part by the Center for Precision Metrology at UNC Charlotte. The authors would also like to thank Jared Tarr at the National Institute of Standards and Technology for his assistance with the fabrication of test samples and Greg Caskey for his assistance with measurements on the Nexview system.

Disclaimer

Certain commercial entities, equipment, or materials may be identified in this document to describe an experimental procedure or concept adequately. Such identification is not intended to imply recommendation or endorsement by the National Institute of Standards and Technology, nor is it intended to imply that the entities, materials, or equipment are necessarily the best available for the purpose.

References

- [1] N. Senin, A. Thompson, R.K. Leach, Characterisation of the topography of metal additive surface features with different measurement technologies, *Meas. Sci. Technol.* 28 (2017) 095003.
- [2] R.K. Leach, D. Bourell, S. Carmignato, A. Donmez, N. Senin, W. Dewulf, Geometrical metrology for metal additive manufacturing, *CIRP Ann.* 68 (2019) 677–700.
- [3] Z.C. Reese, J.C. Fox, J. Taylor, C. Evans, Evolution of Cooling Length in Parts Created Through Laser Powder Bed Fusion Additive Manufacturing, in: *Proc. 2018 ASPE Euspen Summer Top. Meet. - Adv. Precis. Addit. Manuf.*, Berkeley, CA, 2018: pp. 183–188. <https://www.nist.gov/publications/evolution-cooling-length-parts-created-through-laser-powder-bed-fusion-additive> (accessed January 7, 2020).
- [4] R.E. Ricker, J.C. Heigel, B.M. Lane, I. Zhirnov, L.E. Levine, Topographic Measurement of Individual Laser Tracks in Alloy 625 Bare Plates, *Integrating Mater. Manuf. Innov.* 8 (2019). <https://www.ncbi.nlm.nih.gov/pmc/articles/PMC7537414/> (accessed June 18, 2021).
- [5] Z.C. Reese, J.C. Fox, F.H. Kim, J. Taylor, C. Evans, Effect of Subsurface Defects on the Surface Topography of Additive Manufactured Components, in: *Proc. 2018 ASPE Euspen Summer Top. Meet. - Adv. Precis. Addit. Manuf.*, Berkeley, CA, 2018: pp. 127–131. <https://www.nist.gov/publications/effect-subsurface-defects-surface-topography-additive-manufactured-components> (accessed January 7, 2020).
- [6] C. Gomez, R. Su, A. Thompson, J. DiSciaccia, S. Lawes, R.K. Leach, Optimization of surface measurement for metal additive manufacturing using coherence scanning interferometry, *Opt. Eng.* 56 (2017) 111714.
- [7] The Meaning and Measure of Lateral Resolution for Surface Profiling Interferometers, (n.d.). https://www.osa-opn.org/home/articles/volume_23/issue_4/departments/optical_engineering/optical_engineering/ (accessed June 21, 2021).
- [8] Mx Software, v8.0.0.26, Zygo Corporation, Middlefield, CT., 2019.
- [9] N. Emminghaus, C. Hoff, J. Hermsdorf, S. Kaierle, Residual oxygen content and powder recycling: Effects on surface roughness and porosity of additively manufactured Ti-6Al-4V, *Addit. Manuf.* 46 (2021) 102093.
- [10] F. Zhang, L.E. Levine, A.J. Allen, M.R. Stoudt, G. Lindwall, E.A. Lass, M.E. Williams, Y. Idell, C.E. Campbell, Effect of heat treatment on the microstructural evolution of a nickel-based superalloy additive-manufactured by laser powder bed fusion, *Acta Mater.* 152 (2018) 200–214.

Session 2: Integration of AM into a holistic manufacturing process

Improving additive manufactured surfaces properties with post processing techniques

Matthieu Rauch^{1,2}, Jean-Yves Hascoet^{1,2}

¹Centrale Nantes / GeM - UMR CNRS 6183, equipe PMM, 1 rue de la Noe, 44321 Nantes - FRANCE

²Joint Laboratory of Marine Technology (JLMT) Centrale Nantes - Naval Group - FRANCE

matthieu.rauch@ec-nantes.fr

Abstract

Additive Manufacturing (AM) offers new opportunities for the Industry, by providing new design and manufacturing freedoms, by reducing assembly complexities and by decreasing manufacturing costs for high added value components. Thanks to recent scientific progresses, AM processes are now able to produce components with homogeneous mechanical properties. However, the physical phenomena involved make the AM produced surfaces not always suitable for a direct use in mechanical assemblies, where functional requirements can be sharp. Indeed, AM surfaces have a poor roughness and have often breaking lines, which can penalize the fatigue behaviour by initiating cracks. Post processing is sometimes necessary to increase the surface properties, and the selection of the most adapted process with its parameterization shall be in adequacy with the input properties of the AM surface and the requirement to meet. Hence, this paper discusses the interest of various AM post-process techniques that focus on external surfaces finishing. These can base on material removal such as high speed machining or waterjet manufacturing. They can be based on surface properties modifications such as laser polishing. They can be based on material addition such as coating. Influential process parameters are introduced with the objective to evaluate a performance area for each post processing technique. The results of experimental campaigns carried out in the laboratory are provided. They focus on AM components made with various materials such as titanium alloys, aluminium alloys, or stainless steel.

Additive Manufactured surfaces finishing, Laser Polishing, Waterjet manufacturing

1. Introduction

Additive Manufacturing (AM) offers new opportunities for the Industry, by providing new design and manufacturing freedoms, by reducing assembly complexities and by decreasing manufacturing costs for high added value components [1].

Among the AM processes referenced by ISO/ASTM 52900 [2], Laser Metal Deposition is more dedicated to challenging geometries, functional graded materials parts [3] or repair [4]; Wire Arc Additive Manufacturing (WAAM) is more suitable for building large structural parts [5], [6]; whereas Powder Bed Fusion processes, such as Selective Laser Melting (SLM) are rather dedicated to small components with complex geometries [7].

AM processes common principle is to build the components layer by layer, by depositing or creating welded beads. Hence, the physical phenomena involved make the AM produced surfaces not always suitable for a direct use in mechanical assemblies, where functional requirements can be sharp: AM surfaces have a poor roughness and have often breaking lines, which can penalize the fatigue behaviour by initiating cracks [8]. Post processing is sometimes necessary to increase the surface properties, and the selection of the most adapted process with its parameterization shall be in adequacy with the input properties of the AM surface and the requirement to meet. [9]

Several finishing techniques have been proposed to increase AM surface properties and this paper discusses the interest of various AM post-process techniques that focus on external surfaces finishing. These can base on material removal such as high speed machining or waterjet manufacturing. They can be based on surface properties modifications such as laser polishing/remelting. They can be based on material addition such as coating. Influential process parameters are studied with

the objective to evaluate a performance area for each post processing technique. The results of experimental campaigns carried out in the laboratory are provided. They focus on AM components made with various materials such as titanium alloys, aluminium alloys, or stainless steels.

2. AM surfaces properties

Despite their differences, AM processes are based on the same principle of piling layers of material. Due the physical phenomena inside the melt pool, the beads that constitutes the layers have round borders. This generates irregularities on AM surfaces. An example of rough AM surface is given in Figure 1, which shows an Al alloy surface produced with the WAAM process, which is known to generate very rough surfaces. Here the Ra roughness parameter is around 35µm.

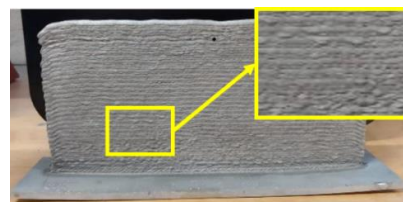


Figure 1: Example of as-built WAAM surface

Other AM processes such as LMD provide better results regarding this parameter but the usage of metallic powder (with a d50 distribution around 60µm) as filler material still affects surfaces properties. A typical example of as-built surface topography is illustrated by Figure 2. Typical LMD defects can be observed: direction texture, chaotic texture with the presence of unmelted powder particles, layer overlap...

These surface topologies are not suitable as soon as severe functional requirements are associated to the component to manufacture: tightness, friction coefficients... In addition, poor surface properties can present fracture initiating zones.

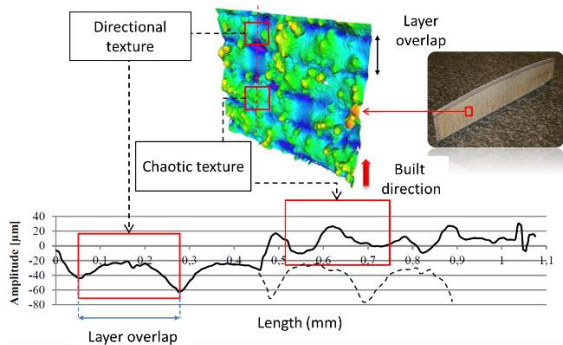


Figure 2. Topography of a LMD surface [10]

Several researchers have investigated this issue by comparing as-built and machined specimens. Thus Bartsch et al. measured the fatigue strength for as built WAAM G3Si1 specimen and concluded on the large effect of the surface roughness on the performance [11]. In [9] Shiyas and Ramanujam aim to list the defects of as built AM parts, including surface properties and then focus on some post processing techniques employed by the researchers and their effects on the improvement of AM components. Bagehorn et al. focused on as built LBM Ti64 specimen and draw the same conclusions concerning fatigue behaviour [12].

3. Material removal processes to finish AM surfaces

Removing as built material aims to improve surface properties but also to remove the skin of the as built component which can concentrate defects (porosities, lack of materials...). This section focused on the most common finishing process HSM and on a promising alternative waterjet machining.

3.1 High speed machining

The principle is quite similar to classical multiprocess workplans by considering AM as primary process, as it is for casting or forging usually, and HSM as secondary process. It can be decided to machine the complete surface of the component or only some specific functional surfaces. In addition, HSM is already used to remove the supports with some AM process such as SLM and can be employed quite naturally as finishing process.

According to various researchers, machining AM surfaces dramatically increased the mechanical properties of the parts, such as fatigue [12], [13] and tensile properties [8].

However, this hybrid manufacturing approach rises new challenges in terms of process planning, typically interprocess interactions AM/HSM [14], as components can show complex geometries and internal surfaces which are no longer reachable for the cutting tool after the AM process. Hybrid manufacturing approaches are consequently needed [15]–[17], and these can benefit from innovative approaches for manufacturing data such as STEP-NC [14] or Cyber Physical Machine Tools, dedicated to multiprocess manufacturing [18].

The same principles can be used with abrasive tools to carry out polishing operations.

3.2 Waterjet machining

Waterjet Machining is an advanced machining technique which is extensively used in industries for cutting applications. It operates on no direct contact between the tool and the work-

piece [19] and provides many benefits such as no heat generated at the cutting zone, reduced cutting forces and the ability to work with reflective or insulated materials [20]. The principle is to use the waterjet stream to polish AM surfaces by removing the component skin. This process is CNC controlled with a variable waterjet tool orientations, it can apply to complex geometries AM surfaces.

In contrast with cutting operations, the use of waterjet machining for finishing operations need a precise control of the axial and radial depths of cut. In particular, feedrate has to be as constant as possible, because any actual feedrate variation generates corresponding axial depth of cut variations on the surface. This can be directly linked to the tool path patterns selected for the surface finishing operations as the machine slows down at the discontinuities and creates a localised high depth of cut. The result for the round spiral highlights also the need to control waterjet start and stop position on the surface. To do so, entry points of the tool path pattern can be located outside the component; if this is not possible, sacrificial sheet metal can be placed on the corresponding location.

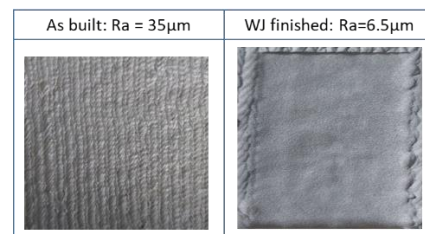


Figure 3. Example of roughness enhancement with waterjet finishing of an Aluminium alloy WAAM surface

Another major advantage of waterjet machining lies into the possibility to create textured surfaces, by selecting specific tool paths pattern, as shown in Figure 4, what will convey specific properties such as residual stresses reduction [21], or hydrodynamic behaviour improvement.

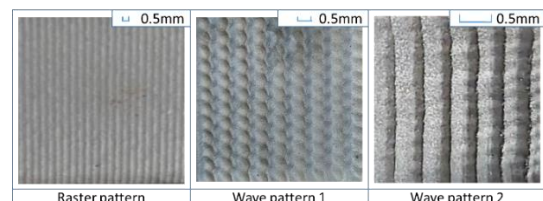


Figure 4: example of various surface texturing patterns with waterjet machining

Concerning AM surface finishing, waterjet can consequently highly reduce surface roughness. Experiment campaigns carried out in the laboratory showed a final roughness $R_a=6.0 \mu\text{m}$ after Waterjet machining on WAAM Aluminium alloy surface which initial roughness was $R_a=34.0 \mu\text{m}$. This process is consequently a solid candidate for AM surface finishing.

4. Surface properties modifications

4.1 Laser polishing

Due to the use of a laser as the heat source of the AM process, laser finishing is mostly applied on LMD and SLM components, although not limited to. The principle is to melt topography peaks created by the AM process: unmelted powder grains, layer overlaps... The surface tension of the melt pool makes the molten material is reallocated to the surface cavities, which smoothes the surface topology (Figure 5).

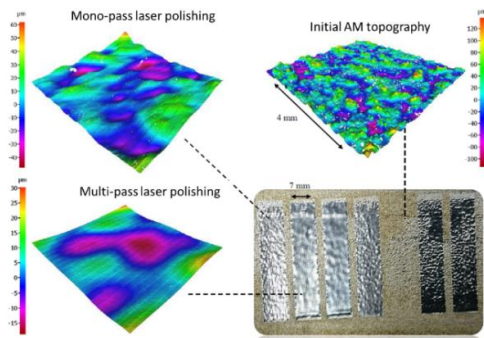


Figure 5. Laser Polishing of a Ti64 wall made with LMD

As for the aforementioned processes, tool paths control is the key of a successful implementation. To do so, prediction models have been developed to prepare and select the most suitable tool paths patterns and parameters (such as laser defocus or scan paths overlap), for laser polishing of Ti64 LMD components [22] or laser polishing of CrCo SLM components [23]. However, laser polishing can affect the mechanical properties of the component by inducing residual stresses on the skin as shown by [24], but these can be relaxed with secondary stress relief processes so that the specimen show improved fatigue strengths as shown by Lee et al. in [25].

Hybrid approaches can also be developed as the AM laser can be employed for polishing purposes and an alternation between the processes can be established to treat non accessible surfaces [10].

4.2 Other surface modification processes

As for laser polishing, some AM process heat sources can be derived to surface finishing applications. Hence, PAW and TIG remelting are strong candidates to enhance surface properties [26] after AM deposition.

Some innovative rapid manufacturing technique have a great potential for AM surface finishing. Friction Stir Process is an [27]. Its working principle is to make a rotating tool travel just below the skin induces heating and plastic flow into the processing material yielding microstructure changes. Magnetic induction can be used as well to heat and remelt component surfaces [28].

5. Material addition processes and other finishing processes

Most of the material addition processes to enhance AM surface properties are coating processes. In contrast with the techniques mentioned in the previous sections, the objective is not to improve surface roughness and mechanical properties but to change other surface properties such as corrosion and wear resistances. Most of the research published measure the bonding conditions between the AM substrate and the coating [29], [30].

However, it can be mentioned that Functional Graded Material AM approaches [3], which are enabled by LMD can achieve the same results by building components which surface properties are rather different, because made with a different material, than the one in the core, as shown in Figure 6.

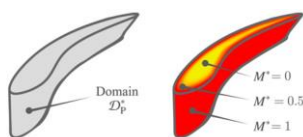


Figure 6. Example of material distribution in a FGM part [3]

The state of the art also refers to other finishing processes Besides some well-known processes which interest for AM finishing benefit from consistent research effort [31], some of

them are at research stage, such as laser shot peening, abrasive flow machining of friction stir processing [9].

6. Conclusions

This paper focused on the post processing techniques employed to improve the surface properties of AM component. Whatever the AM process selected, the surface roughness is usually made of peaks, valley, unmelted particles, layer overlaps that penalize the fatigue strengths. This is the reason why most of the mechanical tests to verify the increased properties are fatigue strength experimental campaigns. Hence, the objective of finishing processes is to erase the initial surface topology by either removing the whole skin, either by remodelling the surfaces or by covering the surface with another material.

It can be highlighted that most of the finishing processes are tool paths based. It means these tool paths have to be chosen and controlled carefully (overlap, depth of work) to avoid defect formations.

In contrast, this can be very beneficial as well. As the tool path parameters are controlled locally, it is possible to fine tune the surface properties locally, by using these processes to produce graded properties surfaces.

High Speed Machining is the most employed process, as it always improves surface roughness and removes unmelted zones on the component skins. The surface roughness is excellent and the process parameters are very well controlled to the widespread strong knowledge on this process. Waterjet machining could be a viable alternative to HSM or polishing, in particular for thin structures as deformation and residual stresses induction can be limited; moreover the process implementation is hardly sensitive to the selected AM material.

Laser finishing is mostly used in combination with laser-based AM. Very good results can be obtained. However, the frequent need to multi-pass strategies combined with the limited size of the laser spot makes this finishing technique more suitable for small of medium parts, due the manufacturing times needed.

Material addition processes such as coating have different purposes and bond another material skin on the AM surface.

Hybrid approaches are very promising to enhance further the surface properties. The tight combination of AM and finishing processes during the build enables to work on inner surfaces; assemblies and component design can be simplified. But these approaches require dedicated multi-process manufacturing equipment and specific manufacturing methodologies to control interprocess constraints together with the constraints associated to each single process.

Eventually, a key challenge to investigate is the AM surface properties needed for their functional applications. Most of the functional requirement come today from other processes and not only the physical properties (roughness, waviness) but also the identification of the surface to be finished is still to be clarified.

References

- [1] R. Ponche, O. Kerbrat, P. Mognol, and J.-Y. Hascoët, 'A novel methodology of design for Additive Manufacturing applied to Additive Laser Manufacturing process', *Robot. Comput.-Integr. Manuf.*, vol. **30**, no. 4, pp. 389–398, Aug. 2014, doi: 10.1016/j.rcim.2013.12.001.
- [2] ISO/ASTM 52900, 'ISO/ASTM 52900:2015', *ISO*. <https://www.iso.org/cms/render/live/fr/sites/isoorg/contents/data/standard/06/96/69669.html> (accessed May 18, 2020).
- [3] P. Muller, P. Mognol, and J.-Y. Hascoët, 'Modeling and control of a direct laser powder deposition process for

- Functionally Graded Materials (FGM) parts manufacturing', *J. Mater. Process. Technol.*, vol. **213**, no. 5, pp. 685–692, 2013.
- [4] J. Um, M. Rauch, J.-Y. Hascoët, and I. Stroud, 'STEP-NC compliant process planning of additive manufacturing: remanufacturing', *Int. J. Adv. Manuf. Technol.*, pp. 1–16, May 2016, doi: 10.1007/s00170-016-8791-1.
- [5] G. Pechet, J.-Y. Hascoët, M. Rauch, G. Rückert, and A.-S. Thorr, 'Manufacturing of a hollow propeller blade with WAAM process - from the material characterisation to the achievement', in *Industry 4.0 – Shaping The Future of The Digital World*, CRC Press, 2020, pp. 155–160. doi: 10.1201/9780367823085-28.
- [6] S. W. Williams, F. Martina, A. C. Addison, J. Ding, G. Pardal, and P. Colegrove, 'Wire + Arc Additive Manufacturing', *Mater. Sci. Technol.*, vol. **32**, no. 7, pp. 641–647, May 2016, doi: 10.1179/1743284715Y.0000000073.
- [7] I. M. Kusoglu, B. Gökce, and S. Barcikowski, 'Research trends in laser powder bed fusion of Al alloys within the last decade', *Addit. Manuf.*, vol. **36**, p. 101489, Dec. 2020, doi: 10.1016/j.addma.2020.101489.
- [8] V. Laghi, M. Palermo, G. Gasparini, V. A. Girelli, and T. Trombetti, 'On the influence of the geometrical irregularities in the mechanical response of Wire-and-Arc Additively Manufactured planar elements', *J. Constr. Steel Res.*, vol. **178**, p. 106490, Mar. 2021, doi: 10.1016/j.jcsr.2020.106490.
- [9] K. A. Shiyas and R. Ramanujam, 'A review on post processing techniques of additively manufactured metal parts for improving the material properties', *Mater. Today Proc.*, vol. **46**, pp. 1429–1436, Jan. 2021, doi: 10.1016/j.matpr.2021.03.016.
- [10] B. Rosa, P. Mognol, and J. Hascoët, 'Laser polishing of additive laser manufacturing surfaces', *J. Laser Appl.*, vol. **27**, no. S2, p. S29102, Feb. 2015, doi: 10.2351/1.4906385.
- [11] H. Bartsch, R. Kühne, S. Citarelli, S. Schaffrath, and M. Feldmann, 'Fatigue analysis of wire arc additive manufactured (3D printed) components with unmilled surface', *Structures*, vol. **31**, pp. 576–589, Jun. 2021, doi: 10.1016/j.istruc.2021.01.068.
- [12] S. Bagehorn, J. Wehr, and H. J. Maier, 'Application of mechanical surface finishing processes for roughness reduction and fatigue improvement of additively manufactured Ti-6Al-4V parts', *Int. J. Fatigue*, vol. **102**, pp. 135–142, Sep. 2017, doi: 10.1016/j.ijfatigue.2017.05.008.
- [13] A. Fatemi, R. Molaei, S. Sharifimehr, N. Phan, and N. Shamsaei, 'Multiaxial fatigue behavior of wrought and additive manufactured Ti-6Al-4V including surface finish effect', *Int. J. Fatigue*, vol. **100**, pp. 347–366, Jul. 2017, doi: 10.1016/j.ijfatigue.2017.03.044.
- [14] R. Laguionie, M. Rauch, and J.-Y. Hascoët, 'Simulation and optimization in a multi-process environment using STEP-NC', in *Control and Automation, 2009. ICCA 2009. IEEE International Conference on*, 2009, pp. 2384–2391.
- [15] P. Stavropoulos, H. Bikas, O. Avram, A. Valente, and G. Chryssolouris, 'Hybrid subtractive–additive manufacturing processes for high value-added metal components', *Int. J. Adv. Manuf. Technol.*, vol. **111**, no. 3, pp. 645–655, Nov. 2020, doi: 10.1007/s00170-020-06099-8.
- [16] L. A. Dominguez, F. Xu, A. Shokrani, J. M. Flynn, V. Dhokia, and S. T. Newman, 'Guidelines when considering pre & post processing of large metal additive manufactured parts', *Procedia Manuf.*, vol. **51**, pp. 684–691, Jan. 2020, doi: 10.1016/j.promfg.2020.10.096.
- [17] J.-Y. Hascoët, S. Touzé, and M. Rauch, 'Automated identification of defect geometry for metallic part repair by an additive manufacturing process', *Weld. World*, vol. **62**, no. 2, pp. 229–241, Mar. 2018, doi: 10.1007/s40194-017-0523-0.
- [18] B. Jeon, J.-S. Yoon, J. Um, and S.-H. Suh, 'The architecture development of Industry 4.0 compliant smart machine tool system (SMTS)', *J. Intell. Manuf.*, vol. **31**, no. 8, pp. 1837–1859, Dec. 2020, doi: 10.1007/s10845-020-01539-4.
- [19] D. Krajcarz, 'Comparison Metal Water Jet Cutting with Laser and Plasma Cutting', *Procedia Eng.*, vol. **69**, pp. 838–843, Jan. 2014, doi: 10.1016/j.proeng.2014.03.061.
- [20] G. A. Escobar-Palafox, R. S. Gault, and K. Ridgway, 'Characterisation of Abrasive Water-jet Process for Pocket Milling in Inconel 718', *Procedia CIRP*, vol. **1**, pp. 404–408, Jan. 2012, doi: 10.1016/j.procir.2012.04.072.
- [21] D. Arola, M. L. McCain, S. Kunaporn, and M. Ramulu, 'Waterjet and abrasive waterjet surface treatment of titanium: a comparison of surface texture and residual stress', *Wear*, vol. **249**, no. 10, pp. 943–950, Nov. 2001, doi: 10.1016/S0043-1648(01)00826-2.
- [22] B. Rosa, P. Mognol, and J.-Y. Hascoët, 'Modelling and optimization of laser polishing of additive laser manufacturing surfaces', *Rapid Prototyp. J.*, vol. **22**, no. 6, pp. 956–964, Jan. 2016, doi: 10.1108/RPJ-12-2014-0168.
- [23] K. C. Yung, T. Y. Xiao, H. S. Choy, W. J. Wang, and Z. X. Cai, 'Laser polishing of additive manufactured CoCr alloy components with complex surface geometry', *J. Mater. Process. Technol.*, vol. **262**, pp. 53–64, Dec. 2018, doi: 10.1016/j.jmatprotec.2018.06.019.
- [24] Z. Xu, W. Ouyang, Y. Liu, J. Jiao, Y. Liu, and W. Zhang, 'Effects of laser polishing on surface morphology and mechanical properties of additive manufactured TiAl components', *J. Manuf. Process.*, vol. **65**, pp. 51–59, May 2021, doi: 10.1016/j.jmapro.2021.03.014.
- [25] S. Lee, Z. Ahmadi, J. W. Pegues, M. Mahjouri-Samani, and N. Shamsaei, 'Laser polishing for improving fatigue performance of additive manufactured Ti-6Al-4V parts', *Opt. Laser Technol.*, vol. **134**, p. 106639, Feb. 2021, doi: 10.1016/j.optlastec.2020.106639.
- [26] L. Zhu *et al.*, 'Effect of TIG remelting on microstructure, corrosion and wear resistance of coating on surface of 4Cr5MoSiV1 (AISI H13)', *Surf. Coat. Technol.*, vol. **405**, p. 126547, Jan. 2021, doi: 10.1016/j.surfcoat.2020.126547.
- [27] F. Rubino, F. Scherillo, S. Franchitti, A. Squillace, A. Astarita, and P. Carlone, 'Microstructure and surface analysis of friction stir processed Ti-6Al-4V plates manufactured by electron beam melting', *J. Manuf. Process.*, vol. **37**, pp. 392–401, Jan. 2019, doi: 10.1016/j.jmapro.2018.12.015.
- [28] J.-Y. Hascoët, J. Parrot, P. Mognol, and E. Willmann, 'Induction heating in a wire additive manufacturing approach', *Weld. World*, vol. **62**, no. 2, pp. 249–257, Mar. 2018, doi: 10.1007/s40194-017-0533-y.
- [29] J. Yao, Y. Wang, G. Wu, M. Sun, M. Wang, and Q. Zhang, 'Growth characteristics and properties of micro-arc oxidation coating on SLM-produced TC4 alloy for biomedical applications', *Appl. Surf. Sci.*, vol. **479**, pp. 727–737, Jun. 2019, doi: 10.1016/j.apsusc.2019.02.142.
- [30] B. Zhang, L. Zhu, H. Liao, and C. Coddet, 'Improvement of surface properties of SLM parts by atmospheric plasma spraying coating', *Appl. Surf. Sci.*, vol. **263**, pp. 777–782, Dec. 2012, doi: 10.1016/j.apsusc.2012.09.170.
- [31] N. E. Uzan, S. Ramati, R. Shneck, N. Frage, and O. Yeheskel, 'On the effect of shot-peening on fatigue resistance of AISI10Mg specimens fabricated by additive manufacturing using selective laser melting (AM-SLM)', *Addit. Manuf.*, vol. **21**, pp. 458–464, May 2018, doi: 10.1016/j.addma.2018.03.030.

Computer vision based zero point estimation for hybrid builds in metal additive manufacturing

Jakob Wilm¹, Eythor R. Eiriksson², Sven D. Sørensen³, Lasse Haahr-Lillevang⁴, Nikolaj K Vedel-Smith⁴, Venkata K. Nadimpalli⁵, Gisli Hjalmtýsson⁶ and David B. Pedersen⁵

¹SDU Robotics, University of Southern Denmark.

²Euler ehf – euler3d.com

³LEGO Group A/S, Denmark.

⁴Danish Technological Institute.

⁵Dept. Mechanical Engineering, Technical University of Denmark.

⁶Reykjavik University, Iceland.

jaw@mmmi.sdu.dk

Abstract

This paper describes a novel computer vision system that is capable of performing automated zero point calibration for hybrid builds in additive manufacturing. This enables users to quickly and accurately locate and print on top of previously machined parts for part repair or hybrid builds jobs. The system was installed on an industrial laser powder bed fusion additive system and its performance evaluated. Results show that reliable zero point calibration can be obtained at high precision and accuracy and in few seconds, minimizing job setup time significantly.

Metal Additive Manufacturing, 3D Printing, Zero Point Calibration, Computer Vision, Hybrid Build, Process Monitoring.

1. Introduction

Metal based additive manufacturing (AM) has seen tremendous growth in the past years where specifically systems based on Laser Powder Bed Fusion (LPBF) have seen significant industrial adoption [1]. These systems can produce metal parts with complex geometries that would be impossible to manufacture using traditional machining or casting processes. A common application is to produce functional end parts that are made significantly lighter using topology optimization and infill meshing [2]. The geometrical flexibility offered has also proven to be an asset when producing tooling with integrated conformal cooling channels such as used in injection or vacuum forming molds. Though the manufacturing speed of such systems is improving with e.g., the addition of more laser units, traditional machining processes are often more accurate, faster and less expensive. To combine the strengths of these different processes, a hybrid build process combines these methods.

As a practical example, injection molds often have large functional sections for which LPBF is not the most efficient production platform. These sections are often flanges or interface regions. In these cases, where the design freedom of AM is not required, it is faster and more accurate to manufacture that portion of the part using milling or turning processes. Finally, the region benefiting for AM would be printed on top of the previously manufactured part. Figure 1 shows a simplified example of such a hybrid build. The system described in this paper is particular suitable, but not limited, to this use-case.

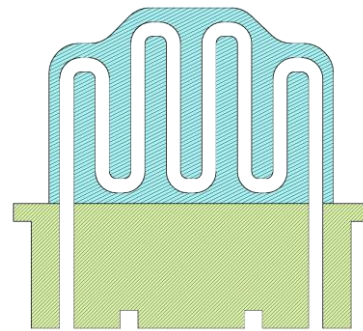


Figure 1. Example of a simple hybrid build design. Top section (blue) manufactured by AM, bottom section (base geometry, green) via traditional milling.

In order to be able to print on top of the pre-manufactured part, a zero point calibration needs to be performed on the work piece. This is the process of estimating the position of the hybrid part in the printer's frame of reference, or in other words the relative transform between the part coordinate system and the machines coordinate system. In traditional CNC machining, the machine will use a contact probe to probe the part or stock to evaluate its position within the machines reference frame. Such contact probe measurements are not possible inside of LPBF systems.

In the current approach to solving this, the part is fixed on the printer's build plate and registered using e.g., dowel pins. The printer's laser is thereafter used to mark or engrave a few visible features, such as crosses, that are visible to the human eye. As

these feature positions are known in the printer's reference frame it is possible to take the hybrid part and measure the features relative to known features on the part itself. This measurement operation needs to be done using e.g., combined optical/tactical CMMs. The downside to this approach is that one needs to trust that the part is re-mounted at precisely the same location on the build plate, which is less than trivial. Furthermore, the method needs expert level know-how, expensive metrology equipment, is time consuming and special care needs to be taken regarding thermal expansion when going for the highest precision.

A less precise, yet much faster approach is to visually estimate the zero point offset using trial-and-error while the part is mounted on the build plate and inside the printer, preferably at operational thermal equilibrium. The offset can be entered in the printers print console and the engraving process repeated. This can be done iteratively until a desired result is obtained. For many applications, this method may be precise enough but remains time consuming.

This paper presents a novel approach of automatically determining the zero point using camera-based computer vision system with a camera inside the build chamber. When given a part geometry to search for, the system is within seconds able to accurately locate the part on the build plate and present its position in terms of the printer's coordinate systems. Our preliminary results show that the system significantly reduces setup time for hybrid builds without sacrificing accuracy.

2. Vision System

The optical system in question has been developed by Euler¹ as part of their off-axis quality assurance solution for LPBF systems. The hardware consists of an industrial camera along with a computation unit, show in Figure 2. The camera is mounted inside the build chamber as shown in Figure 3. In this position, the camera is outside of the laser region, and does not interfere with the inert gas flow inside the chamber. The camera is capable of operating at elevated temperatures up to 70 degrees C and is encapsulated in a housing to be IP67 ingress protected.



Figure 2. Vision system, comprising of an industrial camera and embedding computing system (mounting hardware not shown).



Figure 3. Vision system shown mounted in the build chamber of an EOS EOSINT M270 additive system.

2.1. Intrinsic Camera Calibration

This The camera is intrinsically calibrated by means of a precision calibration checkerboard target using the method of Zhang [3], followed by non-linear bundle adjustment optimization using the Levenberg-Marquardt algorithm. The sensor-lens system is modeled using the plumb-bob model [5] with three radial distortion coefficients, two tangential coefficients, unit aspect ratio and free principal point coordinates. The checkerboard fields are uniquely coded using ArUco binary markers [4], which allows for accurate characterization of the lens also at the image periphery.

2.2. Laser Calibration

To perform alignment in the printer's laser focus plane, the extrinsic parameters describing this plane are estimated in the following way. A flat black anodized aluminium plate is placed on the build plate and its top surface brought into the laser focus plane. A dense asymmetric circle grid pattern of known geometry is then engraved onto its surface by means of a low-power laser exposure. This circles grid is detected in the camera image and a rectifying homography is estimated between detected circle coordinates in the undistorted camera image and their metric 2D coordinates in the laser's coordinate frame. It is therefore possible to geometrically rectify image pixel coordinates and get the corresponding laser coordinates, corresponding to coordinates in the input CAD geometry.

2.3. Zero point calibration

Zero point calibration in this setting corresponds to an alignment or image registration task, in which a 2D rigid transformation (translation vector (x,y) and angle (θ) are to be estimated. Our approach is based on a non-linear optimization in 2D rigid transformation space, which maximizes the overlap of the CAD contour with strong image gradients. Analytical derivatives for this objective function are also utilized, which results in quick and robust convergence if an approximate pose is known (to within a few millimeters).

Specifically, the base geometry STL file is loaded and edges at its top surface are identified as those edges which are shared by triangular faces with a significant angle between normal vectors. These edges are linked, and points are sampled uniformly on the entire edge. We found 2000 points be sufficient for repeatable and accurate results.

Non-linear optimization using the Levenberg-Marquardt optimization scheme is then employed to maximize the squared sum of gradient magnitude below the sample points. The free variables during this optimization are (x,y) and θ . By sampling the gradient magnitude image using a spline interpolator, we can derive an analytical Jacobian of the objective function which

¹ euler3d.com

we found to yield much more robust convergence than numerical derivatives. With a reasonable starting guess around 2mm from the goal, our procedure converges in all cases. Our platform allows the user to interactively provide parameter values for this rough alignment if necessary.

Inspection of the steepness of the objective function at the solution also allows for estimation of uncertainty of the parameter estimates. Mathematically we do this by estimating the covariance of the solutions as the inverse of $J(x^*)^T J(x^*)$, where $J(x^*)$ is the Jacobian matrix at the found solution x^* . Typical values are 20 μ m for translations and 0.01 degrees for the rotation.

3. Operation

The zero point system is operated through a front end web interface which can be accessed from either the computer attached to the AM system, or any other computer on the same network or even over the internet. The interface is shown in Figure 4. It presents the user with a live feed of the camera and allows for upload of STL based geometries for part detection. The alignment functionality can then detect and register the top contour boundaries of this geometry in the current camera image. Estimated transform parameters are presented within seconds. The user can use these resulting zero point values in the printer's software or perform the coordinate correction at a model level in a modelling or slicer software of their choice.

4. Results

The zero-point system was evaluated on a use-case where tooling inserts are to be printed on top of EDM cut kernels. The input STL geometry is the insert fixture seen in Figure 4. By numerous trials, it was determined that the system recovers the zero point transform with accuracy of at worst 50-100 μ m. This result was affected by the galvanometer laser system being slightly out of calibration (material dependent scaling factors were slightly wrong in EOS software). Nonetheless the accuracy is comparable to that obtained by a skilled operator by means of trial-and-error.

The estimated time saving of using the system for one such setup is between 40 to 60 minutes. It was determined that the system can recover transformations up to a few millimeters autonomously, but this number depends on the exact geometry and strength of image gradients.

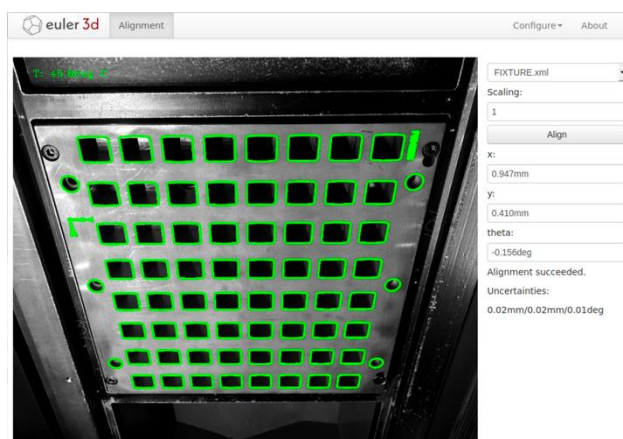


Figure 4. Web interface used to interact with the system, upload CAD geometries and perform zero point calibration. Detected alignment visualized with a green contour.

5. Conclusion

This paper has described the zero-point capabilities of the Euler off-axis print monitoring system and described the use-case of hybrid builds in which structures are printed on top of machined parts. Results show accurate alignment results and a significant time saving. An additional feature of the system is that it can be used to monitor print progress and quality remotely. More information is available at <http://www.euler3d.com>.

Acknowledgement

Part of the work presented in this paper has been funded by the Icelandic Technology Development Fund (Grant nr 188341-0611) and the Manufacturing Academy of Denmark (MADE).

References

- [1] Wohlers et al. Wohlers report 2019: 3D printing and additive manufacturing state of the industry. *Wohlers Associates*, 2019.
- [2] Eiriksson, Eythor. Computer Vision for Additive Manufacturing. *PhD Thesis. DTU Compute* (2018).
- [3] Zhang, Zhengyo. Flexible camera calibration by viewing a plane from unknown orientations. *Proc. IEEE ICCV* (1999).
- [4] OpenCV ArUco contrib module. <http://www.opencv.org>.
- [5] D.C. Brown, Close-Range Camera Calibration, *Photogrammetric Engineering*, pages 855-866, Vol. 37, No. 8, 1971.

Accuracy and microstructure of additively manufactured and post-machined parts

Hans-Christian Möhring, Dina Becker

Institute for Machine Tools - University of Stuttgart

hc.moehring@ifw.uni-stuttgart.de

Abstract

This contribution presents investigations regarding the accuracy and microstructure of additively manufactured specimens before and after post-machining. The additive manufacturing technology of laser metal wire deposition (LMWD) was applied for generating cylindrical test parts out of AlMg5 aluminium alloy. For that purpose, a specific laser power control strategy was implemented in order to achieve a stable material deposition at the thin-walled test structure. The test specimens were analysed with respect to the influence of the additive processing on the geometric properties and the microstructure as well as the porosity of the material. The specimens were subsequently machined by turning, and the influence of this post-processing on the properties of the test parts was analysed regarding the final shape accuracy as well as Martens hardness. The analyses revealed a clear dependence of the material properties on the layer structure that was built during additive manufacturing. The rough shape of the additively manufactured specimens has an influence on the cutting conditions during the post-machining process. These influences also affect the final properties of the additively and subtractively produced parts.

Accuracy, Cutting, 3D printing, Microstructure

1. Introduction

Additive processes offer the possibility for a near-net-shape production of components with locally adapted mechanical properties, which can be optimized by downstream process steps in accordance with the load [1]. However, additively manufactured components do generally not have the required dimensional accuracy and surface quality for functional surfaces such as flanges, guides, bearing seats, etc and therefore have to be reworked by machining operations in most cases [2]. However, this remachining required for the realisation of the necessary function-related geometry and surface accuracies interacts with the result of the additive process, making it indispensable to take both processes into account. Laser-based additive manufacturing processes such as laser cladding or selective laser melting (laser powder bed fusion - LPBF) are used to process metals in the form of powder or wire, achieving strengths comparable with those of conventionally manufactured components. In this way, higher surface qualities are achieved with the powder bed-based processes and graded component conditions. Moreover, the porosity can be adjusted by means of adapted process strategies. In contrast, higher deposition rates are achieved with build-up welding due to a significantly higher average convertible laser power of several kW, compared with only several hundred watts in powder bed-based processes. Although quality is an important factor, the deposition rate must be greatly increased to make AM processes competitive with conventional manufacturing processes by reducing production time. As already mentioned for build-up welding, this can be achieved by using filler materials such as wire. An AM process that also uses this filler metal is the laser metal wire deposition process (LMWD). In recent years, LMWD

has been improved to produce simple 3D-printed parts with low accuracy. Different strategies for 3D printing with wire were evaluated [3]. Aluminium as a filler wire material was also used in some studies to make simple cylindrical parts [4].

This study investigates the accuracy and microstructure of AlMg5 aluminium alloy specimens produced by a controlled LMWD process with subsequent subtractive machining by turning.

2. Test components, process and measurement set-up

The additively manufactured specimens (cylinders) were produced in cooperation with the Institute of Laser Technologies (IFSW) at the University of Stuttgart [5]. Fig. 1. shows the processing head, a schematic representation and the process itself. The production parameters were adapted to produce the most thin-walled cylinders as possible with a high surface quality to maximize the material usage for the post-processing operation. The laser power here was between 1200 and 2640 kW, the fibre diameter was 600 μm , the wavelength was 1030 nm and the track speed was 2 m/min. The cylinders were fabricated with a programmed diameter of 40 mm and a fixed number of layers up to a height of about 37 mm.

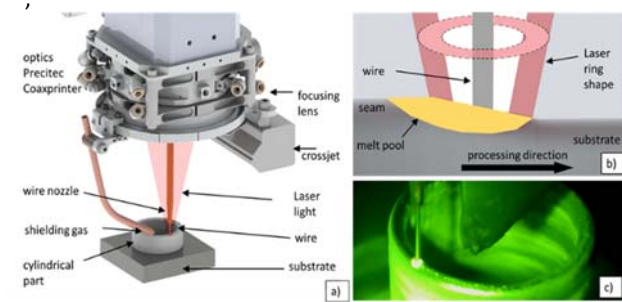


Figure 1. LMWD process: a) processing head; b) laser ring shape and wire; c) deposition process [6]

In order to keep the wall thickness as small as possible with a given AlMg5 wire ($D = 1\text{ mm}$) and to create the cylindrical shape as uniformly as possible, a small beam diameter (2.5 mm) was used. To reduce the wall thickness, the laser power of the LMWD process was reduced with the specimen height. The LMWD process was carried out using inert gas nitrogen with and without track height control by means of optical coherence tomography (OCT).

To produce the desired cylindrical nominal contour of the additively manufactured specimens, these were subsequently machined. The required external longitudinal turning operation was carried out with an R200 turning/milling centre by INDEX-Werke using water-based flood lubrication (Blasocut BC 935 K).

The additively manufactured cylindrical specimens were analysed with a 3D coordinate measuring machine, type MC850 by Carl Zeiss, using an ultrahigh-precision contact probe system with a measuring ball radius of 2.5 mm . The measuring strategy for the specimens was created with the Calypso software to measure the element from the outside and inside with a contact probe. The measuring distance along the additively built direction (Z-axis) was 1 mm .

The 2D roughness of the test specimens was examined with the Formtracer SV-C3200 contact measuring device.

To determine the macroscopic structure of the specimens, the samples were subjected to etching with a 10% NaOH solution heated to approx. 55°C . For this purpose, the samples were carefully separated by means of a cut-off wheel with interrupted cuts, then embedded, ground (grain size 240, 500, 1000, 2000 and 4000, pressure force 20-30 N) and finally polished with a diamond suspension.

The electrolytic etching process of Barker enables the creation of colour etchings in aluminium alloys. The investigated samples were embedded using a 2-component embedding agent based on highly cross-linked methyl methacrylate. Then they were ground up to a grain size of 4000 in steps of 320, 500, 800, 1000, 2500 and 4000. Finally, they were polished with a diamond suspension on a synthetic fibre plate ($3\text{ }\mu\text{m}$).

To determine the hardness, the indentation test was carried out according to DIN EN ISO 14577-1 and ASTM E 2546, using a Picodentor HM500. The Martens hardness (HM) is defined as the ratio of the maximum force to the corresponding contact area and is given in N/mm^2 .

3. Results and discussion

The produced specimen were evaluated after the additive LMWD process and after the machining process. For both processes, metallographic tests as well as hardness tests were investigated and presented.

3.1 Shape accuracy of the LMWD process

The test specimens were produced at decreasing laser power levels to ensure a stable and complete process. The process without track height control started at a high laser power of $2,500\text{ W}$ and ended at a laser power of $2,000\text{ W}$. During the process, the laser power was reduced twice: from $2,500\text{ W}$ to $2,250\text{ W}$ (between $2\text{--}3.5\text{ mm}$) and from $2,250$ to $2,000\text{ W}$ (between $8\text{--}12\text{ mm}$). Regarding the test specimens with OCT control, the laser power was diminished continuously from $2,500\text{ W}$ to $2,000$ during the LMWD process (Fig. 2).

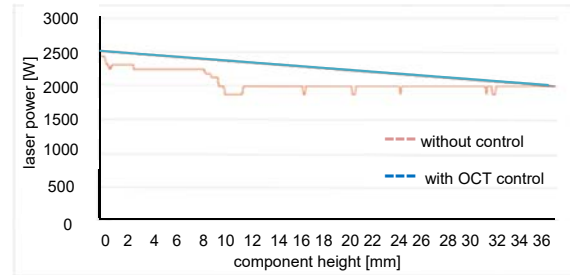


Figure 2. Laser power in the LMWD process

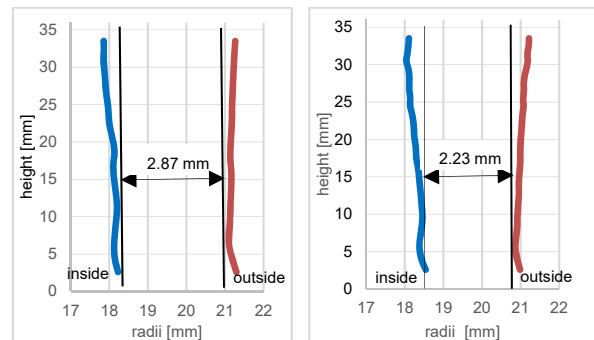


Figure 3. Examples of the wall thickness or outer and inner radii: a) process without control; b) with OCT control

The wall thickness of all test specimens increased because the heat accumulated in the upper part of the samples (Fig. 3). However in the process with OCT control, the homogeneous (effective) wall thickness of the test specimens was significantly thinner and amounted to 2.23 mm (2.87 mm without control). For the cylinder of the process without control, the thin (effective) wall thickness was between $10\text{--}12\text{ mm}$ component height and thus correlated with the great reduction of the laser power from $2,500$ to $2,000\text{ W}$ in the LMWD process. The cylinders of the OCT-controlled processes are thin at the beginning of the additive process but increase continuously with the cylinder height.

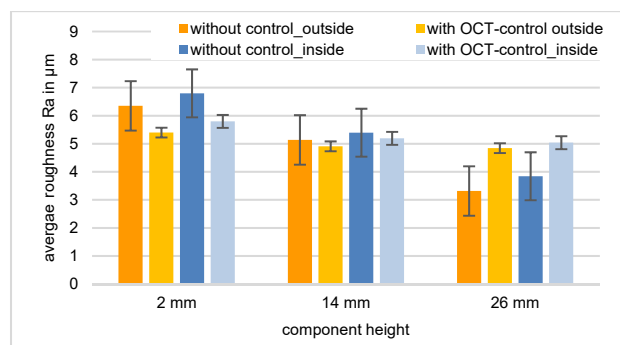


Figure 4. Roughness characteristics Ra on the outside and inside of the specimen

Subsequently, the 2D roughness of the test specimen was examined. The investigations were focussed on determining the characteristic values R_a for the evaluation of the surface quality of the LMWD components. Figure 4 clearly shows that the outer side of all the test specimens produced had R_a -values that were approx. 0.3 - 0.4 mm lower than those of the inner side. The roughness R_a decreased with the component height for all test specimens and reached $R_a = 3.32 \mu\text{m}$ (process without control) and $R_a = 4.84 \mu\text{m}$ (with OCT control) on the outside at 26 mm. In general, the R_a -values at the beginning of the LMWD process (component height of 2 mm) were approx. 1.9 times (process without control) and 1.1 times (process with OCT control) higher than for the component height of 26 mm.

3.2 Subtractive machining

To increase the dimensional accuracy of the test specimen, the specimen was turned from outside (Fig.5). In order to achieve the highest possible efficiency of the overall process, the volume of material to be used in the additive production phase should be as high as necessary and the volume of material to be removed should be kept as low as possible in the subtractive machining phase. The maximum dimensions of an ideal outside cylinder for the samples (best possible cylindricity) were derived from the measurements of the outer radii (Fig. 3). For this reason, the depth of cut was 0.15 mm (calculated starting from r_{min} on the outside), the feed rate was $f = 0.05 \text{ mm/revolution}$ and the cutting velocity was $v_c = 500 \text{ m/min}$. The removed metal amounted to 28.83 mm^3 (without control) and 30.21 mm^3 (with OCT control) of the complete material volume. Fig. 5 shows a typical LMWD test component from outside before and after turning.

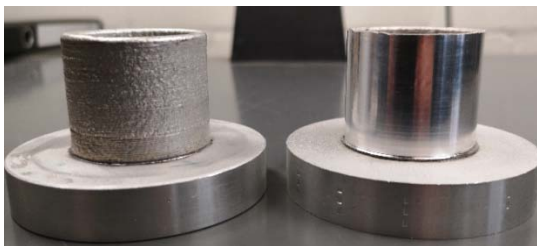


Figure 5. Typical test component before (left) and after the turning process (right).

Regardless of the type of additive process, the roughness values after machining hardly differed and were $R_a = 0.15 - 0.2 \mu\text{m}$ (Fig. 6). As expected, the R_a -values in the lower and upper part area were a little lower than in the middle of the part, as more material was removed there.

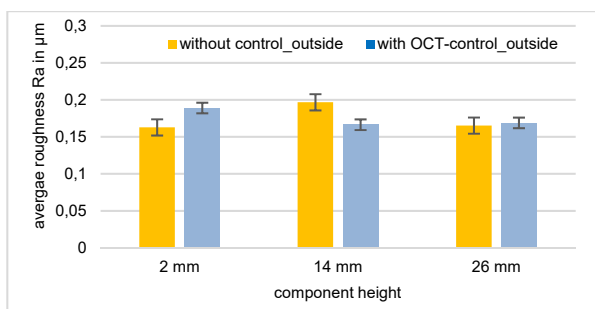


Figure 6. Roughness characteristics R_a on the outside after external longitudinal turning

3.3 Microstructure of additively manufactured and post-machined test components

For the examination of the internal structure of the test specimen, the metallographic sections were prepared. The prepared sections of the test specimen were examined macroscopically and compared with each other (Fig. 7). Analogously to the measured radii (Fig. 3), the layer width increased continuously over the component height for the LMWD process with and without track height control. However, the distance between the layers was different. For the process variant without control, there was a great distance of $750 - 803 \mu\text{m}$ between the layers deposited with the high laser power $2,500 - 2,250 \text{ W}$ (component height of $h = 0 - 8 \text{ mm}$). At a constant laser power of $2,000 \text{ W}$, the layer distance was reduced to $380 - 520 \mu\text{m}$ (component height of $h = 12 - 35 \text{ mm}$). In contrast, no distinct areas with a strongly differing distance between the layers could be found in the test specimens with OCT control. Over the component height, the layer distance varied between $620 - 370 \mu\text{m}$.



Figure 7. Etching of samples a) without control, b) with OCT control (NaOH etching). Cutting plane perpendicular to the feed direction

Another interesting aspect was to compare the components of the microstructure of the additively manufactured specimens without and with OCT control of the track height. The microstructure of the test specimen was evaluated in the middle of the wall of the cross-section according to the method proposed by Ohser and Lorz, by means of linear analysis using spatially random variables [6]. The points of intersection between the test lines and the grain boundaries were considered as random quantities. The test lines were made on a measuring surface of $0.572 \text{ mm} \times 0.431 \text{ mm}$. The distance between two individual vertical lines was $114.4 \mu\text{m}$ and $86.2 \mu\text{m}$ between parallel lines. The point density P_L of the intersections was calculated according to:

$$P_L = N/L \quad (1)$$

The test line length L is the sum of all L_x and L_y segments. N is the number of points of intersection. After the calculation, it was found that the intersection point density and thus the number of grains in the middle of the wall for LMWD samples with OCT control was 1.16 times higher than the intersection point density for samples without control, as can be deduced from Table 1. This indicated indirectly that there was a larger number or a greater compression of grains when the layers were deposited with control of the track height.

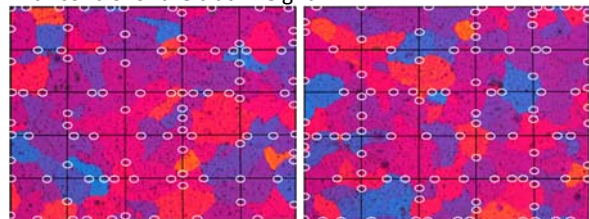


Figure 8. Sample cross-sections in the middle of the wall: process without control (left); with OCT control (right). x 200 magnification with exemplary points of intersection between the test lines and the grain boundaries for a component height of 21 mm, surface of $0.572 \text{ mm} \times 0.431 \text{ mm}$

For the test specimens with OCT control, the microstructure was examined at the outside of the test specimens before and after the turning process. It was found that the machined surfaces showed a significant reduction of scorch marks or pores in comparison with surface areas without machining operations (Fig. 9). The porous, brittle areas were removed during machining. In addition, plastic surface deformation occurred during machining, contributing to the closing of the pores by a filling effect.

Table 1. Exemplary Component of the microstructure (intersection point density)

LMWD process classification	line segment length [mm]	number of intersection points	intersection point density
without control of the track height	6.203	90	14.51
with control of the track height (OCT control)	6.203	105	16.93

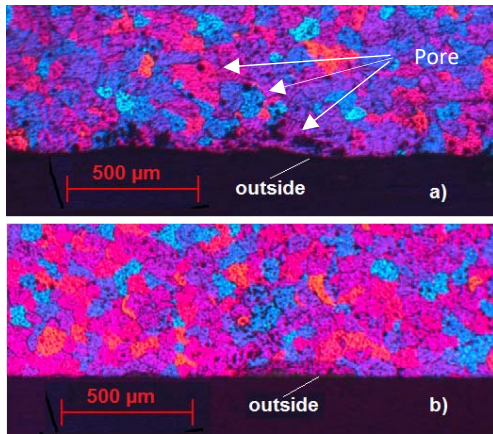


Figure 9. Microstructure of the component sides before (a) and after the turning process (b). x 25 magnification (sample with OCT control). Component height: 21-23 mm, depth of cut: 0.15 mm

Finally, the hardness of the test specimen was examined before and after longitudinal turning. The microhardness was analysed across the prepared microsections (component height of 21 - 22 mm). The measuring points were distributed in five areas. The first (outside) as well as the last area (inside) were approx. 50 µm away from the corresponding wall surface. The tests showed that the additively manufactured test specimens had a comparable hardness before machining. The maximum hardness of $HM = 750 - 760 \text{ N/mm}^2$ was determined in the centre of the wall specimen. After machining, both test specimens had higher hardness values at the turned side compared with the centre of the wall and at the unmachined side (inside). In the centre of the wall, the test specimens without control showed approx. 30 - 50 N/mm^2 higher HM values than the components with OCT control. Although the removed volumes of all test specimens were comparable, those without control had an approx. 0.5 mm greater wall thickness and therefore a higher heat capacity during machining than the thin test specimens from the process without OCT control. This could result in a grain compression in the following solidification.

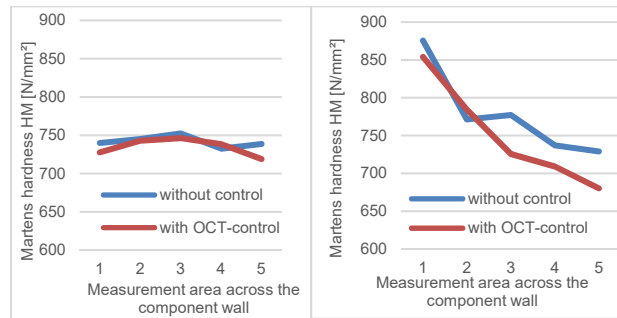


Figure 10. Influence of turning on hardness distribution in the wall cross-section before (left) and after (right) the turning process. Machining parameters: $vc = 500 \text{ m/min}$, $f = 0.05$; measurements of height: 21 - 22 mm

4. Summary

The heating during LMWD at reduced laser power had a strong effect on the wall thickness of the AlMg5 cylinder. By means of OCT-based track height control, cylinders with a wall thickness of 2.23 mm could be produced (2.87 mm without control). The OCT track height control led to a more constant distance between the layers and compression of the grains during the deposition process. By turning the additively produced specimens, it was possible to increase the specimen quality significantly. The porous, brittle areas were removed, and plastic deformation occurred on the machined surface. After the machining operation, the roughness characteristics along the height of the cylinder reached 0.16 - 0.19 µm (before machining: $R_a = 6.35 - 3.3 \text{ µm}$ for samples without control and $R_a = 5.38 - 4.88 \text{ µm}$ with OCT control $R_a = 5.38 - 4.88 \text{ µm}$). The hardness of the machined surface ($vc = 500 \text{ m/min}$, $f = 0.05 \text{ mm/revolution}$) was 12 % higher (without control) and 17 % higher (with OCT control) than in the middle of the component wall.

In future research, it is planned to investigate the influence of further types of LMWD control as well as different machining processes on the microstructure of LMWD components. The aim here will be to produce components with a great accuracy, defined surface roughness and defined values of hardness. Due to the LMWD process speed with high application rates and a material usage of almost 100 percent, the basic research as well as the planned investigations are to be most interesting for users from various industrial sectors.

References

- [1] Liu J. Y 2018 Current and future trends in topology optimization for additive manufacturing *Struct. Multidisc. Optim.* **57** 2457-83
- [2] Ding D., Pan Z., Cuiuri D. and Li H. Y 2015 Wire-feed additive manufacturing of metal components: technologies, developments and future interests *Int. J. Adv. Manuf. Technol.* **81** 465-81
- [3] Nowotny S. Y 2009 Laser-Präzisionsauftragsschweißen mit zentrischer Drahtzufuhr: BMBF-Rahmenkonzept "Forschung für die Produktion von morgen"; Ergebnisbericht zum Verbundvorhaben "Flexible 3D-Bearbeitung durch laserbasierte Fügeverfahren mit integrierter Werkstoffzufuhr" *Flexiglas*
- [4] Froend M., Riekehr S., Kashaev N., Klusemann B. and Enz J. Y. 2018 Process development for wire-based laser metal deposition of 5087 aluminium alloy by using fibre laser *Journal of Manufacturing Processes* **34** 721-32
- [5] Becker D, Boley S, Eisseler R, Stehle T, Möhring H-C, Onuseit V, Hoßfeld M, Graf T Y. 2021 Influence of a closed-loop controlled laser metal wire deposition process of S Al 5356 on the quality of manufactured parts before and after subsequent machining *Production Engineering* **15** 489-507
- [6] Ohser J. and Lorz U. Y. 1994 Quantitative Gefügeanalyse: Theoretische Grundlagen und Anwendungen 1. Aufl. *Freiberger Forschungshefte B Metallurgie und Werkstofftechnik*

Session 3: Focus on micro-nano

Insights into challenges and potentials of two-photon lithography

S. Kühne¹, M. Malcher¹, V. Juzumas², E. Bosler¹, D. Oberschmidt¹

¹Technische Universität Berlin, Department Micro and Precision devices MFG, Germany

²Altechna R&D | Workshop of Photonics, Lithuania

kuehne@mfg.tu-berlin.de

Abstract

In the last decade, additive manufacturing has enormously developed. With a growing range of technologies, an expanded material portfolio, significantly increased reproducibility, and an increasing precision, it overcame the threshold from pure prototyping towards its use in real production. However, the new possibilities also brought challenges. On the one hand, there is the need to discuss the exploitation of opportunities as well as potential complex components. On the other hand, the metrology is still an incompletely solved issue.

With two-photon lithography (TPL), an additive process is available whose precision exceeds the diffraction limits of conventional laser lithography systems and, at the same time, allows the production of 3-dimensional components. Using conventional resists and specialized materials, such as organically modified ceramics, micro-mechanical, micro-fluidic, refractive and diffractive micro-optical systems can be realized. In recent years, the technology has shown its potential regarding various fundamental applications and it is on the transition to an industrial integration. The paper provides insights into the potential of this technology that is used during real production and the emerging challenges for the precision community during the transition period towards integration in manufacturing chains. Selected components are introduced, e.g. from micro cytometry and diffraction optics. Furthermore, the use of standard components intending to classify the precision of TPL systems is discussed.

The system presented here comes with several harmonic generators, providing a wavelength range from the IR to the UV. Thus, the system is able to combine classical laser micro-beam technologies, such as ablation and single-photon lithography, with the potentials of two-photon lithography. Hence, it enables micro-products with significantly advanced precision in the future.

Keywords: micro production, lithography, 2pp

1. Introduction

Two-photon polymerization (2PP) has been used for the production of photonic crystals for two decades [1]. Over the years, it has developed into a scientific tool to produce three-dimensional microstructures. Commercial systems have been available for more than a decade, which, in addition to scientific use, allow the transition to industrial use.

The 2PP works by irradiating the resist to be polymerized with a source whose wavelength provides only half the energy necessary to activate the photoactive component. Thus, two photons must be absorbed almost simultaneously. However, this is only sufficiently probable at very high temporal and spatial photon densities. The material dependence is given by the so-called material specific cross section in the unit Göppert-Mayer, in short GM. The unit was named after Maria Göppert-Mayer, who for the first time described two-photon absorption theoretically [2]. The necessary photon densities are achieved in the focal region of a laser beam. Due to the energy distribution in the Gaussian distributed focal region, a defined elliptical volume unit (voxel) polymerizes, with a size below the diffraction limit. By moving the focus within the resist and thus assembling voxels with the help of the pulsed laser, three-dimensional structures can be created.

Various materials with different properties are available today, allowing the technology to be used for a wide range of applications. Existing UV negative resists like SU8, but also optically and mechanically optimized OrmoCer (organic

modified ceramics) up to soft materials like PDMS [3] can be structured. By means of parametrizing the laser that interacts with a suitable material, even property gradients within the material can be generated [4]. Therefore, applications are to find in all fields of microtechnology, e.g. micro-fluidics [5], micro-optics [6, 7], and microengineering [8].

Due to the diversity of materials, various structural requirements, and precision demands, different writing modes have evolved. It is possible to pattern in immersion as well as with larger working distance. In addition, liquid resists or resists solidified by annealing can be developed. It is also possible to expose the resist through glass slides.

2. System and Material

The system used here is a customized FemtoLAB laser workstation, made by Workshop of Photonics (Lithuania). Starting from laser wavelength 1030 nm, the system generates the wavelengths 515 nm and 343 nm using harmonic generators. This enables 1PP, 2PP, and ablation in one setup.

The system comes with an XYZ precision stage positioning unit and a galvo scanner. These provide optimal writing processes by means of their independent or simultaneous use. In simultaneous operation, the so-called infinite field of view technology achieves a synchronization of the two systems, so that stitching is prevented when writing field sizes that exceed the writing range of the galvo scanner.

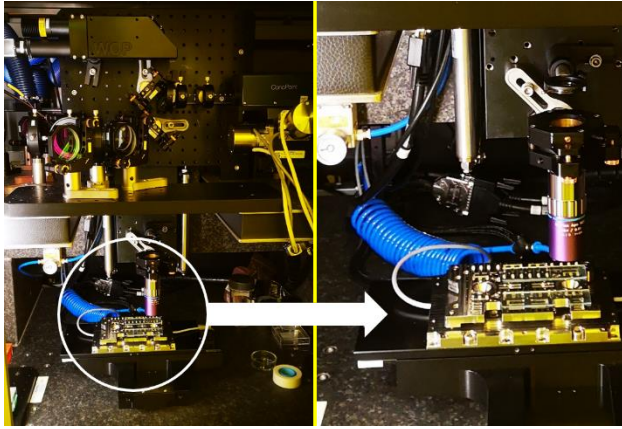


Figure 1. Inside view of the 2PP lithography system

The material used for the experiments is OrmoComp® by microresist Technology GmbH (Germany). The material shows glass-like properties after development. It is, therefore, particularly suitable for optical applications, but also enables mechanical applications.

Table 1 OrmoComp® properties

viscosity [Pa·s]	2.0 ± 0.5
curing wavelength [nm]	300 – 410
recommended exposure dose [mJ/cm ²]	500 – 1500
shrinkage [%]	5-7
refractive index (cured, 589 nm)	1.520
Abbe number	47
CTE (20-150 °C) [ppm/K]	150
dn/dT [10 ⁻⁴ /K]	-2.0
Young's modulus [GPa]	~1
hardness	
via indentation [MPa]	~68
Shore D	75

3. Technological challenges

3.1 Procedure

The writing speed and the quality of the result are influenced by the 2PP process parameters as well as the writing strategy. Both must be weighed against each other. For the writing process, the galvo scanner and the precision positioning unit are basically available. The galvo scanner is characterized by high writing speed and precision, but has only a very limited field of view (FoV), which varies depending on the objectives. The higher the targeted precision, the larger the required numerical aperture (NA), and the more limited is the FoV.

Thus, to produce features that are significantly larger than the FoV, the stage positioning unit must be moved. In the case of sequential movement, exposure is performed locally using the galvo scanner. The stage moves to a programmed position and the galvo scanner operates again. In this case, the positioning inaccuracy, as well as possible volume shrinkage effects of the resist, lead to stitching effects, which cause structural flaws. Depending on the structure, these imperfections may only be an aesthetic problem, or they may compromise the function. To avoid such imperfections, the positioning unit and galvo scanner work synchronously.

Regardless of the used motion strategy, different basic writing strategies are available (see Figure 2. a-c). Analogous to macroscopic additive manufacturing processes, the structures can be completely polymerized level by level after being sliced. In this case, the entire volume must be polymerized during the writing process. This process is very time-consuming. Alternatively, especially in this additive process, only the shell of the component can be polymerized with 2PP. In this case, liquid resist is enclosed in the shell. The enclosed resist can be completely polymerized in a following step by means of a UV flash with 1PP.

This procedure is the fastest option for creating large-volume components. However, the volume shrinkage during UV flash strongly affects the quality of the resulting product.

An intermediate approach is the use of additional support structures. Here, hatching-like structures support the shell and enclose several separate liquid resist volumes that are polymerized through a subsequently performed UV flash. The hatching structures are no longer visible after polymerization but can locally influence the material shrinkage. By using hatching structures, a compromise of time and precision can be achieved.

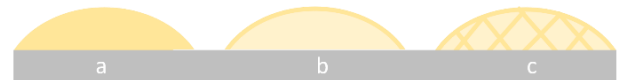


Figure 2. Exposure strategies: a: fully exposed, b: only shell exposed, c: shell and hatching structures exposed

As structures grow larger, such compromises become increasingly important. Even if stitching marks do not occur along the writing trajectories due to synchronization, further problems can arise when writing large-scale structures. No matter how the writing strategy is chosen, depending on the structure it is sometimes unavoidable that certain workpiece areas have to be passed twice. At these intersection areas, overlapping phenomena can occur. For example, local material shrinkage can result in visible shrinkage marks. The influence of these marks on the workpiece quality depends on the strategy, the material and the voxel size. Figure 3 exemplarily shows a trajectory that can lead to such an intersection mark.

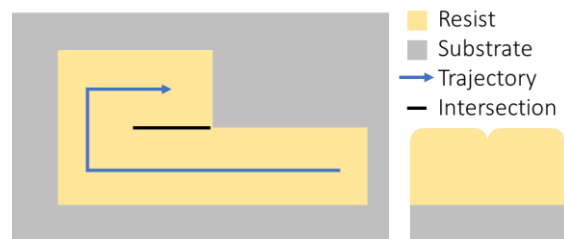


Figure 3. trajectory that can cause an intersection mark

A feature oriented writing strategy is to choose that avoids intersection marks as well as stitching marks or permits them only in areas that are functionally.

3.2. Upscaling

Many published application examples address nm-scale features, especially structures that can be written within the FoV of a galvo scanner. These small structures with a level of detail in the sub-micrometer range are definitely a unique selling point of this technology. However, there is a gap between this technology and other additive processes such as stereolithography (STL). Structured areas that are too detailed for STL but too large in for 2PP are not adequately covered. Therefore, upscaling strategies are necessary in the long term.

One example of upscaling is the prototyping of micro-fluidic structures. Figure 4 shows in detail the hydrodynamic focusing of a micro-cytometer developed by the MFG and Physikalisch-Technische Bundesanstalt (PTB, Germany). The fluidic swirl focuses blood platelets for subsequent size measurement. The original prototyping consists of a sophisticated process chain based on ultra-precision machining. In particular, the sealing of the microchannels of this multilayer structure is complex. By means of 2PP, such structures can be manufactured directly, also as closed cavities.

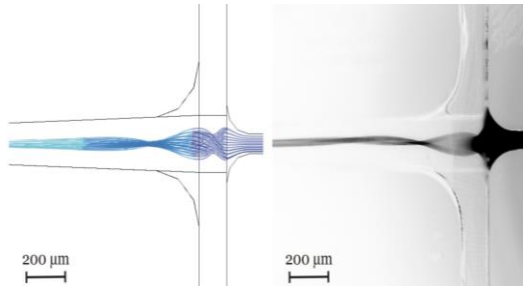


Figure 4. Micro fluidic hydrodynamic focusing invented by TU Berlin and PTB [9]

Direct miniaturization of such structures by 2PP is possible. Figure 5 shows a half-section of the cytometer as a 20x downsized component.

The challenge, however, is upscaling those features with acceptable production times, reliability and maintaining precision in different polymers.

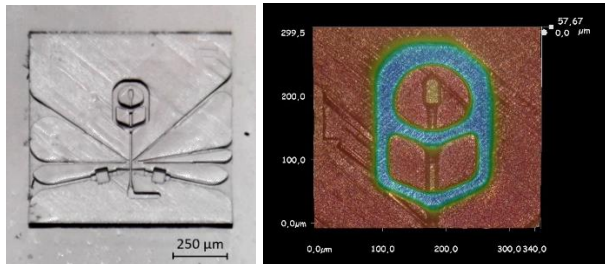


Figure 5. fluidic structure [9] 20x miniaturized (left) and example measurement (right)

4. Test component

In conventional mask-based 1PP UV lithography, the achievable resolution is approximated by simple diffraction considerations using the Rayleigh criterion. In 1:1 shadow exposure it is limited by near-field diffraction as a function of wavelength, resist thickness and proximity distance. In the case of projective exposure, it is limited by the wavelength, the NA and the respective correction constant of the used optics. Experimentally, the resolution can be determined by simple comb structures with variable spatial frequency. The parameter space of the 2PP is much more complex, furthermore an evaluation in three-dimensional domain has to be done, which causes additional metrological challenges.

In the context of multi-axis simultaneous machining, test components are required which allow the performance and quality of the systems to be objectively evaluated and compared. An initial test component is presented here, which is to be extended in the future by further useful structures, which in particular consider the degrees of freedom of 2PP technology. The test component contains macroscopic structures as well as microstructures, e.g. blaze gratings. The macroscopic structures have several levels, so that centricity and height can be detected, additionally. Some features are repeated in order to

be able to evaluate their position to each other. In addition, features were integrated that cannot be written in a single trajectory, so that overlapping areas are forced even when the galvo scanner and positioning unit are synchronized. The individual structures are located on a solid base body. A CAD of the initial test component is shown in Figure 6. A processed OrmoComp® part and a three-dimensional measurement can be seen in Figure 7.

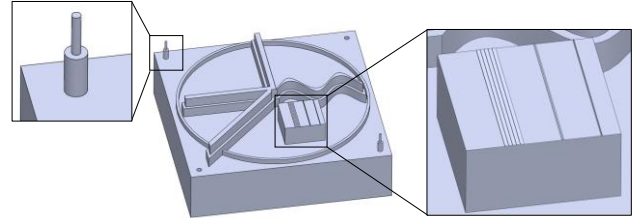


Figure 6. CAD and details of the test component

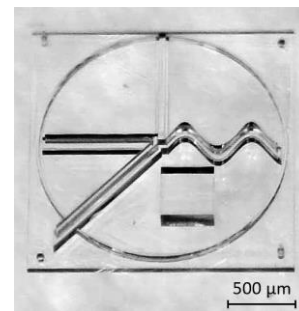


Figure 7. Test component made from OrmoComp®

The component initially addresses the dimensional measuring of tolerances. In the future, it will be supplemented by functional structures to be able to record the quality indirectly as well.

5. Procedure and results

5.1 Procedure

As described, various configurations are available for the exposure of the resist. These can also be implemented in the system used. The configuration used for the experiments is shown in Figure 8. In order to fabricate large-area structures in a time-efficient manner, a Mitutoyo 50x / 0.42 objective was used. This objective is not used in dip-in, but with a working distance. Since the resist used is liquid and to exclude influences of an uneven surface, the resist was enclosed between two precision cover glasses with a defined distance.

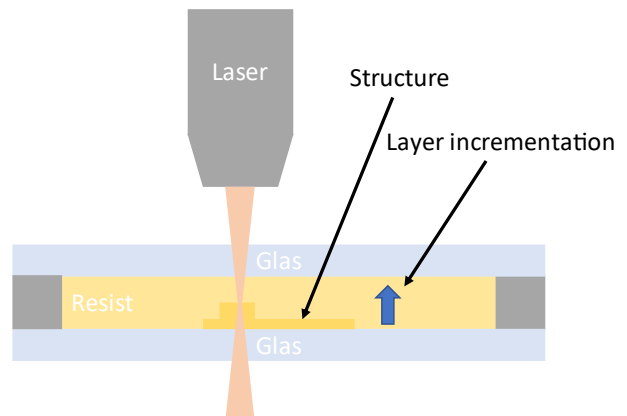


Figure 8. schematic illustration of the exposure configuration used

The following basic parameters are used:

- Laser: 601.8 kHz, 515nm
- Position Synchronized Output (PSO) 10k/mm
- Laser power Controller 25%, Attenuator 40%

In this case, the writing process starts from the surface of the lower glass to ensure that the structure is bonded and built up layer by layer. This may be necessary for liquid resists.

Different writing strategies, full polymerization, partial hatching, and large-scale hatching, were carried out. The layer wise and feature oriented mixture of these methods was also considered. The production times varied between 5 and 10 h.

5.2 Results

An exemplary production result is shown in Figure 7. The results were subsequently observed via microscope (Figure 9) and measured via digital microscope Keyence VHX 2000 (Figure 11) and individual achievable surface defects via Nanosurf Nanite AFM (see Figure 10). A comparison of the structures with and without defect marks can be seen in Figure 9. These surface defects can extend to several micrometers but can be strategically avoided.

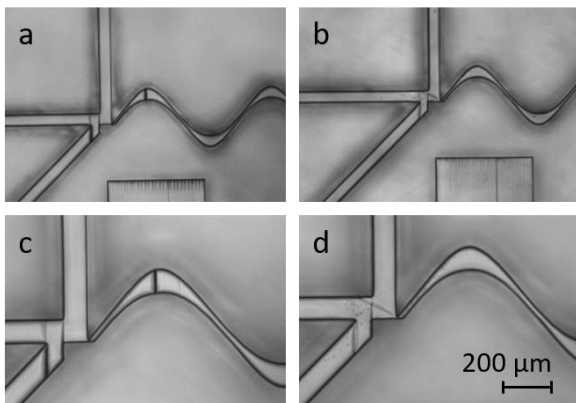


Figure 9. Microscope image of test structures: a and c with, d and b without surface defect marks

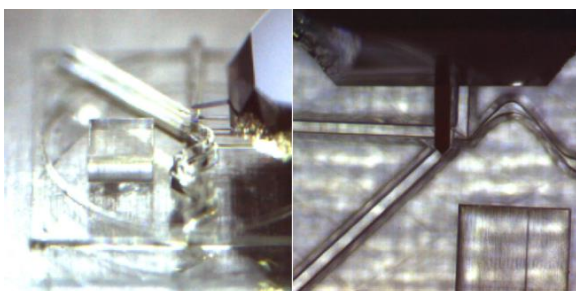


Figure 10. AFM measurement of surface defect marks

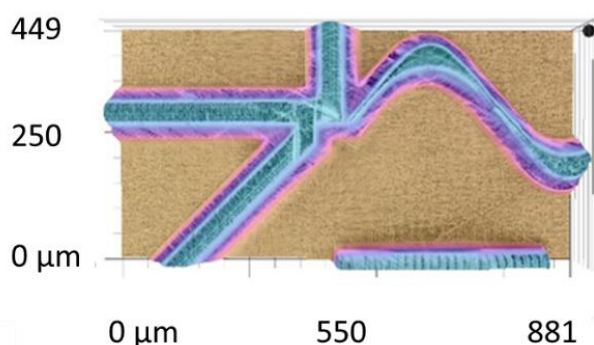


Figure 11. Measurement of test features

However, this requires an individual strategic adjustment, which was carried out iteratively for some sections.

Figure 10 shows detailed images of corresponding sections of the test component with and without defects.

The results are in the sub-micrometre range despite the intended rough voxel structure with the low NA and the chosen parameters, which is due to the temporal optimization. Further experimentation and scaling of the component to use different NA up to immersion, as well as inclusion of new features, will be focused in future activities.

It has been shown that even when creating parts that extend far beyond the field of view of a galvo scanner, synchronization and strategic interventions can enable structures that are highly accurate without stitching and intersection marks.

6. Discussion and outlook

The many international publications of the last decade have shown that the 2PP is of high potential for additive manufacturing in microtechnology. During the transition of this technology from a prototyping tool to a production process as well as during the upscaling of the component sizes, methods are necessary to ensure the process reliability and to evaluate performance objectively. The work presented here contributes to the creation of necessary test components.

However, the potential of the technology goes beyond the dimensions that can be tested here.

Based on this work and in collaboration with the additive manufacturing as well as the metrology community, these methods will be extended in the future.

References

- [1] Sun, H.-B., Matsuo, S., Misawa, H., 1999. Three-dimensional photonic crystal structures achieved with two-photon-absorption photopolymerization of resin 74, p. 786.
- [2] Göppert-Mayer, M., 1931. Über Elementarakte mit zwei Quantensprüngen 401, p. 273.
- [3] Rekštytė, S., Malinauskas, M., Juodkazi, S., 2013. Three-dimensional laser micro-sculpturing of silicone: towards bio-compatible scaffolds. *Opt Express* 21, p. 17028.
- [4] Ocier, C.R., Richards, C.A., Bacon-Brown, D.A., Ding, Q. *et al.*, 2020. Direct laser writing of volumetric gradient index lenses and waveguides. *Light Sci Appl* 9, p. 196.
- [5] Lölsberg, J., Linkhorst, J., Cinar, A., Jans, A. *et al.*, 2018. 3D nanofabrication inside rapid prototyped microfluidic channels showcased by wet-spinning of single micrometre fibres. *Lab Chip* 18, p. 1341.
- [6] Harnisch, E., Russew, M., Klein, J., König, N. *et al.*, 2015. Optimization of hybrid polymer materials for 2PP and fabrication of individually designed hybrid microoptical elements thereof 5, p. 456.
- [7] Malinauskas, M., Žukauskas, A., Purlys, V., Belazaras, K. *et al.*, 2010. Femtosecond laser polymerization of hybrid/integrated micro-optical elements and their characterization 12, p. 124010.
- [8] Power, M., Thompson, A.J., Anastasova, S., Yang, G.-Z., 2018. A Monolithic Force-Sensitive 3D Microgripper Fabricated on the Tip of an Optical Fiber Using 2-Photon Polymerization. *Small* 14, e1703964.
- [9] Theisen, J., 2007. *Ein neuartiges 3D-mikrostrukturiertes Durchflusszytometer*. Technische Universität Berlin.

Characterizing shrinkage and quality of ceramic two-photon printed microstructures

John Cortes¹, Magi Mettry¹, Matthew Worthington¹, Swetha Chandrasekaran¹, Robert Panas¹

¹Lawrence Livermore National Laboratory, Livermore, CA, USA

Corresponding author: JohnCortes@llnl.gov

Abstract

Characterizing the optimal printing parameters and shrinkage of polymer-derived ceramic (PDC) resins is important to integrate these promising materials into future MEMS/NEMS applications. These ceramic materials offer better mechanical and thermal properties for devices which are designed to operate in extreme or highly dynamic environments. This work studies and characterizes the optimal 2-photon polymerization printing parameters for SiOC ceramic resins. The study found that these resins print optimally the Nanoscribe laser power settings are within the 35%-45% range and the scan speed are within 6,000 $\mu\text{m/s}$ to 8,000 $\mu\text{m/s}$. In addition, the qualitative properties of the prints were also studied through SEM imaging. Defects and distortion as a function of laser power and laser scan speed were also characterized. Additionally, the shrinkage of the PDC material was characterized as a function of scan passes (which affects proportion of fully cross-linked volume) before and after the pyrolysis process. This study found that doing up to three passes per voxel can reduce overall linear shrinkage from about 47% to 35%. Lastly, a proposed method of dealing with this shrinkage in functional structures is proposed. Strain relief structures are introduced with the goal of maintaining the structure/s center line aligned during shrinkage. This will be valuable for devices which will require alignment and transfer onto a separate substrate.

Key words: ceramic, microstructures, two-photon printing, shrinkage

1. Introduction

The last ten to fifteen years has brought upon a revolution in prototyping and rapid product development led by advances in additive manufacturing (AM) technologies. Additive manufacturing creates the opportunity to manufacture highly intricate 3D structures using a single, highly repetitive process one layer at a time. Although most of that work has focused on macro-scale printing processes with plastics (and more recently, metals and composites), a significant scientific push has been made to also develop micro-scale processes [1, 2, 3]. Two-photon Polymerization (2PP) is one of the technologies that has allowed for development of 3D printed microstructures. 2PP utilizes femtosecond laser pulses with two-photon absorption to generate features using a wide variety of photon-activated photoresists and resins with a resolution as high as 100 nm [4]. The print resolution of 2PP processes is determined by the exposure dose to the smallest polymerized volume. This dose is determined both by the pulse energy and the scanning speed [5].

Most of these resins result in polymer structures which are limited in their application due to their poor mechanical properties. However, the use of ceramic resins has recently been developed for 2PP processes [6, 7]. They generally come in the form of polymer-derived ceramics (PDC) and are highly tuneable based on their molecular compositions. While these resins feature much more favourable mechanical properties, they tend to shrink anywhere from 30-55% during post-processing [8, 9]. This may not be desirable and difficult to design for in precise MEMS/NEMS applications, therefore it is crucial that this shrinkage be fully understood and characterized.

In this work, we study the shrinkage of 2PP-printed silicon oxycarbide (SiOC) microstructures with a 100:1 aspect ratio. Additionally, we study ways to reduce this shrinkage in self-centering disk structures. 3D printed ceramic flexures at the microscale would be useful in MEMS devices that require complex geometries with low thermal conductivities.

2. Methods

The microscale two-photon printing process was performed using a NanoScribe GmbH Photonic Professional GT system at LLNL's Advanced Manufacturing Laboratory (AML) facility. This system features a 150mW (at 100% power) femtosecond laser source with a center wavelength of 780 nm and a pulse width of ~ 100 fs. A 63x 1.4 NA oil immersion lens (Carl Zeiss) was used for optimal print resolution. A single-side polished silicon chip measuring approximately 1" by 1" was coated with 3-(Trimethoxysilyl)propyl methacrylate (Silane) for 5 minutes at a temperature of 90 °C to enhance surface adhesion. A small drop of the custom polymer-derived ceramic (PDC) resin was applied to the polished side of the silane-treated silicon chip. The structures were printed up-side-down using the "dip-in laser lithography" method. The prints were then developed by submerging them in propylene glycol monomethyl ether acetate (PGMEA) for four hours. This process removes any unpolymerized solution

After full development in the PGMEA solution, the sample was dried using an EMS 3100 critical point drying system. After critical-point-drying, the samples were pyrolyzed in a

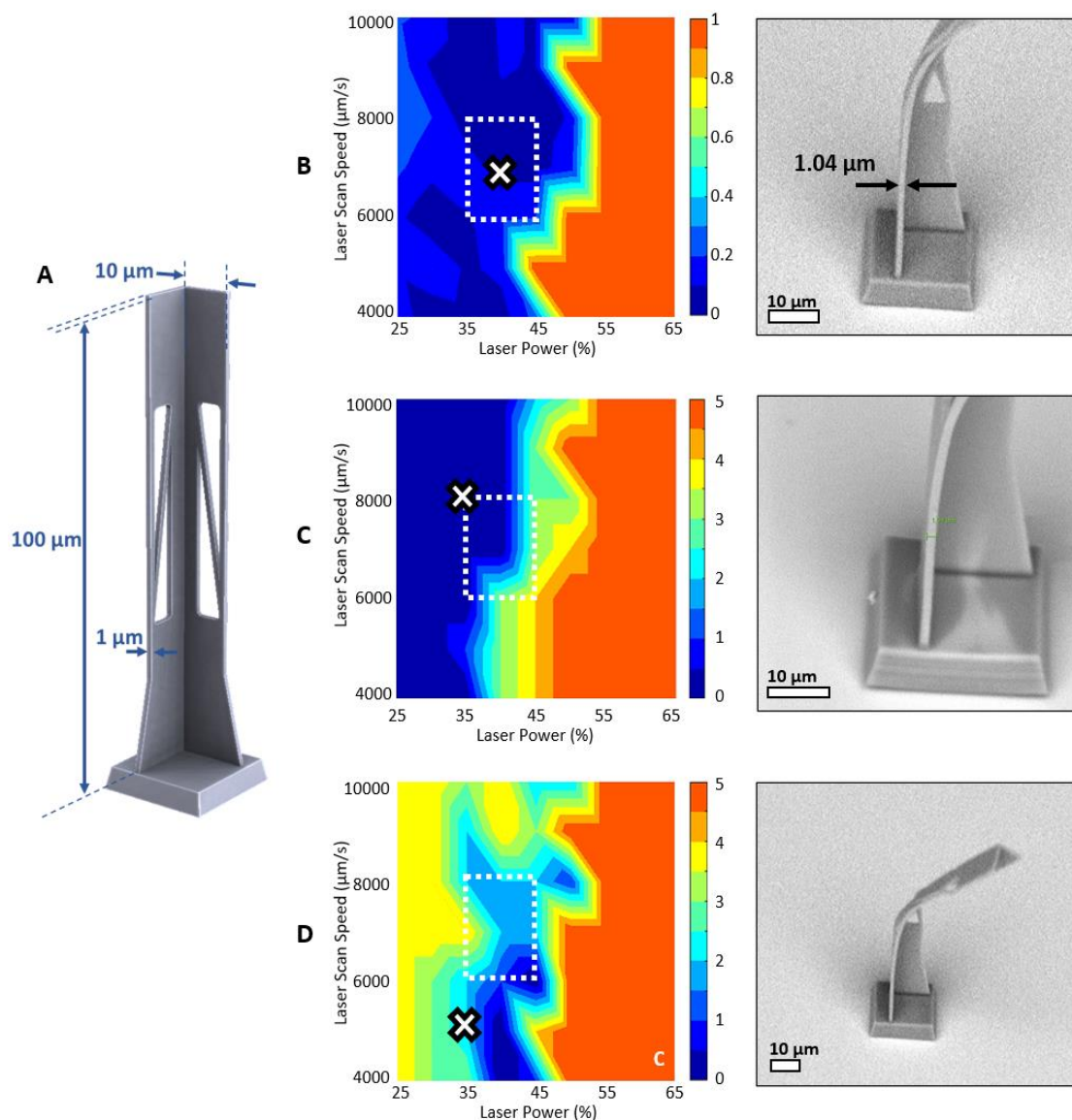


Figure 1. A) CAD model of a 100:1 aspect ratio blade with relevant dimensions. Panel B) shows the deviation from designed dimensions, in μm , where the sample blade (with print settings denoted by an “X” in the contour plot) shows a very small deviation from the $1\ \mu\text{m}$ thickness dimension. Panel C) shows the print defects on a qualitative 0-5 scale (5 is worst), including an SEM image of a blade that has nearly defect-free. Panel D) shows the print distortion on a qualitative 0-5 scale (5 is worst), with the sample SEM image showing a distorted blade which cannot stand in a full vertical position.

conventional tube furnace containing a nitrogen atmosphere at temperatures of 250°C , 400°C , 600°C and $1,000^\circ\text{C}$, for an hour each. The sample was then allowed to cool down to room temperature at a rate of 5°C per minute. The samples were characterized using a Phenom XL benchtop scanning electron microscope (SEM) in between each step to fully characterize the shrinkage effects of each process.

3. Results

First, the overall print quality of the SiOC structures was explored by both qualitative and quantitative methods before subjecting the structure to the pyrolysis process. First, a tall, thin blade structure with a 100:1 aspect ratio was printed. This L-shaped blade features a height of $100\ \mu\text{m}$, a width of $10\ \mu\text{m}$ and a thickness of $1\ \mu\text{m}$, as shown in Figure 1A. Diagonal features were also added to gauge the print quality of non-horizontal and vertical features. These thin, diagonal have a cross section of $1\ \mu\text{m} \times 1\ \mu\text{m}$. There are two ways to modulate the power dosage introduced into the resin voxel during printing. Both the laser power and laser scan speed can be tuned for optimal

performance. For example, a high dosage would require either a higher laser power setting or a lower laser scan speed. It must be noted that the distance between layers in the z-direction was kept at a constant $500\ \text{nm}$.

The first measure of print quality was the deviation from the designed thickness of $1\ \mu\text{m}$. Figure 1B shows a contour plot of the thickness deviation for various laser power and laser scan speed settings. This was achieved by printing an array of structures with scan speed intervals of $1,000\ \mu\text{m/s}$ and laser power intervals of 5% . The dotted box within each contour plot represents the area where the print quality is maximized for the polymer-derived ceramic resin. Figure 1B shows that a very small deviation can be initially obtained with a print speed of $7,000\ \mu\text{m/s}$ and a laser power of 40% . The thickness of a blade with these parameters tends to be within the $0.98\ \mu\text{m}$ and $1.03\ \mu\text{m}$ range.

Similarly, prints performed within this power and speed range tend to feature less defects as well. A qualitative scale from 0-5 was generated to judge the level of defects found in the prints.

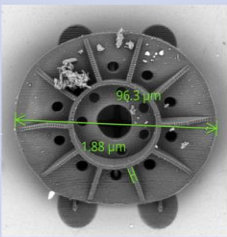
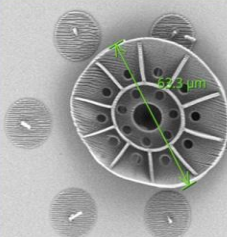
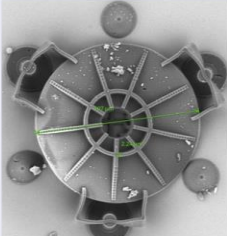
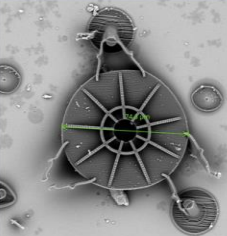
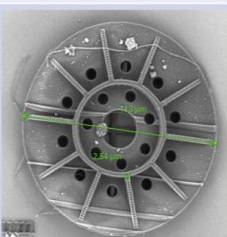
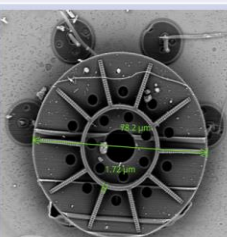
Condition	After Critical Point Drying	After Pyrolysis
Original Design D= 120 μm t= 2.50 μm 	 D= 96.3 μm t= 1.88 μm Shrinkage (D) 19.7%	 D= 63.3 μm t= 1.45 μm Shrinkage (D) 47.2%
	 D= 107 μm t= 2.24 μm Shrinkage (D) 10.8%	 D= 74.6 μm t= 1.98 μm Shrinkage (D) 37.8%
	 D= 113 μm t= 2.54 μm Shrinkage (D) 5.8%	 D= 78.2 μm t= 1.72 μm Shrinkage (D) 34.8%

Figure 2. Scanning electron microscope images of a disk microstructure before and after pyrolysis, ranging from n=1,2,3 scans during the 2PP printing process. These disks also feature two separate designs of strain relief legs that are designed to accommodate for the linear shrinkage and maintain the structures in alignment with the center axis before and after pyrolysis

Figure 1C shows an SEM image of a blade printed at 35% laser power and 8,000 $\mu\text{m}/\text{s}$. This blade is relatively free of defects, with only minor blemishes. Some of the defects that do show up include pinholes and small gaps in the bulk material. Most of these defects can be attributed to a high level of energy being introduced into the voxel, essentially “burning” the material. Similarly, if not enough energy is introduced, the material cannot fully cross-link, resulting in gaps and overall shape distortion.

Prints that were not properly energized also displayed high amounts of distortion. For this particular structure, that meant that the blades featured different degrees of curvature and the inability to stand fully upright. Figure 1D shows an SEM image of a blade printed with a speed of 5,000 $\mu\text{m}/\text{s}$ and 35% laser power. This blade, though free of visible defects, was not properly cross-linked due to an insufficient power input to the voxels. The blade bent easily during the air-drying process. Blades printed with settings within the dotted box tend to stand upright or have a slight bend to them, especially at lower power and higher scan speed settings.

After gaining an understanding of the optimal print parameters, a disk geometry, like the one showed by the left panel of Figure 2, was created to understand how pyrolysis affects shrinkage in the structure and some potential ways to mitigate it. The disk structure features two separate leg designs that function as strain relief structures, bending inward as the disks isotopically shrink. This is meant to keep the center axis of the disk in the same location during shrinkage. The disks themselves are 120 μm in diameter with a characteristic thickness of 2.5 μm .

Using the lessons learned from the first part of the experiment, the disks were printed at 7,000 $\mu\text{m}/\text{s}$ and 40% laser power. One of the key variables that were tested was the number of scanned passes per print. The goal of this experiment was to gauge the effect on shrinkage of the total energy provided to each voxel through a multi-pass approach. For samples that only had a single pass of the scanner, shrinkage was as high as 47.2%. At this large shrinkage, the strain relief structures failed, as shown in the top-right panel of Figure 2. This shrinkage was reduced to 37.8% when two passes were performed. Lastly, three passes per voxel were also tested, resulting in a shrinkage of 34.8%.

Doing more than three passes did not yield any significant improvements in the amount of shrinkage. The material seems to saturate at three passes and is fully cross linked. The majority of the shrinkage occurs during the pyrolysis process, but surprisingly, the material shrinks a significant amount after critical point drying. This is likely due to some of the un-energized material being extracted from the structure during the process. Though it may help with the reduction in shrinkage, the multi-scan process can produce defects in the print.

In particular, the three-pass prints features line that rise from flat surfaces when they should not, as shown in the 3-pass SEM images in Figure 2. These are due to the fact that once the voxel has been energized, its focus plane slightly changes due to the change in the material. This is commonly referred to as a shadowing effect caused by fully or partially polymerized layers. This effect can result in features being shifted in the z-plane by as much as a 0.25-0.5 μm , based on white light profilometer measurements.

4. Conclusion and Future Work

Ceramic materials bring forth a host of advantages of conventional polymer materials. This will allow devices printed with ceramic resins to operate in more extreme environments where high mechanical properties, low thermal conductivity and electrical insulation may be required. Advances in this field can result in technological leaps in the MEMS/NEMS field. However, the problem of shrinkage must be properly addressed and accounted for before many of these advances can occur. This work lays a groundwork for two separate methods of minimizing and/or accounting for this shrinkage. The first method is using a multi-pass approach to increase the overall dosage and cross-linking of the material before it is dried and pyrolyzed. Second, using strain-relief structures to keep the print centered as it shrinks.

Future work will focus on further developing these two methods to combat shrinkage. Additionally, the transfer of ceramic prints onto other substrates will be studied for actuators, micro-mirrors, and other dynamic applications. This process would involve managing shrinkage of the printed devices, maintaining their center line position and having built-in features that would allow for a repeatable double stamp process.

Acknowledgments

This work was performed under the auspices of the U.S. Department of Energy by Lawrence Livermore National Laboratory under Contract DE-AC52-07NA27344 (LLNL-CONF-823399) and supported by LDRD 19- ERD-018.

References

- [1] Saha, et al. "Scalable Submicrometer Additive Manufacturing." *Science*, vol. **366**, no. 6461, 2019, pp. 105–109.
- [2] Chu, et al. "Centimeter Height 3D-Printing with Femtosecond Laser Two-Photon Polymerization." *Advanced Materials Technologies*, vol. **3**, no. 5, 2018, p. 1700396.
- [3] Ngo, Kashani, Imbalzano, Nguyen and Hui. "Additive manufacturing (3D printing): A review of materials, methods, applications and challenges." *Composites Part B: Engineering*, vol. **143** (2018).
- [4] Zheng, Kurselis, El-Tamer, Hinze, Reinhardt, Overmeyer and Chichkov. "Nanofabrication of High-Resolution Periodic Structures with a Gap Size Below 100 nm by Two-Photon Polymerization." *Nanoscale Res Lett.*, vol. **14**, 134 (2019).
- [5] Ovsianikov et al. "Two Photon Polymerization of Polymer–Ceramic Hybrid Materials for Transdermal Drug Delivery." *Int. J. Appl. Ceram. Technol.* 2007, vol. **4**, issue 1, p. 22–29.
- [6] Cui, et al. "Additive Manufacturing and Size-Dependent Mechanical Properties of Three-Dimensional Microarchitected, High-Temperature Ceramic Metamaterials." *Journal of Materials Research*, vol. **33**, no. 3, 2018, pp. 360–371.
- [7] Eckel, et al. "Additive Manufacturing of Polymer-Derived Ceramics." *Science*, vol. **351**, no. 6268, 2015, pp. 58–62. *Nanoscale Res Letters*, vol. **14**, 134 (2019).
- [8] Brigo, Schmidt, Gandin, Michieli, Colombo and Brusatin. "3D Nanofabrication of SiOC Ceramic Structures." *Adv. Sci.* 2018, vol. **5**, 1800937.
- [9] Bauer et al. "Additive Manufacturing of Ductile, Ultrastrong Polymer-Derived Nanoceramics." *Matter*, vol. **1**, no. 6, 2019, p. 1547-1556.

Session 4: Focus on lattice structures

Direct additive manufactured beam shape defect identification from computed tomography and modal decomposition

Marc-Antoine de Pastre¹, Yann Quinsat¹, Claire Lartigue¹

¹LURPA, ENS Paris-Saclay, Université Paris-Saclay, 91190 Gif-sur-Yvette, France

marc-antoine.de_pastre@ens-paris-saclay.fr

Abstract

As one of the main additive manufacturing (AM) advantages, lattice structures are being studied in many applications such as vibration attenuation, weight reduction of components or optimised heat exchangers. However, lattice structures are challenging to produce, and may present some shape defects. Although significant works have been performed in lattice structure defect observations such as overhanging features or resulting porosity, there has been relatively less research in modelling shape defects by defining a geometric description approach. In this paper, a Virtual Volume Correlation (V2C) method is proposed in order to identify metal laser powder bed fusion (LPBF) BCCz struts shape defect directly from volumetric data obtained by X-ray computed tomography (XCT). In the proposed V2C method, a correlation score is calculated between the volumetric data and a virtual volume. This virtual volume is determined according to the computer-aided-design (CAD) model and a shape defect which is defined using a linear decomposition relying on a user-defined defect basis. Shape defects of the studied part are successively, according to a Newton Raphson optimisation scheme, determined by correlation score minimisation. Vertical and inclined beams have been printed and measured with XCT and focus variation (FV). Strut geometries obtained with V2C methodology are compared with extracted ISO_{50%} point clouds, on the one hand, and measured FV point clouds, on the other hand, by computing signed cloud-to-mesh distances. These comparisons bring out that the V2C method is efficient to identify strut shape defects directly from volumetric data, without any post-reconstruction XCT data treatment. The simplification of these data treatment steps then raises the direct and accurate CAD feedback opportunity. Conclusions are drawn regarding the suitability of the proposed V2C method and its further development to more complex LPBF structures.

Computed tomography, virtual volume correlation, modal decomposition, shape defect identification

1. Introduction

With the design freedom enabled by additive manufacturing (AM), complex geometries are not limited by subtractive or formative manufacturing constraints anymore [1]. Lattice structures, which are increasingly studied in the AM field, consist of an elementary cell regularly repeated in the 3D directions to form a network [2, 3, 4]. Lattice structures are not free from defects, which have been reviewed by Echeta *et al.* [4] for powder bed fusion (PBF). Measurement of these defects are mainly performed using computed tomography (CT) for its ability to assess either internal or external dimensional deviations [4, 5]. However, CT dimensional measurements rely on the material boundary determination introducing a threshold uncertainty, prior to any further data treatments [6, 7, 8]. There have been significant efforts in reducing this uncertainty with sub-voxel studies [8, 9] or more recently by conformance approach [10].

In this paper, a virtual volume correlation (V2C) method is proposed in order to find form defect of body-centered cubic with vertical struts geometry (BCCz cells), directly from volumetric data, without boundary thresholding nor additional data treatment. Indeed, recent works have highlighted the interest of virtual correlation techniques for contour or envelope identification in different fields. In the medical field, virtual correlation methods are applied for modelling pelvic organs

from magnetic resonance imaging (MRI) volumetric data [11]. In the mechanical field, virtual correlation techniques have proven their interest for shape boundary identification of curved and elongated structures [12, 13].

The aim of this paper is to assess the proposed V2C method applied to lattice beams relying on a defect basis description. V2C estimated form defect will be compared to extracted ISO_{50%} and measured focus variation (FV) [14] point clouds. In section 2, the V2C method is presented and assessed using vertical and inclined struts, which is representative of a BCCz lattice structure. Results are presented in section 3 and discussed in section 4.

2. Methodology

2.1. Virtual volume correlation

Let f be a physical volume, containing a closed envelope whose displacement field \mathbf{u} should be identified in comparison to an original regular shape. Let $\{X_f\}$ be the voxels defining that envelope. Similarly, let g be a virtual volume and $\{X_g\}$ the voxels defining the virtual envelope. Each point of the physical envelope can be written as:

$$X_f = X_g + \mathbf{u} \quad (1)$$

V2C consists in iteratively minimising the grey level differences between physical and virtual volumes using the least square criterion. A correlation score Φ should be introduced as:

$$\Phi(\mathbf{u}) = \iiint_{ROI} [f(\mathbf{X}) - g(\mathbf{X} + \mathbf{u})]^2 d\Omega \quad (2)$$

where ROI refers to the region of interest in terms of considered voxels, and $\{\mathbf{X}\}$ refers to considered voxels in the physical volume f . The displacement field \mathbf{u} only applies to the virtual contour points, and can be described as a sum of modes i.e. elementary displacement fields. Whereas previous works often modelled strut shape defects as first order ellipse approximations [15, 16], modal decomposition methods [17, 18, 19] consist in expressing the form defect as a linear combination of elementary displacements:

$$\mathbf{u} = \sum_k \lambda_k \mathbf{u}_k \quad (3)$$

where λ_k are the components of $\{\lambda\}$ and refer to the modal amplitude i.e. the amplitude of the elementary displacement descriptor \mathbf{u}_k and are defined by:

$$\{\lambda^*\} = \underset{\lambda}{\operatorname{argmin}} \Phi(\mathbf{u}) \quad (4)$$

λ_k^* are found by combining equations 2 and 3 using a Newton-Raphson optimisation. An illustration of V2C application is shown in Figure 1 for a 2D example of a strut cross-section. From volumetric data (Figure 1a), the shape defect is initially taken as a nominal circle (Figure 1b), and is iteratively identified (Figure 1c).

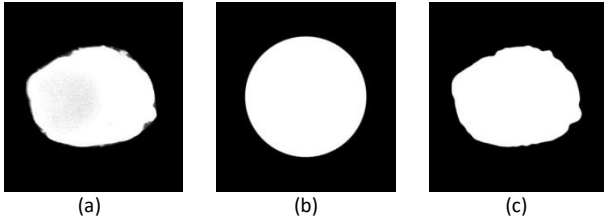


Figure 1. Illustration of V2C on a 2D strut cross-section: (a) XCT physical measurement; (b) initial virtual shape; (c) computed virtual shape defect

2.2. Shape defect basis

This section particularly focuses on the elementary displacement descriptors \mathbf{u}_k introduced in equation 3. In previous virtual correlation works, Semin *et al.* [13] used segmentation 2D descriptors to identify elongated curvilinear shapes whereas Jiang *et al.* [20] and Rhétoré *et al.* [21] used B-spline curves. Jiang *et al.* [11] extended the methodology to the 3D modelling of pelvic organs relying on NURBS geometric descriptors.

In this work, as lattice beams are studied, displacement descriptors \mathbf{u}_k are introduced considering cylinder defects. Indeed, for this geometry, Homri *et al.* [22] noted the modal decomposition usefulness for cylinder shape defect identification.

Therefore, the displacement field is assumed to be four-fold:

- Rigid transformations
- Dilatation
- Vertical defects:
 - Vertical section modification descriptors such as taper or barrel modes
 - Vertical rippled modes
- Plane defects defined by sinusoidal descriptors

Figure 2 illustrates some of the considered modes for the chosen shape defect basis.

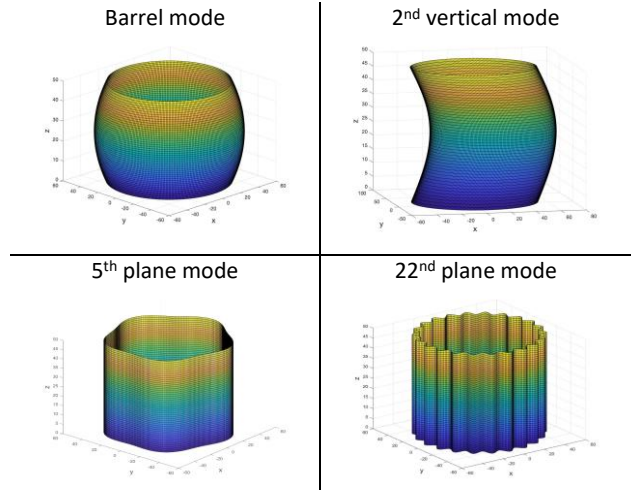


Figure 2. Illustration of some of the considered modes in the chosen basis description (amplitudes have been enhanced for more visibility)

2.3. Sample manufacturing and measurement

2.3.1 Sample manufacturing

Samples consist in vertical and inclined beams in order to be representative of vertical and inclined beams defining a BCCz strut-based lattice structure (see Figure 3). Beam radii have been set to 0.6 mm and have a 5 mm length. Samples were produced by laser PBF on an Addup FormUp 350 using Inconel 718 powder and the printing parameters displayed in Table 1.



Figure 3. Vertical and inclined BCCz representative printed struts. (One strut from each set has been considered in the following)

Table 1: Printing parameters

Powder	Inconel 718
Layer thickness	40 μm
Laser power	220 W
Scan speed	2100 $\text{mm}\cdot\text{s}^{-1}$
Contour scan power	210 W
Contour scan speed	1800 $\text{mm}\cdot\text{s}^{-1}$
Hatch space	55 μm

2.3.2 Sample measurements

Each beam was measured using X-ray CT and FV instruments. Measurement setups are provided hereafter:

- XCT: geometric magnification of 33 % leading to a voxel size of 9 μm . Volumetric reconstruction was performed from 900 projections, tube voltage 150 kV, tube current 40 μA . Projections were saved in a .raw file format.
- FV: 10 \times objective lens with long working distance, numerical aperture 0.3, field of view (2.05 \times 2.05) mm, pixel lateral resolution 2.07 μm , optical lateral resolution 0.91 μm , contrast lateral resolution 0.53 μm , coaxial

These values are relatively low regarding the objective of studying shape defect. Thus, V2C provides a good estimation of lattice strut shape defect, performing the strut roughness separation from shape defect.

5. Conclusion

This paper showed the suitability of the proposed V2C method to identify strut shape defect directly from volumetric measurements, without any additional XCT data treatment. Moreover, the noteworthiness of V2C is to extend shape defect determination relying on modal decomposition relatively to a user-defined defect basis.

However, modal decomposition raises the number of considered modes question. Future works will focus on more precise sensitivity studies in order to better understand how the number of considered modes, as well as the chosen defect basis, will impact the correlated shape defect.

Future works will also focus on a meshed version on V2C adapted to entire lattice structures in order to broaden CAD feedback opportunities.

Acknowledgments This work was performed using HPC resources from the “Mésocentre” computing center of CentraleSupélec and École Normale Supérieure Paris-Saclay supported by CNRS and Région Île-de-France (<http://mesocentre.centralesupelec.fr/>).

CT measurements at ENS Paris-Saclay has been financially supported by the French “Agence Nationale de la Recherche,” through the “Investissements d’avenir” program (ANR-10-EQPX-37 MATMECA Grant)

References

- [1] I. Gibson, D. W. Rosen, and B. Stucker, *Additive manufacturing technologies: rapid prototyping to direct digital manufacturing*. Springer Verlag, 2010.
- [2] A. Hadi, F. Vignat, and F. Villeneuve, “Design Configurations and Creation of Lattice Structures for Metallic Additive Manufacturing,” in *14ème Colloque National AIPPRIMECA*, (La Plagne, France), Mar. 2015.
- [3] C. Beyer and D. Figueroa, “Design and analysis of lattice structures for additive manufacturing,” *Journal of Manufacturing Science and Engineering*, vol. **138**, 06 2016.
- [4] I. Echeta, X. Feng, B. Dutton, S. Piano, and R. Leach, “Review of defects in lattice structures manufactured by powder bed fusion,” *International Journal of Advanced Manufacturing Technology*, vol. **106**, 01 2020.
- [5] L. Chiffre, S. Carmignato, J.-P. Kruth, R. Schmitt, and A. Weckenmann, “Industrial applications of computed tomography,” *CIRP Annals - Manufacturing Technology*, vol. **63**, 12 2014.
- [6] W. Dewulf, K. Kiekens, Y. Tan, F. Welkenhuyzen, and J.-P. Kruth, “Uncertainty determination and quantification for dimensional measurements with industrial computed tomography,” *CIRP Annals*, vol. **62**, no. 1, pp. 535 – 538, 2013.
- [7] J. S. Rathore, C. Vienne, Y. Quinsat, and C. Tournier, “Influence of resolution on the x-ray ct-based measurements of metallic am lattice structures,” *Welding in the World*, vol. **64**, pp. 1367–1376, 2020.
- [8] J. J. Lifton, A. A. Malcolm, and J. W. McBride, “On the uncertainty of surface determination in x-ray computed tomography for dimensional metrology,” *Measurement Science and Technology*, vol. **26**, p. 035003, feb 2015.
- [9] J. Yague-Fabra, S. Ontiveros, R. Jimenez, S. Chitchian, G. Tosello, and S. Carmignato, “A 3d edge detection technique for surface extraction in computed tomography for dimensional metrology applications,” *CIRP Annals*, vol. **62**, no. 1, pp. 531 – 534, 2013.
- [10] S. Petró, L. Pagani, G. Moroni, and P. J. Scott, “Conformance and nonconformance in segmentation-free x-ray computed tomography geometric inspection,” *Precision Engineering*, 2021.
- [11] Z. Jiang, O. Mayeur, J.-F. Witz, P. Lecomte Grosbras, J. Dequidt, M. Cosson, C. Duriez, and M. Brieu, “Virtual image correlation of magnetic resonance images for 3d geometric modelling of pelvic organs,” *Strain*, vol. **55**, no. 3, p. e12305, 2019. e12305 10.1111/str.12305.
- [12] M. L. M. François, A. Bloch, and J. C. Thomas, “Metrology of contours by the virtual image correlation technique,” in *Advancement of Optical Methods in Experimental Mechanics*, Volume **3** (H. Jin, S. Yoshida, L. Lamberti, and M.-T. Lin, eds.), (Cham), pp. 239–246, Springer International Publishing, 2016.
- [13] B. Semin, H. Auradou, and M. François, “Accurate measurement of curvilinear shapes by virtual image correlation,” *The European Physical Journal Applied Physics*, vol. **56**, 10 2011.
- [14] NF EN ISO 25178-606:2015: Geometrical product specification (GPS). Surface texture: Areal. Part 606: Nominal characteristics of non-contact (focus variation) instruments. AFNOR, 2015.
- [15] J. S. Rathore, C. Mang, C. Vienne, Y. Quinsat, and C. Tournier, “A methodology for computed tomography-based non-destructive geometrical evaluations of lattice structures by holistic strut measurement approach,” *Journal of Manufacturing Science and Engineering*, vol. **143**, no. 5, p. 051012, 2021.
- [16] S. Murchio, M. Dallago, F. Zanini, S. Carmignato, G. Zappini, F. Berto, D. Maniglio, and M. Benedetti, “Additively manufactured ti–6al–4v thin struts via laser powder bed fusion: Effect of building orientation on geometrical accuracy and mechanical properties,” *Journal of the Mechanical Behavior of Biomedical Materials*, vol. **119**, p. 104495, 2021.
- [17] S. Samper and F. Formosa, “Form defects tolerancing by natural modes analysis,” *Journal of Computing and Information Science in Engineering*, vol. **7**, no. 1, pp. 44–51, 2007.
- [18] D. Etievant, Y. Quinsat, F. Thiebaut, and F. Hild, “A modal approach for shape defect measurement based on global stereo-correlation,” *Optics and Lasers in Engineering*, vol. **128**, p. 106030, 2020.
- [19] F. Thiebaut, S. Bendjebba, Y. Quinsat, and C. Lartigue, “Non-rigid registration for form defect identification of thin parts,” *Journal of Computing and Information Science in Engineering*, vol. **18**, no. 2, 2018.
- [20] Z. Jiang, J.-f. Witz, P. Lecomte-Grosbras, J. Dequidt, C. Duriez, M. Cosson, S. Cotin, and M. Brieu, “B-spline based multi-organ detection in magnetic resonance imaging: B-spline based multi-organ detection in mri,” *Strain*, vol. **51**, 04 2015.
- [21] J. Réthoré and M. François, “Curve and boundaries measurement using b-splines and virtual images,” *Optics and Lasers in Engineering*, vol. **52**, pp. 145 – 155, 2014.
- [22] L. Homri, E. Goka, G. Levasseur, and J.-Y. Dantan, “Tolerance analysis: Form defects modeling and simulation by modal decomposition and optimization,” *Computer Aided Design*, vol. **91**, 06 2017.

A two step modelling approach to limit the exploitable AM parameter space and optimized parameter selection for finest lattice structures using LPBF

H. Korn¹, P. Koch², S. Holtzhausen², J. Thielsch¹, A. Seidler², B. Müller¹, W.-G. Drossel¹

¹Fraunhofer Institute for Machine Tools and Forming Technology IWU, Germany

²Technische Universität Dresden, Institute of Machine Elements and Machine Design, Germany

hannes.korn@iwu.fraunhofer.de

Abstract

Lattice structures manufactured by Laser Powder Bed Fusion (LPBF) show a high potential for a wide range of applications. But the lack of experience in the reliability regarding defects and precision currently impedes their use. Technological limits are the complex shape of the exploitable Additive Manufacturing (AM) parameter space, the dependency of quality criteria on multiple input parameters and the question which precision can reliably be achieved for lattice structures within a certain optimized parameter window. To handle the first two issues, a model based, two step approach is developed and evaluated on different LPBF machines and with different metal alloys. The achievable precision and repeatability of the manufacturing process under constant conditions is analysed by determining the geometrical precision of about 600 strut-like specimens out of titanium alloy Ti6Al4V. In particular, the manufactured strut thickness can be mapped very well by two process parameters with the model-based approach for all the materials and machines analysed. A generalisable system emerges in terms of correlation between lattice strut diameters and LPBF build parameters. The geometric scatter on the specimens appears to be constant for the case investigated and hardly differs between individual build jobs.

LPBF, Accuracy, Precision, Predictive Modelling, Lattice Structures, Scan Strategies

1. Introduction

Lattice structures manufactured by Laser Powder Bed Fusion (LPBF) show a high potential in numerous applications. However, their use is currently limited, as their mechanical behaviour is difficult to predict or simulate. The finer the manufactured structures are, the more sensitively the resulting diameters of lattice struts depend on the process parameters used. Therefore, defects and scatter introduced by the manufacturing process have a stronger effect on the struts [1, 2]. Previous work predominantly uses the “contour-hatch” scan strategy. The strut thickness of lattice structures is adjusted by drawing the contour line closer around the strut axis. Finer lattice structures can be achieved using point exposure as scan strategy [3]. In this work, a different approach is taken based on point exposure: The precision is achieved by an adapted scan strategy of short scan vectors, which ensures a more homogeneous energy input [2, 4 - 6]. The accuracy of the strut thickness is achieved here by parameterising the LPBF process using a regression model approach. Influences of the manufacturing parameters on the geometry of the lattice structures can thus be compensated for in a targeted manner. There is previous scientific work dealing with modelling using regression models in the context of Additive Manufacturing (AM) [7, - 12]. For example, [12] has used it to investigate the interrelation of process parameters. However, this methodology has not been established in AM yet.

In this work, the usable parameter space is narrowed down by means of regression models on the basis of a few manufactured lattice specimens. As a second step, the strut diameters of these lattice structures are measured and a second regression model is developed to predict the resulting strut diameter in dependence of the laser power and scan speed. Additionally the

achievable precision and repeatability of the LPBF manufacturing process under constant conditions is analysed by determining the geometrical precision of about 600 strut like features on bridge shaped specimens out of titanium alloy Ti6Al4V.

2. Methodology and Experimental Setup

Altogether manufacturing experiments in five different build jobs have been carried out (see Table 1). In order to narrow down the exploitable parameter space and to determine the influence of the process parameters on the strut thickness of lattice structures using different LPBF machines and materials, a total of three build jobs have been produced by using the procedure described in section 2.1. Two further build jobs with bridge-like specimens have been produced in order to determine the achievable precision and repeatability under constant process conditions. These test series are described in section 2.2.

Table 1 overview of build jobs manufactured and analysed in this work.

build job	machine	material	aim
LT_AlSi10Mg	DMG Mori Lasertec 12	AlSi10Mg	strut diameter
M2_316L	Concept Laser M2	316L	strut diameter
TP_316L	Trumpf TruPrint 1000	316L	strut diameter
M2_B1	Concept Laser M2	Ti6Al4V	precision
M2_B2	Concept Laser M2	Ti6Al4V	precision

2.1. Determination of the influence of the process parameters

In order to investigate the influence of the process parameters on the quality and strut diameter of lattice structures, production experiments have been carried out on three different LPBF systems (see Table 1: LT_AISI10Mg, M2_316L, TP_316L). Here, two different materials have been used. Twenty-seven individual specimens have been produced per build job. Each of these specimens consists of a solid cuboid, a thin walled structure and a lattice structure (see Figure 1).

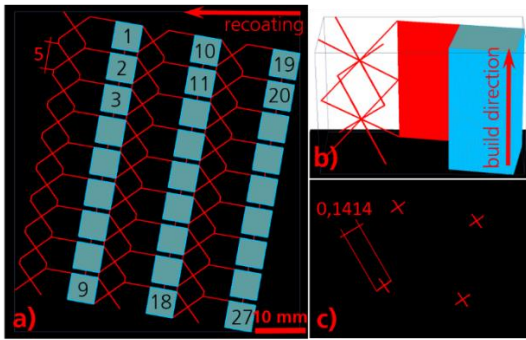


Figure 1. Specimens to determine the influence of process parameters. a) Arrangement of specimens within the build job. b) Geometry of the specimens used. c) In each layer, two crossed scan vectors form each cross-section of a strut.

The unit cells of the lattice structures are bcc cells, the struts are inclined by approx. 35° with reference to the build plate. The lattice structures are not represented by a contour-hatch scan pattern in the production data but by two short crossed scan vectors with a length of 0.1414 mm each. These are arranged around the centre of the strut axis (cp. [2, 4]).

The production data are created using a software tool developed by TU Dresden and Fraunhofer IWU. This ensures that the scan vectors used by the various machines to produce the specimens have been identical for all test series and machines.

The layer thickness has been 25 µm for all build jobs. Line energy, scanning speed and focus diameter have been varied with identical settings and within a wide range for the LT_AISI10Mg and M2_316L tests (laser power: 70 W - 200 W, scanning speed: 100 mm/s - 1400 mm/s, focus diameter: 55 µm - 200 µm). With TP_316L, the same parameter variants have also been used for most specimens. However, this LPBF system has a fixed focus diameter (55 µm), so that samples whose focus diameter deviates from this have been replaced here. In the case of LT_AISI10Mg, it has also been necessary to deviate from the initial test plan for some parameter combinations, as the back reflection triggers a protective device in the AM system in the particular case of high energy inputs. The other system parameters (e.g. protective gas flow, recoater speed) have been selected according to the standard settings of the respective machine for the respective material.

After manufacturing, the specimens have been separated from the build plate by wire EDM and the lattice structures have been manually separated. Microscope images of the lattice structures have been taken using a Zeiss Smartzoom 5 (depth of field by z-stack, 34x zoom, if necessary stitching of individual images).

Based on the microscope images, the three quality characteristics “qInterruptions”, “qDownNose” and “qDownRough” on the individual specimens have been classified manually by assigning into classes between 1 (best quality class) and 5 (worst quality class). Examples for the best and worst quality classes for each of the three quality characteristics are shown in Figure 2.

Furthermore, using the open-source multidimensional image processing software ImageJ, the strut thicknesses of the lattice structures have been measured in the top view and the side view on two struts of each sample at five locations on the strut. These data form the basis of the model for the strut thickness.

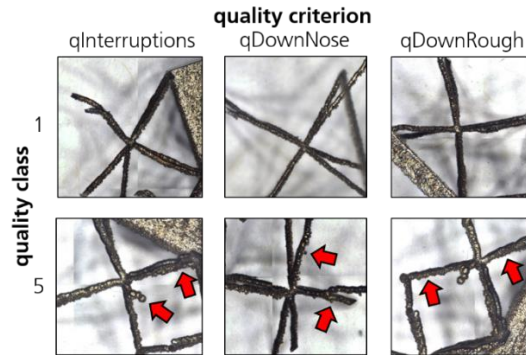


Figure 2. Examples of the "best" (1, top row) and the "worst" (5, bottom row) quality classes for the three quality features qInterruptions, qDownNose and qDownRough for lattice structures. Arrows highlight significant characteristics.

2.2. Determination of precision and repeatability

Based on the build jobs M2_B1 and M2_B2 the achievable precision and repeatability under identical process conditions has been determined. In both build jobs, approx. 150 individual bridge-like specimens have been distributed in a grid across the entire build plate (cp. Figure 3 a). Each of them consist of two strut-like geometry features (altogether approx. 600) that are analysed here. These strut-like specimens are 10 mm in height. The cross-section of each specimen has been exposed by exactly three individual scan vectors with a length of 2 mm and a distance of 100 µm to each neighbouring vector (cp. Figure 3 b). The order of this exposure has been constant across all layers and has been the same for all specimens. Laser parameters laser power $P = 100$ W, scan speed $v_s = 625$ mm/s, focus diameter $d_f = 100$ µm have been kept constant for all specimens.

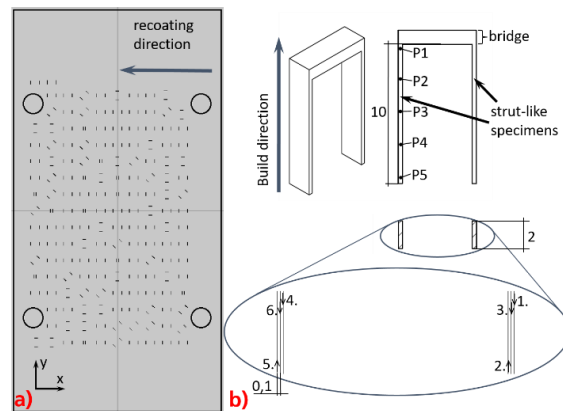


Figure 3. a) Arrangement of the specimens on the two build jobs, b) Geometry of the strut-like specimens and position of the individual scan vectors in one exemplary layer for LPBF manufacturing.

After fabrication, the bridge-like specimens have been detached from the build plate using wire EDM. Depth-focus microscope images of the specimens have then been taken using a Zeiss SmartZoom 5. Afterwards ImageJ software has been used to measure the width of each strut's cross-section at five locations (P1 - P5) per strut as shown in Figure 3 b). These data form the basis for an investigation of the scatter of the width of the specimen cross-section and for a determination of whether this scatter is location-dependent.

3. Evaluation and modelling

The evaluation of the manufacturing experiments has primarily been carried out using statistical methods and by the formation of regression models. The Cornerstone 7.1.2.1 software (camLine GmbH, Germany) has been used for this purpose.

3.1. Limitation of the exploitable parameter space

The exploitable parameter space has been narrowed down separately for each machine and material. The quality characteristics evaluated in classes have also been considered separately from each other. If lattice structures could not be produced with a certain parameter combination, it has been assessed with quality class 5.

For each quality characteristic, an attempt has been made to find a regression model with up to quadratic terms that maps the class values of the quality characteristics particularly well. Subsequently, these models have been used to predict the quality characteristics for the entire parameter space. In a next step, the exploitable parameter space has been determined from these predictions: all parameter combinations that lead to quality characteristics of class 1 or class 2 in the model have been regarded as exploitable parameter space.

3.2. Modelling of the strut diameter

For a better comparability of the different systems and materials, only the specimens manufactured with 55 μm laser focus diameter have been used for the modelling of the strut diameter. For each of the three manufacturing experiments LT_AISI10Mg, M2_316L, TP_316L, a linear regression model with quadratic terms has been calculated. Input variables are laser power and scanning speed, output variable is the strut diameter. There has no distinction been made whether the strut diameter is measured from the top or the side. That is because previous investigations showed only minor differences between these measurement directions. Each model has been optimised using the automatic model optimisation tool in Cornerstone. The quadratic term (laser power)² has improved the models only marginally. Therefore it has been manually removed for simplification.

3.3. Investigation of precision and repeatability

In order to characterise the achievable precision and repeatability of the process, a linear regression model with cubic terms has been formed exclusively from the input variables "x position" and "y position" of the respective strut-shaped sample. The output variable has been the measured strut thickness. The "Adj. R Square" of this model has been determined and its magnitude has been evaluated. A very small Adj. R Square indicates that the occurring scatter cannot be explained by the x and y coordinates of the specimens. In this case, there would be no spatial dependence of this quality characteristic.

4. Results

4.1. Limitation of the exploitable parameter space

Manual assessment of quality characteristics is a very simple measure of narrowing down the usable parameter space that can be carried out with reasonable effort. However, it is also imprecise and subjective. In some cases, there is a risk that the assessments in quality classes are ambiguous – parameter combinations that are very close to each other are frequently assigned to different parameter classes. The models for the screening phase therefore only have a low "Adj. R Square" and a

suitable model cannot be found for all machine and material combinations.

Nevertheless, the model formed from the manual evaluations represents the experimental space relatively well in over 50% of the cases examined (cp. Figure 4 a).

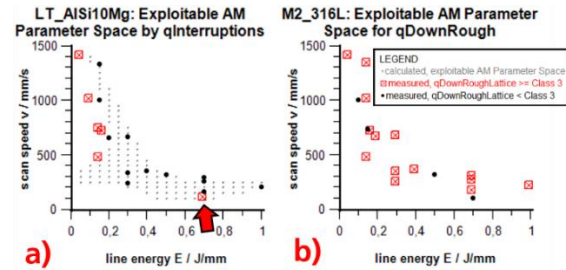


Figure 4. The exploitable parameter space identified by modelling. In a), the exploitable parameter space is well defined. In b), data points representing "good" and "bad" parameter combinations are mixed in such a way that no model for sharp delineation could be found with this approach.

In particular, many of the parameter combinations, for which specimens could not be fabricated successfully, have been avoided. However, it cannot be guaranteed that all unsuitable parameter combinations reside outside the identified parameter space. In particular, if "good" and "bad" samples are very close to each other in the parameter space or are intermixed, no valid parameter space can be determined by this methodology without adjustment of the selection parameters in some cases.

4.2. Modelling of strut diameter

In contrast to the limitation of the usable parameter space, the measured strut thicknesses can be represented very well for all investigated material and machine combinations by regression models with quadratic terms from the input variables laser power and scanning speed. The characteristic values for the models are summarised in Table 2.

Table 2 Characteristic values of the models for description of the strut diameter.

Model name	"Adj R Square"	"Pure Error" / mm	"Residual df"
LT_AISI10Mg	0,89	0,025	155
M2_316L	0,79	0,027	290
TP_316L	0,86	0,025	455

The prediction models examined are shown pictorially in Figure 5. They do match qualitatively. The degressive dependence of the strut diameter on the scanning speed is well represented by a quadratic term, the correlation with the laser power has an almost linear character.

Particularly in the range of low scanning speeds ($v_s < 500$ mm/s), there is still a high dependence of the strut diameter on the scanning speed for all the systems and materials investigated. In this range, the correlation is almost linear. Here it is particularly striking that the gradient between laser power and scanning speed and thus their common effect is almost identical for all the systems and materials considered. However, they differ in terms of absolute values for the various strut diameters. The models for the material 316L show similar sensitivities of the strut diameter to laser power and scanning speed for low scanning speeds on both systems. They differ from each other primarily by an offset on the strut thickness. In the case of material ALSi10Mg on the Lasertec 12 system, a larger dependence of the strut diameter on both the laser power and

the scanning speed can be observed. On the basis of the available data, it is not yet possible to figure out whether this higher sensitivity is mainly caused by the system or the material.

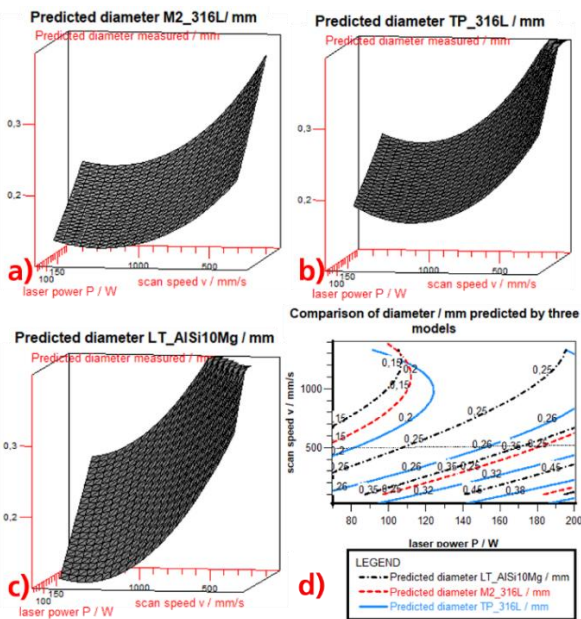


Figure 5. a) - c): Individual diagrams of the strut diameter models and d) comparison of the models in a combined diagram.

4.3. Investigation of precision and repeatability

The model for the effort to explain the strut diameter from x and y position has an Adj. R Square of 0.028. Thus, the occurring scatter can barely be explained by the x or y position of the specimen. It can therefore be assumed that the systematic deviation in the strut diameter caused by location dependence is very small, compared to the typical scatter in the process, and can therefore be disregarded. The scatter of the measured values is shown in Figure 6, listed according to measuring position (P1 - P5) and build job (M2_B1, M2_B2).

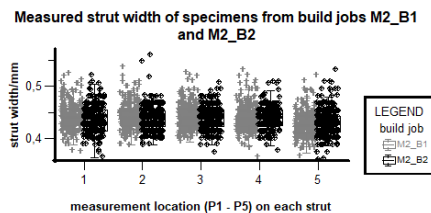


Figure 6. Distribution of the measured strut diameters broken down by measurement location and build job.

5. Summary, conclusions and outlook

Overall, the use of regression models has proven to be very suitable for the generalised analysis and description of the LPBF process: Although the suitable parameter space can be delimited by a regression model from manual assessment of quality characteristics, the result is very much dependent on the quality and validity of the assessment. Without an individual adjustment of the model parameters, a valid model cannot be found in any case. It appears feasible that a subjective assessment of the quality features in five quality classes does not have sufficient discriminatory power. A relative evaluation of the components against one another, instead of a rigid class allocation, has potential for improvement. Furthermore, quality features could be weighted, depending on their importance for manufacturability.

However, the regression approach has shown its strengths in the systematic description of the dependence of the strut

diameter on the process parameters laser power and scanning speed. The qualitative curves of the strut diameter are only shifted and slightly deformed in the series of tests, investigated here for the material 316L. This clearly has the potential to significantly reduce the qualification effort for new materials or systems, as only a few support points have to be determined by manufacturing experiments. However, further experiments have to be undertaken to prove general validity of this system. In the future, the parameterisation of the manufacturing process could be carried out automatically on this basis to achieve an improved accuracy.

Furthermore, it could be shown that, for the investigated specimens, there is no significant spatial dependence of the resulting strut diameters. The expected magnitude of the process scatter is constantly approx. +/- 35 µm for the present case as investigated. This rather large basic scatter limits the achievable precision in LPBF manufacturing under the given conditions. On the other hand, this means that measuring methods with limited precision can be used for measurements of filigree struts, as long as their imprecision is small in relation to the LPBF process scatter.

Acknowledgements

Funded by the Deutsche Forschungsgemeinschaft (DFG, German Research Foundation) – 289647464. The authors also thank their research assistants Merle Bergmann and Louise Elstner for supporting this work by recording microscopic images and manually measuring thousands of struts in diameter as valuable data base for these investigations.

References

- [1] Abele E; Stoffregen H; Klimkeit K; Hoche H; Oechsner M 2015 Optimisation of process parameters for lattice structures *Rapid Prototyping Journal* **21** (1), 117–127
- [2] Korn H; Koch P; Kordaß R; Schöne C; Müller B; Holtzhausen S; Stelzer R 2018 Influences of Scan Strategy and Exposure Parameters on Diameter and Surface Quality of Struts in Lattice Structures. *DDMC - Conference 2018*
- [3] Rehme O. 2009 Cellular design for laser freeform fabrication. *Hamburg-Harburg, Techn. Univ., Inst. für Laser- und Anlagensystemtechnik*
- [4] Korn, H.; Koch, P.; Kordaß, R.; Holtzhausen, S.; Schöne, C.; Müller, B.; Stelzer, R. 2018 Adapted Scan Strategy and Slicing Tool for Improvement of Strut Precision in Lattice Structures *Proceedings of ASPE and euspen Summer Topical Meeting, Berkeley*
- [5] Koch, P.; Korn, H.; Kordaß, R.; Schöne, C.; Müller, B.; Stelzer, R: 2018 A CAD-based Workflow and Mechanical Characterization for Additive Manufacturing of Tailored Lattice Structures *Proceedings of the 29th SFF Symposium*, 782 – 790.
- [6] Gustmann, T; Gutmann, F; Wenz, F; Koch, P; Stelzer, R; Drossel, W-G; Korn, H 2020 Properties of a superelastic NiTi shape memory alloy using laser powder bed fusion and adaptive scanning strategies *Progress in additive manufacturing*, **Vol.5 (2020), No.1**, 11 – 18. DOI: 10.1007/s40964-020-00118-6
- [7] Calignano, F., 2014 Design optimization of supports for overhanging structures in aluminum and titanium alloys by selective laser melting. *Materials & Design* **64**, 203–213.
- [8] Charles, A; Elkaseer, A; Thijs, L; Hagemeyer, V; Scholz, S, 2019 Effect of Process Parameters on the Generated Surface Roughness of Down-Facing Surfaces in Selective Laser Melting. *Applied Sciences* **9** (6), 1256.
- [9] Cloots, M; Zumofen, L; Spierings, A B; Kirchheim, A; Wegener, K, 2017 Approaches to minimize overhang angles of SLM parts *Rapid Prototyping Journal* **23** (2), 362–369.
- [10] Piscopo, G; Salmi, A; Atzeni, E, 2019 On the quality of unsupported overhangs produced by laser powder bed fusion. *International Journal of Manufacturing Research* **14** (2), 198.
- [11] Sun, J; Yang, Y; Di W, 2013 Parametric optimization of selective laser melting for forming Ti6Al4V samples by Taguchi method. *Optics & Laser Technology* **49**, 118-124.
- [12] Huxol, A; Villmer, F-J, 2019. DoE Methods for Parameter Evaluation in Selective Laser Melting *IFAC-PapersOnLine* **52** (10), 270–275.

Influence of the processing parameters on the dimensional accuracy of In625 lattice structures made by laser powder bed fusion

Lucas Fournet-Fayard^{1,2}, Charles Cayron¹, Imade Koutiri², Valérie Gunenthiram³, Pierrick Sanchez⁴, Anne-Françoise Obaton¹

¹ Laboratoire Commun de Métrologie (LCM), Laboratoire National de Métrologie et d'Essais (LNE), 75015 Paris, France

² Laboratoire PIMM, Arts Et Métiers Institute of Technology, CNRS, Cnam, HESAM University 75013 Paris, France

³ CETIM – Additive Factory Hub (AFH), 91191 Gif-Sur-Yvette, France

⁴ Carl Zeiss Services, 95000 Neuville-sur-Oise, France

lucas.fournetfayard@lne.fr

Abstract

Lattice parts made in Inconel 625 with laser-powder bed fusion (L-PBF) process have been manufactured with a variation of processing parameters, namely laser power and scanning speed, in order to determine their influence on the dimensional accuracy of the lattices' structure. Four combination sets of laser power and scanning speed have been chosen, and three parts per set were manufactured for repeatability. Then, the lattice structures have been scanned by X-Ray Computed Tomography (XCT), and the dimensions of the struts as well as the volume of the parts were measured using VGStudioMax on the XCT images. While the vertical struts are thinner than the nominal value, the horizontal struts are thicker, and no correlation to the processing parameters was possible due to the roughness of the struts. However, the volume measurements showed an increase with the energy density, i.e. the ratio of the power over the speed, and thus the average thickness of the struts increases accordingly.

Dimensional accuracy, Laser Powder Bed Fusion, Metrology, Metal, X-Ray Computed Tomography, Lattice

1. Introduction

Metal additive manufacturing and especially Laser Powder Bed Fusion (L-PBF) utilization is increasing in the industrial field since the last decade, partly thanks to its ability to produce parts with very complex geometries, such as lattice structures. Lattices are widely investigated for their interesting weight to mechanical properties' ratio and energy absorption in the industry [1], or bone and tissue reconstruction in the medical field [2].

However, if the mechanical properties have been well described in the literature [3], it is less the case for the dimensional accuracy of those parts, which remains difficult to master and control. In addition, lattice structures cannot be machined afterwards to make up for the deviations observed, contrary to fully dense parts. The issue is that the deviations can alter the properties of the part (mechanical properties, weight, porosity...) if the overall dimensions of the struts differ from the designed part.

Nevertheless, some work can still be found in the literature about the dimensional accuracy of lattice structures, with either different processes or materials. For example, Yan et al. [4] showed that the strut size was higher than the designed value for gyroid lattice structure made with a 316L steel alloy. Qiu et al. [5] demonstrated that the deviations in strut dimensions increased with the laser power due to the increase of the melt pool width on AlSi10Mg. About the influence of the nominal dimension, Sufiiarov et al. [6] found that the minimum deviations were observed for strut sizes between 0.35 mm and 0.45 mm, on a range of dimensions that vary from 0.1 mm to 0.9 mm. Finally, regarding geometrical properties, Ameta et al. [7]

managed to evaluate flatness of lattice structures' top surface, using the theory of supplemental surfaces.

The point of the research presented here is to determine the influence of the linear energy density (LED), laser power and scanning speed on the dimensional accuracy of lattice structures, by studying the size of the struts and the volume of the whole lattice structure. Laser power and scanning speed's influences on the dimensional accuracy are first order parameters, which is why they have been chosen for the study. The characterization is performed by X-Ray tomography (XCT).

In this article, the experimental method will be presented first, followed by the results and discussion on the measurements.

2. Experimental methodology

2.1. Parts' fabrication

The lattice structures have been manufactured in Inconel 625 with a 3DSystems ProX DMP320 L-PBF machine, equipped with a polymer scraper and an Ytterbium fiber laser and its spot diameter has been measured to be 70 μm . The cell type used for the lattice parts is a simple orthogonal cell, with a strut thickness of 300 μm , and a cell size of 2 mm (Fig 1a).

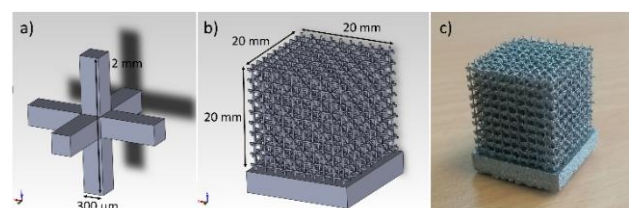


Figure 1. Illustration of a) CAO design of the lattice cell, b) CAO design of the full lattice structure, c) a manufactured lattice part

This cell type has been chosen to make it easier to characterize. The cell is repeated in order to have a lattice structure with a cubic shape of 20 mm per side (Figure 1 b and c). The design has been made with Solidworks.

Table 1. Set of parameters investigated

Set of parameters	Power (W)	Scanning speed (m/s)	LED (J/m)
1	250	1.85	135
2	250	1	250
3	400	1.6	250
4	350	1	350

The different processing parameters are recorded in the Table 1 and concern only the filling step. The chosen parameters are ordered by increasing the LED, which is defined by:

$$LED = \frac{P}{v} \text{ in J/m} \quad (1)$$

where P is the laser power in W and v the scanning speed in m/s .

This ordering has been chosen to determine the influence of the LED on the dimensional accuracy. The second set of parameters is the one that is recommended by the constructor and the third set has the same LED, but with higher laser power and scanning speed.

Three lattice samples are manufactured per set of processing parameters for repeatability. There is one contour step with a laser power of 180 W, and a scanning speed of 1.9 m/s, which are both kept constant for all of the parameters. The hatching space is 100 μm , and the layer thickness is 60 μm . The scanning strategy consists of back and forth trajectories with a rotation of 66° between each layer. No downskin or upskin is performed, and the contour step occurs before the filling step. Supports are used to remove easily the parts from the build tray.

Regarding the software used, 3DExpert has been used to prepare the fabrication (position, supports, scanning strategy) and DMPVision has been used to set the power and scanning speed parameters, as well as for the launching of the fabrication.

2.2. XCT scanning of the parts and measurement protocol

The parts have been scanned with an X-Ray computed tomography system, METROTOM by ZEISS, with a voltage of 200 kV, a current of 135 μA and a voxel size of 30 μm . Then the

calliper tool from the software VGStudioMax is used to perform dimensional measurements of the struts.

Concerning the measurements, two planes are considered: the XY plane, parallel to the building plate, in blue in the Figure 2 1a), and the XZ plane perpendicular to the building, in green in the Figure 2 2a). It is assumed that the XZ and YZ planes are equivalent. In the XY plane, the dimensions of the struts are measured in the x direction, red circles in the Figure 2 1b). In the XZ plane, struts are measured in the Z and X directions, respectively blue and red circles in the Fig 2 2b). The struts in the Z direction refer to the vertical struts while the struts in the X direction refer to the horizontal struts. Also, struts in the X direction are measured on both the XY and XZ planes in order to take into account the asymmetry for the horizontal direction.

There are three measurements per analysed strut with the calliper tool. Moreover, to have values that are relevant of the whole structure, measurements are performed on the corner and on the center of the observed plane, and this for the top, middle and bottom rows of the lattice structure (Figure 2). Thus, in total, twelve horizontal struts and six vertical struts are measured per sample. The volume are determined via VGStudioMax after removing the base of the part, and applied on the whole lattice structure.

Concerning the analysis of the results, the values displayed are relative errors in percent: $\frac{\text{Measured value} - \text{Nominal value}}{\text{Nominal value}} \times 100$. The error bars on the graphs represent the standard deviations among all of the measurements, struts or volume, for the three samples per set of parameters.

3. Results

3.1. Struts' dimensions

The results of the horizontal and vertical struts dimensions are respectively recorded in the Figure 3 and the Figure 4. The first remark that can be done is the fact that the vertical struts' are thinner than the nominal value, while the horizontal ones are thicker, regardless of the processing parameters used.

However, the size of the error bars make it impossible to compare the results, even though a trend is visible. Firstly, it appears that the errors on the vertical strut dimensions are around 20 % lower than the nominal value, and that the recommended processing parameters do not display the lowest deviations. The same can be said for the horizontal struts, which

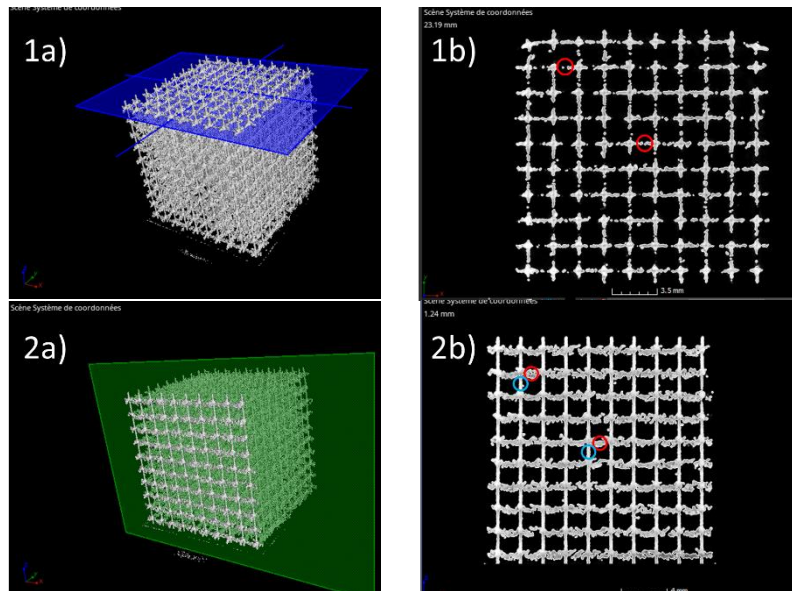


Figure 2. Tomography images of a lattice structure: 1a) 3D visualisation of the lattice top row in the XY plane; 1b) measured struts in the XY plane for the top row; 2a) 3D visualisation of the lattice top row in the XZ plane; 2b) measured struts in the XZ plane for the top row

have relative errors going from 7 to 69 %, with higher variation following the parameters used and higher disparity of the results.

It seems that the size of the strut increases with the LED, which results in decreasing deviations for the vertical struts, and increasing for the horizontal struts. However, there seems to be differences for the dimensions of lattices' struts between the parts that have the same LED. The parameter sets with higher laser power seem to grant bigger dimensions for both directions, even if the difference is thin for the vertical struts.

3.2. Volume

The relative errors on the volume of the overall lattice structure are displayed in the Figure 5. It appears that the LED has a great influence on the volume of the lattice structure. The lower LED has almost 25 % less volume than in theory, while the higher LED is 12 % bigger.

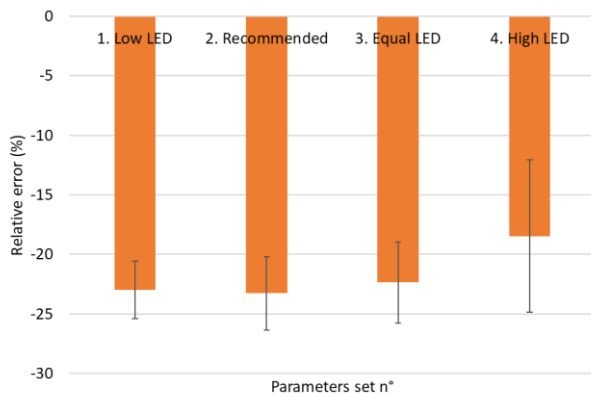


Figure 3. Relative errors for lattices' vertical strut dimensions with different processing parameters

The recommended parameters allow -5 % of error on the volume, and the third set of parameter, which has the same LED, has a dimensional error under 3 %. Thus, it appears that there are differences for two processing parameters with the same energy density but with different laser power and scanning speed. Indeed, the second set is under the theoretical value, and the third one is above.

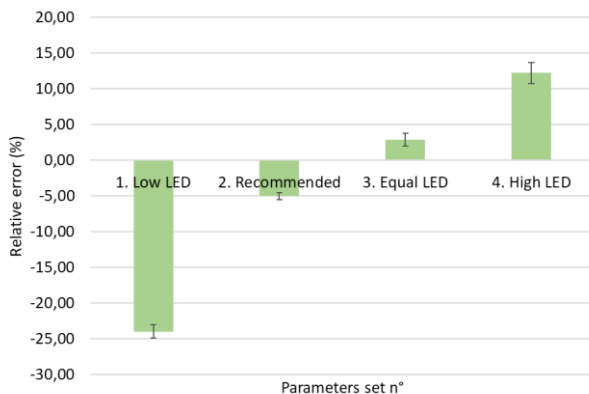


Figure 5. Relative errors for the lattice structures' volumes

4. Discussion

The results on the dimensions of the lattices' struts are difficult to analyse due to the important error bars' values. It is important to note that the measured values for the struts dimensions were consistent from one lattice to another for a given set of

processing parameters. This means that the error bars come from the disparity among the struts from each lattice structure.

Concerning the vertical struts, it seems that the processing parameters have little influence on the dimensional accuracy. On the other hand, the values of the horizontal struts' dimensions show clear variations for the different parameters, but the error bars are too important to conclude anything quantitative.

These error bars can be explained by the asymmetry on the horizontal struts. As seen in the Figure 2 1a) and 2a), there is a clear difference between the size of the struts in the x direction as seen from above (XY plane) and from the side (XZ plane). Moreover, it is difficult to measure the horizontal struts' dimensions in the XZ plane, due to the bad surface roughness (Figure 6). This non-smooth surface roughness on the horizontal struts is due to their orientation.

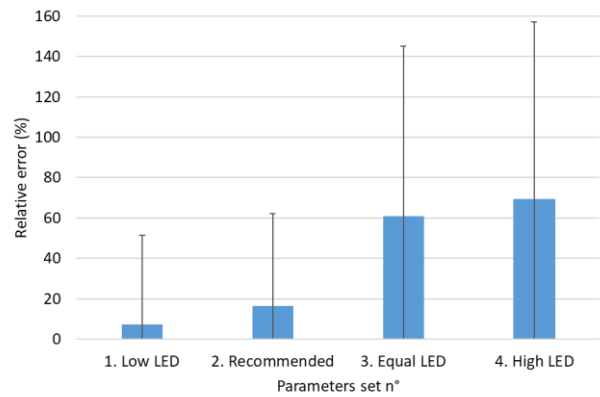


Figure 4. Relative errors for lattices' horizontal strut dimensions with different processing parameters

The overhanging horizontal struts, that would in theory need supports, overheat during the melting due to the bad thermal conduction provided by the underlying powder, leading to an agglomeration of neighbouring powder. Moreover, the powder is not dense enough to support the recoil pressure resulting from the laser-matter interaction during the scanning. This causes a collapse of the melt pool during the scanning, explaining the severe surface roughness observed [8]. This phenomenon also explains the differences of dimensional accuracy between the horizontal and vertical struts. What can also be said is that the measurements on the horizontal struts are not representative on a dimensional perspective, and this could require another method of measurement to characterize the dimensions in order to take into account the surface roughness for example.

When looking at the volume measurements in Figure 5, it is clear that an increase in the LED induces an increase in the volume. If the strut measurements did not enable to conclude about the influence of the LED on the dimensional accuracy due to the error bars, they managed to provide better understanding. The increase in volume attests of the increase in dimensions of the struts. The origin of this increase with the LED certainly come from the increase of the melt pool width which also increases with the LED [9]. From the graph, it is also possible to observe a difference of volume between the two parameters with equal LED. This highlights the fact that one parameter has more influence over the dimensional errors than the other. It would be interesting for further research purpose to perform a design of experiment to determine this.

By observing the volume measurements of the processing parameters n°2 and 3 with low relative errors < 5 %, one could conclude that these parameters offer good dimensional accuracy. Yet, the volume measurements should not be considered without the measurement of the dimensions of the struts, as neither the vertical nor the horizontal struts display such accuracy, due to the reasons mentioned above. In addition, since the vertical struts are thinner than in theory, and the horizontal struts thicker, a compensation effect at the scale of the volume distorts the results. Finally, the internal porosity has not been considered and surely can affect the results.

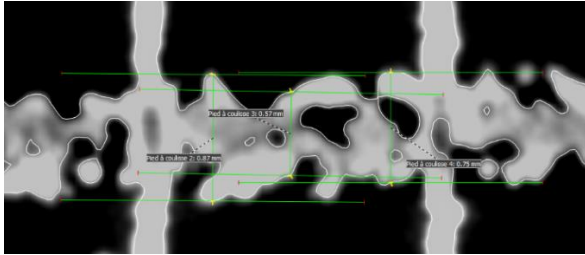


Figure 6. Example of measurement of the dimension of a horizontal strut with bad surface texture

5. Conclusion

In this study, four processing parameters with different laser powers and scanning speeds have been used to determine their influence on the dimensional accuracy of lattice structures, made by L-PBF with Inconel 625 as a material. The measurements obtained by XCT allowed the determination of the dimensions of the struts and of the volume of the lattice structures.

These results show several interesting facts:

Firstly, the quantitative analysis of the dimensions of horizontal struts is not possible due to the important roughness, which disturb the dimensions' measurements. The origin of the roughness comes from the build orientation of the whole lattice causing the struts to overheat due to the bad thermal conduction, and the melt pool to collapse due to the recoil pressure, not supported by the powder.

All of the processing parameters caused the vertical struts to be about 20 % thinner than the design, while the horizontal struts display asymmetrical and thicker struts dimensions.

Even if the evaluation of the dimensions of the struts did not enable the comparison, the volume measurement indirectly showed an increase of the struts' size with the linear energy density (LED). The increase in the struts dimensions is correlated with the melt pool width, which also increases with the LED. Although, there is a difference in the strut's size for a similar LED with higher laser power and scanning speed.

This difference in dimensional accuracy for similar LED should be the object of future work, by the mean of a design of experiment, allowing the understanding of potential interactions between the laser power and scanning speed, or the eventual prevalence of one parameter over the other on the dimensional errors.

Further investigation will focus on the establishment of a more representative measurement method, which could take consideration of the roughness impact. This could be done using volume measurement for the struts for example.

Finally, it will be interesting to study the influence of other processing parameters such as the orientation, the layer thickness or the scanning strategy on the dimensional accuracy of lattice structures.

Acknowledgements

This work was performed in the framework of Additive Factory Hub (AFH), which is a private platform financing academic research in the field of metal additive manufacturing. Carl Zeiss Services is thanked for the XCT scans and their help in the measurement protocol.

References

- [1] Yan C, Hao L, Hussein A, Bubb S L, Young P and Raymont D 2014 Evaluation of light-weight AlSi10Mg periodic cellular lattice structures fabricated via direct metal laser sintering *J. Mater. Process. Technol.* **214** n°4 856-864
- [2] Obaton A F, Fain J, Djemaï M, Meinel D, Léonard F, Mahé E, Lécuelle B, Fouchet J J and Bruno G 2017 In vivo XCT bone characterization of lattice structured implants fabricated by additive manufacturing *Heliyon* **3** n°8 e00374
- [3] Kok Y Tan X P, Wang P, Nai M L S, Loh N H, Liu E and Tor S B 2018 Anisotropy and heterogeneity of microstructure and mechanical properties in metal additive manufacturing: A critical review *Mater. Des.* **139** 565-586
- [4] Yan C, Hao L, Hussein A, Young P and Raymont D 2014 Advanced lightweight 316L stainless steel cellular lattice structures fabricated via selective laser melting *Mater. Des.* **55** 533-541
- [5] Qiu C, Yue S, Adkins N J E, Ward M, Hassanin H, Lee P D, Withers P J and Astallah M M 2015 Influence of processing conditions on strut structure and compressive properties of cellular lattice structures fabricated by selective laser melting *Mater. Sci. Eng. A* **628** 188-197
- [6] Sufiiarov V, Sokolova V, Borisov E, Orlov A and Popovich A 2020 Investigation of accuracy, microstructure and properties of additive manufactured lattice structures *Mater. Today Proceed.* **30** 572-577
- [7] Ameta G, Fox J C and Witherell P W 2018 Tolerancing and Verification of Additive Manufactured Lattice with Supplemental Surfaces *Procedia CIRP* **75** 69-74
- [8] Das P, Chandran R, Samant R and Anand S 2015 Optimum Part Build Orientation in Additive Manufacturing for Minimizing Part Errors and Support Structures *Procedia Manuf.* **1** 343-354
- [9] Keshavarzkermani A, Marzbanrad E, Esmaeilzadeh R, Mahmoodkhani Y, Ali U, Enrique P D, Zhou N Y, Bonakdar A and Toyserkani E 2019 An investigation into the effect of process parameters on melt pool geometry, cell spacing, and grain refinement during laser powder bed fusion *Opt. Laser Technol.* **116** 83-91

Design and measurement strategy of additive manufacturing lattice benchmark artefact

Younes Chahid¹, Radu Racasan¹, Paul Bills¹, Liam Blunt¹

¹EPSRC Future Metrology Hub, School of Computing and Engineering, University of Huddersfield, HD1 3DH Huddersfield, UK

Younes.chahid@hud.ac.uk

Abstract

Currently, no additive manufacturing (AM) benchmark artefact has been solely made for lattices. The objective of this research is to design an AM lattice benchmark artefact that AM users can use to assess their machine's capability, accompanied by a measurement strategy to evaluate the lattice characteristics using X-ray computed tomography (XCT). This novel AM benchmark lattice artefact design allows for a simplified method to evaluate the machine's capability in manufacturing different strut thicknesses or type of unit cells by only having to print one part. The parametric and gradient nature of the design allows engineers to easily choose and merge different types of lattices and strut thickness ranges. This method removes the need of printing multiple parts, resulting in decreased powder use, reduced print/measurement time while limiting chances of a print failure.

Keywords: Lattice structures; Additive Manufacturing; Benchmark artefact; X-ray Computed Tomography; Metrology.

1. Introduction

When commissioning a new additive manufacturing (AM) machine or when using a new powder material, it is common practice to additively manufacture different types of benchmark artefacts for different purposes such as assessing the mechanical properties of the produced part, optimising the different printing/post processing workflows, or to evaluate the AM machine geometric resolution limits, surface roughness and more. While more than 65 AM benchmark artefacts have been reported in literature [1], only a few have included a lattice as a complimentary design. The objective of this research is to design an AM lattice benchmark artefact that AM users can use to assess their machine's capability, accompanied by a measurement strategy to assess the dimensional, surface and porosity of the produced lattice using X-ray computed tomography (XCT).

2. Methodology

This paper starts by analysing the previous AM geometric benchmark artefacts and assessing their strengths and weaknesses. Secondly, this research investigates and uses ISO/ASTM 52902 [2] "Additive manufacturing - Test artifacts - Geometric capability assessment of additive manufacturing systems" as a guide to develop design constraints, features, and measurement strategies that are optimised for lattice structures. These features include, but are not limited to strut diameter resolution, node positioning error, surface roughness and porosity. Measurement strategy was optimised for XCT as it could match the measurement complexity needed to assess internal features or porosity of lattices.

A lattice is composed of uniformly repeated unit cell designs composed of different nodes and struts forming the general geometry. While ISO/ASTM 52902 does not provide information about measuring lattices, some suggested designs and measurement methods can be translated to achieving the task.

For example, the pin diameter resolution, hole resolution and linear axis accuracy from the standard can be translated

respectively to strut resolution, external porosity (designed internal lattice spacings) resolution and linear node positioning error.

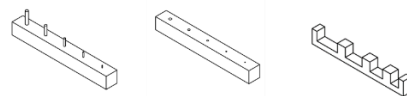


Figure 1. Example of ISO/ASTM 52902 suggested reference geometries as shown from left to right the pin diameter resolution, hole resolution and linear axis accuracy [2].

To represent the features shown in figure 1, the suggested design in this study has a gradient field to incorporate into one design, a range of lattice strut diameters and external pores sizes as can be seen in figure 2. This gradient approach is different from previously suggested designs in literature where multiple lattices with different strut and cell sizes have to be produced.

2.1. Results and discussion

The resulting design has Body Centred Cubic (bcc) type unit cell, this being one of the most used type of lattices in literature [1] and a box size 18.7 x 18.7 x 27 mm. Ntopology software was used to design a gradient that resulted in a varying strut diameter and cell size seen in figure 2.

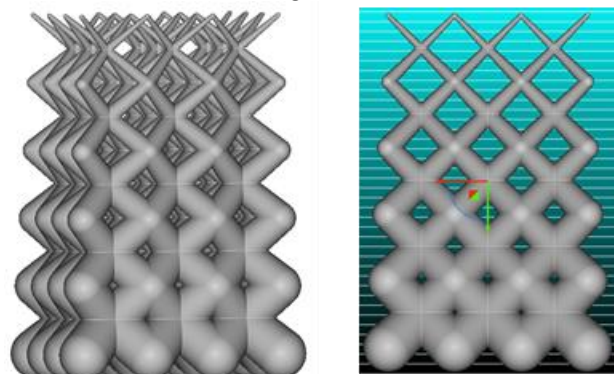


Figure 2. Suggested AM lattice benchmark artefact showing the gradient strut thickness and cell size.

The measurement strategy relies on using X-ray computed tomography (XCT) to image the additive manufactured part. While the gradient design allows for a visual and qualitative inspection, a quantitative inspection using XCT will be more thorough, especially when it comes to internal features that are inaccessible using conventional measurement instruments.

To simulate the measurement strategy beforehand, the measurements were applied on the produced CAD. For example, the lattice strut resolution can be measured using a wall thickness analysis as seen in figure 3. The external pore resolution can be measured using foam analysis module here performed using VGStudio MAX 3.4.3 as seen in figure 4.

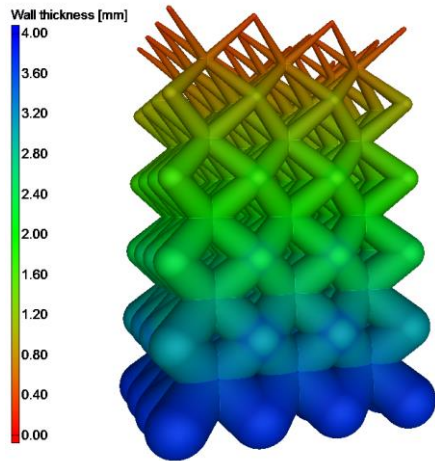


Figure 3. Wall thickness analysis performed on the AM lattice benchmark artefact CAD showing the strut resolution.

To evaluate the node positioning axis error, and instead of adding spheres to the design, the nodes can be thresholded from the wall thickness analysis to isolate the spheres already existing in each node. The measurement strategy in this case can include measuring the centre distance between multiple spheres in each X, Y and Z axis to evaluate the axis node positioning error. Another measurement can include the overlay of CAD and produced AM node spheres and compare their centre-to-centre distance. Example of spheres thresholded from the CAD nodes can be seen in figure 4.

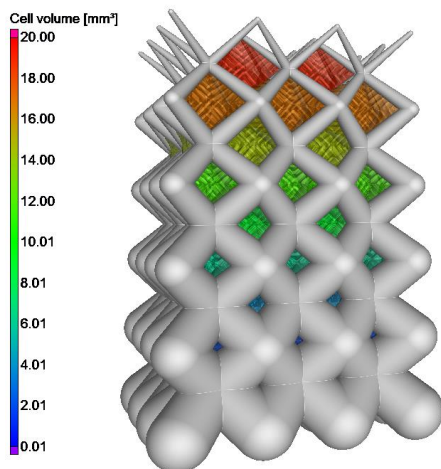


Figure 4. Foam analysis performed on the AM lattice benchmark artefact CAD showing the external porosity resolution.

Finally, deviation analysis can also be performed as well as surface data analysis as previously completed by the author [3]. Also, and while not mentioned in ISO/ASTM 52902, porosity analysis can also be performed on the produced AM lattice since

the small geometry can be easily affected by the existence of internal pores.

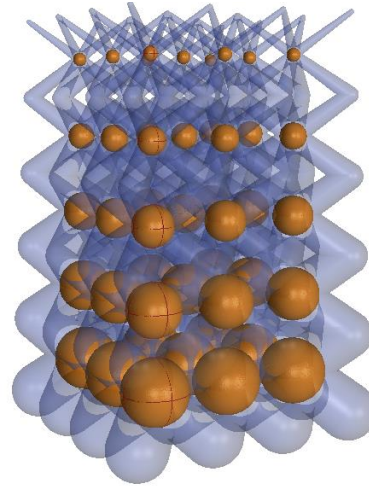


Figure 5. Isolated spheres existing in every lattice node used for node positioning error measurement.

3. Conclusion and future work

This study suggests a novel AM lattice benchmark artefact that can be used for assessing the machine capability using for example different hatching methods and layer height to evaluate parameters like the smallest achievable lattice strut or external pore. Process repeatability and stability can also be assessed since lattice designs already have duplicated features across each layer.

Instead of producing multiple lattices, each with a fixed strut and cell size, the suggested design is based on a gradient that allows for reduction of the number of specimens and print time making the process cost efficient. The suggested design also minimises the chances of print failure since the fine features are at the top and are printed last. The paper also suggests, a measurement strategy based on XCT and applied as seen above on the CAD design converted to a virtual volume.

Future work will include the additive manufacturing of the AM lattice benchmark design and demonstration of the suggested measurement strategy. Dimensional deviations and defects are expected to be predominant at the top part of the lattice due to minimising lattice strut diameter.

Acknowledgements

The authors gratefully acknowledge the UK's Engineering and Physical Sciences Research Council (EPSRC) funding of the Future Metrology Hub (Grant Ref: EP/P006930/1). The authors also gratefully acknowledge Ntopology for providing the license of Ntop and Volume Graphics for providing the license of their VGSTUDIO MAX 3.4 software.

References

- [1] Toward a common laser powder bed fusion qualification test artifact, *Addit. Manuf.* 39 (2021) 101803. <https://doi.org/10.1016/j.addma.2020.101803>.
- [2] 14:00-17:00, ISO/ASTM 52902:2019, ISO. (n.d.). <https://www.iso.org/cms/render/live/en/sites/isoorg/contents/d/ata/standard/06/72/67287.html> (accessed March 25, 2021).
- [3] Y. Chahid, R. Racasan, L. Pagani, A. Townsend, A. Liu, P. Bills, L. Blunt, Parametrically designed surface topography on CAD models of additively manufactured lattice structures for improved design validation, *Addit. Manuf.* 37 (2021) 101731. <https://doi.org/10.1016/j.addma.2020.101731>.

Testing the similarity conditions in the CT measurement of additively manufactured lattice structures

M. Pranievicz¹, M. Ferrucci¹, J. Fox¹, C. Saldana²

¹National Institute of Standards and Technology*, USA

²Georgia Institute of Technology, USA

maxwell.praniewicz@nist.gov

Abstract

X-ray computed tomography (CT) enables the non-destructive measurement of hidden internal features that are inaccessible by tactile or optical coordinate measuring systems. This makes CT the technology of choice for inspecting complex components made by additive manufacturing (AM), lattice structures being a prime example. Uncertainty assessment in CT dimensional measurements is limited to the substitution method, which prescribes strict similarity conditions between the test object and a separate, calibrated reference object. The notoriously rough surfaces and form deviations in AM components present a challenge in terms of ensuring similarity with respect to the idealized reference object, particularly as these deviations pertain to changes in X-ray penetration lengths during CT measurement. Currently, though, there is no literature on how to quantify ‘similarity’ and to what extent these conditions can be stressed while ensuring that uncertainty in the CT measurement of AM parts can be correctly determined. In this study, we investigate the effect that varying degrees of dissimilarity in object shape and size have on the image quality of their tomographic reconstruction in the context of establishing a quantitative measure of similarity.

X-ray computed tomography, Lattice structures, Similarity

1. Introduction

Lattice structures produced using additive manufacturing (AM) can provide improved stiffness/weight, energy absorption, heat transfer, and bio-integration of conventionally designed components [1–3]. X-ray computed tomography (XCT) is widely used to non-destructively characterize lattice structures, e.g., for mechanical testing [4–7]. However, XCT measurements succumb to various uncertainty contributors, including the material and geometric characteristics of the object to be measured. Uncertainty in the XCT measurement of lattices has been studied to a limited extent [8, 9]. In general, the assessment of uncertainty in CT is limited to the substitution method, which is described in the VDI/VDE 2630-2.1 guideline [10]. This approach relies on the presence of a separate, calibrated reference object that meets strict similarity conditions in terms of material, shape, and size with respect to the test object. The similarity conditions are specified to ensure that bias, repeatability, and other uncertainty components determined from the measurement of the reference object are equally applicable to the measurement of the test object. In other words, the response of the CT system to any differences between reference and test objects should be approximately linear [11].

The notoriously rough surfaces of AM components present a challenge in terms of ensuring similarity, particularly in terms of shape and size, between as-built test objects and the corresponding reference objects, which are typically

manufactured with smooth surfaces to enable low uncertainty calibration of the relevant measurands by tactile coordinate measuring machine (CMM). These geometric dissimilarities can result in significant differences in X-ray penetration length during the CT measurement of small, complex parts such as lattice structures.

The non-linear relationship between penetration length and polychromatic X-ray absorption, i.e., the term in the exponent of the Beer-Lambert equation, and the monochromaticity assumed in conventional tomographic reconstruction algorithms result in so-called beam hardening artifacts. Differences in penetration lengths between reference and test object will result in different manifestations of beam hardening artifacts in the reconstructed volumes, which can compromise the similarity conditions prescribed in VDI/VDE 2630-2.1 guidelines. However, there is currently no literature on how to quantify ‘similarity’ and to what extent these conditions can be stressed while ensuring that uncertainty in the CT measurement of AM parts can be correctly determined. In this study, we investigate the effect that varying degrees of dissimilarity in object shape and size have on the image quality of their tomographic reconstruction in the context of establishing a quantitative measure of similarity.

To simulate the effect of AM-induced form errors, several test lattice objects are designed with varying strut diameters. Polychromatic cone beam CT acquisitions of the test objects are simulated, and each dataset is subsequently reconstructed using conventional Feldkamp-Davis-Kress (FDK) filtered back projection. The similarity between the various reconstructed test objects is determined using a slightly modified

* Certain commercial entities, equipment, or materials may be identified in this document to describe an experimental procedure or concept adequately. Such identification is not intended to imply recommendation or endorsement by the National Institute of Standards and Technology, nor is it intended to imply that the entities, materials, or equipment are necessarily the best available for the purpose.

implementation of the contrast discrimination function (CDF) described in ASTM E1695 [12]. The same image quality metric is then applied to the simulated measurement of a realistic test lattice (defined by the surface model extracted from a previous experimental CT measurement).

2. Methodology

A lattice-like structure with struts of 0.5 mm nominal diameter (Figure 1a) was additively manufactured with the struts oriented horizontally with respect to the build direction. This AM component was then scanned using XCT and processed in VGStudio MAX 3.4 (Figure 1 b) [13]. Cylinders were then least-squares fit to each strut and the cylindricity error was evaluated. Figure 1c displays the cylindrical form error of one strut. Across the nine cylinders of the structure, form errors of approximately ± 0.15 mm were observed. The magnitude of these form errors was used to guide the experiment conducted in this work.

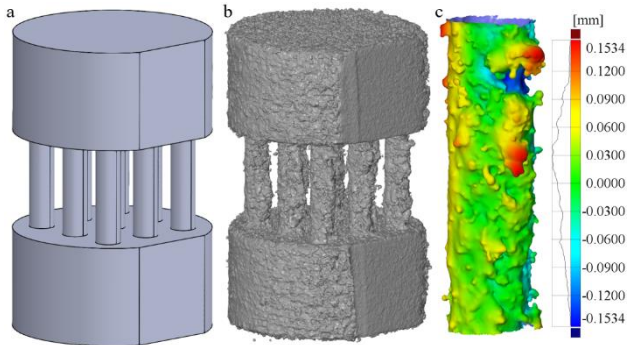


Figure 1. Example of form error in AM lattice components: (a) Component design geometry with strut diameter 0.5 mm, (b) Surface model of manufactured AM component acquired through XCT, (c) Example cylindricity error in a single AM strut

2.1. XCT Simulation

Monochromatic and polychromatic XCT acquisitions were simulated using aRTist software [14]. Five cylinder arrays similar to the lattice-like structure in Figure 1 were simulated, each array comprising different cylinder diameters (0.3 mm, 0.4 mm, 0.5 mm, 0.6 mm, 0.7 mm). The acquisition geometry (a), the polychromatic X-ray spectrum (b), an example projection (c), and a sample slice of the reconstructed volume (d) can be seen in Figure 2. The simulation parameters are shown in Table 1. The polychromatic X-ray spectrum was generated using source parameters from an actual industrial X-ray source at the Georgia Institute of Technology, while the energy in the monochromatic simulations was given by the weighted mean the polychromatic

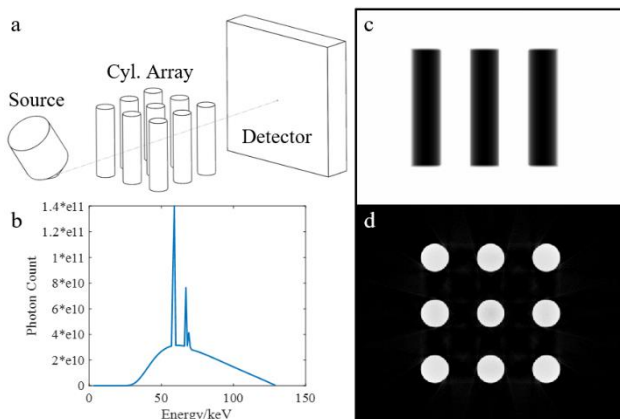


Figure 2. XCT Simulation: (a) Simulation configuration (not to scale), (b) Source spectrum used in polychromatic simulations, (c) Sample polychromatic project (0.5 mm diameter), (d) Sample central slice from polychromatic reconstruction (0.5 mm diameter)

spectrum, similar to the average energy in [15]. Noise and unsharpness (geometric or detector) were not included in the simulated acquisitions.

Table 1 XCT Simulation Parameters

Parameter	Value	
Source	Target material	W
	Target angle	45°
	Window material	Be
	Window thickness	0.2 mm
	Acceleration voltage	130 kV
	Current	0.061 mA
	Physical filter	0.5 mm Cu
Detector	Energy (mono)	71.2 keV
	Pixel size	0.127 mm
	Number of pixels (WxH)	500 x 350
Object Positioning	Source to detector distance	803.359 mm
	Source to rotation axis distance	60.506 mm
Data acquisition	Number of projections	900
	Reconstruction algorithm	FDK
	Bit depth (reconstruction)	32bit

2.2. XCT Data analysis

The reconstructed volumes were imported into MATLAB and processed using a modified implementation of the technique to determine the CDF described in ASTM E1695 [12]. For each volume, background correction was first performed by subtracting from all voxel-wise gray values in the volume the average voxel value in the background, defined as the region from the blue box to the lateral edges of the volume defined in Figure 3a. A global threshold value was calculated utilized using the ISO50 method for the entire volume and was used to determine the boundary between the material and background for the volume. The central slice along the rotational axis of the volume was then isolated for analysis in this study.

Regions of interest were created around each cylinder in the central slice (shown as red squares in Figure 3) to enable cylinder-wise analyses. The CDF was calculated for each region using the tiling method described in ASTM E1695. It is recommended that the tile size (D^*) is increased until "...the size

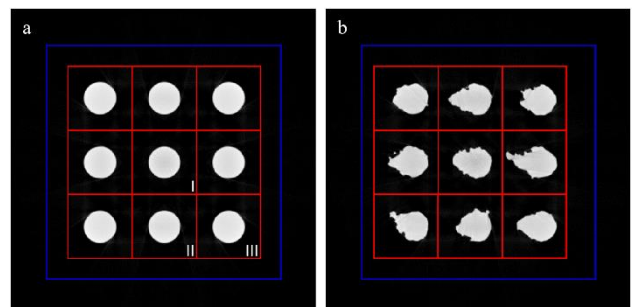


Figure 3. Central slices through reconstructed cylinder arrays. (a) Middle reconstruction slice (0.5 mm diameter). The region outside the blue square and to the outer edges of the slice was used for background compensation. The regions inside the red boxes indicate the regions of interest for each cylinder. (b) Middle reconstruction slice of AM lattice model (0.5 mm nominal diameter).

of the tiles becomes too large to obtain a statistically significant number of tiles. It is recommended that the minimum number of tiles is about 25" [12]. While this recommendation is reasonable for the XCT measurement of the relatively larger cylindrical phantom prescribed in ASTM E1695, it is generally difficult to satisfy when measuring the small struts of lattice structures. Hence, in this work, the minimum number of tiles for a given D^* is set to 4. The results of the reconstructions were assumed to be axisymmetric with respect to the lateral axes of the volumes, and therefore only the results of the center cylinder (I in Figure 3), a side cylinder (II in Figure 3), and a corner cylinder (III in Figure 3) were evaluated. Monochromatic and polychromatic acquisitions of the AM component surface model shown in Figure 1b were also simulated. The CDFs of these simulations were determined using the previously described method.

3. Results

Ideal cylinder arrays

The center cylinder of the array is subject to stronger cupping artifacts than the other cylinders. Figure 4 displays the CDF curves of the center cylinder for both monochromatic and polychromatic simulations in the 0.3 mm, 0.5 mm, and 0.7 mm diameter cylinder arrays. All monochromatic scans appear to show an approximately linear decrease in the CDF value with increasing D^* . This indicates that only statistical noise is observed in the monochromatic scans, as pure statistical noise should follow a slope of -1 on the log-log plot [12]. This observation was made in the monochromatic simulations of all cylinder diameters. In the polychromatic simulations, the CDF of the 0.3 mm diameter cylinder closely follows its monochromatic CDF but deviates at larger values of D^* . As D^* increases, the number of tiles used in the CDF calculation continues to drop until the predefined minimum of 4. With a low sample size, a higher variance in the CDF values is expected. However, the polychromatic CDFs of the 0.5 mm and 0.7 mm diameter cylinders depart from their monochromatic CDFs at low values of D^* , indicating an increased variation in reconstructed gray values within the cross section of the cylinder, i.e., more pronounced cupping artifacts. This departure increases with increasing cylinder diameter.

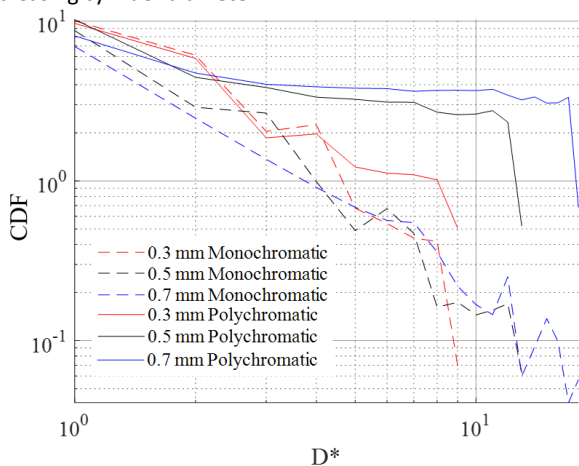


Figure 4. CDF curves for the center cylinder of both monochromatic and polychromatic simulations in 0.3 mm, 0.5 mm, 0.7 mm diameter arrays

To further examine this behavior, the CDF acquired from the monochromatic simulations (CDF_M) was subtracted from the CDF acquired from the polychromatic simulations (CDF_P) for all arrays. Figure 5 displays these results for the center cylinder at all diameters; as the diameter of the cylinder array increases, CDF_P increasingly deviates from CDF_M . This trend is expected as there are stronger cupping artifacts in larger cylinders.

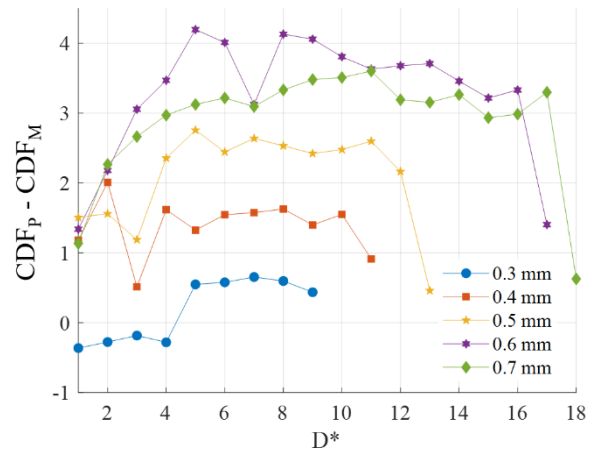


Figure 5. Difference between CDF_P and CDF_M in the center cylinder for all diameters

Figures 6 and 7 show the difference between CDF_P and CDF_M for the side and corner cylinders, respectively, of each array. A reduction in magnitude between the side and corner cylinders, and the center cylinder is apparent. This behavior is expected, as the side and corner cylinders are subject to reduced cupping artifacts. The average difference in CDF value is observed to be lower in the corner cylinders for the 0.3 mm, 0.4 mm, and 0.5 mm compared to the side cylinders. Interestingly, this trend is not observed in the 0.6 mm and 0.7 mm diameter arrays.

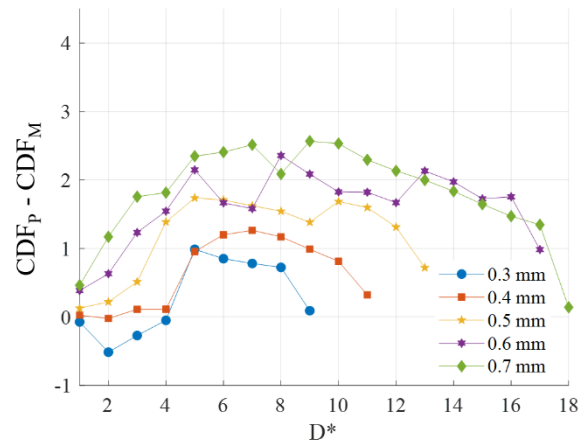


Figure 6. Difference between CDF_P and CDF_M in the side cylinder for all diameters

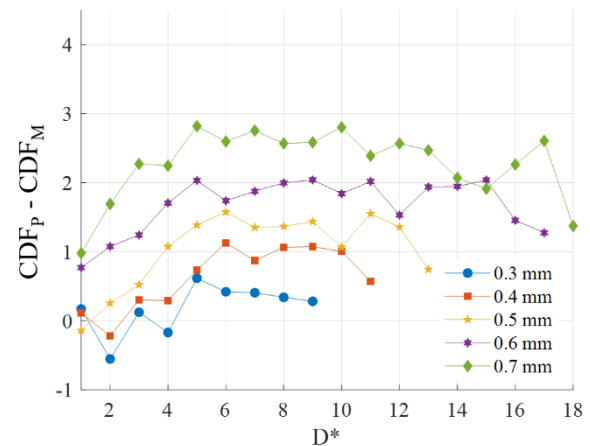


Figure 7. Difference between CDF_P and CDF_M in the corner cylinder for all diameters

AM cylinder array

Figure 8 displays the difference between CDF_P and CDF_M for three cylinders (center, side, and corner) in the AM component. Differences in the plot trends between the ideal cylinder arrays

and the AM component are immediately noted. A much higher difference between the CDF_P and CDF_M is observed at $D^* = 1$ for all three cylinders, indicating a much higher standard deviation of voxel-wise gray values in the polychromatic simulation. Upon closer visual examination of the reconstructed slice, windmill artifacts (due to aliasing in the reconstruction of sharp edges) were noted.

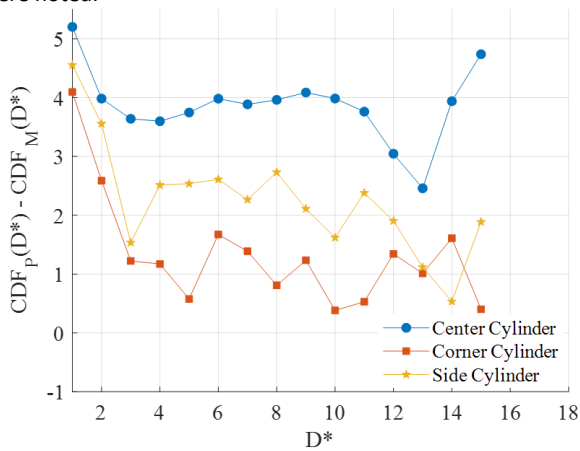


Figure 8. CDF curves for AM component

Nevertheless, the trend observed in Figures 5, 6, and 7, in which the difference between the polychromatic and monochromatic simulations increases as the cylinder in question becomes more central in the array for 0.5 mm diameter, is also observed here. The internal gray values, normalized here with respect to the highest and lowest gray values in the region of interest, on the different cylinder locations are investigated. While the gray values of the monochromatic simulations are relatively uniform across the cross section of the cylinder, with minor fluctuations due to statistical variation, the gray values in the polychromatic simulation are not uniform. Figure 9 displays the normalized gray values for the center, side, and corner cylinders in the 0.7 mm diameter array. Significant variations in the gray values across the cross-sectional area of the cylinder can be observed as a function of cylinder position. This variation could explain why the CDF results between the side and corner cylinders in the 0.6 mm and 0.7 mm diameter arrays did not appear to follow the same trend as in the other diameters. While the CDF appears to detect some differences between the cylinders, it is not able to capture changes in the gray value distribution across the cross-sectional area of the cylinder. It is not entirely clear at what point the presented results are definitively dis-similar. Furthermore, it is not immediately apparent that the results from the various arrays are similar. Thus, this raises a question regarding similarity analysis: in the comparison of two sets of results, should the null hypothesis be similarity or dis-similarity.

It should be noted that the authors also attempted to evaluate the spatial resolution of each dataset using the methodology described in ASTM E1695. However, the described methodology could not be applied to the AM component, as form errors would invalidate the creation of the edge response function.

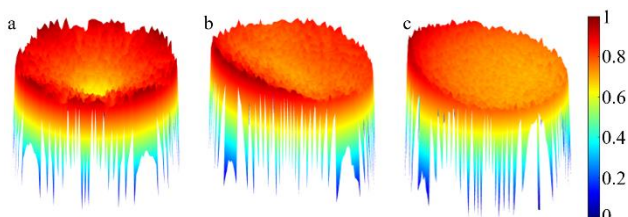


Figure 9. 3D surface plots of the relative internal intensity of various cylinders in the 0.7 mm diameter array: (a) Center cylinder (b) Side cylinder (c) Corner cylinder

4. Conclusion

There is currently no quantitative basis with which we can assert sufficient similarity to warrant the use of the substitution method for a test object deviating, e.g., in terms of X-ray penetration length, from the reference object. In this study, we investigate the use of the CDF, an image quality metric prescribed in ASTM E1695, to expose differences in the manifestation of cupping artifacts due to differences in X-ray penetration lengths. These results indicate that changes in form error can potentially lead to significant variations in CDF within a lattice structure. Furthermore, these results show that variations in the CDF can also occur between individual struts of a lattice based on their position. Future work will investigate new approaches to determine spatial resolution that are robust to non-ideal geometries, and will evaluate the efficacy of other metrics as measures of similarity. This and future studies should stimulate discussions and further work on determining a cut-off for similarity based on these metrics.

References

- [1] A. Nazir *et al.*, "A state-of-the-art review on types, design, optimization, and additive manufacturing of cellular structures," *Int. J. Adv. Manuf. Technol.*, vol. 104, no. 9, pp. 3489–3510, Oct. 2019, doi: 10.1007/s00170-019-04085-3.
- [2] B. K. Nagesha *et al.*, "Review on characterization and impacts of the lattice structure in additive manufacturing," *Mater. Today Proc.*, vol. 21, pp. 916–919, Jan. 2020, doi: 10.1016/j.matpr.2019.08.158.
- [3] A. du Plessis *et al.*, "Beautiful and Functional: A Review of Biomimetic Design in Additive Manufacturing," *Addit. Manuf.*, vol. 27, pp. 408–427, May 2019, doi: 10.1016/j.addma.2019.03.033.
- [4] A. D. Dressler *et al.*, "Heterogeneities Dominate Mechanical Performance of Additively Manufactured Metal Lattice Struts," *Addit. Manuf.*, 2019, doi: <https://doi.org/10.1016/j.addma.2019.06.011>.
- [5] M. Dallago *et al.*, "On the effect of geometrical imperfections and defects on the fatigue strength of cellular lattice structures additively manufactured via Selective Laser Melting," *Int. J. Fatigue*, vol. 124, pp. 348–360, 2019, doi: <https://doi.org/10.1016/j.ijfatigue.2019.03.019>.
- [6] C. Yan *et al.*, "Evaluations of cellular lattice structures manufactured using selective laser melting," *Int. J. Mach. Tools Manuf.*, vol. 62, pp. 32–38, 2012, doi: <https://doi.org/10.1016/j.ijmachtools.2012.06.002>.
- [7] D. Ashouri *et al.*, "Mechanical behaviour of additive manufactured 316L f2ccz lattice structure under static and cyclic loading," *Int. J. Fatigue*, vol. 134, p. 105503, 2020, doi: <https://doi.org/10.1016/j.ijfatigue.2020.105503>.
- [8] F. Zanini *et al.*, "Uncertainty of CT dimensional measurements performed on metal additively manufactured lattice structures," presented at the 10th Conference on Industrial Computed Tomography, 2020.
- [9] M. Pranievicz *et al.*, "An exploration of XCT measurement of AM lattice structures: Uncertainty in calibrated reference object measurement. (Under review)," *Precis. Eng.-J. Int. Soc. Precis. Eng. Nanotechnol.*, 2021.
- [10] Verein Deutscher Ingenieure (VDI), "VDI/VDE 2630 Blatt 2.1 Computed tomography in dimensional measurement: Determination of the uncertainty of measurement and the test process suitability of coordinate measurement systems with CT sensors," Düsseldorf, Germany, 2015.
- [11] M. Ferrucci *et al.*, "Charting the course towards dimensional measurement traceability by X-ray computed tomography," *Meas. Sci. Technol.*, Mar. 2021, doi: 10.1088/1361-6501/abf058.
- [12] ASTM International, "ASTM E1695 - 20: Standard Test Method for Measurement of Computed Tomography (CT) System Performance," ASTM International, West Conshohocken, PA, 2020.
- [13] Volume Graphics GmbH, "VGStudioMax 3.4".
- [14] C. Bellon *et al.*, "Radiographic simulator aRTist: version 2," 2012.
- [15] A. M. Hernandez *et al.*, "Tungsten anode spectral model using interpolating cubic splines: Unfiltered x-ray spectra from 20 kV to 640 kV," *Med. Phys.*, vol. 41, no. 4, Art. no. 4, 2014.

Session 5: In-process metrology and data fusion

Smart machines for fused filament fabrication based on multi-sensor data fusion, digital twins and machine learning

A. Rossi¹, M. Moretti¹, N. Senin¹

¹University of Perugia, Italy

arianna.rossi2@studenti.unipg.it

Abstract

Among additive manufacturing technologies, fused filament fabrication (FFF) is becoming increasingly important for high-performance applications, e. g. in the biomedical and pharmaceutical fields, which require products to conform to strict functional and geometric specifications. At the state-of-the-art, in-process monitoring is being actively investigated to improve FFF: monitoring the machine and the part during the fabrication provides opportunities for keeping quality under constant control, allowing for early process termination or for taking corrective actions in case issues are detected.

In this work, ongoing research towards the implementation of a “smart” FFF machine is illustrated, where sensing and machine learning are combined to achieve real-time process monitoring and capability for self-adjustment. Through sensors, a smart FFF machine can monitor extrusion rate, temperatures and pressure. Machine vision can be used to monitor the geometry and topography of the current layer, detecting both topographic defects and part shape errors as they appear. A fundamental role is played by the presence of digital twins, i.e. computer simulations of the part being fabricated and of the FFF system, which are used by the machine AI as an aid to the decisional process, and are continuously updated through sensor data to reflect the current state of fabrication. The current opportunities and open challenges of developing a smart FFF machine are highlighted through the illustration of an open, modular architecture which we have been developing as a testbed for multisensing and AI in FFF. Issues are discussed through the application to a selected set of test cases.

Artificial intelligence, 3D printing, In-process measurement, Monitoring

1. Introduction

Fused Filament Fabrication (FFF) is an additive process in which objects are fabricated by extruding a thermoplastic material deposited in consecutive layers. Thanks to the development of innovative highly engineered materials [1,2] and to the freedom and flexibility allowed in part design, FFF is becoming increasingly appealing for high-performance applications, especially in the biomedical [3] and pharmaceutical [4] sectors and for the production of electric motor components [5] and embedded sensors [6]. High-performance applications require products to adhere to strict application-related design specifications, therefore FFF technologies are required to evolve to achieve higher part quality. To this effect, diverse in-process monitoring systems have been investigated as means to keep part and process quality indicators under control. Accelerometers have been used to detect nozzle clogging [7] and step losses [8]. Extrusion pressure and temperatures have been monitored using sensors embedded in the nozzle [9]. By means of infra-red thermal imaging, the extrusion temperatures and the processing condition of the layer have been observed [10], [11]. Acoustic emissions have been used to detect extruder failures [12] and other machine faulty states [13]. Layer imaging in the optical range has a fundamental role in process monitoring. Vision systems have been implemented to detect layer flaws [14], in some cases exploring the possibility to trigger corrective actions [15]. Optical imaging has also been used to observe the part from the side during the fabrication process [16] and to detect errors such as the detachment of the part

from building platform and part deformation [17]. Finally, a system for extracting the outer boundary of each layer using layer images taken from above has been proposed [18].

In this work, we illustrate the ongoing development of a modular hardware-software framework to test new data analysis methods, machine learning and multisensor data fusion technologies applied to FFF. The system currently allows to monitor extrusion process parameters (extrusion pressure, material transport and temperatures), nozzle-part relative movement, and layer quality via optical imaging. Using imaging, the system is also able to reconstruct the evolving geometry of the part as it grows layer after layer. Finally, digital twins (DTs) of the extrusion process and of part geometry are maintained and used to aid in-process quality monitoring and defect detection.

2. The FFF hardware-software framework

The framework under development is based on the architecture of a commercial FFF machine [19] modified in order to accommodate heterogeneous sensing solutions and machine learning capabilities. The machine features a Cartesian architecture: the building plate moves along X and Y axes, while the extruder, mounted on a horizontal gantry, is moved along the vertical direction (Z).

The position of the extruder relative to the part under fabrication is monitored through three optical encoders (Broadcom-Avago AEDM-5810-Z12 [20]) installed on the axes X, Y, Z. Another two optical encoders are used to monitor filament transport and slippage events. Two shear beam load cells are

positioned above the hot end of the extruder, to measure extrusion pressure. The hot end is equipped also with four J-type thermocouples, three of which located in the nozzle, lodged in three blind holes machined with 30° tilt with respect to the extruder axis and angularly spaced by 120°. The fourth thermocouple is inserted in the heat block, in the same slot used for the system thermistor.

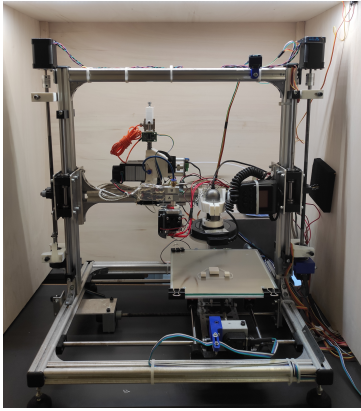


Figure 1. The FFF machine prototype inside the enclosure.

The sensor data streams are collected using a modular architecture based on National Instruments hardware [21]. The system is composed of a chassis Ni cDAQ 9185 on which four modules, dedicated to specific signal acquisition, are installed. The Ni cDAQ communicates with a PC, which manages the acquisition process through a Labview-based software, capable of reading and storing data provided by sensors while the machine is fabricating the part. An imaging system is mounted on the horizontal gantry, parallel to the extrusion system, and can host interchangeable cameras, to acquire top-down pictures of the part under fabrication. In Figure 1, the system is equipped with a digital video microscope (Dino-Lite Edge AM4515ZT 1.3 MP 20x~220x) and a ring-light source. The acquisition is triggered using one of the control board auxiliary digital ports which respond to specific command in the part fabrication program. Depending on the optics setup, the imaging system can be used to capture the entire layer in one shot or stitchable sequences of higher-resolution regions, depending on monitoring target (small-scale defects vs part form errors). Also depending on the characterisation objectives, the FFF machine can be positioned inside a dedicated enclosure designed to cut out external light (Figure 1) and produce more uniform illumination conditions for imaging.

The machine control board is a Megatronics v3.2 [22], which features auxiliary digital ports useful to deliver custom command signals. These have been used to trigger the image acquisition, as mentioned above, and to generate a counter to tag the execution of g-code commands, so that sensor data can be mapped to the specific g-code command that triggered the execution of a specific portion of part program. The control board, equipped with Marlin firmware [23], is connected to a PC via serial interface and the communication is managed by the software Repetier-Host by Hot-World GmbH [24]. Data processing and analysis via machine learning are performed by a separate computer which receives the sensor data streams from the Ni cDAQ. By aggregation of heterogeneous sensor information, the monitoring system achieves a comprehensive view of the process and can detect issues that could not be reliably detected using a single sensor. The data streams are also routed to the associated digital twins (DTs), so that the simulation models can be updated in real time to support fabrication monitoring and the decisional process. In the

following, to exemplify the capabilities of the framework, two subsystems are illustrated, one dedicated to monitoring process parameters during layer deposition and highlighting the potential of multi-sensor data fusion; the other dedicated to monitoring the outer contour of each layer and the growth of part geometry, highlighting the potential advantages of using digital twins to support data interpretation and process monitoring.

3. Monitoring the deposition process using multi-sensor data

Data recorded in-sync from positional encoders can be used to reconstruct the real extruder path followed during the entire fabrication process. The real path can be compared to the nominal one (calculated from automated analysis of the part program) in order to identify anomalies related to axis positioning errors. An example of this type of monitoring is reported in Figure 2 in relation to a test pyramid with base 20x20 mm and height 10 mm. The fabricated part (Figure 2a) is clearly defective due to an abrupt loss of positional reference happened roughly at mid-build. The issue is immediately detected through the analysis of multi-sensor data as illustrated in Figure 2b, where the real path as recorded by the encoders is plotted and coloured by deviation (local Euclidean distance) from the nominal path defined in the part program.

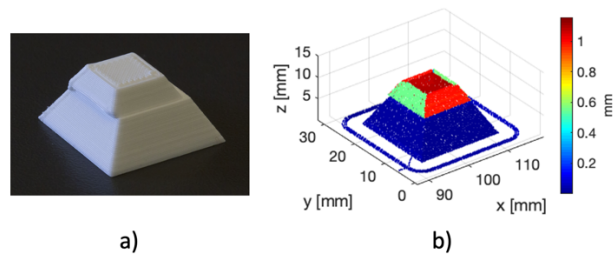


Figure 2. a) test pyramid with defective geometry due to axis reference loss; b) the anomaly is immediately visible via analysis of the encoder data and comparison with nominal expectations (part program).

As stated earlier, the framework is designed so that heterogeneous sensor data streams can be temporally and spatially co-localised. This allows for unprecedented freedom on the types of analyses which can be performed for process monitoring and optimisation. In Figure 3 extrusion paths related to individual layers are visualised, where coordinates have been extracted from the encoder data streams, whilst colouring is based on data from another two sensors, i.e. temperature at the extrusion nozzle (Figure 3a) and filament transport error due to slippage (Figure 3b). Both the maps refer to layers extracted from the pyramid shown in Figure 2. The data in Figure 3a shows how colder and hotter regions of the build can be detected, whilst Figure 3b allows to investigate for correlations between filament transport error and specific part regions. Similar plots using data from other sensors are illustrated in [25].

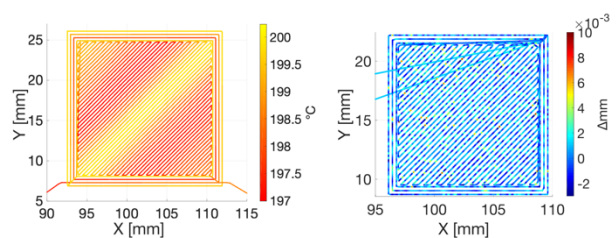


Figure 3. Layer extrusion path coloured by: a) local extrusion temperature; b) local filament slippage error.

4. Layer contour monitoring with machine vision and digital twins

The layer contour monitoring subsystem is based on the analysis of high-resolution images depicting portions of the layer contours. In this case, the microscope operates at ~ 8 mm from the surface, achieving a rectangular field of view of (9.34×7.48) mm, which, captured by a (1280×1024) pixel detector, results in a resolution of $\sim (7.3 \times 7.3)$ $\mu\text{m}/\text{pixel}$ (data obtained after calibration). The calibrated pixel size is about one order of magnitude smaller than the preset deposited filament width of ~ 350 μm , thus allowing to detect irregularities in the shape and lay of the strand. An example image acquired with this method is depicted in Figure 4.

Images are acquired along each layer contour after the fabrication of the layer itself. The number and the position of the images is automatically determined with the help of a DT dedicated to estimating where the layer contours should be located at the current stage of fabrication and thus drives the positioning of the camera. The complete layer contour is obtained by stitching the single images.

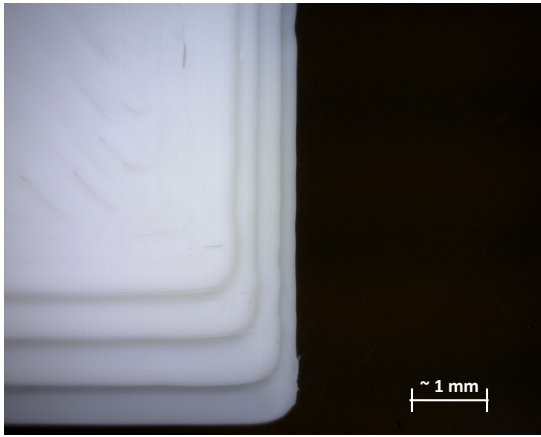


Figure 4. Example image acquired by the microscope, centred on a layer corner of a test part.

Image analysis is tasked with detecting the layer edges in the image. As the operation is challenged by the presence of complex topographic formations belonging to the current and previous layers, as well as by shadows and generally low contrast, a second DT is used to support scene interpretation. In this case, the digital twin reconstructs local layer topography using: nominal information from the part program (extrusion path); numerical simulation of the extrusion process (to compute thickness of the deposited strand); information from the sensors (real extrusion path to adjust the prediction on position of the deposited strands). This information is used by machine vision to interpret the scene based on (simulated) expectations, in order to correctly locate the real edge amongst possible candidates preselected via a Canny-based algorithm [26]. The complete layer contour is obtained by joining the contours detected in the stitched images, as shown in Figure 5.

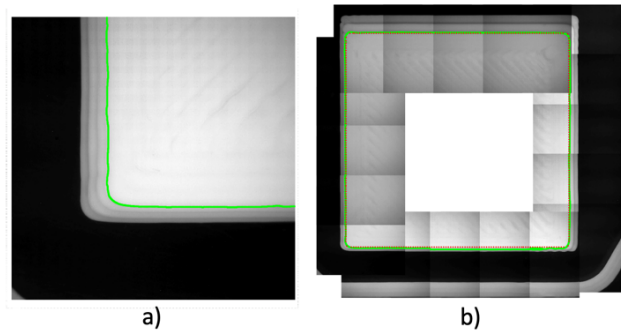


Figure 5 a) result of the contour detection process on a corner, the green line is the detected contour; b) reconstruction of the complete contour for a layer. The stitched images are shown overlaid. The red dotted line indicates the expected contour, the continuous green line is detected one.

As the digital twin is capable of predicting the shape and location of the layer contour for an in-control process, the result of machine vision can be used to also assess if the currently detected contour features any significant discrepancy with respect to the expectation, indicating potential out-of-control conditions [27]. Therefore, the DT is also used to support in-process monitoring. An example is shown in Figure 6, where a corner anomaly is highlighted, due to material over-extrusion. The anomaly can be immediately detected by the monitoring system as an unusual discrepancy between the locally reconstructed edge contour and the expectation produced by the DT.

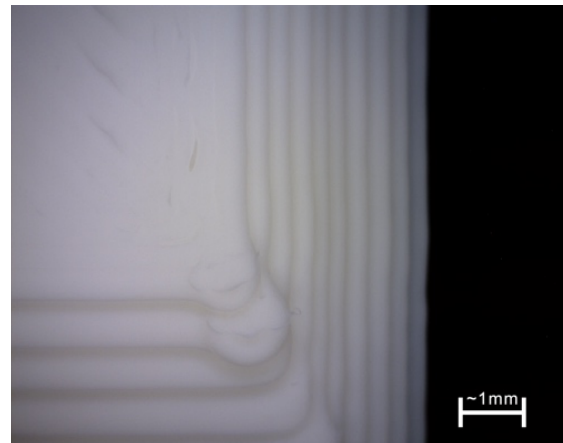


Figure 6. Top view image of a defected pyramid corner, showing the results of over-extrusion.

The geometry of the whole part can be obtained by vertical stacking of the detected layer contours, while the fabrication is in progress. The evolving geometry is continuously compared to the expectations from the DT in order to detect geometric anomalies that propagate through layers, eventually affecting the geometry of the entire part. An example of this is shown in Figure 7. The surfaces of the test pyramid are reconstructed by contour stacking. Colouring is proportional to local distance from the expected surfaces, as simulated by the digital twin. Note how the same local corner anomaly previously described in Figure 6 is also visible in Figure 7 (the red portion of contour visible at the corner of one of the layers).

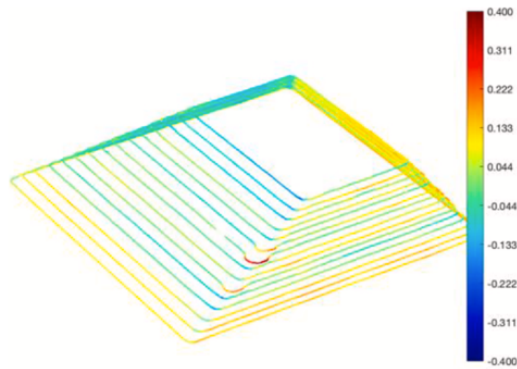


Figure 7. Pyramid surfaces reconstructed by contour-stacking and comparison with the nominal expectations predicted by the digital twin (color proportional to local Euclidean distance (signed, units in mm)).

5. Conclusions

In this work the development of an open and modular framework for testing new data analysis methods, multi-sensor data fusion and the use of digital twins for in-process monitoring of FFF has been illustrated. The illustration has focused on the current implementation of two subsystems, one dedicated to layer contour monitoring and making use of machine vision supported by digital twins, and the other dedicated to multi-sensor data fusion for the co-localisation and analysis of process data related to the layer fabrication process. Numerous other possibilities exist to exploit multiple heterogeneous sensing and the use of digital twins for automated process monitoring and adaptive optimisation of process parameters.

Particular attention for ongoing and future work is currently given to automated scene interpretation supported by digital twins, where the latter are used to build an expectation of what a scene should look like in nominal conditions, so that anomalies can be isolated. Our research efforts are also currently dedicated to study the integration of mainstream and experimental machine learning technologies into the framework, to explore further avenues for data analysis and processing, and automated decision-making in novel “smart” additive machines.

References

- [1] Laureto J, Tomasi J, King JA, Pearce JM 2017 Thermal properties of 3-D printed polylactic acid-metal composites *Prog Addit Manuf.* **2** 57–71.
- [2] Ramanath HS, Chua CK, Leong KF, Shah KD 2008 Melt flow behaviour of poly-ε-caprolactone in fused deposition modelling *J. Mater. Sci. Mater. Med.* **19.7** 2541-50
- [3] Youssef A, Hollister SJ, Dalton PD 2017 Additive manufacturing of polymer melts for implantable medical devices and scaffolds. *Biofabrication* **9.1** 012002
- [4] Gbureck U, Vorndran E, Müller FA, Barralet JE 2007 Low temperature direct 3D printed bioceramics and biocomposites as drug release matrices *J Control Release* **122** 173–80
- [5] Liu L, Ding C, Lu S, Ge T, Yan Y, Mei Y, Ngo KD, Lu GQ 2018 Design and Additive Manufacturing of Multipermeability Magnetic Cores *IEEE Trans Ind Appl* **54** 3541–47
- [6] Maurizi M, Slavič J, Cianetti F, Jerman M, Valentinčič J, Lebar A, Boltežar M 2019 Dynamic measurements using FDM 3D-printed embedded strain sensors *Sensors* **19** 1–15
- [7] Tlegenov Y, Hong GS, Lu WF 2018 Nozzle condition monitoring in 3D printing *Robot Comput Integr Manuf* **54** 45–55
- [8] Kim JS, Lee CS, Kim SM, Lee SW 2018 Development of Data-Driven In-Situ Monitoring and Diagnosis System of Fused Deposition Modeling (FDM) Process Based on Support Vector Machine Algorithm *Int J Precis Eng Manuf - Green Technol* **5** 479–86
- [9] Anderegg DA, Bryant HA, Ruffin DC, Skrip Jr SM, Fallon JJ, Gilmer EL, Bortner MJ 2019 In-situ monitoring of polymer flow temperature and pressure in extrusion based additive manufacturing *Addit Manuf* **26** 76–83
- [10] Pollard D, Ward C, Herrmann G, Etches J 2017 Filament Temperature Dynamics in Fused Deposition Modelling and Outlook for Control *Procedia Manuf* **11** 536–44
- [11] Dinwiddie RB, Love LJ, Rowe JC 2013 Real-time process monitoring and temperature mapping of a 3D polymer printing process *Thermosense Therm Infrared Appl XXXV* **8705** 87050L
- [12] Wu H, Wang Y, Yu Z 2016 In situ monitoring of FDM machine condition via acoustic emission *Int J Adv Manuf Technol* **84** 1483–95
- [13] Liu J, Hu Y, Wu B, Wang Y 2018 An improved fault diagnosis approach for FDM process with acoustic emission *J Manuf Process* **35** 570–79
- [14] Holzmond O, Li X 2017 In situ real time defect detection of 3D printed parts *Addit Manuf* **17** 135–42
- [15] Liu C, Law ACC, Roberson D, Kong Z (James) 2019 Image analysis-based closed loop quality control for additive manufacturing with fused filament fabrication *J Manuf Syst* **51** 75–86
- [16] Lyngby RA, Wilm J, Eiriksson ER, Nielsen JB, Jensen JN, Aanaes H, Pedersen DB 2017 In-line 3D print failure detection using computer vision *Dimens. Accuracy Surf. Finish Addit. Manuf.*
- [17] Baumann F, Roller D 2016 Vision based error detection for 3D printing processes *MATEC Web Conf.* **59** 3–9
- [18] He K, Zhang Q, Hong Y 2018 Profile monitoring based quality control method for fused deposition modeling process *J Intell Manuf* **30** 947–58
- [19] RepRap. 3Drag 3D Printer Kit. Open Store Electron 2019. <https://store.open-electronics.org/3Drag-3D-printer-KIT>.
- [20] Broadcom. High Resolution 3-channel Housed Encoder Module Kits with Snap-on Cover 2019. <https://www.broadcom.com/products/motion-control-encoders/incremental-encoders/transmissive-encoders/aedm-5xxx>.
- [21] National Instruments. LabVIEW. 2020. <https://www.ni.com/en-us/support/downloads/software-products/download.labview.html>
- [22] Meijer B. Megatronics v3.2 Datasheet. 2018. <https://repreapworld.com/datasheets/datasheet-megatronicsv32.pdf>
- [23] Marlin. Marlin Firmware 2021. <https://marlinfw.org/>
- [24] Repetier. Software Repetier Host 2018 <https://www.repetier.com>
- [25] Moretti M, Bianchi F, Senin N 2020 Towards the development of a smart fused filament fabrication system using multi-sensor data fusion for in-process monitoring *Rapid Prototyp J* **26.7** 1249-61
- [26] Canny J 1986 A Computational Approach to Edge Detection *IEEE Trans Pattern Anal Mach Intell* **6** 679-98
- [27] Moretti M, Rossi A, Senin N 2021 In-process monitoring of part geometry in fused filament fabrication using computer vision and digital twins *Addit Manuf* **37** 101609

Fast measurement of metal laser powder bed fusion layer surfaces using light scattering and principal component analysis

Mingyu Liu¹, Nicola Senin^{1,2}, Richard Leach¹

¹Manufacturing Metrology Team, Faculty of Engineering, University of Nottingham, Nottingham, UK

²Department of Engineering, University of Perugia, Italy

mingyu.liu1@nottingham.ac.uk

Abstract

To address the future challenges in quality monitoring of metal laser powder bed fusion, a novel method is proposed to detect topographic anomalies on layer surfaces, which may appear during the manufacturing process. The method combines light scattering and principal component analysis. Scattering patterns, experimentally generated from real surfaces representative of in-control processes and encoded as digital images, are collected and used to build a reference set, which is then further populated by simulation. Principal component analysis is then applied to the set. A certain number of principal components is extracted and used to define a transform to map any scattering pattern to principal component space. Using the created transform, any new scattering pattern can be transformed to principal component space and then back into the original space (reconstruction), with some reconstruction error. The error is expected to be low if a pattern from the reference set is processed. However, if a different pattern is processed, e.g. generated by an out-of-control layer topography, then the reconstruction error is larger. In this work, a layer monitoring system is proposed, capable of detecting out-of-control topographies through observation of the reconstruction error. The system was implemented and experimentally validated through application to a selected test case.

Measurement, laser powder bed fusion, light scattering, principal component analysis

1. Introduction

With the rapid development of metal additive manufacturing (AM) techniques [1], topography measurement of layer surfaces has become increasingly important for in-process monitoring of the quality of fabricated parts [2]. Any problem discovered in the topographies of the layer surfaces may be indicative of problems in the manufacturing process and affect the final product. In metal AM processes, such as laser powder bed fusion (LPBF), non-intrusive methods to monitor layer topography are required, where the speed of measurement is essential to avoid slowing down the manufacturing process and possibly altering the physics of the process itself [3].

In previous work [4, 5], we have developed a method to measure grating surfaces combining light scattering and machine learning, which is suitable for fast and in-process surface measurement. We then further developed the method to monitor the quality of LPBF surfaces using an autoencoder [6]. In this paper, we present a fast method to measure topographical changes of LPBF layer surfaces, which combines light scattering and principal component analysis (PCA). In the proposed method, laser light is projected onto the layer surface and scattered light is captured by a camera. The scattering pattern is then processed by a PCA-based monitoring system which detects anomalous changes in the scattering pattern as an indication of possibly detrimental changes in layer topography.

Experiments performed using a prototype implementation based on the off-line measurement of test LPBF surfaces, show that the proposed monitoring solution can be used to discriminate between in-control and out-of-control LPBF topographies. Data processing in the prototype implementation is fast enough to warrant future in-process application without

the need for slowing down or temporarily halting the fabrication process. Therefore, the proposed method has the potential to be integrated into a commercial LPBF machine for real-time, in-process quality monitoring.

2. Methodology

The schema of the proposed method is shown in Figure 1. Scattering patterns from reference surfaces (manufactured under in-control states using optimal parameters) are collected experimentally as digital images, and used to populate a reference dataset, which is then augmented by simulation (algorithmic shifts and rotations applied to the measured images). PCA is then applied to the reference dataset. The principal components represent the inherent multidimensional features of the scattering patterns from the reference surfaces. A PCA-based encoding and decoding system is then created using a certain number of principal components (the first 50% components). Using the encoding/decoding system, scattering images can be encoded into principal component space and then back into images, with a small reconstruction error. As the PCA-based encoding and decoding system has been tuned specifically for in-control surfaces (i.e. the reference dataset), any out-of-control scattering pattern processed through the

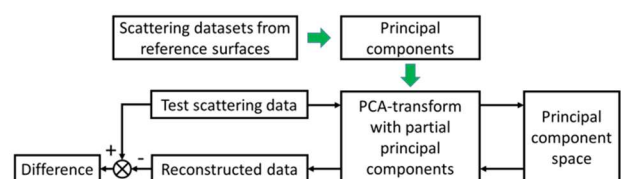


Figure 1. Schema of the proposed method

same system will result in a larger reconstruction error. Thus, reconstruction error itself can be used to detect out-of-control patterns.

Figure 2 shows the experiment setup to evaluate the proposed method. Collimated laser light with a wavelength of 633 nm and an approximate beam diameter of 0.8 mm is projected to a mirror and reflected onto the measured LPBF sample. The sample is mounted on a rotation stage, to simulate different surface orientations. Scattering light is reflected to a 150 mm × 150 mm screen. The scattering pattern can then be captured by a camera and further processed by a PC.

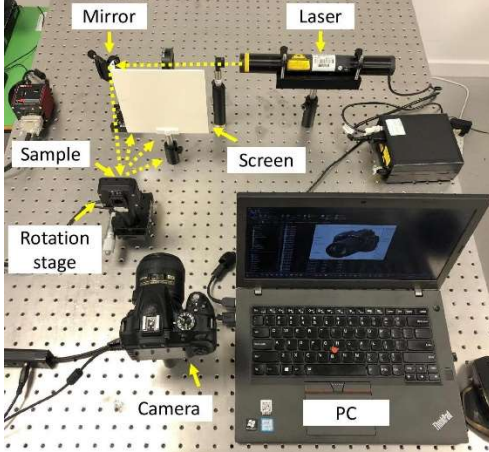


Figure 2. Experiment setup

3. Results and discussions

Two LPBF samples were used for the experiment; one was a reference surface produced by an in-control LPBF process, whilst another was representative of an out-of-control process. The topographies of the two surfaces are shown in Figure 3 and their manufacturing parameters are shown in Table 1. The reference surface was manufactured using optimal parameters, resulting in evenly distributed textures, as shown in Figure 3(a). The defective surface was manufactured using significantly lower energy density, which resulted in large humps on the surface (due to insufficient melting energy), as shown in Figure 3(b).

Both samples were used to perform the scattering experiment in the setup shown in Figure 2. For each sample, thirty-six scattering patterns were measured by rotating the surface every 10°. The scattering patterns were then further populated in simulation by algorithmically shifting the digital images by six steps in both the x and y directions and by rotating ten steps with 1° per step. As a result, there were $36 \times 6 \times 6 \times 10 = 12960$ datasets for each sample. A circular mask was applied for each dataset to make the effective area rotationally symmetric, eliminating the corner effect due to rotating the square-shaped dataset. The original pixel densities of the measured images were 6000×4000 . The images were cropped according to the size of the screen and were eventually resized to 20×20 pixels. As a result, the data size was significantly reduced. The intensity values in the pixels of the reference set were then processed by mapping to the standard normal distribution (zero mean, unit variance) [7] and used to perform the PCA. In total, there were $20 \times 20 = 400$ principal components. In this study, we used the first half of the principal components, i.e., 200 principal components, to reduce the dimension of the datasets and establish the PCA-transform.

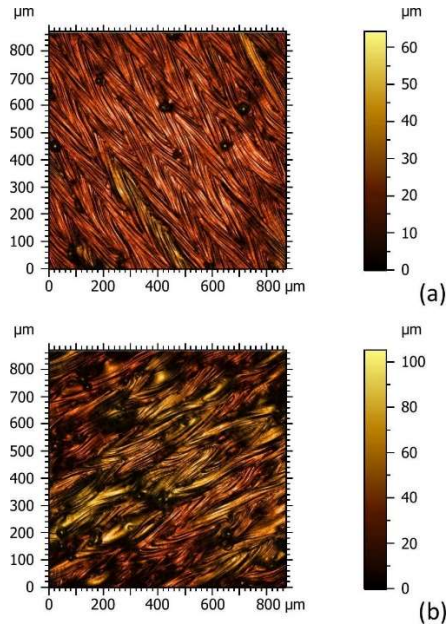


Figure 3. Topographies of LPBF samples, (a) reference surface, and (b) defective surface, measured by Zygo NexView NX2 with 20× objective lens

Table 1 Manufacturing parameters for the LPBF samples

Surface	Laser power/W	Scan speed/m s ⁻¹	Energy density/J mm ⁻²
Reference	170	1.1	2.1
Defective	120	1.1	1.5

Figure 4 shows the results for one dataset from the reference surface. Figure 4(a), Figure 4(b) and Figure 4(c) are the input scattering pattern, reconstructed scattering pattern and the reconstruction error, respectively. The results show that the reconstructed scattering pattern is visually similar to the original one. The reconstruction error is determined by the deviations from the reconstructed scattering pattern to the input scattering pattern. The root mean square (RMS) value of the reconstruction error is 0.089, which is relatively small, indicating that the PCA-transform can efficiently transform and reconstruct the scattering pattern measured from the reference surface.

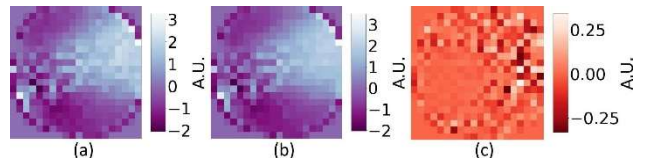


Figure 4. Results for the reference surface, (a) original scattering pattern, (b) reconstructed scattering pattern, and (c) reconstruction error. All subfigures are 20×20 pixels

The results for one dataset from the defective surface are shown in Figure 5. Comparing to the results for the reference surface, the RMS value of the reconstruction error is significantly larger, which is 0.214. The large reconstruction error is due to the low efficiency of the encoding/decoding process for the defective surface, whose datasets were not used to establish the PCA-transform. The results of the reconstruction errors for the reference surface and the defective surface are also summarised in Table 2.

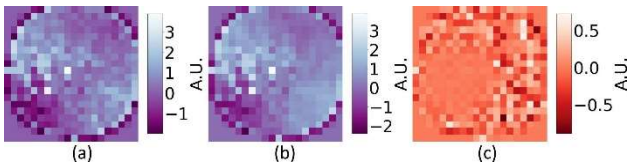


Figure 5. Results for the defective surface, (a) original scattering pattern, (b) reconstructed scattering pattern, and (c) reconstruction error. All subfigures are 20×20 pixels

Table 2 Reconstruction errors for the reference surface and defective surface

Surface	RMS of reconstruction error/A.U.
Reference	0.089
Defective	0.214

The RMS values for the reconstruction error for all datasets from both reference and defective surfaces are summarised in Figure 6. The mean value for those from the reference surface is 0.055 whilst it is 0.155 for the defective surface. These two types of surfaces can be easily discriminated by thresholding the reconstruction error. In this study, we set the threshold to be 0.1, i.e., if the RMS error is less than 0.1, the measured surface is classified as a non-defective surface, otherwise a defective surface. As a result, 12861 and 99 datasets from the reference surface were classified as non-defective and defective, respectively. On the other hand, 12938 and 22 datasets from the defective surface were classified as defective and non-defective surface, respectively. The confusion matrix can then be summarised as shown in Table 3. The overall accuracy of the classifier is 0.995, indicating that the proposed method has good performance.

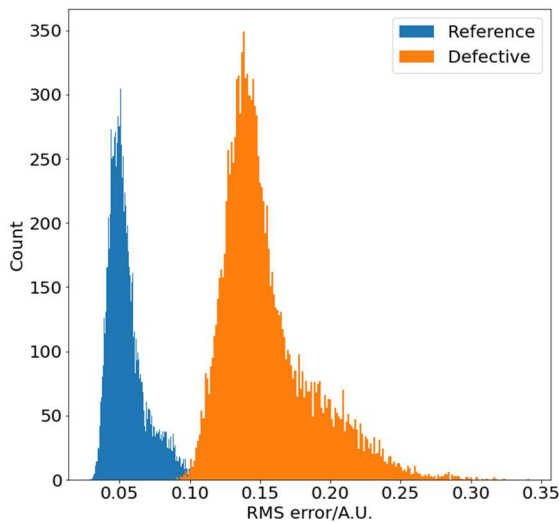


Figure 6. Histogram of results for all the datasets from the reference surface and defective surface

Table 3 Confusion matrix

	Predicted: Non-defective	Predicted: Defective
Actual: Non-defective	12861	99
Actual: Defective	22	12938

4. Conclusions

The paper presents a fast method to measure the LPBF layer surfaces combining light scattering and PCA. A PCA-based encoding/decoding system is developed and tuned on a reference dataset made of scattering patterns experimentally acquired from reference surfaces and further augmented by simulation. The PCA-based encoding/decoding system can then be used to convert scattering pattern images into the principal component space, and then back into images. The reconstruction error can be used to classify whether the measured surface has significantly different topography from the reference surfaces, possibly produced from an out-of-control process. The accuracy of the classifier was experimentally determined to be as high as 0.995, which indicates the good performance of the proposed method, although more and more diverse datasets are needed to obtain a more comprehensive assessment of performance. The computational burden of the PCA-based encoding/decoding process is relatively low, which makes the system able to achieve fast response times, an essential prerequisite for in-process utilisation. The relatively simple and low-cost design makes the proposed method potentially suitable for implementation in modern LPBF machines.

Acknowledgements

We acknowledge the support of the Engineering and Physical Sciences Research Council [EP/R028826/1], European Union's Horizon 2020 Research and Innovation Staff Exchange Programme [MNR4SCell, 734174].

References

- [1] Leach R K and Carmignato S 2020 *Precision Metal Additive Manufacturing* (CRC Press)
- [2] Leach R K, Bourell D, Carmignato S, Donmez A, Senin N and Dewulf W 2019 Geometrical metrology for metal additive manufacturing *CIRP Annals* **68** 677-700
- [3] Grasso M, Remani A, Dickins A, Colosimo B M and Leach R K 2021 In-situ measurement and monitoring methods for metal powder bed fusion – an updated review *Meas. Sci. Technol.* in press
- [4] Liu M, Cheung C F, Senin N, Wang S, Su R and Leach R K 2020 On-machine surface defect detection using light scattering and deep learning *Journal of the Optical Society of America A* **37**
- [5] Liu M, Senin N, Su R and Leach R K 2020 Cascaded machine learning model for reconstruction of surface topography from light scattering *Proc. SPIE* 113520Q
- [6] Liu M, Senin N and Leach R K 2021 Intelligent quality monitoring for additive manufactured surfaces by machine learning and light scattering *Proc. SPIE* 1178206
- [7] Abdi H and Williams L J 2010 *Principal component analysis Wiley Interdisciplinary Reviews: Computational Statistics* **2** 433-459

Stereo camera based in-situ monitoring of L-PBF process stability by spatter detection

Daniel Brummerloh^{1,2}, Dennis Jutkuhn^{1,3}, Zheng Yang⁴, Alexander Penn², Claus Emmelmann³

¹Fraunhofer Research Institution for Additive Manufacturing Technologies IAPT, Germany

²Institute of Process Imaging, Hamburg University of Technology, Germany

³Institute of Laser and System Technologies, Hamburg University of Technology, Germany

⁴Hexagon Technology Center GmbH, Switzerland

Daniel.brummerloh@tuhh.de

Abstract

The stability and reproducibility of the melting process is a decisive factor for the quality of the printing process and the final part. Stereo-vision in-situ monitoring based on two high-speed cameras in combination with fringe projection is used to investigate the three-dimensional layer topography, process spatter and residue of the melting process of laser powder bed fusion (L-PBF) process. The stereo camera system provides intensity data and a depth map of the working plane. The depth map has a lateral resolution of 40 μm and a depth variance σ^2 of 3.76 μm . The stability of the printing process can be estimated by monitoring the development of spatter and residue. Both are undesired by-products of the L-PBF process, which can indicate the present melting conditions. By optimizing the process conditions and reducing the scrap rate of printed parts, manufacturing costs can be reduced. This paper proposes a method to localize and quantify spatter emitted during the melting process, by combining the obtained depth data and the raw intensity data. The proposed method is evaluated in the course of an empirical investigation, which consists of three experiments. Within the experiments, unsuitable process conditions are caused intentionally by process parameter variation. In a real-life situation, these impairing process parameters could have been caused by defective machine components or miscalibration, and would possibly remain undetected without the technical ability to reliably monitor process stability. By measuring concentration, size and shape of the emitted spatter, the change in process parameters could be quantified and detected successfully by the proposed method. Especially overheating of material due to high local energy input and the dependency on the size of exposed area could have been identified reliably.

Algorithm, in-process measurement, selective laser melting (SLM), topography

1. Introduction

Additive manufacturing has been successfully used in series production for years, yet these processes continue to be restricted by inconsistency in manufacturing quality. A major cause is the nonexistence of universally applicable process parameters. Transferability of process parameters between manufacturing machines and parts to be built might not be given. Data and in-depth knowledge regarding the processes could be used, to find parameters for each individual case. Also, process parameters that guarantee long-term robustness during production are an actual challenge. To overcome these limitations, technical solutions are needed that would allow for the permanent monitoring and consequently for the assurance of the process parameters. To ameliorate systemic limitations of additive manufacturing, various measurement techniques allowing for the direct or indirect measurement of different process parameters have been researched in previous work.

Moreover, integrated stereo camera systems have promising potential to research various process parameters and to provide effective in-situ process monitoring capabilities. In this paper, a method is proposed to measure Laser Powder Bed Fusion (L-PBF) process stability indirectly through the quantification of spatter. Spatter is quantified by a processing chain that is executed on depth data acquired by a high precision stereo camera system. The spatter detection method is then empirically tested and evaluated in the experimental phase.

2. Process stability assessment through spatter quantification

The method proposed in this paper allows for in-situ monitoring of process stability of the L-PBF process. The method is based on depth data acquired by a stereo camera system. More precisely, the depth data is used to detect, localize and quantify individual droplets of spatter to indirectly assess the present process stability.

Spatter consists of cooled metal droplets that are ejected due to material overheating and evaporation during the laser exposure of the L-PBF process. They are emitted above an overheated melting pool and land locally around and within the processing area, influenced by the gas flow direction and intensity present in the building chamber [1]. The development of spatter can be seen as an undesired condition of the melting process. In general, spatter can have negative effects on the melting conditions and the process stability: with spatter droplets located on the powder bed and exposed areas, the material deposition can be interfered with [2]. Spatter droplets, that have been fused to the underlying part, pose a fixated obstacle that could even damage the recoating mechanism [3]. Furthermore, the energy input provided by the laser might be insufficient to remelt any spatter droplets in the exposed areas, so the fabrication of later layers might suffer from part defects. Beyond these disadvantages in manufacturing, the development of spatter can be used as a well-suited indicator of the present process stability.

Figure 1 shows an intensity image I (left) of a powder bed after laser exposure. Three exemplary spatter droplets are marked. The example shows that a high variation of the visual appearance or rather the resulting imaging data can be obtained. The variation is the result of different shapes, sizes and altered illumination based on their relative position within the build plane. Because of the variation, spatter detection based on intensity data is difficult and failure-prone.

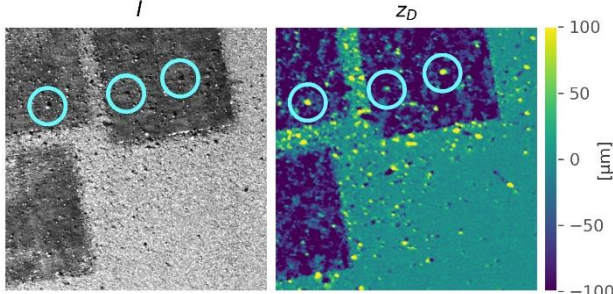


Figure 1. Monochrome intensity image I (left) of powder bed after laser exposure and resulting difference image z_D (right). Three exemplary spatter droplets are marked.

On the contrary, these variations are not to be observed within the depth data produced by the structured light system. Depth data is therefore more suitable for a robust detection algorithm. The right image of figure 1 shows a so-called difference image, that indicates change in topography caused by the laser exposure, see section 3.2. Individual spatter droplets are clearly visible in the form of a circular local maximum. Spatter droplets located outside the laser exposed areas also feature a preceding negative bump from the direction of its trajectory. This hollow is formed when the spatter droplets impinge on the powder bed surface. Examples of these pairs of local minima and maxima are marked with their approximate trajectory direction in figure 2. It should be noted that the spatter droplet trajectory can only be approximated right before impact. On the contrary, the origin and the initial trajectory cannot be determined, as the trajectory is not uniform under the influence of the laminar gas flow in the building chamber. Here, the gas flow is directed from the right to the left side in all the figures given in the paper.

By means of process stability monitoring through spatter detection, it is assumed that process accuracy and feasibility can be improved [4].

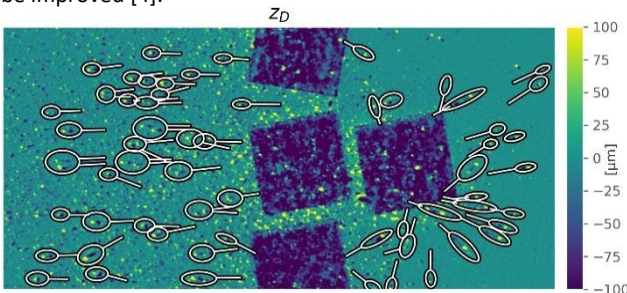


Figure 2. Difference image of depth data from exemplary depth map scan with approximated spatter trajectories.

3. Methodology

This section describes the complete process from data acquisition, over data processing to data evaluation. Additionally, the measurement hardware and its operating principle are being elaborated.

3.1. Acquisition of three-dimensional topography data

The depth data used to detect the spatter is acquired by a stereo camera system developed by Hexagon Technology Center GmbH. It consists of two high resolution monochrome cameras

($7\,920 \times 6\,004$ pixels) with Scheimpflug adapter and a mechanical slide projector. Fringe projection is used to reconstruct a three-dimensional scene of the build plane [5, 6]. By using two cameras and various stripe patterns, redundant measurement data is collected to fully construct the depth information of the build plane, which has a size of 170×170 mm. Prior calibration is used to ensure a high level of precision.

During three-dimensional scene reconstruction, the system produces a three-dimensional triangle mesh with 32m polygons. However, such high resolution is not required to employ the spatter detection method proposed in this paper. Therefore, the triangle mesh is resampled into a uniformly structured depth map of $2\,000 \times 2\,000$ pixels resolution. The ability to deploy the method on the resampled resolution offers multiple advantages: the execution of the data processing runs at higher speed and the decreased amount of data allows for long-term storage to build up an extensive process knowledge database.

The accuracy of the system has also been examined within the scope of this work. Hereby, only the random error was examined by comparing repeated measurements. The systematic error is of little interest, as the method proposed in this paper is based on relative measurement change, i.e. systematic errors would sum to zero. The depth variance σ^2 was determined by calculating the difference in z-direction between sixty consecutive scans. The experiment had been repeated five times. The accuracy of the depth data provided by the structured light system was then determined to be $\sigma^2 = 3.76 \mu\text{m}$. The 95th percentile interval of the random error is bounded at $8.45 \mu\text{m}$. The accuracy examination was based on the resampled depth maps of $2\,000 \times 2\,000$ pixels resolution.

Currently, the data acquisition and the data processing both take around 15 s respectively. The utilized system is a prototype that has not been optimized for operational speed yet, so both parts could be heavily optimized in the future. The operation potential of the structured light system in terms of speed is finally being discussed in section 6.

3.2. Difference Image

With two depth scans available, the change of the topography between two scans can be isolated by calculating their difference. To isolate emerging spatter, two scans are taken before ($t = t_0$) and after ($t = t_1$) laser exposure. The topography difference is calculated at each point (x, y) individually:

$$z_D(x, y) = z_{t_1}(x, y) - z_{t_0}(x, y)$$

As seen in figure 1, spatter droplets are clearly isolated and visible in the visualization of z_D .

3.3. Morphological operations

During the solidification of the material powder, the material exposed by the laser exposure gets compacted [2]. As a result, the surface level gets decreased by a small amount. This can also be seen in the depth data difference z_D in figure 2, as the quadratic, exposed areas show up in dark shades, indicating a negative shift.

The height normalization is performed with a morphological operation that is called reconstruction by dilation. During a normal dilation, high values replace neighbouring lower values. This spread of the highest values is then limited by maximum spread distance. Similarly, with the reconstruction by dilation, high values replace neighbouring lower values. However, the spread is not limited by distance but by a mask, which has to be specified as a second input to the operation. Thus, a reconstruction by dilation takes two inputs to produce an output image: a seed image and a mask image. The procedure is visualized in a one-dimensional example in figure 3.

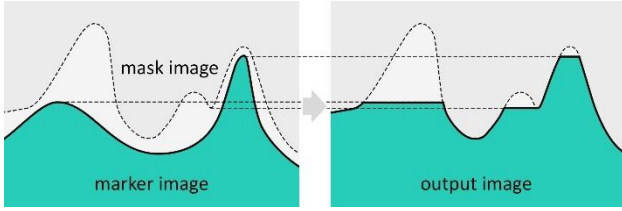


Figure 3. Qualitative functioning of the reconstruction by dilation in dependence of the chosen input image and mask image.

The algorithm used for the reconstruction is described in [7]. The desired normalization of the powder bed can be achieved by a special choice of seed image and mask image. In general, the values of the marker image need to be greater or equal to the values in the seed image. Within the scope of the proposed method, the mask image is chosen equal to z_D . The seed image is chosen as specified in the formula below. The seed image is also chosen equal to z_D except for the pixels along its contour Ω . The pixels in Ω are set equal to $\min(z_D)$ instead.

$$\begin{aligned} R_{\text{mask}}(x, y) &= z_D & \forall (x, y) \\ R_{\text{seed}}(x, y) &= z_D & \forall (x, y) \notin \Omega \\ R_{\text{seed}}(x, y) &= \min(z_D) & \forall (x, y) \in \Omega \end{aligned}$$

These rules for the deduction of mask and seed images have been applied in the example shown in Figure 4. In this specific case, $\min(z_D) = 2$.

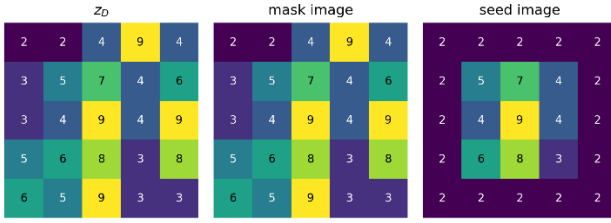


Figure 4. Mask image and seed image deduced from an exemplary depth map z_D .

The result of the reconstruction by dilation z_R on a real-world depth scan z_D can be seen in figure 5 (middle). The normalized depth data difference \tilde{z}_D can be calculated as follows. The result is visualized in figure 5 (right).

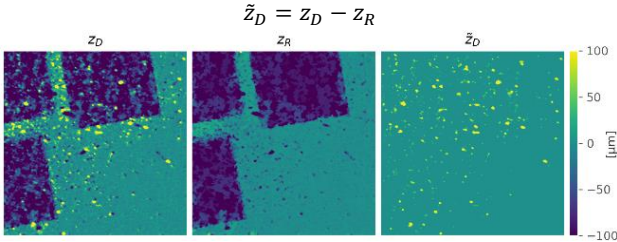


Figure 5. Difference image from depth data z_D (left), result of the reconstruction by dilation z_R (middle) and normalized difference image (right).

3.4. Spatter droplet segmentation

After the height normalization of the depth data difference image, spatter droplets are now isolated in \tilde{z}_D . More importantly, this applies both for spatter droplets within and outside the laser exposed areas in the powder bed. Individual blobs can be segmented by searching for connected regions with $\tilde{z}_D > 0$. For this labelling task, horizontal only connectivity is used. The utilized algorithm for region segmentation is described in [8].

3.5. Depth data cleaning

As with any measurement technique, the acquired depth data is subject to observational error. Very small droplets of spatter are hardly separable from signal noise. Fortunately, they are of little interest in the context of the process stability monitoring due to their little disturbing influence on the process. The data

is therefore cleaned in such a way that small spatter droplets are excluded from the subsequent data analysis. The first step is to globally shift \tilde{z}_D by $3 \mu\text{m}$ in negative direction.

$$\tilde{z}_{D,s}(x, y) = \tilde{z}_D - 3\mu\text{m}$$

By doing so, individual spatter droplets are separated more distinctively when the threshold $\tilde{z}_{D,s} > 0$ used for binary segmentation is applied. The resulting segmentation map S is visualized in figure 6 (middle). The shift of $3 \mu\text{m}$ has been determined empirically and depends on the depth data measurement accuracy, see section 3.1. As a third step, connected regions Φ_i or rather individual spatter droplets in with a size of 10 pixels or fewer are removed from the binary mask S . The threshold of 10 was also chosen empirically and with the relevance for the process stability monitoring in mind.

3.6. Volume Calculation

With the spatter droplets segmented, the droplets individual volume can now be quantified. The volume of each individual spatter droplet V_i is calculated by integrating the unshifted depth data difference image z_D over the area of the segmented spatter droplet Φ_i . V_i is shown in figure 6 (right).

$$V_i = \int_{\Phi_i} z_D dA$$

It should be noted that this technique only accounts for the spatter volume located above the reference layer, which is defined by the powder bed before laser exposure.

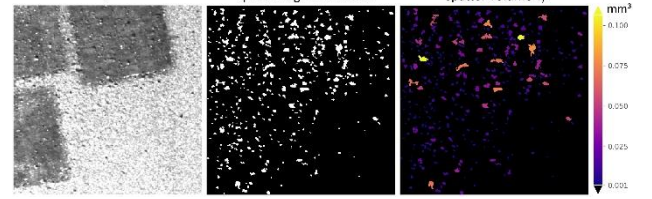


Figure 6. Intensity image I (left), binary segmentation map S (middle) and spatter volume V_i (right).

4. Experiment and empirical validation

The proposed method is verified experimentally within the scope of three build jobs. The build jobs were executed with an L-PBF machine AconityLAB from Aconity3D. AISi10Mg was used as building material for printing geometries of simple cubes. Each build job consists of ninety-nine layers, which are split into three equally large phases. In each phase, process parameters are varied. The goal of the experiment is to verify whether a change in process parameters is visible when observing and quantifying spatter volume with the proposed technique. In all three phases, the laser power of 400 W had been used. However, the energy flow into the material is altered by using different laser scanning speeds, as indicated in table 1.

Table 1. Process parameter variation for the three phases of build job execution.

Parameter variation	Name	Energy input level
1	Standard	100 %
2	Underheated	66 %
3	Overheated	200 %

The build job consists of 7 cubes with base area of either 1 cm^2 or 2 cm^2 . The cubes are rotated by 10° towards the laser trajectory direction. Also, the gas flow is altered for one build job to investigate its impact on the spatter development. The build job variations are listed in table 2. Each build job is executed and observed in-situ with the structured light system. The total spatter volume V of each layer is calculated, by summing up the individual spatter droplet volumes V_i .

Table 2. Variations of build job geometry and gas flow for the experiments. A_e is the summed part cross-section per layer.

Build job variation	Total exposed area A_e	Gas flow
1	1 400 mm ²	100 %
2	1 400 mm ²	70 %
3	700 mm ²	100 %

$$V = \sum V_i$$

The result for each of the build job variations is plotted in the upper graph of figure 7. As the spatter development is caused by laser exposure, the spatter development can also be correlated to the laser exposure area defined in the build job A_e . The measured total spatter volume V divided by its build job laser exposure area A_e is plotted in the lower graph of figure 7.

$$V_r = V/A_e$$

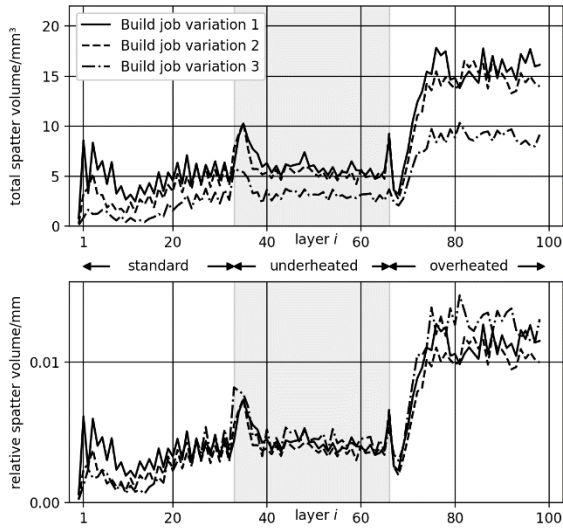


Figure 7. Spatter volume V (top) and relative spatter volume V_r (bottom).

5. Discussion of results and conclusion

The graphs in figure 7 show the measured spatter volume for different build jobs and different process parameters. All three graphs follow the same trend, which indicate a high level of reproducibility.

Looking at the temporal development of each measurement, the initial layers of each phase show divergent and fluctuating behaviour. Only around fifteen layers, the total spatter volume reaches some kind of equilibrium. The reason for this had not been investigated, however temperature effects could very well explain the phenomenon. When laser exposure begins, i.e. at the beginning of the build job, the temperature of the material rises continuously with each layer printed until the temperature reaches an equilibrium. This heating procedure is repeated when the build job phases transition, i.e. at layer 33 and layer 66. For technical reasons, the build job had to be on hold for around five minutes during this transition. During this time, the material cools down again. Different material temperatures could then cause different levels of spatter development.

The measurement of total spatter volume V indicates a strong correlation between developing spatter volume and the process condition, caused by the employed process parameters. Through quantifying spatter during manufacturing, impaired process stability is successfully detected through the measured data. However, the significance for overheating is much higher compared to underheating.

Furthermore, the relative spatter volume V_r indicates a second, strong correlation between total spatter volume and the size of the exposed area. This is expected, as spatter develops during laser exposure. This correlation also suggests some kind of build job geometry invariance, which would allow for a general application of the method.

Finally, the observed spatter distribution indicates a notable affiliation between spatter droplet trajectory and gas flow direction and intensity.

6. Operational potential of spatter detection and future work

It was shown that process monitoring based on fringe light projection to detect and quantify the concentration of spatter on the powder bed yields an indication for measuring the current process stability per layer. The reproducibility shown allow a high robustness of the measurements to be expected. The priority influences from the various process conditions could also be determined from the measured data and allow an interpretation of the measurement data in relation to the assessment of the process stability.

Nevertheless, the selected process parameters and conditions allowed for a good evaluation of the process stability. A statement in all process conditions has yet to be validated. This requires further experiments based on significantly more process parameter sets as well as different part geometries and materials in order to increase the database and to prove the interpretability of measured data even for small changes of state during the manufacturing process.

In the current state, the system acquires thirteen images per camera - seven binary patterns, four sine patterns and two reference images. With an analogue slide projector in use, the measurement or data acquisition of a single depth map takes over 15 s. The data processing takes similarly long.

To reduce data acquisition time, the total number of images used to reconstruct the three-dimensional information can be reduced. An investigation by Hexagon Technology Center GmbH has shown, that as little as four images per camera are sufficient to reconstruct a simple, primarily flat and almost two-dimensional topography as found on the powder bed. Additionally, the use of a digital projector can drastically increase the number of projected patterns per unit of time. Assuming a maximum refresh rate of 30 fps for the cameras and the projector, the theoretical data acquisition time can be as low as 133 ms ($4 \cdot 1/30$ s) per depth scan. A refresh rate of 30 fps is well within state-of-the-art performance for both components.

Equally, several ways of speeding up the data processing exist. Algorithmic optimization, the possibility of parallelization on GPUs and the ongoing development in terms of hardware performance advances result in a vast optimization potential. While data processing in a real time fashion is a realistic goal, many applications don't even depend on that and allow for delayed measurement results.

Potential applications of defect detection can be found in benchmarking process parameters as well as the assessment, maintenance and long-term monitoring of the process capability of L-PBF manufacturing machines in single-part and series production to ensure final part quality.

References

- [1] Ahmad Bin Anwar, Quang-Cuong Pham 2019 *Additive Manufacturing* **22** 86-97
- [2] Wischeropp T M, Emmelmann C, Brandt M and Pateras A 2019 *Additive Manufacturing* **28** 176-183
- [3] zur Jacobsmühlen J, Kleszczynski S, Schneider D and Witt G 2013 *IEEE Int. Instrumentation and Measurement Tech. Conf.* 707-712
- [4] Kleszczynski S, zur Jacobsmühlen J, Reinartz B, Sehr J, Witt G and Merhof D 2014 *Improving Process Stability of LBM Systems*
- [5] Zhang B, Ziegert J, Farahi F and Davies A 2016 *Additive Manufacturing* **12** 100-107
- [6] Land W S, Zhang B, Ziegert J and Davies A 2015 *Procedia Manufacturing* **1** 393-403
- [7] Robinson K 2004 *Pattern Recognition Letters* **25** 1759-1767
- [8] Wu K, Otoo E and Shoshani A 2005 *Optimizing connected component labeling algorithms*

Design of a multi-sensor measurement system for in-situ defect identification in metal additive manufacturing

Afaf Remani¹, Richard Williams², Adam Thompson¹, John Dardis³, Nick Jones³, Paul Hooper², Richard Leach¹

¹Manufacturing Metrology Team, Faculty of Engineering, University of Nottingham, Nottingham, NG8 1BB, UK

²Department of Mechanical Engineering, Imperial College London, SW7 2AZ, UK

³Renishaw Plc, New Mills, Kingswood, Wotton-under-Edge, GL12 8JR, UK

Afaf.Remani@nottingham.ac.uk

Abstract

The lack of quality assurance in additive manufacturing, and specifically in metal laser powder bed fusion (MLPBF), is a major barrier to the adoption of these technologies in high-value industrial applications. Despite its potential for producing complex components, MLPBF is afflicted by the occurrence of in-process defects that affect the integrity of finished parts and impact their dimensional accuracy. However, while defects are generally undesirable, not all of them are necessarily detrimental to the functionality of the part, and a suitable approach is required to discriminate harmful defects from neutral faults. Such knowledge is vital to understand the manufacturing process, and without it, it is not possible to determine whether a part is functional or scrap. We call this the 'Hard Problem' and propose addressing it through a series of in-process and post-process measurements. Several measurement techniques have been developed to detect the occurrence of defects; however, very few have attempted to tackle the Hard Problem. In this work, we present a multi-sensor approach to correlate the layer-by-layer development of the part with its post-process mechanical properties. First, the MLPBF build will be monitored in-process using a multi-view fringe projection system, a high-speed thermal camera and other systems, to capture defects as they form during the process. Next, the finished part will be scanned using X-ray computed tomography, to examine the defects that exist within the finished part. Finally, the part will be mechanically tested to failure to locate critical defects. The aim of this experiment is to establish meaningful connections between in-process phenomena and defects and develop methods of distinguishing between neutral anomalies and critical defects. Here, the methodology and experimental plan of this approach will be discussed, and the integration of the multi-sensor system inside a commercial MLPBF system will be described, alongside its anticipated measurement capabilities.

Keywords: Metrology, multi-sensing, metal laser powder bed fusion (MLPBF), defect detection, effect of defect

1. Introduction

Metal laser powder bed fusion (MLPBF) is, at present, the most widely employed AM technique for the manufacturing of metal parts [1,2]. While this growing interest has been encouraged by its ability to manufacture complex and optimised designs, the process is still held back by a lack of confidence in the quality of as-built parts, namely their structural integrity and mechanical properties. These barriers are due to the complex thermo-mechanics inherent to MLPBF that govern interactions between deposited materials and substrates [3]. As a result, defects are always present to some degree in MLPBF parts and are unavoidable even with the most optimal processing parameters. Part acceptance or rejection, however, cannot be conducted on the mere basis of defect occurrence, but on their effects on part functionality. On this basis, the 'Hard Problem' is defined as follows: Can in-process phenomena be correlated with function-critical defects to discriminate them confidently and reliably from neutral faults?

In most publications, focus is generally put on the monitoring of the MLPBF process or the inspection of finished parts for defect detection. Several techniques have been proposed for in-process inspection, such as off-axis optical systems [4,5], co-axial pyrometry [6,7] or a combination of these methods with machine learning [8,9]. Other methods, particularly fringe projection [10,11], have also been presented. Through layer-by-

layer image acquisition, these techniques have allowed for the identification of geometrical deviations and various powder bed defects, as detailed in our recent review [12]. Post-process techniques have, on the other hand, permitted the inspection of the volume of the part to reveal the defects therein. However, in-process and post-process techniques alike are insufficient to tackle the Hard Problem if not combined with appropriate mechanical assessment. In this work, we present a multi-sensor approach that combines a variety of in-process and post-process techniques, through a methodology that correlates in-situ continuous topographic and thermal measurements with the final volume and integrity of the part. The layer-by-layer development and final states of defects will be matched with their impact on mechanical properties, and appropriate conclusions will be drawn to discriminate critical defects from harmless flaws and provide insight into the Hard Problem.

2. Methodology

A measurement pipeline is currently being developed to tackle the Hard Problem in metal AM parts built inside a Renishaw AM250 MLPBF machine. The system will consist of three sensing systems integrated within the commercial machine to perform in-situ measurements on a (250 × 250) mm powder bed. The system combines multi-view fringe projection, IR thermography and high-speed thermal imaging technologies to perform a series of in-process measurements, following the layerwise

paradigm. Each layer of the build will be individually imaged by the different sensors right after laser melting is completed. This approach will not disrupt the normal flow of the MLPBF process, as a suitable external trigger has been implemented to initiate imaging immediately after laser scanning and before the deposition of the next layer. Naturally, the total build time will not increase as the build process does not need to be paused for measurements to take place. Upon build completion, the multi-sensing approach extends to performing post-process measurements on as-built parts using X-ray computed tomography and mechanical testing, to inspect the final volume of the part and test its mechanical properties.

There are numerous measurable quantities that can provide relevant information about the interacting physical phenomena and thermal stability of the MLPBF process, as well as the onset of defects that can occur [12]. In the context of in-situ sensing, these quantities were first referred to by Mani et al. [13] as ‘process signatures’ and can be classified into ‘observable’ or ‘derived’. The in-process sensing phase of this study focuses on the measurement of observable process signatures, as information that can be directly acquired in-situ. We will investigate these signatures on two levels, starting from the most easily visible signature and scaling down to a higher level of detail. The first process signature is the powder bed, particularly the printed layer and the surrounding unprocessed powder, and will be investigated using two techniques: a multi-view fringe projection system to obtain topographic information of the bed and an IR thermography system to monitor temperature changes across build layers. The acquisition of such topographic and thermal surface data can provide information about the occurrence of defects. Critical defects, such as hotspots, were previously revealed using these techniques [14]. The second process signature that this study looks at is the melt pool, by means of a high-speed thermal imaging system. This signature provides insight into the phenomena that occur within the laser melting zone and their influence on the formation of defects. Moreover, most common defects in MLPBF are on the same size scale as the melt pool [15], which makes melt pool monitoring critical to solving the Hard Problem.

The general methodology of this study consists of conducting said in-process measurements and comparing the detected defects with those present in the finished part. In practice, it is not guaranteed that the 2D layer defects identified in-situ will remain in the bulk in the same size, shape or population when 3D volume faults are examined. MLPBF process dynamics dictate that, due to the inherent sequence of the build process, some defects might ‘self-heal’ while others could amass at layer level or even form inter-layer clusters [16]. This is why subsequent post-process measurement is vital to understanding the types of defects that have persisted in the part and their impact on mechanical properties (sometimes referred to as “effect of defect” [16]).

2.1. In-process measurements

2.1.1. Multi-view fringe projection

The multi-view fringe projection system proposed in this study is an enhanced version of the prototype described elsewhere [17,18], where a (250 × 250) mm powder bed is monitored from four different perspectives. Major adjustments were made to the assembly to allow for operation within the environment of a Renishaw AM250 build chamber and to overcome spatial constraints. The system hardware consists of four Basler ace acA5472-17uc camera sensors (pixel array: 5472 × 3648, maximum frame rate: 17 frames/s, sensor size: 13.1 mm × 8.8 mm), each equipped with a Basler C10-1214-2MS

12.5 mm focal length lens, and a DLP4710 0.47 projector (pixel array: 1920 × 1080, maximum binary pattern rate: 1440 Hz, brightness: 1000 lumens). The cameras are tilted at 47° from the vertical to view the powder bed and are shielded from metal condensate using additively manufactured enclosures, capped with replaceable UV filters. The camera assembly is fixed onto the circular lens cover of the chamber and suitably positioned such that the laser optics are not obstructed. Due to spatial constraints limiting camera working distances, the resolution capabilities of the system are optically limited rather than sensor limited. A resolution of 57.62 μm/pixel is anticipated to be achieved in both lateral directions, which is sufficient to view a wide range of common defects in MLPBF, such as some keyhole pores (10 μm to 125 μm [6]) and lack of fusion flaws (40 μm to 340 μm [19]). The projector is placed on top of the build chamber ceiling and positioned at 24.6° downwards from the vertical. An optical mirror (flatness: 4-6 λ, wavelength range: 400 nm to 700 nm, coating: protected aluminium) is installed such that it receives the projector beam and reflects it onto the powder bed. The dimensions of the projected fringes are (250.38 × 140.84) mm and thus achieve a satisfactory coverage of the powder bed. A CAD model of the multi-view fringe projection system is shown in figure 1. The data collected from each camera during the build process will be aligned and fused to reconstruct the surface. The final output of the multi-view fringe projection system consists of a height map that can indicate surface irregularities and geometrical distortions in the printed layer.

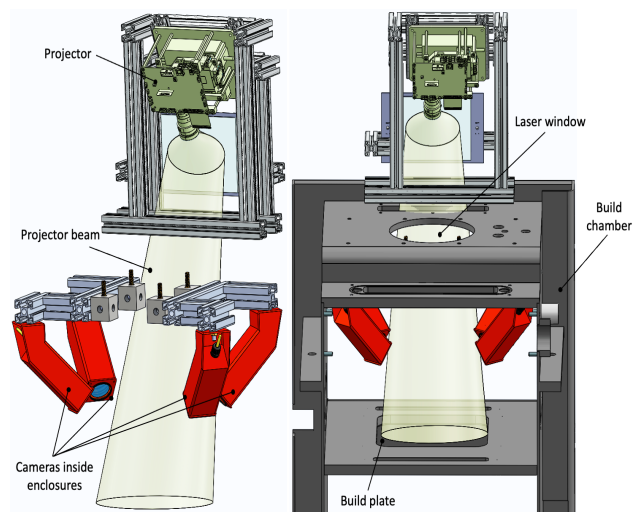


Figure 1. CAD models of the multi-view fringe projection system (left) and the open uninstalled model (right) integrated into the AM250 build chamber.

2.1.2. Full-field IR thermography

To measure temperature changes across powder layers, a new in-situ wide-field IR thermography system [1] is proposed for thermal sensing. A forward looking infrared (FLIR) A35 IR camera is housed inside a vacuum-tight enclosure to shield the optics from dust and condensate, and views the powder bed through a germanium window, as shown in figure 2. The camera is tilted downwards at 66° from the horizontal and captures a full view of the build area at a resolution of 1 mm/pixel in both directions (image size = 320 × 256 pixels). Simultaneously, a recording of the build process is taken at 60 Hz. Given these spatial and temporal resolutions, the camera is only capable of acquiring temperatures at large scales and the melt pool cannot be viewed [1]. However, the most prevalent temperature changes across layer surfaces, such as overall temperature drops, can be resolved. The IR thermography system outputs raw IR images

that can visibly show the areas currently being scanned by the laser, the zones previously scanned emitting residual heat, and spatter. The camera is calibrated using a simple empirical method described elsewhere [1].

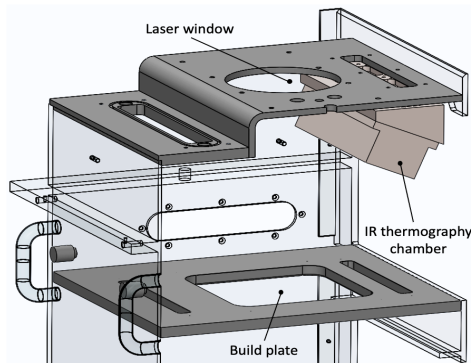


Figure 2. CAD model of the IR thermography system installed inside the AM250 build chamber.

2.1.3. Melt pool monitoring

On the same Renishaw MLPBF machine, a high-speed thermography imaging setup, detailed elsewhere [20], is installed to capture thermal variations in the melt pool. The laser beam path was modified to allow for coaxial imaging. The optical train follows two paths: one to obtain melt pool emissions and another to ensure that they reach the imaging enclosure. In the first path, a dichroic beamsplitter is placed before the scan head to reflect laser wavelengths and pass shorter ones through. The resultant light is then passed via a low-pass filter to further filter out laser specular reflections. Inside the imaging enclosure, the light is focused towards a long-pass dichroic beamsplitter and bandpass filters to transmit the bands of interest to the imaging sensors. The setup includes two Photron FASTCAM SA5 high-speed cameras imaging at two wavelengths, 700 nm and 950 nm, to ensure maximal transmission and account for emissivity changes [20]. A recording speed of up to 500 000 frames/s can be reached and images are captured with a resolution of 20 $\mu\text{m}/\text{pixel}$ (image size = 128 \times 128 pixels) [1]. The system renders video recordings of the melt pool at a predetermined (x,y) location and during a specified timeframe. Recordings can be broken up into a sequence of still frames that display a colour-coded thermal map of the melt pool at different instances in time. Such data enables the analysis of melt pool metrics (length and width), area, thermal stability and cooling rates, from which qualitative and quantitative inferences could be made. However, despite its merits, the minimum detectable temperature range of the proposed high-speed thermography system is restricted by the saturation of the imaging sensors.

2.2. Post-process measurements

2.2.1. X-ray computed tomography

We propose the use of X-ray computed tomography (XCT) to visualise imperfections in finished parts. This is a critical step in tackling the Hard Problem, given the non-destructive insight it provides on the volumetric integrity of the part and its dimensions. Following their manufacture, as-built parts will be measured using an XCT system to assess their porosity levels, pore distributions and resultant defects (populations, sizes and locations). The resultant data, in the form of 3D volumetric information, will assist to coordinate between data collected in-process and eventual destructive mechanical testing. First, XCT voxel data will be compared with layer topographic and thermal data to flag the defects that appear in both datasets and those that do not. Final defects will then be characterised in terms of size, distribution and population and categorised as either pores,

spatter or lack of fusion. Second, these defects will serve as focal points of interest and as a guiding tool for mechanical testing to reveal their impact on microstructural properties. As shown in various studies [21,22], XCT is capable of detecting micrometre-sized and sub-micrometre-sized defects and provides high-quality 3D data. However, its accuracy is affected by internal structures and complex shapes, and the smallest pores are often missed due to resolution limitations [22]. The final resolution is also restricted by sample size, such that in some cases, the best attainable voxel resolution is 2000 times smaller than the width of the measured part [23].

2.2.2. Mechanical testing

Numerous correlations can be made between the sizes and distributions of flaws and their impact on part mechanical properties. However, such associations remain speculative until the part has been tested to failure to reveal the actual effects of defects. With the help of the acquired in-process and XCT data, we aim to direct mechanical assessment towards the regions where the defects, thought to be harmful, have occurred, to reveal their real impact. There are several mechanical properties of interest (tensile strength, ductility, toughness, etc.) and various methods of testing them. However, the most relevant property in this study is tensile strength as its assessment allows for the identification of cases of premature failure. As such, we will use tensile testing on finished specimens to evaluate their resistance to failure and locate failure points. These locations will be matched with XCT volume data to pinpoint the cause of failure and determine life-limiting defects. However, it is worth noting that minimum prescribed values for tensile testing parameters (elongation and yield strength) are material specific, and that, although most of these values have not yet been determined for all powder materials in AM, some dynamic loading standards for cast materials can be applicable to MLPBF built components [16,24]. In addition to tensile testing, part microstructure will be thoroughly examined using sectioning and electron backscatter diffraction to evaluate the grain size, orientation, and morphology of the sectioned parts. Regions where large pores and defect clusters have occurred will be specifically investigated to assess changes in the surrounding microstructure. With the obtained data, a set of correlations can be established to discriminate harmful defects from neutral faults and provide meaningful insight into the Hard Problem.

3. Discussion and future work

Several challenges have been encountered thus far during the design and integration phase of the multi-sensor system inside the Renishaw MLPBF machine. In addition to the instrument limitations already mentioned, other obstacles can be classified into two categories: challenges due to the in-process nature of MLPBF and challenges due to the spatial and environmental constraints imposed by chamber design. Starting with the former, the in-process nature of MLPBF dictates that the flow of process events (powder deposition, laser melting, etc.) happens both sequentially and rapidly. This poses a challenge to the implementation of a monitoring system that can carry out measurements at a high temporal resolution and exactly when required. In other words, the ability of the multi-sensor system to cope with the MLPBF process is dependent on its data acquisition rates and on the instances at which measurements are triggered in every layer. The machine vision cameras installed in the fringe projection system have an acquisition rate of up to 17 frames/s. Although a higher rate is always desirable, this rate is sufficient to carry out layerwise measurements. Additionally, the fringe projection system has been fitted with an external trigger that continuously acquires signals from

machine modules (the recoating mechanism, platform and laser) and triggers imaging when the bed is clear. The IR and high-speed thermography systems are not concerned with these changes as they acquire continuous data. Other challenges faced during the design phase were mainly related to the environment and space within the build chamber. These included limited space availability, restricted installation locations and risks of laser obstruction and contamination of the optics. Cameras were shielded inside enclosures while the projector was installed on top of the chamber ceiling between the machine wall and the laser galvanometer. However, an issue that persists is that, due to the current placement of the IR camera housing, the IR camera cannot be operated concurrently with the fringe projection system. At present, it is required to uninstall the IR camera while the fringe projection system is imaging. This issue will be addressed in the future, but in the meantime, the IR system can still be used by itself for result validation or for the acquisition of additional in-situ thermal data.

Presently, the multi-view fringe projection system is being assembled and installed on a workbench for testing. While that happens, it is crucial to trace a roadmap to establish data correlations and address the Hard Problem. We will interpret the data acquired from all in-process sensing systems and interrelate powder bed defects with melt pool data for individual layers of the build. When comparing in-situ findings with XCT volume scans, we will classify defects by type, size and distribution. Such qualitative and numerical data will serve to determine thresholds above which defects appear to yield a detrimental effect when the part is mechanically tested. Predictions that pores smaller than a critical size have no effects on mechanical properties and that irregular lack of fusion pores often act as stress concentrators [16], can be verified. In cases where the cause of mechanical failure is not apparent, thresholds indicating the smallest defects that can go undetected by the multi-sensing system will be deduced. To establish meaningful correlations from the entirety of monitoring information and destructive testing, we will address the following questions: at what level does pore formation become a problem? What types/sizes of defects induce failure in a certain geometry? How are failure mechanisms driven by defect populations and distributions? Which defects are less likely to impact yield strength? How does part microstructure change around killer/detrimental defects?

Acknowledgements

The authors would like to acknowledge the support of Imperial College London throughout their partnership in this project, as well as Renishaw plc and the Faculty of Engineering at the University of Nottingham for funding this work.

References

- [1] Williams R, Piglione A, Ronneberg T, Jones C, Pham M, Davies C and Hooper P 2019 In situ thermography for laser powder bed fusion: Effects of layer temperature on porosity, microstructure, and mechanical properties *Addit. Manuf.* **30** 100880
- [2] DebRoy T, Wei H, Zuback J, Mukherjee T, Elmer J, Milewski J, Beese A, Wilson-Heid A, De A and Zhang W 2018 Additive manufacturing of metallic components – Process, structure and properties *Prog. Mater. Sci.* **92** 112–224
- [3] Gouge M and Michaleris P 2018 Chapter 1 - An Introduction to Additive Manufacturing Processes and Their Modeling Challenges *Thermo-Mechanical Modeling of Additive Manufacturing* ed. Butterworth-Heinemann (State College, PA: Elsevier) p 3–18
- [4] Zur Jacobsmühlen J, Achterhold J, Kleszczynski S, Witt G and Merhof D 2019 In situ measurement of part geometries in layer images from laser beam melting processes *Prog. Addit. Manuf.* **4** 155–65
- [5] Mahmoudi M, Ezzat A and Elwany A 2019 Layerwise Anomaly Detection in Laser Powder-Bed Fusion Metal Additive Manufacturing *J. Manuf. Sci. Eng.* **141** 031002
- [6] Forien J, Calta N, DePond P, Guss G, Roehling T and Matthews M 2020 Detecting keyhole pore defects and monitoring process signatures during laser powder bed fusion: A correlation between in situ pyrometry and ex situ X-ray radiography *Addit. Manuf.* **35** 101336
- [7] Jayasinghe S, Paoletti P, Sutcliffe C, Dardis J, Jones N and Green P Automatic Quality Assessments of Laser Powder Bed Fusion Builds from Photodiode Sensor Measurements *Preprints* 2020040055
- [8] Renken V, Von Freyberg A, Schünemann K, Pastors F and Fischer A 2019 In-process closed-loop control for stabilising the melt pool temperature in selective laser melting *Prog. Addit. Manuf.* **4** 411–21
- [9] Okaro I, Jayasinghe S, Sutcliffe C, Black K, Paoletti P and Green P 2019 Automatic fault detection for laser powder-bed fusion using semi-supervised machine learning *Addit. Manuf.* **27** 42–53
- [10] Kalms M, Narita R, Thomy C, Vollertsen F and Bergmann R 2019 New approach to evaluate 3D laser printed parts in powder bed fusion-based additive manufacturing in-line within closed space *Addit. Manuf.* **26** 161–65
- [11] Zhang B, Ziegert J, Farahi F and Davies A In situ surface topography of laser powder bed fusion using fringe projection *Addit. Manuf.* **12** 100–107
- [12] Grasso M, Remani A, Dickins A, Colosimo B and Leach R K 2021 In-situ measurement and monitoring methods for metal powder bed fusion – an updated review *Meas. Sci. Technol.*
- [13] Mani M, Lane B, Donmez M, Feng S and Moylan S 2017 A review on measurement science needs for real-time control of additive manufacturing metal powder bed fusion processes *Int. J. Prod. Res.* **55** 1400–18
- [14] Grasso M, Valsecchi G and Colosimo B 2020 Powder bed irregularity and hot-spot detection in electron beam melting by means of in-situ video imaging *Manuf. Lett.* **24** 47–51
- [15] Khairallah S, Anderson A, Rubenchik A and King W 2016 Laser powder-bed fusion additive manufacturing: Physics of complex melt flow and formation mechanisms of pores, spatter, and denudation zones *Acta Mater* **108** 36–45
- [16] Du Plessis A, Yadroitsava I and Yadroitsev I 2020 Effects of defects on mechanical properties in metal additive manufacturing: A review focusing on X-ray tomography insights *Mater. Des.* **187** 108385
- [17] Dickins A, Widjanarko T, Lawes S, Stavroulakis P and Leach R K 2018 Design of a multi-sensor in-situ inspection system for additive manufacturing *Proc. ASPE/Euspen Advancing Precision in Additive Manufacturing (Berkeley, USA, 22-25 July 2018)*
- [18] Dickins A, Widjanarko T, Sims-Waterhouse D, Thompson A, Lawes S, Senin N and Leach R K 2020 Multi-view fringe projection system for surface topography measurement during metal powder bed fusion *JOSA A* **37** B93–105
- [19] Zhang M, Sun C, Zhang X, Goh P, Wei J, Hardacre D and Li H 2017 Fatigue and fracture behaviour of laser powder bed fusion stainless steel 316L: Influence of processing parameters *Mater. Sci. Eng. A* **703** 251–61
- [20] Hooper P 2018 Melt pool temperature and cooling rates in laser powder bed fusion *Addit. Manuf.* **22** 548–59
- [21] Frazier W 2014 Metal Additive Manufacturing: A Review *J. Mater. Eng. Perform.* **23** 1917–28
- [22] Thompson A, Maskery I and Leach R K 2016 X-ray computed tomography for additive manufacturing: a review *Meas. Sci. Technol.* **27** 072001
- [23] Yadroitsev I, Krakhmalev P, Yadroitsava I and Du Plessis A 2018 Qualification of Ti6Al4V ELI Alloy Produced by Laser Powder Bed Fusion for Biomedical Applications *JOM* **70** 372–77
- [24] Pei C, Shi D, Yuan H and Li H 2019 Assessment of mechanical properties and fatigue performance of a selective laser melted nickel-base superalloy Inconel 718 *Mater. Sci. Eng. A* **759** 278–87

Session 6: Metrology

Direct part density inspection in laser powder bed fusion using eddy current testing

Adriaan B. Spierings¹, Marvin A. Spurek^{1,2}, Marc Lany³, Gilles Santi³, Bernard Revaz³, Konrad Wegener²

¹inspire AG, Innovation Center for Additive Manufacturing (icams), CH-9014 St.Gallen, Fürstenlandstrasse 122, Switzerland

²Swiss Federal Institute of Technology, ETH Zurich, Institute of Machine Tools and Manufacturing, CH-8092 Zurich, Leonhardstrasse 21, Switzerland

³Sensima Inspection SARL, 1196 Gland, 2 Route Cite Ouest, Switzerland

spierings@inspire.ethz.ch

Abstract

The direct qualification of additively manufactured (AM) metal components fabricated by laser powder bed fusion (LPBF), or the certification of the corresponding AM processes, remains a challenge due to the many influencing parameters, and process-inherent variability. Hence, components lack consistent quality regarding dimensional accuracy, surface quality, and material integrity, since internal defects such as pores and cracks are typical characteristics of such components. Different sensing technologies such as melt-pool monitoring are considered for in-process material integrity assessment, and for process control. However, although melt-pool monitoring provides process related information on the laser-material interaction such as melt-pool temperature and size, it does only indirectly provide sufficient information on the quality and integrity of the layer-wise generated material. Eddy current testing (ECT) is a well-established NDT technique for part quality inspection in many industries, and specifically suited to detect near-surface material defects such as e.g. cracks. This characteristic makes ECT a promising monitoring technology for the layer-wise monitoring of material quality in AM processes. Its integration into a LPBF-machine allows to generate direct material integrity data while the layer-wise acquisition offers potentials to monitor the individual part quality over a full build process, minimizing thereby post-process quality assessment measures. The basic feasibility of an ECT system to directly measure part density demonstrated, using LPBF processed SS316L samples with different densities.

Laser powder bed fusion, Eddy Current, part integrity monitoring

1. Introduction

Additive manufacturing (AM) technologies offer industrially relevant advantages for the tool-less production of highly complex parts directly from CAD data. Thereby, Metal Laser Powder-bed-fusion processes (LPBF/M) as characterized by ISO-17296-2 [1] enable the processing of various metals, such as stainless and hot-work steel [2, 3], Aluminum [4, 5], Titanium [6] and Ni-based materials [7, 8]. Consequently, additively manufactured parts can be used in various industrial applications, such as in the tooling industry [9], lightweight engineering in automotive and aerospace [10], or components for the energy sector such as turbine blades and injection nozzles, next to applications in medical engineering like implants or instruments [10].

However, additive manufacturing technologies such as LPBF-M are still on the threshold to widespread industrial adoption, since the process characteristics limit a fast and cost-efficient qualification of the respective processes, and the corresponding parts. This is related to the fact that AM processes are categorized as master forming technologies where not only the components are manufactured, but also the incorporated material and part properties are generated in-situ with the manufacturing processes. Typically, LPBF-processed materials contain some remaining porosity, including gas porosity, next to other types of defects such as lack-of fusion or even cracks, as described by Brennan et al. [11]. Thereby, material and part properties depend on various input parameters along the process chain, including the powder properties [12-15], the main process parameters [16], build job planning including part orientation and positioning [17, 18] as-well as the readiness of

quality relevant machine components, as described by Wegener and Spierings et al. [19].

For these reasons it is important to develop and implement a comprehensive quality management system along the AM process chain [19]. Such a system needs to be able to in-line acquire information about the material integrity of the processed components. McCann et al. [20] and Wegener et al. [19] provide an overview on the various monitoring technologies that are being investigated in this context. For example, Krauss et al. [21] developed a continuously monitoring system with an off-axis bolometer and a thermal detector to acquire the thermal signature of each layer and to compute a digital twin of the parts produced. Thereby, a simulated thermal diffusivity model serves to gather information about the process stability and the resulting part quality. Furthermore, various melt-pool monitoring technologies have been developed aiming to correlate the melt-pool properties and material integrity of the manufactured components. For example, Clijsters et al. [22] used an optical melt-pool monitoring system and developed routines to generate interpretable process images to estimate the quality of the part. On the other hand, Aminzadeh et al. [23] integrated as a layer-by-layer working system using a high resolution camera to image the scanned part cross-sections to assess the layer quality, and to detect top-layer porosity using a Bayesian classifier. However, defects in the top layer might be re-molten during the processing of subsequent layers, and do not necessarily remain in the components. Rieder et al. [24] demonstrated the feasibility of an ultrasonic probe mounted underneath the build platform to online monitor the AM processes through the build-platform by correlating the signals obtained with porosity generated by process instabilities. The capabilities of this approach however might be limited especially

for the production of complex shaped or fine structures. Furthermore, no information on local, real porosity can be achieved.

Common to most of the existing technologies used for material integrity assessment is the fact that material defects are detected only in an indirect way, by correlating for instance a thermal signature with certain defect types, for which machine learning methods can provide the appropriate computational methods. However, there remains a need for an in-line monitoring technology that provides direct information about the existence of local porosity of a material being processed.

Eddy current testing (ECT) is a standardized non-destructive testing technology as described by ISO-15549 [25]. It is a widely accepted quality inspection technology in industry, for instance to control and certify the quality of electrically conductive parts such as the integrity of metal structures, or turbine components. Thereby, ECT can detect material defect at the surface, or in close proximity to the surface of the components, like pores or cracks as reported by García-Martín [26]. By this, ECT seems to be a promising material integrity monitoring technology also for LPBF processes.

In this study, the suitability of the ECT for material porosity detection is demonstrated. For this purpose, LPBF manufactured specimens are scanned by ECT on a laboratory setup, and the ECT signals are correlated with relative material density. As an outlook, the integration of an ECT system into a commercial LPBF machine is demonstrated. The results underline that ECT is able to provide direct information on local material porosity, and that the proposed monitoring setup does not affect the process productivity. ECT is therefore well suited for industrial AM part quality monitoring.

2. Materials and Methods

2.1. Sample manufacturing

10 cubic SS316L samples with a size of 25 x 30 x 10 mm³ were manufactured using a Concept Laser M2 machine operated at a Nd-YAG laser power P = 180W and with a laser spot size of 105 μm. Each sample was processed with the same layer thickness t_L = 30 μm and hatch distance d = 100 μm, but with different scan speeds v_s = 650, 750, 850, 950, 1000, 1050, 1150, 1250, 1500 and 2000 mm/s to obtain samples at density levels between ≈ 90% and 99.5%. The relative densities of the samples were measured using the Archimedes method as described by Spierings et al. [27].

2.2. Eddy current testing

The samples were EC measured in a laboratory setup allowing a x-y raster scan over the sample area (Figure 1). Linear encoders with a resolution of 0.1 mm were mounted on the axis to map sensor signals and the respective position during the raster scan area, using a pitch of 0.5mm. An eddy current instrument (UPEC Sensima Inspection) connected to a ferrite rod coil sensor with a diameter of 3mm (L = 47 μH) was used. The sensor was operated in bridge configuration at a frequency f = 200 kHz, and the coil impedance was monitored in absolute mode as described by Bowler [28].

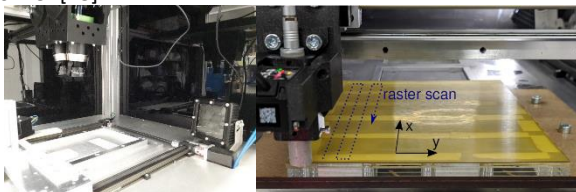


Figure 1. Left: Laboratory test bench. Right: ECT probe mounted on the recoater axis and test samples under an interlayer of 0.5 mm thickness.

Together with the electrical conductivity $\sigma = 1.38 \text{ MSm}^{-1}$ and magnetic permeability $\mu = 1.02$, the standard penetration depth δ is calculated according to equation 1 [26].

$$\delta = \frac{1}{\sqrt{\pi f \sigma \mu_0 \mu_r}} \quad (1)$$

3. Results and discussion

3.1. Material density

Fehler! Verweisquelle konnte nicht gefunden werden. shows the material density for the 10 SS316L cubes, displaying a processing window range. The material defects are caused by lack of fusion and keyhole formation [11].

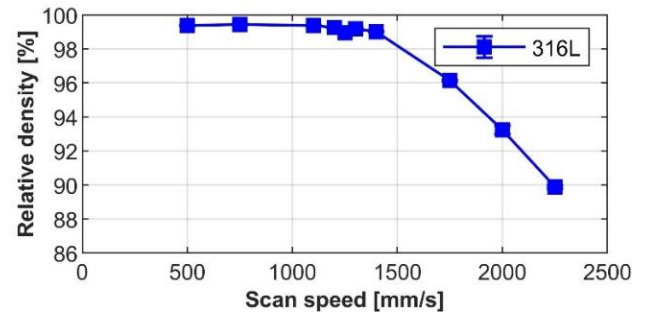


Figure 2. Relative Density of LPBF-manufactured SS316L samples

The Archimedes density, as used for Figure 2, provides only a mean density value over the entire sample volume. This assumption for homogeneously distributed pores over the sample volume is also used for industrial component production where the relative material density is not actively controlled, but the processing window is selected based on statistically validated experiments prior and in parallel to production.

3.2. Eddy current testing

Figure 3 shows the results of the ECT raster scans over the samples. Small variances in the EC sensor signals are observed in Figure 3. This indicates a high sensitivity of the ECT system to local density variations within the samples.

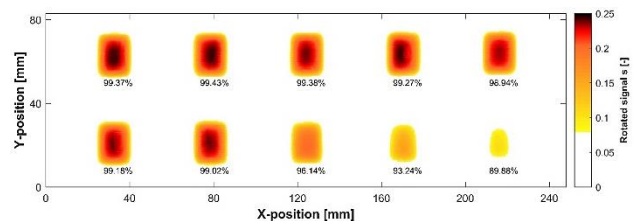


Figure 3. ECT scanning heatmap for the 10 SS316L samples

The samples were only measured by ECT on the top surface. Considering the coil diameter of 3 mm, a penetration depth of the eddy currents $\delta = 945 \mu\text{m}$ and a layer thickness of t_L = 30 μm, it is clear that the ECT signals provide information on the sample porosity over a comparably large local measurement volume. Hence, the current sensor design is mainly suitable for local porosity monitoring, rather than providing information on individual small defects.

Figure 3 also shows an edge effect in the signals, since towards the edge of a sample the eddy currents have to flow differently compared to the situation in the middle of a part. Therefore, only EC sensor signals from the inner region of the parts were used for further analysis. This edge effect could be further minimized by a miniaturization of the EC probe.

Figure 4 shows the correlation between the Archimedes material density measured over the cube samples, and the EC sensor signal. A very high correlation coefficient $r^2 = 0.997$

underlines the suitability of EC sensing for a local density measurement. Even small differences in the relative density in the range of 0.05% can be statistically distinguished, as reported by Spurek et al. [29].

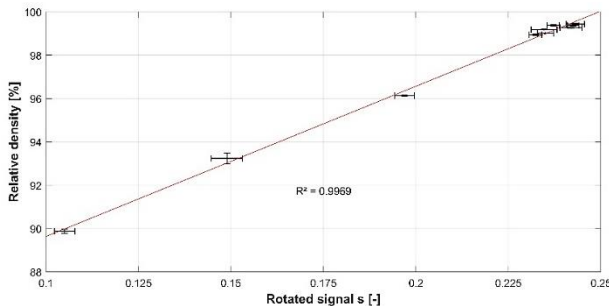


Figure 4. Correlation of relative material density and ECT sensor signal

3.3. Machine integration

To enable in-process part density monitoring the integration of an ECT system into any PBF-LB/M machine is required. Figure 5 shows a further integrated ECT system (“AMIquam”) mounted on the recoater of a commercial machine, with two sensors to be placed at the positions of interest along the y-axis of the recoater. The collected data are sent to an acquisition computer outside of the machine via a wireless communication protocol, to facilitate the machine integratability.

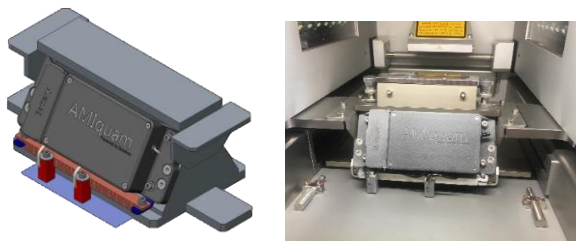


Figure 5. EC scanning system with 2 EC sensors integrated in a commercial LPBF system.

Fehler! Verweisquelle konnte nicht gefunden werden. shows a build job on the aforementioned commercial LPBF machine with four cubic samples that were ECT scanned. The build process was interrupted at certain layers, and then continued.

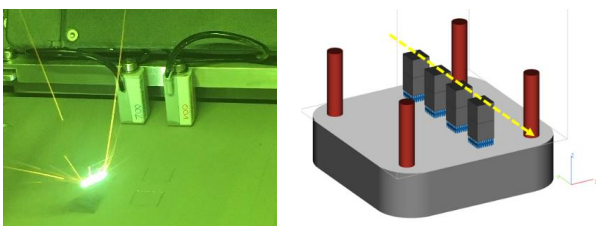


Figure 6. Left: Build process on the commercial PBF-LB/M machine with instrumented AMIquam ECT system. Right: Respective build job design.

Figure 7 shows the ECT signals as acquired over all layers of the 4 parts from the build job shown in Figure 6.

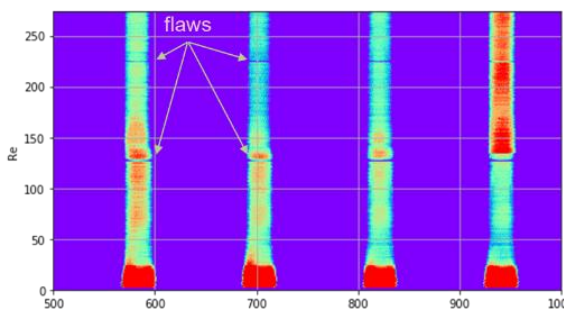


Figure 7. Image of the x-z plane of the parts obtained by ECT.

The indicated flaws represent density variations resulting from process interruptions. The layerwise monitoring of selected sections of interest within a part enables the direct generation of a digital twin of the parts by providing detailed information on real local part density.

4. Conclusions

The measured part of the ECT signal is mainly dependent on electrical conductivity σ of the material. The high coefficient of determination between relative material density ρ and electrical conductivity σ demonstrates the general suitability of the ECT technology to provide information about local porosity in the material. Hence, ECT is suitable for providing a direct path to an in-line part integrity monitoring solution for LPBF processes.

Furthermore, the statistical process control (SPC) on ECT data supports the assessment of the process window stability, and the identification of trends. Such trends in the ECT signals could be related to a drift in the condition of specific machine components, such as the cleanliness of optical components along the laser beam path, the filter system, or a drift in the laser power. A deeper integration of ECT monitoring into the control of a LPBF process and machine will further enable closed feedback loops to control processing windows to adopt for influences e.g. from changing powder properties.

The important advantages of the proposed ECT system are manifold:

- It is a cost efficient monitoring solution when compared e.g. to melt-pool monitoring
- It is an industrially widely adopted NDT technology, which can be easily integrated into commercial LPBF systems without requiring a deeper access to the machine control.
- There is no impact on LPBF process productivity.

Hence, in-process ECT monitoring can support various aspects of process monitoring and control in LPBF. It is therefore considered as an important element in a LPBF quality management system as suggested by Wegener and Spierings [19]. By that ECT is considered as an important solution to simplify process qualification and component certification and thereby to reduce related costs.

References

1. ISO-17296-2, 2020. p. 8.
2. Averyanova, M. and P. Bertrand. in *Int. Conference on Advanced Research in Virtual and Rapid Prototyping*. 2010. Leiria, Portugal: CRC Press / Balkema.
3. Spierings, A.B., et al. in *Virtual and Rapid Manufacturing: Advanced Research in Virtual and Rapid Prototyping*. 2011. Leira, Portugal: CRC Press, Taylor & Francis, London.
4. Berkau, A. in *16. Anwenderforum Rapid Product Development*. 2011. Stuttgart: citim GmbH.
5. Buchbinder, D., et al., 2014, *Journal of Laser Applications*, **26**(1).
6. Murr, L.E., et al., 2009, *Journal of the Mechanical Behavior of Biomedical Materials*, **2**(1): p. 20-32.
7. Rickenbacher, L., et al., 2013, *Rapid Prototyping Journal*, **19**(4): p. 282 - 290.
8. Mumtaz, K.A. and N. Hopkinson, 2009, *Rapid Prototyping Journal*, **15**(2): p. 96-103.
9. Reggiani, B. and L. Donati, 2018, in *Light Metal Age*. South San Francisco, CA. p. 10-17.
10. Suresh, G., K.L. Narayana, and M.K. Mallik, 2017, *Additive Manufacturing*, **9**(14): p. 745-755.

11. Brennan, M.C., J.S. Keist, and T.A. Palmer, 2021, *Journal of Materials Engineering and Performance*, **30**(7): p. 4808-4818.
12. Brika, S.E., et al., 2020, *Additive Manufacturing*, **31**: p. 100929.
13. Riener, K., et al., 2020, *Additive Manufacturing*, **101286**.
14. Spurek, M.A., et al., 2020, *Additive Manufacturing*, **submitted**.
15. Haferkamp, L., et al., 2021, *Metals* **11**(418): p. 14.
16. Delgado, J., J. Ciurana, and C.A. Rodríguez, 2012, *The International Journal of Advanced Manufacturing Technology*, **60**(5): p. 601-610.
17. Robinson, J., et al., 2018, *Additive Manufacturing*, **23**: p. 13-24.
18. Druzgalski, C.L., et al., 2020, *Additive Manufacturing*, **34**: p. 101169.
19. Wegener, K., et al., 2021, *CIRP Journal of Manufacturing Science and Technology*.
20. McCann, R., et al., 2021, *Additive Manufacturing*: p. 102058.
21. Krauss, H., T. Zeugner, and M.F. Zaeh, 2014, *Physics Procedia*, **56**: p. 64-71.
22. Clijsters, S., et al., 2014, *The International Journal of Advanced Manufacturing Technology*, **75**(5): p. 1089-1101.
23. Aminzadeh, M. and T.R. Kurfess, 2019, *Journal of Intelligent Manufacturing*, **30**(6): p. 2505-2523.
24. Rieder, H., et al., 2016, in *World Conference on Non-Destructive Testing 2016*. Munic, Germany. p. 130002.
25. ISO-15549, 2019, in *Non-destructive testing - Eddy current testing - General principles*. International Organization for Standardization (ISO).
26. García-Martín, J., J. Gómez-Gil, and E. Vázquez-Sánchez, 2011, *Sensors (Basel)*, **11**(3): p. 2525-65.
27. Spierings, A.B. and G. Levy. in *Proceedings of the Annual International Solid Freeform Fabrication Symposium*. 2009. Austin, Texas.
28. Bowler, N., 2019, 1 ed. *Springer Series in Measurement Science and Technology*. New York: Springer-Verlag.
29. Spurek, M.A., et al., 2021, *Metals*, **submitted**.

Analysis of metal powder geometrical characteristics influencing the quality of additively manufactured parts

Filippo Zanini¹, Nicola Buzzacchera¹, Simone Carmignato¹

¹Department of Management and Engineering, University of Padova, Vicenza, Italy

filippo.zanini@unipd.it, simone.carmignato@unipd.it

Abstract

Laser powder bed fusion (LPBF) is increasingly used to produce metal industrial components for high value-added sectors, such as aerospace, automotive and biomedical. However, mechanical and structural properties of LPBF parts are often hindered by the large quality variability, poor geometrical and dimensional accuracy, complex surface texture and low density. The quality of the feedstock material is an important aspect to be taken into account, as it significantly influences such possible issues. In particular, metal powder used in LPBF should have shape and size distribution designed to facilitate good flowability and packing behaviour, so that the final fabricated parts have acceptable density, surface finish and mechanical properties. The powder size and shape can be simultaneously measured from three-dimensional reconstructions obtained by X-ray computed tomography (CT). This work investigates the accuracy of these CT measurements of powder characteristics. X-ray CT is compared with other methods such as laser diffraction and scanning electron microscopy. The influence of powder characteristics evaluated by X-ray CT on the surface texture and density of LPBF parts is also discussed.

Laser powder bed fusion, X-ray computed tomography, metal powder, metrology, quality

1. Introduction

Among additive manufacturing (AM) technologies, laser powder bed fusion (LPBF) is increasingly used to produce metal industrial components for high value-added sectors, such as aerospace, automotive and biomedical [1]. However, mechanical and structural properties of AM parts are often hindered by the large quality variability, poor geometrical and dimensional accuracy, complex surface texture and low density [2]. In order to overcome these quality and performance issues, the major efforts are commonly oriented to the optimization of LPBF process parameters [3]. Another important aspect that is currently receiving increasing attention is the quality of the feedstock material [4,5]. For example, metal powder used in LPBF should have shape and size distribution designed to facilitate good flowability and packing behaviour, so that the final fabricated parts have acceptable density, surface finish and mechanical properties [6]. Two techniques that are used for the evaluation of such powder characteristics are scanning electron microscopy (SEM) and laser diffraction (LD) [7,8], the first being limited to the analysis of bi-dimensional (2D) images and the second limited to evaluate only the size distribution. X-ray computed tomography (CT) is a valid alternative that is currently under investigation for the powder characterization as it enables the measurement of both powder size and shape based on a three-dimensional (3D) reconstruction of powder particles [9]. This paper is part of a wider work aimed at enhancing the accuracy of CT metal powder measurements. In particular, X-ray CT measurements are compared here with characterizations obtained by the other methods. The possibility of using CT measurements of powder size and shape to effectively study the relationship of such powder characteristics with density and

surface texture of LPBF fabricated parts is also discussed as future development of this research.

2. Materials and methods

This section presents the metal powders investigated in this work (Section 2.1) and the instruments and methodologies used to characterise them (Section 2.2).

2.1. Metal powder

Three powder batches of different materials were investigated in this work: Ti6Al4V, CuCrZr, and AlSi10. All batches are composed of powders recycled after being used, but not processed, in laser powder bed fusion process. The reasons behind the choice of analysing recovery materials are: (i) the importance of recycling for sustainable manufacturing [10], (ii) recycled powder allows reducing process-related costs and (iii) recycled powder is typically characterized by particles with more complex morphology with respect to newly-produced powder [11], with possible effects on the microstructure and mechanical behaviour of products [12]. This latter aspect is relevant for this work, because the measurement of particles with complex morphology is not trivial. For example, laser diffraction technique is limited to the evaluation of particle size distribution but does not give outcomes on particles shapes, and image analyses (e.g. using SEM) are commonly limited to a single side of powder particles, which might lead to results not representative of the actual particle morphology. On the contrary, X-ray CT measurements are potentially capable of obtaining complete geometrical information of powder particles including size and shape, but the measurement accuracy has not been thoroughly investigated so far.

2.2. Powder characterization

The powder batches described in Section 2.1 were characterized using three different methods: X-ray computed tomography, SEM image analysis and laser diffraction.

X-ray CT scans were conducted using a metrological X-ray CT system (Nikon Metrology MCT225; X-Tek Nikon Metrology, UK), equipped with micro-focus X-ray tube (minimum focal spot size equal to 3 μm) and 16-bit flat panel detector composed by 2000 \times 2000 pixels. SEM analyses were performed with a FEI Quanta 400 scanning electron microscope (FEI Company, USA). Laser diffraction was executed with a Malvern Mastersizer 2000 instrument (Malvern Panalytical Ltd, UK).

To compare X-ray CT with SEM image analysis, a number of particles were attached to the top surface of a polymeric pillar, as illustrated in Figure 1a. The diameter of the top circular surface of the pillar was equal to 4 mm. The contained dimensions were designed to enable CT scans of the powder with the maximum achievable resolution [13]. In particular, the upper part of the pillar was CT scanned as schematized in Figure 1b. The pillar was then mounted on the SEM rotary table and powder particles were imaged in two different configurations. In the first configuration (Figure 1c), the table was kept horizontal and the powder was imaged from above; while in the second configuration (Figure 1d), the table was tilted by 60° to image the powder particles from a lateral view.

In order to compare X-ray CT with laser diffraction, a higher number of powder particles were inserted into a thin polymeric cylindrical pipe with external diameter of 4 mm. Also in this case, CT scans could be conducted with the highest achievable resolution.

The CT reconstructions were elaborated through the following steps: (i) local-adaptive surface determination using the analysis and visualization software VGStudio MAX 3.2 (Volume Graphics GmbH, Germany), (ii) binarization based on the determined surface, (iii) watershed algorithm to separate individual particles and (iv) size and shape computation based on volume and surface measurements. The last three steps were performed using the open-source software ImageJ (National Institutes of Health, USA).

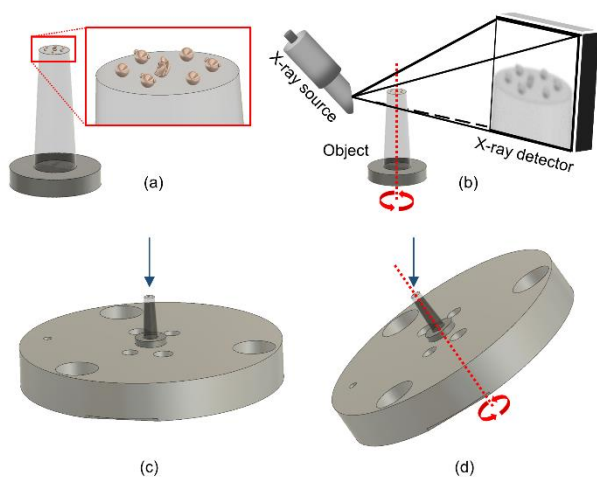


Figure 1. Schematic representations of: (a) powder particles disposed above a polymeric pillar for CT and SEM analyses, (b) CT scanning of powder particles and (c, d) configurations used for SEM analyses. Blue arrows represent the observation direction for both configurations. The top circular surface of the pillar has a diameter of 4 mm.

3. Comparison of characterization methods

This section presents the results obtained by comparing X-ray CT powder characterisation with SEM image analysis (Section 3.1) and with laser diffraction (Section 3.2).

3.1. X-ray CT - SEM

While X-ray CT enables the 3D reconstruction of powder geometry, the comparison with SEM images was performed in 2D, due to the 2D nature of SEM data. In particular, the CT reconstructed powder particles were firstly aligned on the screen according to the SEM point of view and then 2D images were taken. Figure 2 shows the comparison between CT and SEM concerning three particles taken as examples, one for each investigated material. The first one made of Ti6Al4V is spherical, the second one made of CuCrZr is more elongated, and the third one made of AlSi10 has a more intricate shape.

The overall shape of each particle is well represented by CT, even if the resolution is lower than SEM. The smallest details (e.g. the small particles attached to the powder surface) are instead not all visible.

SEM and CT images of a single particle were compared from different points of view, according to the configurations illustrated in Figure 1c and 1d.

Concerning the measurement of the equivalent diameter, percentage deviations below 5 % were found for Ti6Al4V and AlSi10, and below 20 % for CuCrZr.

From these preliminary results, it was observed that dimensional deviations between CT and SEM were in all cases negative. This suggests a possible bias, probably due to the surface determination procedure. Further investigations are ongoing to better understand the cause of the bias and if it can be corrected to improve the accuracy of CT measurement results.

As far as the circularity (chosen here as morphological index) is concerned, deviations below 14 % were found for Ti6Al4V and AlSi10, and below 30 % for CuCrZr. The higher deviations determined for CuCrZr can be due to the higher X-ray attenuation coefficient of this alloy, which leads to more intense image artefacts (e.g. beam hardening and metal artefacts [13]).

Figure 3 shows an example of three different SEM images of the same CuCrZr powder particle taken at three different angles: the image in Figure 3a is acquired from the top (as seen in Figure 1c), while images in Figure 3b and 3c are acquired laterally by tilting the SEM table (similarly to the scheme shown in Figure 1d). It can be observed that, for non-spherical particles, the SEM results are highly dependent from how the particle is positioned on the plane. The computed areas are, in fact, respectively equal to $3.8 \cdot 10^{-4} \text{ mm}^2$, $2.9 \cdot 10^{-4} \text{ mm}^2$ and $2.5 \cdot 10^{-4} \text{ mm}^2$. This confirms that a 3D analysis is to be preferred to better evaluate the actual dimension and shape of powder particles.

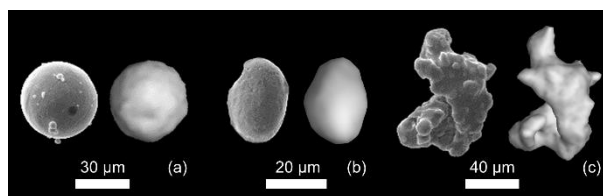


Figure 2. Comparison of SEM images (left) and CT images (right) for three different materials: Ti6Al4V (a), CuCrZr (b) and AlSi10 (c).

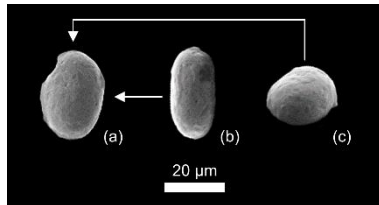


Figure 3. Comparison of SEM images of the same particle taken at different angles: from above (a) and laterally with directions shown by the white arrows (b and c).

3.2. X-ray CT – laser diffraction

Figure 4 shows the cumulative size distribution curves obtained in the case of CuCrZr powders by using both X-ray CT and laser diffraction. In addition, Table 1 reports D10, D50 and D90 values derived from Figure 4. Deviations up to 2.2 µm were found.

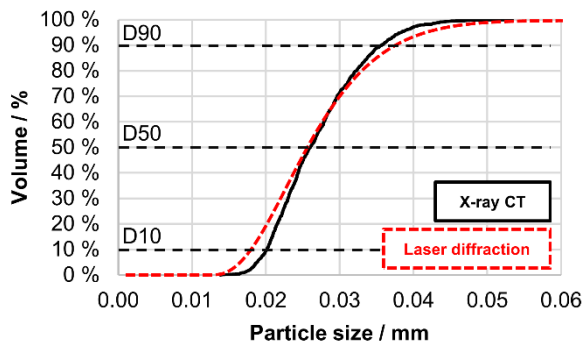


Figure 4. Cumulative size distribution curves obtained with X-ray CT and laser diffraction in the case of CuCrZr powder.

Table 1 D10, D50 and D90 values derived from the cumulative size distribution curves related to X-ray CT and laser diffraction.

	X-ray CT	Laser diffraction
D10 / µm	20.2	18.0
D50 / µm	26.0	25.6
D90 / µm	35.7	37.6

4. Conclusions and future works

This paper was focused on the comparison of CT powder measurements with powder analyses performed by scanning electron microscopy and laser diffraction. Results confirmed that X-ray CT is a promising solution, especially thanks to the possibility of conducting 3D measurements of both size and shape of powder particles, overcoming the limitations of the other investigated methods.

Even if the spatial resolution was not as good as in the SEM images, CT was proved to be capable of obtaining a good representation of the powder morphology. In addition, dimensional deviations were determined to be below 5 % for Ti6AlV and AlSi10, and below 20 % for CuCrZr. Since a bias was found (mean deviations had negative sign), additional investigations are planned to evaluate if the correction of systematic errors is appropriate to reduce deviations and improve measurement accuracy. The comparison with laser diffraction showed a maximum deviation of 2.2 µm, with regard to D10, D50 and D90 values.

Future works will further address the evaluation and improvement of the accuracy of CT metal powder characterisation. In addition, the improved results will be used to map the actual relation between powder geometrical characteristics and the quality of LPBF parts, particularly in terms of surface texture and density. In fact, as observable in the

examples reported in Figure 5, the surface texture as well as the internal porosity – which can be measured non-destructively by X-ray CT – are strongly related to the powder characteristics. For example, the surface profile shown in Figure 5a is characterized by protrusions that have similar shapes and dimensions in the same order of magnitude than metal powder. Moreover, Figure 5b shows typical examples of lack-of-fusion voids, with non-totally melted powder entrapped inside.

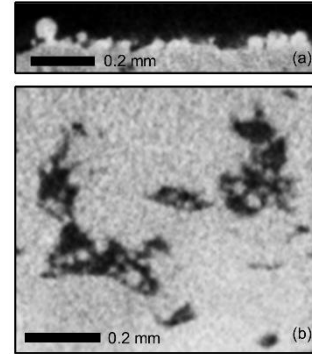


Figure 5. Examples of surface profile (a) and lack-of-fusion pores (b) of a sample fabricated by laser powder bed fusion.

References

- [1] Leach, R., Carmignato, S. (Eds.). (2020). Precision Metal Additive Manufacturing. CRC Press.
- [2] Gibson, I., Rosen, D., Stucker, B., Khorasani, M. (2021). Additive manufacturing technologies. New York: Springer.
- [3] Oliveira, J. P., LaLonde, A. D., Ma, J. (2020). Processing parameters in laser powder bed fusion metal additive manufacturing. Materials Design, 193, 108762.
- [4] Balbaa, M. A., Ghasemi, A., Fereiduni, E., Elbestawi, M. A., Jadhav, S. D., Kruth, J. P. (2021). Role of powder particle size on laser powder bed fusion processability of AlSi10Mg alloy. Additive Manufacturing, 37, 101630.
- [5] Brika, S. E., Letenneur, M., Dion, C. A., Brailovski, V. (2020). Influence of particle morphology and size distribution on the powder flowability and laser powder bed fusion manufacturability of Ti-6Al-4V alloy. Additive Manufacturing, 31, 100929.
- [6] Vock, S., Klöden, B., Kirchner, A., Weißgärber, T., Kieback, B. (2019). Powders for powder bed fusion: a review. Progress in Additive Manufacturing, 1-15.
- [7] Slotwinski, J. A., Garboczi, E. J., Stutzman, P. E., Ferraris, C. F., Watson, S. S., Peltz, M. A. (2014). Characterization of metal powders used for additive manufacturing. Journal of research of the National Institute of Standards and Technology, 119, 460.
- [8] Grubbs, J., Tsakopoulos, K., Massar, C., Young, B., O'Connell, A., Walde, C., ... Cote, D. (2021). Comparison of laser diffraction and image analysis techniques for particle size-shape characterization in additive manufacturing applications. Powder Technology.
- [9] Du Plessis, A., Sperling, P., Beerlink, A., Du Preez, W. B., Le Roux, S. G. (2018). Standard method for microCT-based additive manufacturing quality control 4: Metal powder analysis. MethodsX, 5, 1336-1345.
- [10] Ford, S., Despeisse, M. (2016). Additive manufacturing and sustainability: an exploratory study of the advantages and challenges. Journal of cleaner Production, 137, 1573-1587.
- [11] Mohd Yusuf, S., Choo, E., Gao, N. (2020). Comparison between Virgin and Recycled 316L SS and AlSi10Mg Powders Used for Laser Powder Bed Fusion Additive Manufacturing. Metals, 10(12), 1625.
- [12] Cordova L., Bor T., de Smit M., Carmignato S., Campos M., Tinga T. (2020), Effects of powder reuse on the microstructure and mechanical behaviour of Al–Mg–Sc–Zr alloy processed by laser powder bed fusion (LPBF). Additive Manufacturing, 36, 101625.
- [13] Zanini, F., Carmignato, S. (2017). Two-spheres method for evaluating the metrological structural resolution in dimensional computed tomography. Measurement Science and Technology, 28(11), 114002.
- [14] Carmignato, S., Dewulf, W., Leach, R. (Eds.). (2018). Industrial X-ray computed tomography. Cham: Springer International Publishing.

Comparison of dimensional measurements from images acquired by synchrotron tomography with VGSTUDIO MAX and ImageJ

C. Cayron¹, A. De Soete¹, Y. Gaillard², C. Yardin¹, N. Coutant³, R. Nanjareddy³, P. Bouvet², A.-F. Obaton¹

¹Laboratoire Commun de Métrologie (LCM), Laboratoire National de Métrologie et d'Essais (LNE), 75015 Paris, France

²Centre Technique des Industries de la Fonderie (CTIF), 92318 Sèvres, France

³Volume Graphics (VG) GmbH, 69115 Heidelberg, Germany

charles.cayron@lne.fr

Abstract

Initiated by a working group of the French Confederation for non-destructive testing (NDT) (COFREND), a comparison using an artefact produced by an FA process was conducted between different laboratories. The artefact contained several type of defect inherent to the building process and was scanned by synchrotron radiation.

In this study, the tomographic images of two defects (spherical and cylinder) were analysed with two software: an open source software, ImageJ, (used by CTIF and LNE) and a commercial software, VGSTUDIO MAX (used by VG). For ImageJ software, we have determined the influence of the operator effect in the reproducibility of the measurement for each kind of defect and all size (from 0.3mm to 0.8mm). It appears that operators have a significant part in the reproducibility of the measurement by ImageJ. However, the values of spherical volume and cylinder area obtained by ImageJ are consistent with the values of VGSTUDIO MAX. Unfortunately, the real value of defect (spheres and cylinders) are unknown.

Control, Dimensional, Image

1. Introduction

Thanks to the numerous developments that have been made over the years, additive manufacturing (AM), or 3D printing, currently appears to be the most relevant industrial solution to optimize the production of complex parts, almost impossible to implement by standard manufacturing processes [1]. However, the processes used in AM are still not fully mastered and a significant number of defects, inherent to the manufacturing method, can appear in the parts produced. The laser powder-bed fusion (L-PBF) process is one of the most used process for the manufacturing of metallic parts, especially for the aeronautic or medical fields. In this process, the defects occurring in the parts are layer defects, cross layer defects and the presence of unfused trapped powder [2]. X-ray computed tomography (XCT) is currently the most efficient method to characterize parts produced by additive manufacturing (AM) for its potential to inspect deep internal cavities in complex parts but also internal defects as well as to identify the different types of defects inherent to the used AM processes [3]. To characterize these type of defects, the most widely and efficient method used today is X-ray computed tomography (X-CT), which produces 2D X-ray images of an object from several angles to create a 3D data image by reconstruction. Then to analyse the integrity and perform dimensional measurements of the characterized objects from the images, a specific processing software needs to be used. The objective of this study is to observe the influence of this analysis software on the characterization of defects, resulting from the L-PBF process, between the commercial software VGSTUDIO MAX and the free

software ImageJ. Within the ImageJ software, the study also wanted to determine if the operator processing the data had a significant influence on the value of the measured defect. This article will present first the experimental methodology of the study, then the data processing and finally the comparison between both software for each kind of defect.

2. Experimental protocol

2.1. Standard and software descriptions

Designed within the ISO/TC261-ASTM/F42 AM standardization joint group 59 "NDT for AM parts" and carried out by the French (LNE) and American (NIST) national metrology laboratories, the artefact used, called "Star Artefact", was produced in chrome-cobalt by the L-PBF process (Figure 1). This artefact contained several defects representative of the process and in particular two types of defects that will be studied in this paper: trapped powder in spheres and vertical cylinders (Figure 2). The size of the diameters of the spheres and cylinders varies between 0.2 mm and 0.8 mm. The "star artefact" was scanned with synchrotron radiation at the European Synchrotron Radiation Facility (ESRF) based in Grenoble (France) [4]. In this study, we used two different softwares to analyse spherical and cylinders defect presents in the Star Artefact. The first one is ImageJ, an open source image-processing program designed for scientific multidimensional images. The other software, VGSTUDIO MAX, is a high-end software for analyse and visualisation of computed-tomography data. First, to allow the measurement with ImageJ in the correct coordinate system (as ImageJ was not able to align the volume data from Synchrotron), it was necessary to align it previously with VGSTUDIO MAX.

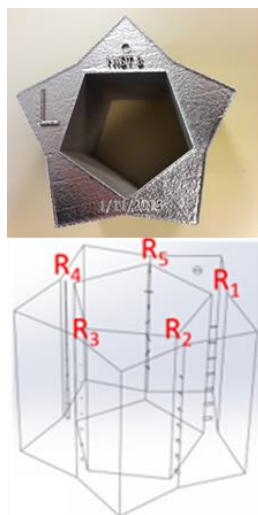


Figure 1. Picture (top) and schematic (bottom) of the star artefact

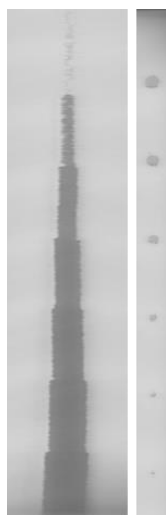


Figure 2. Images of vertical connected cylinders and spheres present in the star artefact

2.2. Measurement protocol for the spheres

ImageJ approach:

The measurement of the volume of the spheres (in number of voxel) is done in several steps determined by the operator. The measurement of the volume of each sphere is realised by calculating the area of the sphere on each 2D image and then summing them over all 2D images (77 2D images in our case). For the step one, the operator selects the sphere to measure and extracts the image volume from the original file. In the step 2, we inverse the colours on each image to determine the area of the sphere. (Figure 3). Then, the operators determines (step 4) the threshold on the lightest shade of grey to optimize the best area (Figure 4). As we can see, the threshold is determined according to the appreciation of each operator, which can affect the value of the measurement. Finally, the exercise being carried out according to the aspect of the sphere on a single view (according to x, y or z), rotations of 90° are performed on the image of the sphere to calculate the volume according to the other axes. Thus, for each sphere, the volume is calculated according to an average value on three different view of the sphere: front view, top view and left view.

The operator repeats all the operations three times in order to determine also the reproducibility of the process.



Figure 3. Spherical view after colour inversion



Figure 4. Spherical view after threshold determination

VGSTUDIO MAX approach: (released version 3.4.5)

The defect analysis procedure consists of two steps:

- Each voxel is checked whether it is part of a defect. Groups of connected defect candidates are created.
- Each group of defect candidates is checked whether it matches the parameters specified by the user. This algorithm identifies voxels as defects based on the actual local grey value of the material in relation to a specified local contrast threshold and can detect defects that are connected to the surrounding

air. Finally, the borders of each defect candidate are locally adapted to the greatest grey value gradient. This approach calculates certain defect properties with *subvoxel* accuracy.

2.3. Measurement protocol for the cylinder

ImageJ approach:

For vertical cylinders characterization, a part of the cylinder was sliced in 119 images and we calculated the area for each slice. To facilitate the operations, an algorithm specific to ImageJ has been set up to take over the systematic operations that do not require a decision from the operator (cylinder positioning, size of the surface, extraction window, etc.). The first step is to, from the image of the aligned cylinders (Figure 2), position the extraction rectangle to select the area of the cylinder that he wishes to characterize (first contribution in operator effect). The algorithm defines rectangle's width in order to have the same number of measurements per operator. Next, the algorithm performs the operations of rotation (in order to see the cylinder from the front), binarize the image in black and white (Figure 5) and offers to the operator a list of filters (Figure 6) that he can use to calculate the area of each cylinder stack of 2D images. Therefore, in step 2, the operator chooses three different filters to apply on the cylinder surface images (second contribution in operator effect). Thus for each cylinder, 119 slices are made and the area is calculated (in number of pixels) for each slice according to three filters. For this part of the study, eight operators participated for measurements. Moreover, to facilitate the analysis of the results, the areas are measured in number of pixels (whose edge measures 23.52 μm).

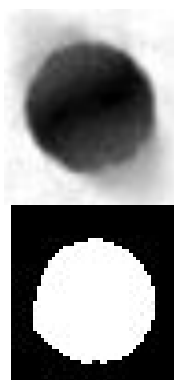


Figure 5. Example of image of the slice of the cylinder before and after applying a filter (here Default filter)

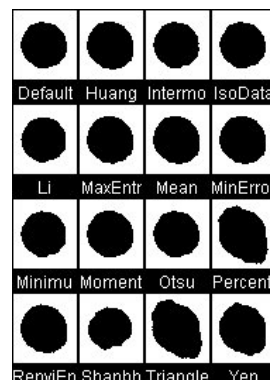


Figure 6. Proposal filters for area determination

VGSTUDIO MAX approach: (released version 3.4.5)

Surface determination including removing of noise particles and scanning artifacts was performed using the Advanced (classic) approach of VGTSTUDIO MAX, leading to a locally adaptive, subvoxel precise surface. This minimizes variance caused by operator influence. The star artefact was then aligned, and 48 regularly spaced Gauss circles were adjusted to the surface for each theoretical diameter. The area was then calculated using the mean diameter of the circles for each theoretical diameter.

3. Data processing

First, we checked the relevance of the data provided by the operators: standard statistical tests were conducted to test the dispersions of the values (Cochran test), the variance of the means (Fisher test) and the study of extreme values (Grubbs test). These tests allowed us to validate the consistency of the measurements made by the different operators, but also to identify the presence of outliers in the data sets of the different

operators. The outliers were then extracted from the data so as not to disturb the variance and mean calculations. In the case of the spheres, 16 values were removed out of a total of 756 values. In the case of cylinders, 4 values out of 48 measurements were not retained.

Nevertheless, the operator remains the main actor in the measurement chain and his different actions can influence the measurement result. One of the questions of this study was therefore to determine and quantify, if necessary, the impact of the operator on the measurement using ImageJ. Indeed, in the case of the measurement of the volume of a sphere, the operator can influence the measurement during the last processing step, when he performs the thresholding step to define the grey area to calculate. The operator defines the level of threshold he wants apply on the stack of images which will defines the final volume of the sphere.

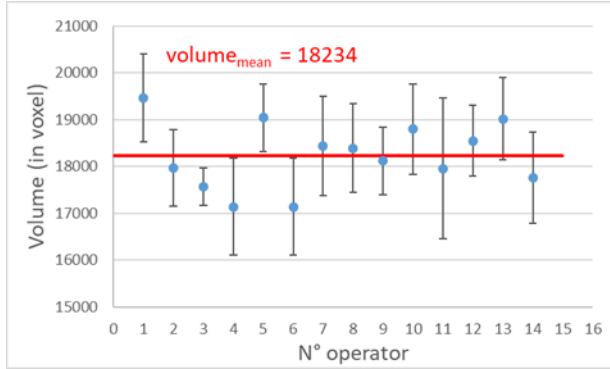


Figure 7 : volume measured by each operator for spherical of 0.8 mm

Figure 7 shows the result of the volume measurements for each operator in the case of the 0.8 mm sphere. The values presented by operator are the average values over the 3 measurements that were made on all the views (for recall top, front and left view). All the measurements show volume values in a range from 17000 voxels to 20000 voxels. From these measurements, we determined the influence of the operator from the following equation:

$$\sigma_{op}^2 = \sigma_R^2 - \sigma_r^2 \quad (1)$$

where σ_r and σ_R are the standard deviation of repeatability and reproducibility, respectively.

The reproducibility of the measurements is determined from the calculation of the variance over all the measurements of all the operators, while the repeatability is calculated from the standard deviations of each operator by the relation:

$$\sigma_r = \sqrt{\frac{\sum_i \sigma_i^2}{N}} \quad (2)$$

where N is the number of operator and $i = 1, \dots, N$

4. Results

For all the measured spheres, we were able to determine the influence of the operator on the measurement error. Table 1 summarizes all the results for spheres from 0.3 mm to 0.8 mm.

We can see from Table 1 that the smaller the theoretical volume of the sphere to be measured, the greater the error in the measurement. Similarly, the impact of the operator on the value of the measured volume is also more important when the size of the sphere is decreasing. Indeed, the smaller the volume of the sphere is, the less the sphere slice contains pixels. Thus, when the operator defines his thresholding level, a small variation of this level will affect more the small volumes than the large volumes. Moreover, due to its manufacturing process, the 0.3 mm sphere is less defined than the 0.8 mm sphere that also affects the quality of the measurement.

Table 1: Results of spherical volumes and operator effect by ImageJ

Theoretical diameter	Measured volume (voxel)	σ_r	σ_R	Operator effect
0.8 mm	18234	939	1122	613
0.7 mm	11696	656	844	532
0.6 mm	7038	547	648	348
0.5 mm	3245	250	342	233
0.4 mm	1208	128	196	148
0.3 mm	353	99	151	114

From these results, we compared the volume measurements made by ImageJ with those made by the VGSTUDIO MAX software that provides 3D volume defect in subvoxel accuracy.

Table 2: Spherical volumes comparison for ImageJ and VGSTUDIO MAX

ImageJ		VGSTUDIO MAX	Relative difference (%)
Measured volume (voxel)	σ_R	Measured volume (voxel)	
18234	1122	18512	-1.50%
11696	844	11895	-1.67%
7038	648	7216	-2.46%
3245	342	3508	-7.51%
1208	196	1319	-8.39%
353	151	331	6.52%

Table 2 shows the results of the sphere volume measurements according to the two software. First, we can see that the values obtained are consistent with each other: the values obtained by VGSTUDIO MAX are always within the standard deviations related to the reproducibility of the measurement by ImageJ. Moreover, we can also note that the larger the sphere, the smaller the relative difference between the measurements of the two software. Indeed, the larger the sphere is, the less the error on the contour of the sphere will have consequences on the result. Finally, it seems that, with the exception of the 0.3 mm sphere, the ImageJ software always overestimates the volume of the sphere compared to the VGSTUDIO MAX software. In the case of the 0.3 mm sphere, this different behaviour may come from the difficulty to measure precisely its volume: the reproducibility of the measurement by ImageJ is equivalent to half the value of its volume.

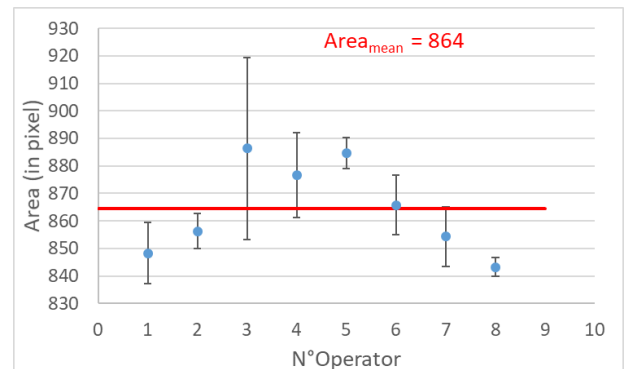


Figure 8 : Surface measured by each operator for cylinder of 0.8 mm

Figure 8 shows the result of the average value of the areas calculated using the set of filters chosen by each operator for the

cylinder of 0.8 mm. The set of measurements shows a mean value of 864 pixels for a data dispersion between 840 pixels and 890 pixels. First analysis on the average shows that operator effect is not on the average value of the area but in the dispersion of values between operator. This dispersion is principally due to the filter used to determinate the area. In fact, we can see that operator 3 has a much larger dispersion between its used filters than operator 8.

This difference can be explained by the difference in filters used: operator 3 used the Minimum, Li, Default filters while operator 8 chose the Default, Mean, Otsu filters. Indeed, each filter has its own convolution method to define the area to be measured, which can therefore give different values: it seems that the combination of some filters, such as Default, Mean, Otsu or Huang, shows very close values of areas while the combination of other filters Li, Minimum and Default gives more dispersive values.

Then for this cylinder (as for all the cylinder), we have applied the Cochran test and it appeared that the operator 3 has an aberrant value of dispersion that should not be consider for the operator effect analyse.

Table 3: Mean area of cylinder slice and operator effect with ImageJ

Theoretical diameter	Area (pixel)	Repetability σ_r (pixel)	Reproducibility σ_R (pixel)	Operator effect (pixel)
0.8 mm	864	17	17	0
0.7 mm	631	19	19	0
0.6 mm	436	11	19	16
0.5 mm	289	8	13	15
0.4 mm	165	6	6	0
0.3 mm	76	8	8	0

Table 3 summarizes all the area values obtained for each cylinder diameter with the values of repeatability, reproducibility and the operator effect. It is noticeable that for four cylinder on six, there is no operator effect (repeatability and reproducibility being equal). This can be explain by the choice of the filter made by each operator: for both cylinder that have an operator effect, operators used principally filter that gave a bigger dispersion of value. Then, for cylinder that has not operator effect, the repeatability take count of the filter influence.

Table 4: Cylinders areas comparison for ImageJ and VGSTUDIO MAX

Theoretical diameter	ImageJ		VGSTUDIO MAX		Relative difference (%)
	Area (pixel)	σ_r (pixel)	Area (pixel)	σ_r (Pixel)	
0,8 mm	864	17	854	1,7	1,2%
0,7 mm	631	19	623	1	1,3%
0,6 mm	436	19	418	1,2	4,2%
0,5 mm	289	13	280	1,2	3,2%
0,4 mm	165	6	160	1,2	3,0%
0,3 mm	76	8	69	1,2	10,5%

Table 4 shows the results of the measurements of the average area of the cylinder slices by the analysis of both software: ImageJ and VGSTUDIO MAX. The repeatability σ_r of VGSTUDIO MAX values are calculated on the 48 Gauss cercles.

The results obtained are consistent with each other: the reproducibility errors of ImageJ values overlap the VGSTUDIO MAX values. As in the case of sphere volume measurements, the areas calculated by ImageJ are systematically greater than those

obtained by VGSTUDIO MAX. The Gaussian approach used in this case should better define the boundaries compared to the one used by ImageJ which is a convolution method of the pixel colors with respect to the neighbours.

5. Conclusions and discussion

In this study, we have seen that in the case of spheres measurements, the operator effect is the main component of the reproducibility. For cylinder measurement, it appears that the choice of the filter is the principal contributor to the reproducibility. We also compared the values obtained by the two software and found that the values obtained were comparable, even if the values obtained by ImageJ are generally higher than those obtained by VGSTUDIO MAX.

To go further in this analysis, it would be interesting, within the framework of the measurement of the cylinders, to better determine the influence of the choice of the filter independently of the selected region. Two possibilities could be envisaged: the first one is to increase the size of the selected region to include nearly all the cylinder (if possible). The second possibility is to study the whole of the filters in order to determine, for the same selected region, all the differences related to them, then to perform once again the comparison of the operators by fixing in the protocol the filters.

Finally, it should be noted that the comparison between these software was not carried out under the best conditions: the data obtained by VGSTUDIO MAX were diameters (in mm) for cylinders while those of ImageJ were surfaces or volumes in number of pixel (respectively voxel). It would therefore be relevant to make a new comparison without having to convert a type of data from one software to another. It would be necessary, after we determine all the influent parameters of the operator effect for ImageJ, to do the same study on a case where real values are known.

Acknowledgement

Authors would like to thanks all the operators of this study and specifically L-F. Lafon, L. Fournet-Fayard, A. Choubib, S-C. Togue-tagne, S. El Ghazouali, Y. Longa, A. Mouillet, I. Mouslime, G. Le Breton, L. Diez-Jahier.

This work has been investigated in the frame of a XCT group of the French Confederation for non-destructive testing (COFREND) leads by L. Gay.

References

- [1] W. Tao, M. C. Leu, "Design of lattice structure for additive manufacturing," Proceedings of ISFA2016, 2016 International Symposium on Flexible Automation, Cleveland, Ohio, U.S.A., 1 - 3 August, 2016
- [2] A-F. Obaton, B. Butsch, S. McDonough, E. Carcreff, N. Laroche, Y. Gaillard, J. Tarr, P. Bouvet, R. Cruz, A. Donmez, "Evaluation of Nondestructive Volumetric Testing Methods for Additively Manufactured Parts. In Structural Integrity of Additive Manufactured Parts", N. Shamsaei, S. Daniewicz, N. Hrabe, S. Beretta, J. Waller, and M. Seifi: West Conshohocken, PA, pp 51–91, 2020, <https://doi.org/10.1520/>
- [3] B. Dutton, W. Vesga, J. Waller, S. James, and M. Seifi, "Metal Additive Manufacturing Defect Formation and Nondestructive Evaluation Detectability," in Structural Integrity of Additive Manufactured Parts, ed. N. Shamsaei, S. Daniewicz, N. Hrabe, S. Beretta, J. Waller, and M. Seifi (West Conshohocken, PA: ASTM International, 2020), 1–50. <https://doi.org/10.1520/STP162020180136>
- [4] A. du Plessis, I. Yadroitsev, I. Yadroitsava, and S. G. Le Roux, 'X-Ray Microcomputed Tomography in Additive Manufacturing: A Review of the Current Technology and Applications', 3D Print. Addit. Manuf., vol. 5, no. 3, pp. 227–247, Jul. 2018, doi: 10.1089/3dp.2018.0060

Quantifying the influence of local porosity on the colour differences of dyed laser sintered polyamide-12 with X-ray CT

S. Bellens¹, M. Janssens¹, T. Craeghs¹, P. Vandewalle², W. Dewulf³

¹Materialise NV, Technologielaan 15, Leuven, Belgium

²EAVISE, PSI, Dept. Of Electrical Engineering (ESAT), KU Leuven, Jan Pieter de Nayerlaan 5, Sint-Katelijne-Waver, Belgium

³Dept. Of Mechanical Engineering, KU Leuven, Celestijnenlaan 300, Heverlee, Belgium

simon.bellens@materialise.be

Abstract

Aesthetic quality requirements for polymer laser sintered parts are becoming stricter to meet the high requirements of end-use applications. For laser sintered parts, several post-processing steps exist to improve the appearance of the parts, including sandblasting, tumbling or colouring. However, local changes in the porosity can influence the absorption of the colour dye and generate undesired colour differences. Test samples with altered build orientations are produced and post-processed by tumbling and colour dyeing. X-ray computed tomography is used to quantify the open and sub-surface porosity of the samples. The colour of the test samples is measured with an RGB colour camera. Device-dependent RGB values are converted to device-independent colour spaces (CIEXYZ and CIELAB), using a target-based colour characterization. Local ΔE^* colour differences are calculated and aligned with 2D porosity maps of the open and sub-surface porosity. A strong correlation between the open pore volume and colour differences on the samples was observed.

Laser Sintering; Colour differences; Polyamide-12; X-ray Computed Tomography

1. Introduction

Polymer Laser Sintering (LS) is a versatile and flexible additive manufacturing (AM) technology to produce end-use functional parts. While the number of end-use applications is increasing, there still remain quality aspects that have to be addressed [1,2]. For end-use applications, the aesthetic quality requirements cannot be omitted and are becoming of equal importance as dimensional accuracy and material properties. Several post-processing steps exist, including sandblasting, tumbling, colouring or a combination of the previous, to improve the appearance of a part. For laser sintered parts, one can easily alter the colour of the part with colour dye methods due to the inherent porosity of the material [3]. Griessbach et al. proposed and patented a non-destructive immersion quality control procedure for LS PA12 parts [4]. The authors showed a strong correlation between the colour saturation and the measured porosity levels for PA12 LS parts. For higher porosity levels a higher colour saturation was observed [4]. However, it is not completely clear how deviations in the open and closed porosities alter the absorption of the materials and generate colour differences in the parts.

Spectrophotometers or colorimeters can easily measure the reflectance curves or colour of parts in a predefined colour space. However, the values represent an average value for a certain region and are difficult to register with the exact location on the parts. To obtain 2D colour information of objects, RGB colour cameras are frequently used [5,6]. The obtained RGB values are device dependent and have to be converted to a device-independent colour space (e.g. CIEXYZ and CIELAB). An in-depth explanation of camera characterization can be found in [7,8].

2. Methodology

To investigate the influence of open and closed porosities on the colour of the parts, ten test samples were printed, post-processed and colour dyed. The orientation of the samples was altered to create differences in the porosity levels near the surface. The test samples were scanned with X-ray computed tomography and analysed with a python script to determine the porosity levels. Thereafter, images of the test samples were obtained with a colour camera to measure the colour of the parts in the CIELAB colour space and to calculate ΔE_{00}^* colour differences. 2D porosity maps of the open and sub-surface pores were created from the XCT data and aligned with the CIELAB images. The same regions of interest were extracted from the 2D colour difference map and 2D porosity maps to study correlation between both.

2.1 Test samples

2.1.1 Production of the test samples

Cuboid samples with a size of 13x13x26 mm³ were built in a state-of-the-art LS machine equipped with the Materialise Control Platform (MCP). PA2200 PA12 powder with a virgin and recycled power ratio of 50/50 was used. The test samples were consecutively rotated around the Z-axis (0 - 22.5 - 45 degrees) and X-axis (0 - 15 - 30 - 45 degrees). Table 1 lists the process parameters of the LS machine.

2.1.2 Post-processing of the test samples

After sand blasting, the test samples were tumbled for 8 hours and ultrasonically cleaned. Thereafter, the samples were colour dyed in a light brown colour with a pot dyeing procedure for 120 minutes. After dyeing, the parts were rinsed with water and

ultrasonically cleaned. Finally, the samples were dried in an oven at 60°C.

Table 1: LS process parameters to produce the test samples

General parameters	Value
Layer thickness	120 μm
Scan strategy	X-Y alternate
Contour parameters	
Laser power	45 W
Scan speed	4000 mm/s
Laser diameter	0,5 mm
Hatching parameters	
Laser power	60 W
Scan speed	6000 mm/s
Laser diameter	0,6 mm

2.2 Porosity measurements

2.2.1 X-ray computed tomography measurements

The test samples were scanned with a Nikon cone-beam computed tomography system. The cuboid samples were only partially scanned to achieve sufficient resolution in the XCT scans. Table 2 shows the settings of the XCT system. The settings were adopted from [2] to achieve a high Signal-to-Noise Ratio (SNR) and Contrast-to-Noise ratio (CNR) in the 3D reconstructions. VG studio MAX 3.4 was used to align the samples and to export regions of interest as 16-bit image stacks. Python code was used to analyse the XCT reconstructions and to calculate the open and closed porosity values.

Table 2: XCT settings to scan the test samples, adopted from [2]

Parameters	Value
Target Material	Molybdenum
X-ray source voltage	110 kV
X-ray source power	14 W
Detector exposure time	1415 ms
X-ray filter	None
Projections	3143
Magnification/Voxel size	18/0.011115 μm

2.2.2 Determine open and sub-surface porosity

The 16-bit grayscale image stacks are imported and processed as 3D arrays. Otsu's global segmentation algorithm was used to segment the 3D reconstruction [9]. Pores represented by less than 8 voxels were removed from the segmentation and assigned as material. The largest connected air region is separated from the pores and is considered as the background of the XCT scan. Thereafter, a 3D binary morphologic closing operation with a ball kernel with a radius of 15 voxels was applied on the segmented volume. The morphologic operation closes the open pores or valleys in the surface and thereby approximates the form of the surface [10]. The peaks or hills of the surface remain unaffected. The overlapping regions of the background and the morphologic closed volume therefore represent the open porosity of the material. Figure 1 shows the four main steps to determine the open porosity level.

Closed pores, connected regions completely encapsulated by the material, with a centre point within 200 μm from the original surface are considered as sub-surface pores. Other pores were excluded during the analysis. 2D porosity maps, inspired by [11], from the open and sub-surface pores were created from the 3D voxel models by counting the number of open or sub-surface voxels, respectively for each column.

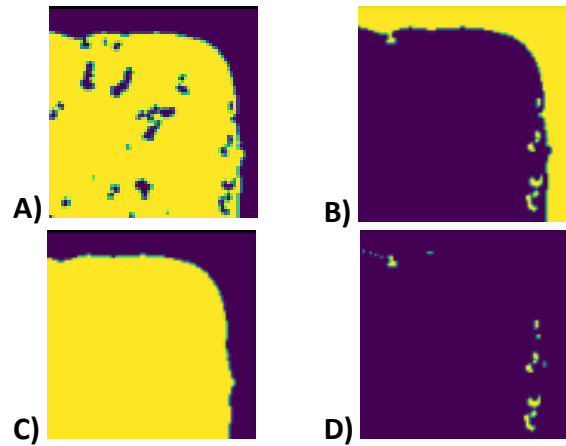


Figure 1: Four main steps to determine the open porosity of the test samples. A) Segmented volume with Otsu's global segmentation algorithm; yellow represents material, purple represent air. B) Background of the XCT (yellow). C) Morphologically closed volume. D) Open pores in the material, defined as the intersection between the background (B) and the morphologically closed volume (C). Note that air regions can be completely encapsulated in the 2D representation but are connected with the background in 3D.

2.3 Colour measurements

2.3.1 Camera setup

A Basler acA5472-17uc 20 MP camera, equipped with a Fujinon CF25ZA-1S lens with a fixed focal length of 25 mm, was positioned in a basic light booth (byko-spectra basic from BYK, see Figure 2). The output of the camera system are RGB images without white-balance correction or post-processing. The camera aperture and exposure time were set to achieve sufficient depth of view and avoid pixel saturation. Throughout the experiments, the D65 light source from the light cabin was used. The camera setup was positioned in a temperature (20 $^{\circ}\text{C} \pm 0,5$ $^{\circ}\text{C}$) and relative humidity controlled metrology lab. To avoid the influence of surrounding light, the lights in the room are turned off during the acquisition of the images and no windows were present in the room. Before each measurement, the camera and lights were turned on for at least 60 minutes to reach a stable working condition.



Figure 2: RGB colour camera mounted in a BYK light cabin

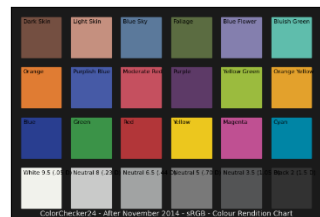


Figure 3: Render of a Macbeth ColorChecker chart (Classic X-rite chart)

2.3.2 Geometric calibration and distortion correction

To perform a geometric calibration of the camera system a checkerboard pattern with 12 by 13 square patches and a patch size of 4 mm was used. OpenCV implementations were used to detect the checkerboard corners with subpixel accuracy, perform the camera calibration and remove distortion from the acquired images. Approximately 25 images of the checkerboard were acquired to perform the geometric calibration and distortion correction. For the geometric calibration, a root mean square reprojection error of approximately 0,21 pixels was obtained.

2.3.3 Colour characterization of the camera

A colour characterization of the camera was performed to convert the device dependent RGB values to a device independent colour space (e.g. CIEXYZ). A target-based colour characterization was used to define a mapping between the device-dependent RGB values and device-independent CIEXYZ colour space. A classic X-rite ColorChecker with 24 target patches was used as a reference target and is shown in Figure 3. To compensate for differences in illumination of the target and the parts, a spatial correction was performed as described in [12]. From the spatially corrected image of the X-rite ColorChecker, the RGB values for the target patches were calculated as the average values from a region of interest of 100 by 100 pixels in each colour patch. Before the colour characterization, the linear response of the RGB colour camera was evaluated, using the 6 achromatic patches of the X-rite ColorChecker. A R^2 of at least 0.998 was obtained for each colour channel. Based on the measured RGB values from the camera and the target XYZ values, a mapping is created using the method as proposed by Cheung et al.[8]. The quality of the mapping between RGB and XYZ values was evaluated by calculating ΔE_{00}^* values after converting the obtained XYZ values to the CIELAB values. An average ΔE_{00}^* of 0,56 was obtained. The same conversion is then applied to the RGB images of the parts to obtain CIELAB images.

2.3.4 Alignment procedure colour images and XCT

Images of the parts were captured while the parts were positioned on the checkerboard. The corners of the checkerboard are detected to perform a 4-point perspective transformation on the images and compensate for possible tilt of the samples. Thereafter, the edges of the parts were detected using a canny edge detection algorithm. The distance between the edges was used to rescale the images from the camera images to the voxel size of the XCT scans. Consecutively, the edges of the parts were used align the camera images with the 2D porosity maps of the XCT measurements.

2.3.5 Colour differences

$$\Delta E^* = \sqrt{(\Delta L^*)^2 + (\Delta a^*)^2 + (\Delta b^*)^2} \quad (1)$$

In CIELAB colour space, a colour difference is defined as the Euclidean distance between the coordinates of two points in the colour space (equation 1) [12]. However, the latest definition according to CIEDE2000 was used to calculate the colour differences. The entire formula of the ΔE_{00}^* can be found in [12]. A ΔE_{00}^* value for each pixel in the CIELAB images of the parts was calculated while using the lightest observed colour as a reference. This implies that larger ΔE_{00}^* values belong to darker region in the parts

3. Results and Discussion

3.1 Microscopic images of the cross section

A microscopic image of the cross section was obtained after cutting, embedding and grinding the sample in consecutive steps. From Figure 4, one can observe the limited penetration depth of the colour dye, which is approximately 100 to 150 μm . Therefore, only open pores and sub-surface pores were considered as the main influencing factors to cause colour differences in the parts. For the microscopic images, a darker colour was preferred to obtain sufficient contrast between the colour dye and the material. Note also the large differences in penetration depth of the colour dye.



Figure 4: Cross section of a polymer laser sintered part after tumbling and colour dyeing with a dark green colour. A limited penetration depth of the dye and local deviations in the penetration depth can be observed.

3.2 Qualitative comparison between colour differences and porosity maps

Figure 5 shows a comparison between the calculated colour differences and the open and sub-surface porosity maps for two different sides of sample 1. For Side A, one can observe an increasing colour difference towards the right side of the part. In the porosity maps, one can also observe a slight increase in the open porosity level. While comparing the two sides of the object, larger colour differences and an increase in the open porosity level can be noticed. However, for the sub-surface porosity map the difference between both sides remains relatively small. A higher open porosity value is believed to result in a larger surface area, hence ability of the colour dye to penetrate the material. A higher absorption of the colour dye results in less reflection of the original white colour of the part and results in darker regions. As for Cube 01 no rotation around the X-axis and Z-axis was applied, the colours for both sides were expected to be the same. However, in the toolpath one can observe a larger distance between contour and hatching vectors for Side C. This results in a lower local energy density near the surface of Side C and immediately translates to a local increase in the porosity.

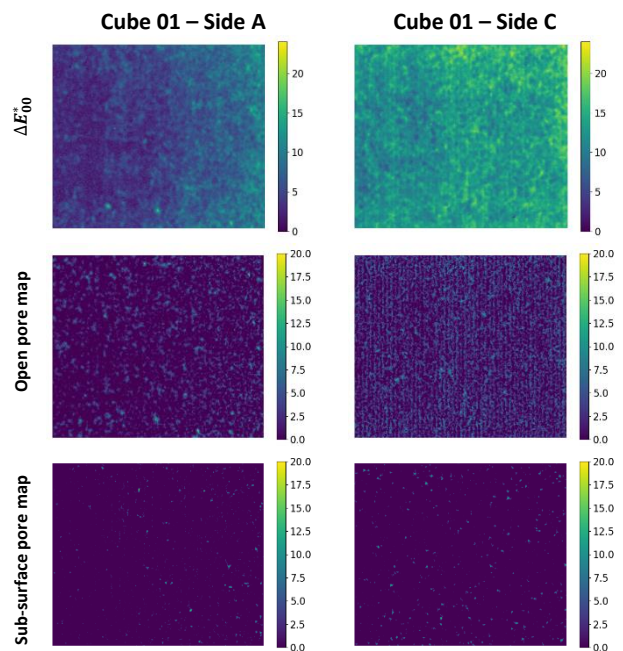


Figure 5: Colour difference maps, open and sub-surface porosity maps for Side A and Side C of Cube 01. Notice the large colour difference and variations in open porosity for both sides.

3.3 Quantitative comparison between colour differences and porosities

Regions of interest were cropped from the ΔE_{00}^* images and the 2D porosity maps of the parts. The average values and standard deviations for the region of interest in the ΔE_{00}^* images were calculated. The open and sub-surface pore volumes from the same region of interest were obtained by counting the number of porosity voxels of each category in the same region of interest and multiplying by the volume of one voxel. Figure 6 shows the average colour difference for 5 regions of interest of 200 by 200 pixels from one side of the 10 cubes against the calculated open pore volume. A clear correlation between both values was observed. A higher open pore volume results in a larger colour difference, hence darker colour of the test sample. This is observed in between the 5 regions for each cube as well in between the different cubes. Figure 7 shows the same colour differences against the sub-surface pore volume. Larger deviations in the porosity levels were observed and a lower correlation with the colour differences was obtained. Table 3 shows the Pearson correlation coefficient between the open and sub-surface pore volumes with different sizes for the regions of interest. A decreasing size of the region of interest results in a lower Pearson correlation coefficient. This is especially the case for sub-surface porosities. However, the Pearson coefficient remains rather high for open porosities which implies that the colour is mainly determined by the open porosity of the material and colour differences are caused by differences in the open porosity of the material.

4. Conclusion

Test samples with altered build orientations were printed, post-processed and colour dyed to create test samples with altered open and sub-surface porosity levels, hence part colour. The open and sub-surface porosity levels of the test samples were determined with X-ray computed tomography measurements and we derived 2D porosity maps of the open and sub-surface porosities. The parts were imaged with an RGB colour camera, which was characterized with a target-based colour characterization to achieve CIELAB images of the parts. The correlation of the open and sub-surface porosities and the colour differences was investigated. A strong correlation between the open porosity and colour differences was observed. A higher local open pore volume results in a higher colour difference, hence darker colour. To reduce or avoid undesired colour differences, the surface of the parts therefore has to be produced in a more consistent or stable way. Next steps can investigate alternative toolpaths and hereby increase the consistency of the local energy density and improve the stability of the open porosities near the surface of the parts.

Table 3: Pearson correlation coefficient calculated for the average colour difference in relation to the open and sub-surface pore volume.

Pearson correlation coefficient (R)	Region of interest size of 200 by 200 pixels	Region of interest size of 50 by 50 pixels
Open porosity	0.967	0.919
Sub-surface porosity	0.803	0.394

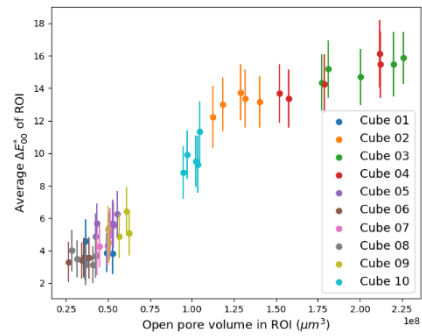


Figure 6: Colour differences for 5 regions of interest (ROI) with a size of 200 by 200 pixels for one side of the 10 cubes plotted against the open pore volume in the same ROI.

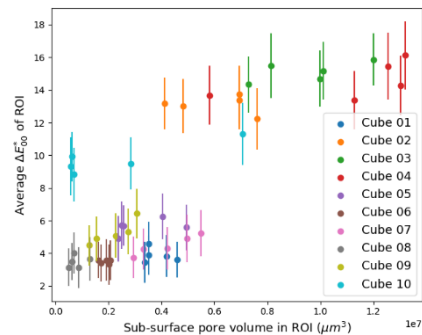


Figure 7: Colour differences for 5 regions of interest (ROI) with a size of 200 by 200 pixels for one side of the 10 cubes plotted against the sub-surface pore volume in the same ROI.

References

- [1] R.D. Goodridge, C.J. Tuck, R.J.M. Hague, Laser sintering of polyamides and other polymers, *Prog. Mater. Sci.* 57 (2012) 229–267.
- [2] M. Pavan, T. Craeghs, J.P. Kruth, W. Dewulf, Investigating the influence of X-ray CT parameters on porosity measurement of laser sintered PA12 parts using a design-of-experiment approach, *Polym. Test.* 66 (2018) 203–212.
- [3] I. Gibson, D. Rosen, B. Stucker, *Additive Manufacturing Technologies*, 2015.
- [4] S. Griessbach, R. Lach, W. Grellmann, Structure-property correlations of laser sintered nylon 12 for dynamic dye testing of plastic parts, *Polym. Test.* 29 (2010) 1026–1030.
- [5] K. León, D. Mery, F. Pedreschi, J. León, Color measurement in L*a*b* units from RGB digital images, *Food Res. Int.* 39 (2006) 1084–1091.
- [6] N.A. Valous, F. Mendoza, D.W. Sun, P. Allen, Colour calibration of a laboratory computer vision system for quality evaluation of pre-sliced hams, *Meat Sci.* 81 (2009) 132–141.
- [7] G.D. Finlayson, M. Mohammadzadeh Darrodi, M. Mackiewicz, The alternating least squares technique for nonuniform intensity color correction, *Color Res. Appl.* 40 (2015) 232–241.
- [8] V. Cheung, S. Westland, D. Connah, C. Ripamonti, A comparative study of the characterisation of colour cameras by means of neural networks and polynomial transforms, *Color. Technol.* 120 (2004) 19–25.
- [9] N. Otsu, A Threshold Selection Method From Gray-Level Histograms., *IEEE Trans Syst Man Cybern.* SMC-9 (1979) 62–66.
- [10] S. Lou, X. Jiang, P.J. Scott, Applications of morphological operations in surface metrology and dimensional metrology, *J. Phys. Conf. Ser.* 483 (2014).
- [11] W. Dewulf, M. Pavan, T. Craeghs, J.P. Kruth, Using X-ray computed tomography to improve the porosity level of polyamide-12 laser sintered parts, *CIRP Ann. - Manuf. Technol.* 65 (2016) 205–208.
- [12] M.A. Kriss, L.W. Macdonald, M.D. Fairchild, *Computational colour science using MATLAB*, 2012.

Characterisation of high speed sintering surface topography with re-entrant open surface pores using 3D surface texture parameters and material ratio curve

S. Lou¹, Z. Zhu², W. Zeng¹, C. Majewski³, P. J. Scott¹, X. Jiang¹

¹EPSRC Future Metrology Hub, University of Huddersfield, Queensgate, Huddersfield, HD1 3DH, UK

²Advanced Forming Research Centre, National Manufacturing Institute Scotland, Renfrewshire, PA4 9LJ, UK

³EPSRC MAPP Future Manufacturing Hub, University of Sheffield, Sheffield, S10 2TN, UK

s.lou@hud.ac.uk

Abstract

High Speed Sintering (HSS) is a polymer powder bed additive manufacturing process for economical volume production of end-use parts. The surface of HSS components often contains 3D features, e.g. re-entrant open surface pores. X-ray computed topography is capable of capturing these features, allowing measurement data to be used for surface texture characterisation. This paper focuses on characterising HSS surface topography based on the newly developed 3D surface texture parameters with a special interest in the re-entrant surface pores. In comparison to the conventional areal counterparts, the 3D surface texture parameters pioneered in this study have been proven to be able to fully characterise re-entrant features, and thus better reflect the 3D nature of HSS surface topography. The selected three 3D height parameters (i.e. Sa, Sq and Sv) and the three 3D hybrid parameters (i.e. Sdq, Sdr and Srf) are useful to quantify re-entrant open surface pores from different perspectives, e.g. variation, depth, gradient, area. The material ratio curves of HSS surfaces vary in their shapes and display recess shapes at the surface heights where the re-entrant pores start to build up. Furthermore, the volume parameter Vvv is utilised to characterise the volume density of open surface pores.

Keywords: Additive manufacturing; high speed sintering; surface topography; open surface pores; X-ray computed tomography; material ratio curve.

1. Introduction

High Speed Sintering (HSS) is a polymer additive manufacturing (AM) process aimed at economical series production of end-use parts. It uses powder as the feedstock material, which is spread onto the powder bed. A layer of the cross-section of the part is formed by jetting the ink onto the area of interest followed by the sintering process using the infrared lamp. The ink rapidly absorbs the thermal energy from the lamp, causing the underlying powder to sinter and solidify. A new layer of powder is then coated and this process continues until the part is fully built.

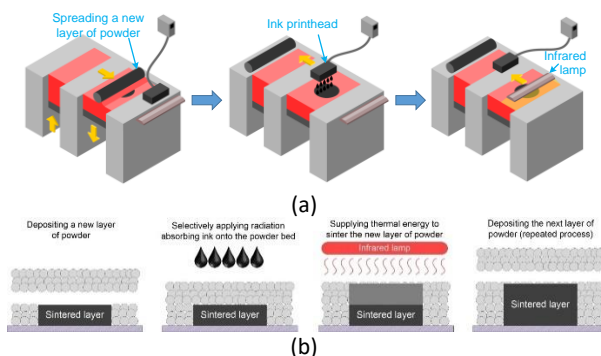


Figure 1. High Speed Sintering process: (a) schematic of the High Speed Sintering process; (b) Detailed view of the sintering process, adapted from [1].

HSS surface topography is three-dimensional in nature, comprised of open surface pores, see Figure 2. These 3D topography feature cannot be measured using conventional

tactile and optical measurement techniques due to the line-of-sight limit, but can be instead captured by X-ray computed tomography (XCT) which has no constraint on surface geometry. The use of XCT for AM surface texture, in recent years, has been a focus of the AM metrology community [2-5], bringing in the advantages that enable not only the capture of 3D topography features, but also the non-destructive measurement of internal surfaces.

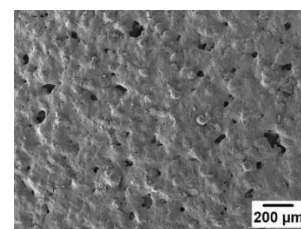


Figure 2. SEM micrographs of HSS surface.

This paper aims to characterise the 3D HSS surface topography measured by XCT. A special interest is dedicated to the re-entrant open surface pores, which are open pores on the surface and the near surface pores with the channels connected to the external surface.

2. Surface roughness, open surface pores relating to HSS process and mechanical properties

AM process and associated process variables have direct impacts on the quality of produced parts, including surface roughness, open surface pores and internal porosity, and the resultant mechanical properties.

In the HSS process, lamp powder and speed, and the ink grey level are the dominant process variables that have a substantial influence the surface quality and porosity of printed components. In principle, a greater amount of energy that is input into and/or absorbed by the part on the powder bed leads to a more complete melting of particles and subsequently particle coalescence and solidification, resulting in reduced voids. Given that the volume of material increases as it is melted from a solid to a liquid state, the melted particles flow outwards, generating a smoother surface. As the layer-by-layer melting process continues, the excess heat dissipates downwards and penetrates through the current layer, whereby the previous layer is remelted. This further closes down the voids between particles, leading to a reduced level of open surface pores on the layer surface. The reduced porosity enhances the bonding strength between particles, as a result, reduces the tendency of crack initiation and propagation between melted particles, which consequently improves mechanical properties of the printed part. A good correlation was found between surface texture parameters (e.g. Sa, Sq, Sv) and the internal porosity as well as the tensile strength [6]. AM's rough surface texture, particularly surface notches, some of which are open surface pores, could lead to a shortened fatigue life [7,8].

3. HSS Samples and 3D Surface Measurement

3.1. HSS samples

Night sets of HSS samples were fabricated using different combination of primary process parameters, i.e. sinter speed, lamp power, and ink grey level. Figure 3 shows a set of the fabricated samples. These samples were used to investigate surface texture, porosity and tensile strength, and an effort was made to correlate these three properties [6].



Figure 3. A set of test samples produced by the HSS process [6].

3.2 HSS sample surfaces measured by XCT

HSS samples developed in [6] were scanned by XCT (Nikon Custom Bay 225/320, voxel size 10 μm , exposure time 500 ms, voltage 100 kV, Otsu surface determination provided by FEI Avizo 9), whereby the 3D surface topographies were extracted. Three sets of samples are employed in this paper. Set 1 indicates the sample produced using industrially established HSS process parameters, while Set 2 and Set 3 are two sets of samples produced from less appropriate parameters i.e. reduced amount of energy input (please note that Set 1, Set 2, and Set 3 in this work are identical to Set 2, Set 6 and Set 7 in [6] respectively). All these surfaces present open surface pores, despite different levels, see Figure 4-6. Table 1 lists their surface roughness Sa measured by the focus variation (FV) microscope and the overall porosity by XCT. Please note that the roughness parameters are the averaged value from five measurements on the top surface of each sample set.

Table 1. Surface roughness and porosity of three sets of HSS samples.

Set No.	Set 1	Set 2	Set 3
Sa (μm)	10.5	16.0	18.6
Sq (μm)	13.9	21.3	24.5
Sv (μm)	84.6	132.2	138.7
Porosity (%)	6.9	15.3	34.5

The surface topography of Set 1 is smooth with only a few visible surface pores, see Figure 4(b). Surface topographies of Set 2 and Set 3 are rougher than that of Set 1. Although Sa of Set 2 and Set 3 measured by FV microscope are close (difference less than 3 μm), their 3D surface topographies show that Set 3 has a much higher density of open surface pores than Set 2, see Figure 5(b) and 6(b).

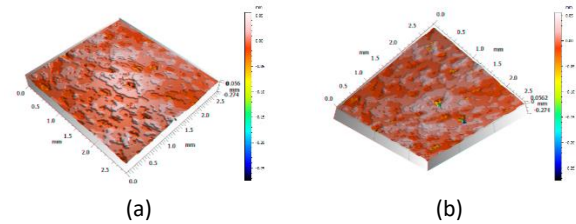


Figure 4. 3D surface topography of Set 1 top surface: (a) top view; (b) bottom view.

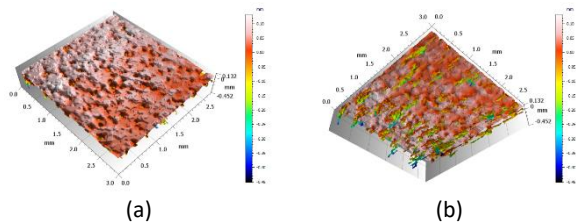


Figure 5. 3D surface topography of Set 2 top surface: (a) top view; (b) bottom view.

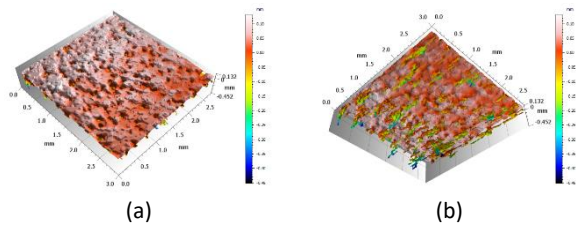


Figure 6. 3D surface topography of Set 3 top surface: (a) top view; (b) bottom view.

4. Use of 3D Surface Texture Parameters and Material Ratio Curve for 3D HSS Surface Characterisation

3D surface texture parameters were recently developed by the University of Huddersfield, which allow XCT measurement data to be used for the assessment of 3D surface topography. The 3D surface parameters include height parameters [9, 10], hybrid parameters [9], volume parameters [11] as well as feature parameters based on 3D watershed segmentation [12, 13]. Different from the traditional areal surface texture parameters calculated on the base of surface height maps, 3D parameters are resulted from the 3D surface topography (usually measured by XCT and presented by triangular mesh). The impact of re-entrant features is considered while calculating these 3D parameters. A sequence of height parameters, hybrid parameters and volume parameters are selected for HSS surface characterisation. Please note that surface filtration is not applied before the computation of 3D parameters. This is to avoid the suppression of topographical features with certain wavelength bandwidths.

4.1. 3D height parameters

Sa (arithmetical mean height) and Sq (root mean square height) are the two most popular height parameters used to represent an overall measure of surface texture. The 3D Sa and Sq are computed by

$$Sa = \frac{1}{A_{form}} \iint_{\Sigma_{form}} |r_{sl}(u, v)| d\sigma_{form}$$

$$Sq = \sqrt{\frac{1}{A_{form}} \iint_{\Sigma_{form}} r_{sl}^2(u, v) d\sigma_{form}}$$

where $r_{sl}(u, v)$ represents the scale limited surface, $d\sigma_{form}$ is the infinitesimal areal element, and A_{form} is the area of the form surface. More details can be referred to [9]. Sv is simply the deepest valley of the measured surface.

Sa, Sq and Sv values of three sets of HSS samples are listed in Table 2. The 3D Sa and Sq take re-entrant features into consideration of their computation. This feature is not possible with the conventional areal counterpart. It, therefore, generates much higher values for the surfaces with a large number of open surface pores, e.g. the Set 2 and Set 3 surfaces. The 3D Sa and Sq of the three sample surfaces also quantitatively reflect the characteristics of the open pore clusters. It is, however, not quite evident from the conventional roughness values in Table 2. It is also interesting to find out that the change trend of 3D Sa and Sq, in comparison to the conventional counterparts, aligns better with the general porosity, see Figure 7. Sv, although based on a single extreme value, could indicate the deepest height of open surface pores of three surfaces.

Table 2. 3D Sa, Sq and Sv of three sets of HSS samples.

Set No.	Set 1	Set 2	Set 3
Sa (μm)	10.4	65.0	114.6
Sq (μm)	14.6	74.1	136.1
Sv (μm)	271.8	487.1	789.0

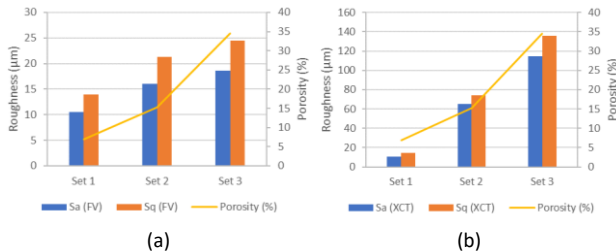


Figure 7. Comparison of the alignment of Surface Texture with Porosity: (a) areal parameters based on FV measurement; (b) 3D parameters based on XCT measurement.

4.2. 3D hybrid parameters

Hybrid parameters incorporates both height and spatial information. Three hybrid parameters Sdq, Sdr and Srf are particularly useful for the characterisation of HSS 3D surface topography.

Sdq is the weighted mean of the squares of the gradient of a function defined on a surface. Please refer to [9] for the details of its computation. A greater Sdq value indicates steeper topographical features.

Sdr indicates the developed interfacial area ratio, representing the ratio of the increased surface area in comparison to the normal form surface. Sdr is computed as:

$$Sdr = \frac{A - A_{form}}{A_{form}}$$

where A is the area of the actual surface and A_{form} is the area of the form surface.

Srf indicates the percentage of the re-entrant features on the form surface and is defined as

$$Srf = \frac{A_{form} - A_{shadow}}{2 \cdot A_{shadow}}$$

where A_{shadow} is the area of the shadow on the form surface.

Table 3 lists the results of three hybrid parameters. The open surface pores have sharp flanks, resulting the Sdq values of Set 2 and Set 3 nearly double of that of Set 1. Sdr reflects the increase of surface area. The Set 3 surface having the largest number of open surface pores results in 131% increment of surface area. In comparison, the Set 1 surface only generates 8.9% surface area increment due to having only a few open surface pores. Srf offers a quantification of the percentage of re-entrant features. The Set 3 surface results in the highest Srf 57%, followed by the Set 2 13%, while the Set 1 surface only generates 0.5%.

Table 3. 3D Sdq, Sdr and Srf of three sets of HSS samples.

Set No.	Set 1	Set 2	Set 3
Sdq	2.4	4.5	4.9
Sdr (%)	8.9	61.3	130.9
Srf (%)	0.5	12.9	57.4

4.3. 3D material ratio curves and volume parameters

The Abbott-Firestone curve is also named as the material ratio curve or bearing area curve. Mathematically it is the cumulative probability density function of the surface profile's height and can be calculated by integrating the profile traces, see Figure 8.

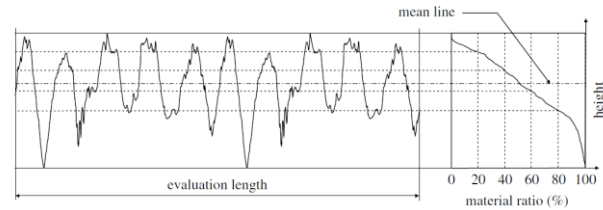


Figure 8. Material ratio curve.

The material ratio curves of the three sample surfaces are illustrated in Figure 9. Recesses are found on the curves of Set 2 and 3 (more significant on Set 3). In the valley zone, the void volume shows big differences among three sets: the curve of Set 1 drops down sharply when approaching to the end, i.e. at the ratio of 98%; Set 2 starts decreasing rapidly at the ratio of 90%; the dramatic drop of Set 3 starts even earlier, at around the ratio of 78%. This indicates that material ratio curve can provide rich information of the development of open surface pores.

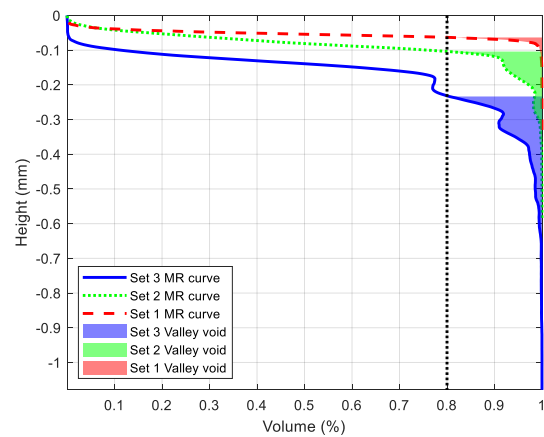


Figure 9. Set Mr2 based on the default value of ISO 25178-2 [14].

The material ratio curve is often divided into three zones, i.e. the peak zone, the core zone, and the valley zone, to match three tribology stage of automotive engineering surfaces, e.g. cylinder liner surfaces, see Figure 10. To adopt this concept into the context of AM, the valley zone is where open surface pores reside. Therefore, it is natural to employ the valley void volume V_{vv} parameter among the volume parameter family, which is used to indicate the void volume per unit area, to characterise open surface pores. ISO 25178-2 [14] assumes that void valley ranges from 80% to 100% of the material ratio. This 80% Mr_2 ratio (used to determine valley void areas), however, is to a large extent proposed based on the experience of automotive industry, and might not be directly applicable to AM. Figure 9 illustrates the valley void areas of three HSS samples. It is evident on the material ratio curve of Set 3 that the surface height corresponding to Mr_2 80% is below the first recess position (-0.2 mm), and thus its valley void area only covers part of open surface pores, leading to an inadequate assessment of these pores.

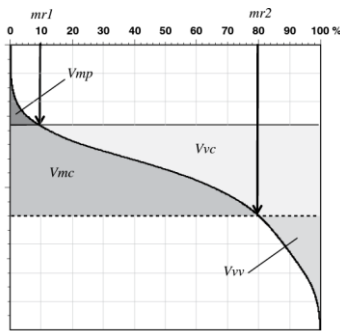


Figure 10. Volume parameters in ISO 25178-2 [15].

To determine a reasonable value of Mr_2 for HSS open surface pores, alternative methods must be explored instead of fixing it to 80%. This complies with the statement that Mr_2 can be set flexibly upon specific application [16]. With a careful observation of 3D surface topography of Set 3, a large portion of open surface pores starts to develop near the surface height on the material ratio curve where it experiences the first dramatic fall. Therefore, setting Mr_2 ratios on the first sharp drop of material ratio curves yields a good covering of open surface pores, see Figure 10. The Mr_2 ratios and their corresponding V_{vv} values of the material ratio curves of HSS surfaces using this approach are listed in Table 4. V_{vv} is a quantitative indicator to reflect the volume density of open surface pores. This parameter is potentially very useful for HSS process optimisation and HSS product performance assessment.

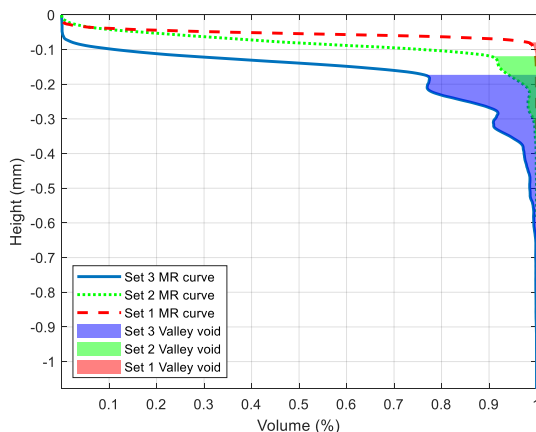


Figure 11. Determination of Mr_2 based on the first sharp drop on the material ratio curve.

Table 4. Mr_2 ratios and V_{vv} values of the HSS material ratio curves.

Set No.	Set 1	Set 2	Set 3
Mr_2 (%)	90.1%	90.2%	77.4%
V_{vv} (mm^3/mm)	2.172×10^{-7}	3.79×10^{-6}	7.491×10^{-5}

5. Conclusion

HSS surface topography is in nature 3D, comprised of re-entrant open surface pores. An advantage of 3D surface texture parameters over the conventional counterpart is the ability to address re-entrant features. The selected 3D height parameters, 3D hybrid parameters and the volume parameter based on the material ratio curve enable the quantitative evaluation of the HSS open surface pores from various perspectives, e.g. variation, depth, gradient, area and volume. This makes 3D surface texture parameters an effective analysis tool to address the 3D nature of HSS surface topography, and thus enables surface texture to better link with HSS process optimisation and product performance evaluation.

Acknowledgements

S. Lou would like to acknowledge the support of the UK's Engineering and Physical Sciences Research Council (EPSRC) via New Investigator Award (EP/S000453/1), and the support of the 3M Buckley Innovation Centre via 3M BIC Fellowship. The authors from the University of Huddersfield gratefully acknowledge EPSRC funding of the Future Advanced Metrology Hub (EP/P006930/1). The authors also thank Digital Surf for providing the MountainsMap software.

References

- [1] O'Connor H J, Dickson A N, Dowling D P 2018 *Addit. Manuf.* **22** 381-387
- [2] Townsend A, Pagani L, Scott P J, Blunt L 2017 *Precis. Eng.* **48** 254-264
- [3] Thompson A, Senin N, Giusca C, and Leach R 2017 *CIRP Ann.* **66** 543-546
- [4] Fox J C, Kim F, Reese Z, Evans C 2018 *ASPE and euspen Summer Topical Meeting-Advancing Precision in Additive Manufacturing*
- [5] Zanini F, Pagani L, Savio E, Carmignato S 2019 *CIRP Ann.* **68** 515-518
- [6] Zhu Z, Lou S, Majewski C 2020 *Addit. Manuf.* **36** p.101402.
- [7] Nasab M H, Romano S, Gastaldi D, Beretta S, Vedani M 2020 *Addit. Manuf.* **34** p.100918
- [8] Du Plessis A, Beretta S. 2020 *Addit. Manuf.* **35** p.101424
- [9] Pagani L, Qi Q, Jiang X, Scott P J 2017 *Measurement* **109** 281-291
- [10] Abdul-Rahman H S, Lou S, Zeng W, Jiang X, Scott P J 2016 *Measurement* **92** 172-182
- [11] Pagani L, Townsend A, Zeng W, Lou S, Blunt L, Jiang X, Scott P J 2019 *Measurement* **141** 442-459
- [12] Lou S, Pagani L, Zeng W, Jiang X, Scott P J 2020 *Precis. Eng.* **63** 177-186
- [13] Lou S, Pagani L, Zeng W, Ghori M U, Jiang X, Scott P J 2019 *Bio-Des. Manuf.* **2** 55-64
- [14] ISO 25178-2 2012 Geometrical product specifications (GPS) — Surface texture: Areal — Part 2: Terms, definitions and surface texture parameters
- [15] Blateyron F 2013 The areal field parameters. In *Characterisation of areal surface texture* 15-43
- [16] Lou S, Zhu Z, Zeng W, Majewski C, Scott P J, Jiang X 2021 *Surf. Topogr-Metrol.* **9** p.015029
- [17] ISO 13565-2 1998 Geometric product specifications (GPS). Surface texture: Profile method. Surfaces having stratified functional properties. Height characterization using the linear material ration curve

Exploratory research on the correlation of probability of detection and image quality during the tomographic characterisation of additive manufacturing defects

M. Sinico^{1,2}, S. Bellens^{1,2,3}, T. van Herreweghen¹, G.M. Probst^{1,2}, W. Dewulf¹

¹Department of Mechanical Engineering, KU Leuven, 3001 Leuven, Belgium

²Member of Flanders Make - Core Lab MaPS, KU Leuven, 3001 Leuven, Belgium

³Materialise NV, 3001 Leuven, Belgium

mirko.sinico@kuleuven.be

Abstract

This contribution reports on exploratory research to streamline the Probability of Detection (PoD) calculation for defect analysis with industrial X-ray Computed Tomography (XCT). Reliable, reproducible and universally applicable PoD information is becoming relevant for all non-destructive testing (NDT) methods, like XCT, where many acquisition parameters can affect the final inspection quality. Especially for complex shaped parts, where XCT is often the only suitable NDT inspection system, the a-priori determination of the inspection limit is paramount to confidently meet the required acceptance levels. In this work, three additively manufactured (AM) metal parts are employed as reference measurands to generate a set of PoD curves, using a binary response, for different XCT acquisition conditions. For this goal, an initial high resolution/quality XCT acquisition was considered as ground truth for measuring the size of the components' internal defects. Subsequently, the image quality of the different CT datasets was evaluated employing a set of quality metrics. The measured strong correlation between the PoD response and the image quality metrics suggests that an estimation of the PoD stemming directly from the quantification of CT image quality is viable and could shorten the XCT PoD assessment.

Computed Tomography, Additive Manufacturing, Probability of Detection, NDT, Image Quality, Porosity Analysis

1. Introduction

Probability of Detection (PoD) is used in various industry sectors to determine the capability of an inspection to detect flaws [1]. A PoD curve can be useful to value a-priori whether the inspection equipment is suitable for the inspection goal, and to estimate the likelihood of detecting a flaw in function of a characteristic parameter (e.g. size). However, PoD determination can be time consuming or even impractical for detection systems where a large number of variables contribute to the final quality of the measurement. For instance, the achievable scan quality of X-ray Computed Tomography (XCT) is influenced by numerous parameters, stemming from the CT system characteristics, the operator's choice of measurement strategy and scan settings, and the workpiece material, geometry and orientation [2]. Therefore, while calculating the PoD can be straightforward for one fixed CT inspection condition (if a ground truth is available for the measurand), this PoD will only be valid for the given set of parameters.

In the effort of gathering reproducible and universally applicable XCT PoD curves, the direct approach becomes the design and implementation of large experimental tests, where all the influencing factors are classified and correlated to the resulting achievable defect detection [3,4]. Another, more recent, approach is the automatic generation of arbitrarily large synthetic data set of realistic CT scans [5]. This data can be employed to train deep learning neural networks for e.g. improved defect segmentation [6], while at the same time it can be used to virtually estimate the PoD of a real CT machine as long as the realism of the simulation is validated. Additionally, the simulation model can be merged with the experimental

results, through e.g. a Bayesian multilevel statistical model [7], with the goal of extending the measurement range while keeping XCT experimental costs low.

Nonetheless, all the aforementioned approaches rely on considerable amounts of data and analysis steps to finally derive a PoD for a specific XCT machine and parameter ranges. Yet, it is well known that defect detection performance can be just reduced as a direct result of the achieved XCT image quality after reconstruction, since image quality directly affects defects measurement [8]. Today, various image quality metrics (IQM) have been developed and implemented in different software packages [9], and can be employed to quantify the amount of noise, blur, perceptual quality, etc. Therefore, if an image can be correctly described with a selected combination of quality metrics, the same quantifiable metrics could be directly correlated to the achievable PoD. Undoubtedly, biases can be introduced, since the correlation will be highly dependent on the IQMs in use which might not describe completely the subtle variations between different XCT images. Nevertheless, achieving such goal would streamline a PoD estimation, enabling PoD assessment directly after XCT inspection. Furthermore, this estimate would be agnostic of the XCT equipment and capabilities, since it relies solely on the image metrics and the used defect detection algorithm/thresholding.

We therefore explore this correlation by experimentally determining PoD curves for three AM objects, employing a fixed 2D porosity analysis method, and subsequently studying how their PoD relate to different IQMs.

2. Materials and methods

Three reference metallic objects produced through the Laser Powder Bed Fusion (LPBF) technique were utilized in this study to assess the Probability of Detection of AM defects for different XCT acquisition parameters. The objects are presented in Figure 1, consisting of a manifold, a turbine and a cooler all fabricated in Ti-6Al-4V. The objects had been manufactured on a bygone LPBF system, and present various AM porosities such as gas, lack of fusion (LOF), and keyholing pores [10]. Each object was first inspected in a Nikon XTH 225ST machine to provide a high resolution, detailed scan of the object's overall dimensions and internal defects. Subsequently, the components were inspected again employing a Nikon XTH 450 machine and a diversified range of inspection parameters considering a Taguchi Orthogonal Array Design of Experiment (OA-DoE). Next, Probability of Detection curves were calculated using the hit and miss method, with a binary analysis that considers the true size of the defect (a) extrapolated from the high quality XCT inspection (i.e. our reference ground truth) against the signal response of the defect, from the inspections performed on the Nikon 450 system. Finally, for each XCT scan, multiple image quality metrics were computed through the MATLAB 2020a Image Processing Toolbox and correlated to the PoD values.



Figure 1. The three LPBF objects which are subjects of this work; from left to right an additively manufactured manifold, turbine and cooler.

2.1. XCT experiment design

Object's preparation prior to the tomographic characterisation consisted in fixing each component on one end of a $\varnothing = 16$ mm Plexiglas tube, where also three reference $\varnothing = 2.5$ mm stainless steel spheres were glued to the tube. The three spheres, together with the object itself, were used to align the different datasets after FDK reconstruction, in the VGSTUDIO MAX 3.4.3 software. The centre-to-centre distance between the spheres was moreover employed to avoid any voxel rescaling error between the distinct acquisitions. Following object's preparation, the ground truth scan on the 225 machine was performed according to the parameters listed in Table 1.

Table 1. XCT acquisition parameters for the 225 GT (ground truth) scan and the latter inspections on the 450 XCT machine.

Parameter	225 GT	450 L5F	450 S5	450 L2	450 S2F
Projections	3142	3142	3142	3142	3142
Magnification	11	5	5	2	2
Voxel size [μm]	18	40	40	100	100
Source spot size [μm]	<6	~80	~80	~80	~80
Exposure time [ms]	4000	2000	1415	2000	1415
Filter	Cu_1mm	Cu_1mm	-	-	Cu_1mm

The subsequent four separate acquisitions per component on the 450 machine were completed following a Taguchi Orthogonal Array design of experiment, where the variables

filter, magnification and exposure time are studied at two levels. The X-ray source current was used as a free variable to adjust the brightness of the X-ray projections. The Taguchi Orthogonal Array design acquisition parameters are also summarized in Table 1. As expected, the inspections acquired with the 450 system resulted in lower quality datasets, considering both the lower spatial resolution achievable in the system, and the employed magnifications. A glimpse on the ground truth image quality compared to 450 data can be appreciated in Figure 2.

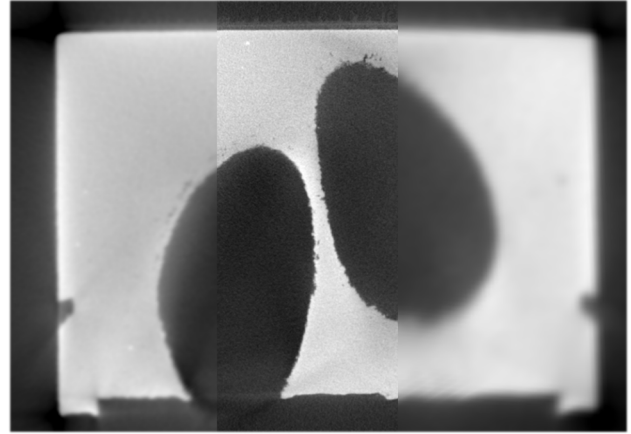


Figure 2. Reconstructed slices of the manifold object; from left to right, 450 S5 image, 225 GT image and 450 S2F image.

2.2. Probability of Detection calculation

In order to compute the PoD curves, every dataset was aligned and exported creating image stacks with a voxel resolution equal to the 225 GT scan (18 μm). Therefore, the image stacks from the 450 acquisitions were exported in interpolation mode, to compensate for the difference in voxel size. Since the subsequent porosity analysis was implemented on the exported 2D images, the interpolation of the 450 data was deemed necessary to accurately compare positions in the 225 GT data to corresponding positions in the 450 data. Next, for each dataset the list of defects was determined with MATLAB using first a global Otsu thresholding, for background removal, and second a local adaptive thresholding together with the function regionprops, for defects identification inside the material.

Subsequently, every defect list was binned considering the average of the defect's major and minor axis lengths (ϕ_{avg}) with a bin size of 9 μm and, for each bin, a binary analysis was performed. The binary analysis considers the original defect found in the 225 GT scan, determines a cut-out region around the defect (adding a safety margin of 3 pixels) and computes a hit or miss response by looking at the same cut-out region in the 450 datasets. This is enough to finally calculate the PoD values; for a bin a with a total bin defect count n_a in the ground truth, all hits and misses are considered as:

$$PoD(\phi_{avg}) = \frac{\sum_{k=1}^{n_a} H_k}{n_a} \text{ where } \begin{cases} H = 1 \text{ if Hit} \\ H = 0 \text{ if Miss} \end{cases}$$

Figure 3 shows the obtained PoD curves for the cooler object.

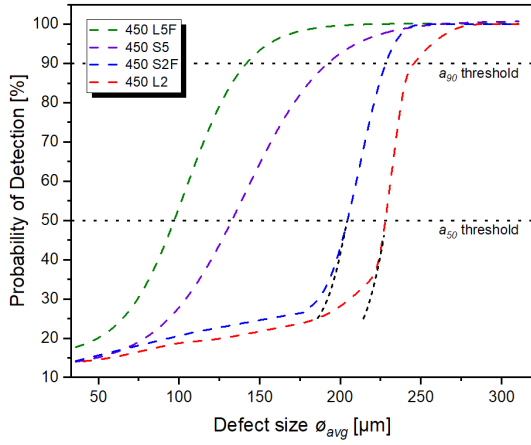


Figure 3. Calculated Probability of Detection curves for the cooler object. The curves are derived as sigmoidal fits over the raw data points.

2.3. Determination of the image quality metrics

From the 12 OA-DoE datasets, 10 % of the images in each image stack were selected randomly to compute the IQMs. All the metrics available in the MATLAB 2020a Image Processing Toolbox were determined [9]; in addition, a blur metric -which reflects what F. Crete et al. proposed in [11]- and the signal-to-noise ratio (SNR) were calculated. In this essay, only the mean-squared error (MSE), the structural similarity index (SSIM), the blind image spatial quality evaluator (BRISQUE) and the blur metric (BM) are discussed. MSE and SSIM are full reference (FR) metrics, whereas BRISQUE and BM are blind or no reference (NR). This is based on whether a reference image is required to calculate the score. For the FR metrics, the reference image was the corresponding image in the 225 GT dataset.

3. Results and discussion

3.1. Probability of Detection

Albeit the goal of this research is not the correlation of the PoD with the employed XCT settings, it is still valuable to briefly comment on the resulting insights. At first sight, looking for example at Figure 3 for the PoD of the cooler object, it is already clear how the magnification plays the major role on the final position of the PoD curve. The use of an X-ray filter and exposure time instead are less significant factors, with the exposure time being statistically non-significant. This of course is valid only for the DoE, objects and XCT machine in play. The statistical response is calculated with a linear regression model (R^2 of 93.1 %), where the PoD from all the objects and XCT measurement conditions is the response and the DoE parameters are the categorical predictors. Their interaction is as well accounted for, and a Pareto chart can be defined as in Figure 4.

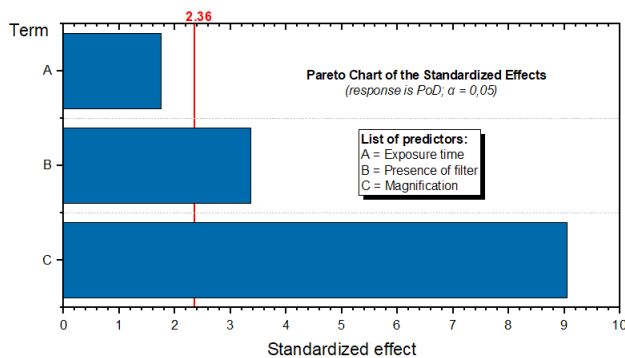


Figure 4. Pareto chart of standardized effects for the regression model calculated over the DoE results; PoD is the response.

It must be pointed out that the PoD curves for low magnification scans present an unexpected declining tail for the low values of PoD (below ~30 %), which is not consisted with the resolution limit and the conventional 'S' shape. The main reason for this behaviour can be traced back to the way the ϕ_{avg} is calculated for each bin size, considering the average of the defect's major and minor axis lengths. For non-spherical, elongated defects, such as cracks or lack of fusion, this method can introduce a bias in the PoD response, since the average of the defect's axes can be low but detectability is still achieved. As a consequence, the PoD is increased in the lower response region. Determining ϕ_{avg} with a different method, like the equivalent diameter, could fix this issue. Another less elegant approach would be performing the sigmoidal fit only in the centre region of the 'S' curve, obtaining more steep lower curves as the black dashed lines in Figure 3.

3.2. Image quality metrics

For exemplification, the IQMs for the manifold object are listed in the following Table 2.

Table 2. Image Quality Metrics for the manifold object.

Manifold datasets	Full reference		No reference	
	MSE·10 ⁻³	SSIM	BRISQUE	BM
450 L5F	1.7	0.81	45.41	0.77
450 S5	7.4	0.79	45.90	0.80
450 S2F	4.1	0.76	58.13	0.93
450 L2	9.4	0.75	64.45	0.93

The general trend of the selected IQMs meets the expectations. The MSE values more the presence or not-presence of the filter, due the difference in between corresponding pixels of the DoE images and the GT images. This effect stems from the introduction of pronounced beam hardening artefact at the edge of the objects in the absence of filtering, and the possible shift in the global grey-values histogram. All the remaining IQMs follow the same trend of the PoD curves, as the scores worsen with decreased magnification or removal of filtering. It is worth stating that the BRISQUE IQM can be as well trained on sets of images with similar distortions as the images to be scored. This could further improve the reliability of the metric; however, for this exploratory research, the standard training LIVE IQA database was employed.

3.3. Correlation between IQM and PoD

Correlation or dependence can be studied by multiple means in statistics. A simple approach which can take into account multiple IQMs is, for instance, the implementation of a multi-criteria decision-making (MCDM) analysis where IQMs are first studied individually and then ranked according to their performance. A final MCDM score normally transfers this ranking to individual weights w_i for each criteria, and subdivides the criteria themselves in benefit or cost criteria.

The use of MCDM can be powerful when the effects to be measured are clearly defined, being for IQMs the single impact of e.g. noise, blur, contrast, luminance, etc. In the case of the four IQMs described in this paper, a combination of their IQMs can be made for each set as:

$$score_{set} = \sum_{i=0}^4 (w_i \cdot IQM_{i,set})$$

Specifically, in this following example, for the MSE metric we defined half the weight w_i (and hence importance) compared to the other IQMs, given the fact that MSE is skewed towards beam hardening ranking, a XCT artefact less troublesome for internal

defect detection. A linear min-max normalization is applied beforehand on the IQMs, to normalize their range between 0 and 1. The final MCDM score for each set can be directly correlated with the PoD response, using different α thresholds. In Figure 5, the dependence of the PoD a_{90} against the IQMs MCDM score can be appreciated.

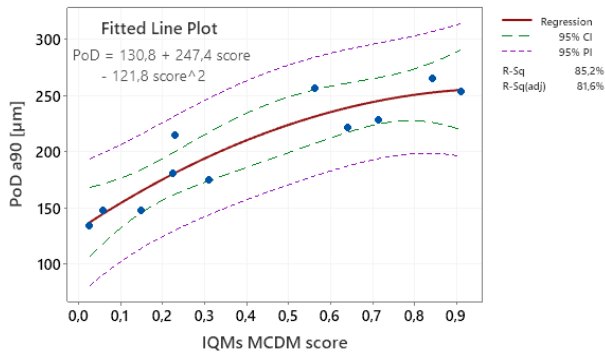


Figure 5. Regression analysis for PoD a_{90} against the IQMs MCDM score.

By all means, this simple MCDM analysis is far from being a usable tool for PoD estimation, since it relies on a small amount of datasets and utilizes only a small selection of IQMs for demonstration. However, the concept is ready to be extended to a more complex correlation analysis.

Besides, this MCDM approach still employs some full reference metrics, which might not be usable without a ground truth. For a more universally applicable correlation model, only NR IQMs should be selected. In the case of the two NR IQMs listed in section 3.2, the correlation with the PoD a_{90} can be visualized with a simple contour plot after a full quadratic response analysis, as in Figure 6.

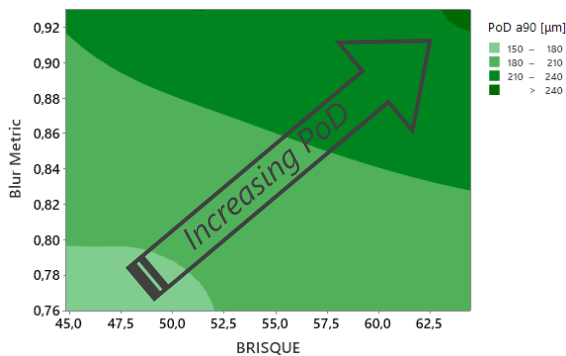


Figure 6. Contour plot of PoD against the BM and BRISQUE NF metrics; obtained R^2 for the full quadratic response analysis is 93.6 %.

Other means of correlation could rely only on a trained BRISQUE model, as described in section 3.2, even if, by employing a single metric, the risk is to lose the capability to later tune or rank your global score on individual image properties. Finally, deep learning algorithm could also be viable, as long as suitable training and validation data is accessible.

The most important take away from this exploratory research is that correlation between PoD and IQMs is possible and, being agnostic of XCT settings and/or machine type, should be applicable in every situation where the user has direct access to the raw image stack after reconstruction.

5. Conclusions

In industrial sectors like aeronautic or aerospace, the availability of Probability of Detection information for the employed NDT inspection systems is paramount. However, the

determination of reliable PoD curves can be extremely time and resource intensive.

In this work, we proposed a novel approach where PoD estimation for industrial X-ray Computed Tomography is disjointed from the XCT settings and/or machine type in use. We suggest the possibility of deriving PoD information through the sole computation of image quality metrics on the reconstructed image stack after CT inspection. To model this correlation, an initial set of PoD curves was calculated for three metal AM objects, while at the same time IQMs were determined for each CT scanning condition. Both full reference (FR) and blind or no reference (NR) metrics were used for the scope. Afterwards, a simple correlation study was performed, connecting the PoD to a global MCDM score which took into account normalized IQMs and weight criteria.

The results of the study confirm the strong dependency of the PoD response with the selected IQMs. The results also suggest how an estimation of the PoD stemming directly from the quantification of blind-NF IQMs is viable, as long as the correlation is initially determined for a larger XCT dataset at different scanning conditions. This larger initial training data would be best determined through calibrated XCT artifacts like the one described in [12]. Finally, the resulting PoD response from IQM data, even if considered as an estimate, could still aid the initial screening of XCT conditions for a proper MIL-1823A [13] compliant PoD determination.

Acknowledgements

This research was funded in the framework of the VLAIO SIM-ICON project ALMA, grant agreement HBC.2018.0427. In addition, Simon Bellens acknowledges the Baekeland mandate grant HBC.2020.2280.

References

- [1] European Commission - Joint Research Centre. *Institute for Energy. Probability of detection curves: statistical best practices*. LU: Publications Office; 2010.
- [2] Carmignato S, Dewulf W, Leach R, editors. *Industrial X-Ray Computed Tomography*. Springer International Publishing; 2018.
- [3] Amrhein S, Rauer M, Kaloudis M. Characterization of Computer Tomography Scanners Using the Probability of Detection Method. *J Nondestruct Eval* 2014;**33**:643–50.
- [4] Kiefel D, Scius-Bertrand M, Stöbel R, GmbH T. Computed Tomography of Additive Manufactured Components in Aeronautic Industry. *8th Conference on Industrial Computed Tomography (iCT) 2018*, 2018, p. 7.
- [5] Fuchs P, Kröger T, Dierig T, Garbe CS. Generating Meaningful Synthetic Ground Truth for Pore Detection in Cast Aluminum Parts. *9th Conference on Industrial Computed Tomography (iCT) 2019*, 2019, p. 10.
- [6] Bellens S, Vandewalle P, Dewulf W. Deep learning based porosity segmentation in X-ray CT measurements of polymer additive manufacturing parts. *Procedia CIRP* 2021;**96**:336–41.
- [7] Kim FH, Pintar A, Obaton A-F, Fox J, Tarr J, Donmez A. Merging experiments and computer simulations in X-ray Computed Tomography probability of detection analysis of additive manufacturing flaws. *NDT & E International* 2021;**119**:102416.
- [8] Pavan M, Craeghs T, Kruth J-P, Dewulf W. Investigating the influence of X-ray CT parameters on porosity measurement of laser sintered PA12 parts using a design-of-experiment approach. *Polymer Testing* 2018;**66**:203–12.
- [9] Image Quality - MATLAB & Simulink - MathWorks Benelux n.d. https://nl.mathworks.com/help/images/image-quality.html?s_tid=CRUX_lftnav (accessed June 27, 2021).
- [10] Sola A, Nouri A. Microstructural porosity in additive manufacturing: The formation and detection of pores in metal parts fabricated by powder bed fusion. *Jnl Adv Manuf & Process* 2019;**1**:10021.
- [11] Crete F, Dolmiere T, Ladret P, Nicolas M. The blur effect: perception and estimation with a new no-reference perceptual blur metric. *Electronic Imaging* 2007, 2007, p. 649201.
- [12] Hermanek P, Carmignato S. Reference object for evaluating the accuracy of porosity measurements by X-ray computed tomography. *Case Studies in Nondestructive Testing and Evaluation* 2016;**6**:122–7.
- [13] Virkkunen I, Koskinen T, Papula S, Sarikka T, Hänninen H. Comparison of a Versus a and Hit/Miss POD-Estimation Methods: A European Viewpoint. *J Nondestruct Eval*; **38**:89.

Poster Session

Surface irregularities of metal SLM part with different surface inclinations and their impact on surface texture characterization

S. Ramadurga Narasimharaju¹, W. Liu¹, W. Zeng¹, T. L. See², P. J. Scott¹, X. Jiang¹, S. Lou¹

¹EPSRC Future Metrology Hub, University of Huddersfield, Queensgate, Huddersfield, UK

²Laser Processing Group, Manufacturing Technology Centre, Ansty Park, Coventry, UK

shubhvardhan.narasimharaju@hud.ac.uk

Abstract

Additive manufacturing (AM) offers numerous advantages like unlimited freedom to design the most complicated parts without expensive support tools and moulds at reduced lead-times. However, AM is not completely established to meet compliance of industrial standards due to intrinsic fabrication process induced rougher surface quality and poor dimensional tolerance especially the inclined and curved AM components. It is paramount to address the evolution of surface irregularities such as the staircase effect, the spatters, the adhered un-melted or partially-melted particles that impart poor surface quality on the inclined and curved metal AM surfaces. Hence, this research is focused on investigating the emergence of surface irregularities and their impact on the resultant surface texture with respect to various surface inclination angles. Focus variation measurement (FVM) method is employed to acquire the surface topography of bespoke metal truncheon artefact produced by SLM with various surface inclinations from 0° to 180°. The areal surface texture characterization and the particle-based feature analysis reveal that there exists a strong intertwining relationship between the resulted surface topographies and the surface inclination angles.

Keywords

Selective laser melting (SLM), surface irregularities, varying surface inclinations, areal surface texture characterization.

1. Introduction

AM is gaining attention among researchers and manufacturers from aerospace, biomedical, automotive industrial fraternity, because light weight cellular and lattice type structures, various medical and dental implants, bionics are manufactured and used in functional applications [1]. In addition to the fabrication of complex light weight parts, a paradigm shift from mass production to mass customization are the new prospective of AM applications [1-3].

Although AM offers countless advantages, poor repeatability, dimensional accuracy and surface quality are the main factors that are limiting the rapid advancement of AM process [4]. It has been noted that surface quality (surface texture) is critical on the part functionality of conventional process, which account for the 10% of part failure rate [5], and it is estimated to be even more in case of AM processes [6]. AM surface quality is influenced by several factors like power of heat source, scan speed, hatch spacing, layer thickness, heat source incidence, part orientation, power size distribution etc. Amongst all layer thickness is a critical parameter responsible to establish the staircase effect particularly on curved and inclined metal AM parts [7,8]. Due to the complex thermophysical layer-by-layer approach of AM processes often induce rougher surface. It turns to be extremely hard to control the surface quality of curved or inclined AM components, which is generally dictated by inevitable surface irregularities such as ripple effect, staircase effect, spatters, un-melted, partially-melted powder particles [9-13]. It is utmost importance to address this prevailing condition pertaining to the surface quality of AM components. Hence, this research is focused to examine the intertwining relationship between the various surface irregularities emerge on the up-skin and down-skin surfaces of the truncheon artefact with different inclination angles.

2. Research methodology

2.1. SLM artefact design and fabrication

Renishaw AM400 SLM machine was used to build truncheon artefact using 316L stainless steel alloy powder. The following SLM parameters were used, laser power 110W, scan speed 5000 mm/s, hatch spacing 110 μm , and layer thickness 50 μm . Artefact design contains 31 square sections (3° increments) with different inclination angles from 0° to 180° (Fig. 1a & 1b). 0°-90° surfaces are defined as the up-skin surfaces, whereas 90°-180° are denoted by the down-skin surfaces.

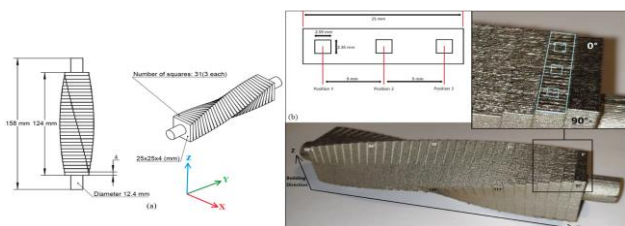


Figure 1. Schematic illustration of (a) Truncheon artefact drawing with dimensions, (b) SLM built artefact with measurement details

2.2. Measurement strategy

Alicona G4 infinite FVM system was employed to measure areal topography of SLM artefact. However, down-skin surfaces measurement was limited to 132°, beyond this all the surface inclinations were severely damaged by the support structures. FVM measurement configurations are: magnification lens 20X, ring light illumination, lateral resolution 1 μm , vertical resolution 0.7 μm , sampling distance 0.878 μm (in both X and Y directions), and measurement size 2.59 x 2.36 mm (stitched).

2.3. Data processing and surface texture characterization

The captured data was analysed using Digital surf MountainsMap software. Fig. 2 shows the procedure of FVM data extraction and processing. The imported data is first processed by filling non-measurement points (NMP) followed by least square levelling. Resulted data is then filtered using the S-filter (nesting index 5 μm) to remove short spatial wavelength components like noise. Similarly, to separate particle features from underlying staircase surface, robust gaussian filter with nesting index 80 μm was applied due to its robustness against outliers [14]. The analysed data is useful to interpret staircase effect and particle features.

The spectrum of ISO 25178-2 areal surface texture parameters adopted to interpret surface topographical features are height parameters, spatial parameters, functional parameters, hybrid parameters, feature parameters, and particles analysis [15] (see Table 1).

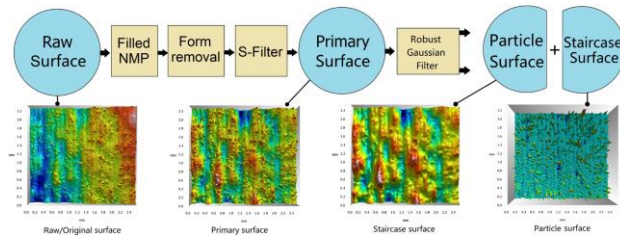


Figure 2. Extraction of primary, staircase and particle surfaces using suitable filters

Table 1 List of areal surface texture parameters explored in this research

Categories	Surface texture parameters
Height Parameters	Sa (μm) -Arithmetical mean height
	Sq (μm) -Root mean square height
	Ssk -Skewness
	Sku -Kurtosis
Hybrid Parameters	Sdq -Root mean square gradient
	Sdr (%) -Developed interfacial area ratio
Functional parameters	Smr1 (%) -Material ratio related to the peak zone
	Vmp (mm^3/mm^2) -Peak material volume
Spatial Parameters	Sal (μm) -Autocorrelation length
	Str -Texture aspect ratio
Feature parameters	Spd ($1/\text{mm}^2$) Density of peaks
Particles analysis	Particles number/density/coverage

2.4 Surface roughness prediction model

A mathematical model based on trigonometric modelling of the staircase effect was adopted [16], to predict the staircase features of SLM truncheon artefact. The roughness based on the trigonometric modelling functions is given by Eq. (1), where 'L' is layer thickness, and ' α ' is inclination angle (with reference to the building surface and edge of the stair-step). Computer-aided design (CAD) software was used to generate the ideal 3D inclined surfaces based on the trigonometric model (see Fig. 3). Selected layer thickness (50 μm) is the same value used while fabricating SLM test artefact. Since the ideal faces 0°–90° and 90°–180° comprise symmetrical features, only 0°–90° range is considered with increments of 3°. Areal surface texture parameters (Sa, Sq, Ssk, Sku, and Sal) values of ideal surfaces are calculated and compared with the actual measurements.

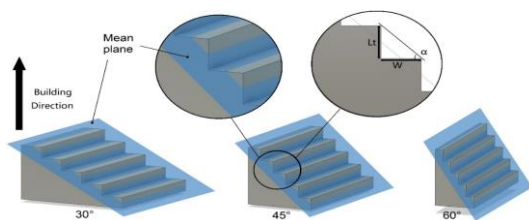


Figure 3. Three-dimensional (3D) representation of the prediction CAD model to illustrate the staircase effect.

$$Ra = \frac{1}{L} \int_0^L |y(x)| dx = \frac{1}{4} L_t \cos(\alpha) \quad (1)$$

3. Results and discussions

3.1 Height parameters

Sa and Sq plots for primary and staircase surfaces demonstrate identical trends for all inclination angles (see Fig. 4 & 5). A higher indeterminacy can be observed at 0°, which could be related to the ripple effect caused by the rapid movement of laser. Rapid increase in surface roughness between 3°–6° is attributed to the staircase effect, which steadily decreased till 45°. Beyond this inclination angle, staircase effect started to disappear and was completely replaced by adhered particles at 90°. An increasing roughness for all down-skin surfaces is clearly evident (~140%), credited to the increased number of adhered particles due to intermittent heat transfer.

A quick change in predicted Sa and Sq from 0°–3° is credited to the transition from a flat surface to a strong staircase induced surface. A constant declining trend thereafter between 3°–90° is attributed to the decreasing strength of the staircase effect. This is followed by an increasing trend after 90° (down-skin surfaces) due to the re-appearance of the staircase effect in opposite direction. Overall, Sa and Sq trends of the measurements for all cases tend to closely follow the theoretical mathematical model.

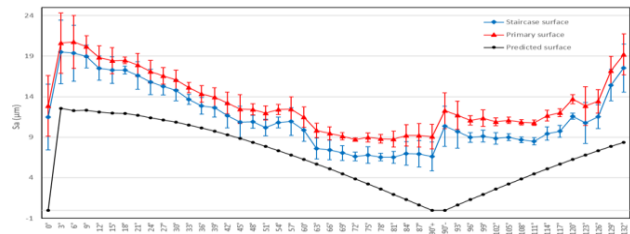


Figure 4. Sa values for predicted, primary and staircase surfaces

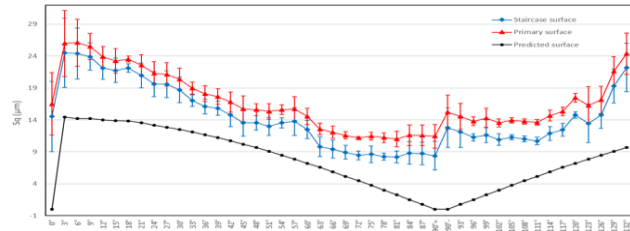


Figure 5. Sq values for predicted, primary and staircase surfaces

The majority of Ssk remained to be positive for all up-skin surfaces, signifying mostly peaks dominates the surface, while the Ssk tend to be unstable for down-skin surfaces, plus negative skew reported at 114°. This is ascribed to the deep valleys and redundant peak features (see Fig. 6). A closer look in to prediction model reveal, the Ssk values are nearly zero, because the number of peaks and valleys is considered to be the same.

Sku values for all surface inclinations tend to be marginally above the nominal value 3, indicating surface height distribution is basically a spiky natured normal distribution (see Fig. 7). Predicted surface displays a Sku value lesser than 3 for all the cases, plus there are no peaks and valleys at 0°, 90°, and 180°; hence, Sku is considered to be infinite in these cases.

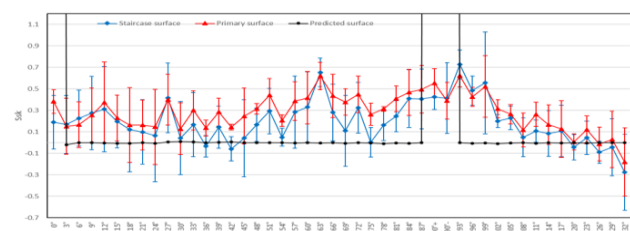


Figure 6. Ssk of predicted, primary and staircase surfaces

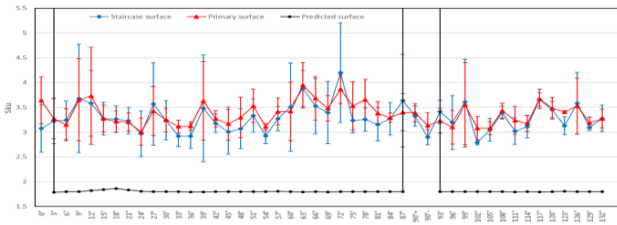


Figure 7. Sdr values for predicted, primary and staircase surfaces

3.2 Spatial parameters

Sal is defined by the shortest autocorrelation length of the new location with respect to the original location. Sal displays an oscillating pattern overall, see Fig. 8. A closer view demonstrates a decreasing trend for the up-skin surfaces, whilst an increasing trend for the down-skin surfaces. This characteristic is consistent with the fact that the width of staircase reduces towards 90°. If the particle features remain on the staircase surface then it can introduce significant turbulence in Sal trend.

Sal for the predicted surface displays a very interesting trend consisting of a sharp steep peak at 3°, and a steady decline to become flat at 90°. Based on the prediction model, Sal decreases with the increase of the inclination angle, which completely aligns with the reduction of the step width illustrated in Fig. 9. The predicted surface at 0° presents a completely flat surface (melt tracks are not taken into consideration); thus, Sal is zero. This is same in the case of 90° (no staircase at all). Sal of the predicted down-skin surface maps the changing trend of the up-skin surface by reflection in terms of 90°.

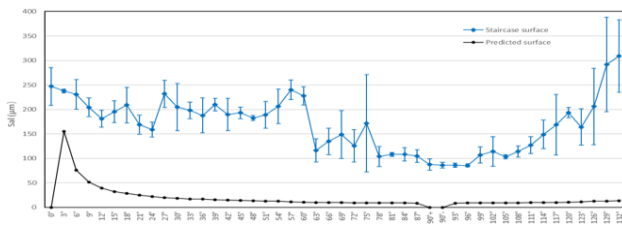


Figure 8. Sal values of predicted surface staircase surface

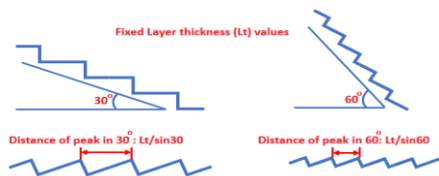


Figure 9. Schematic illustration of change in staircase width

Str (texture aspect ratio) is a measure of uniformity of a surface texture. Str for the particle surface remained almost stable (except between 0° & 27°) with the values approaching to 1; indicating the isotropic nature of particles (see Fig. 10). Str for both the primary and staircase surfaces displayed similar fluctuating trends (like Sal) with the value close to 0 signifying the anisotropic characteristics of these two surfaces. The staircase effect is the main factor that affects Str.

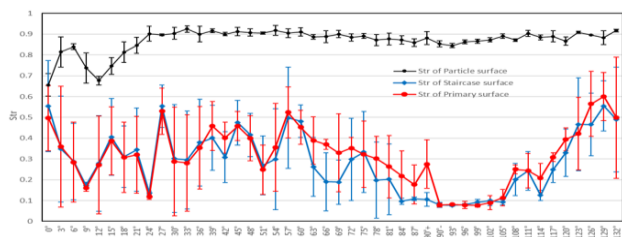


Figure 10. Str of primary, staircase surface and particles surface.

3.3 Hybrid parameters

Sdr is mainly used in surface coating, lubrication and heat exchanger applications, where functional performance is linked to surface area. Sdr results for the primary and staircase surfaces displayed identical trends and the specific values are very close, signifying the staircase effect is less significant (see Fig. 11). Key for Sdr results is the adhered particle features.

Sdq is usually employed to distinguish the surfaces with similar roughness. Sdq results between 0°-90° showed a minor increasing oscillation pattern, whereas the down-skin surfaces exhibit a V-shaped trend. Overall, the changing trend of the up-skin surface Sdq is relatively uniform, whilst the down-skin surface is more turbulent (see Fig. 12).

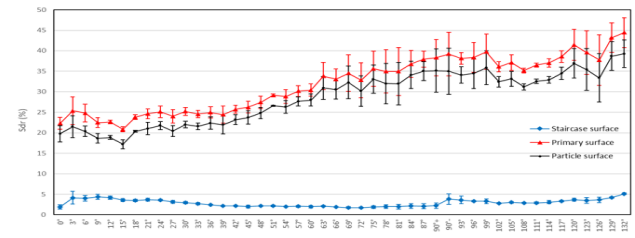


Figure 11. Sdr of primary, staircase surface and particles surface.

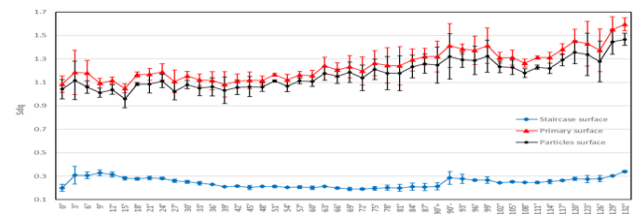


Figure 12. Sdq of primary, staircase surface and particles surface.

3.4 Functional parameters

Functional parameters are developed to characterize the functional characteristics like wear and tribological properties. The peak material volume parameter (Vmp) used to investigate the volume density of particle features. Steady increase in Vmp for all up-skin surfaces is attributed to the increasing adherence of un-melted, partially melted particles onto the edges of the stair steps (see Fig. 13). The down-skin surfaces did not display any interesting fact except irregular changing pattern.

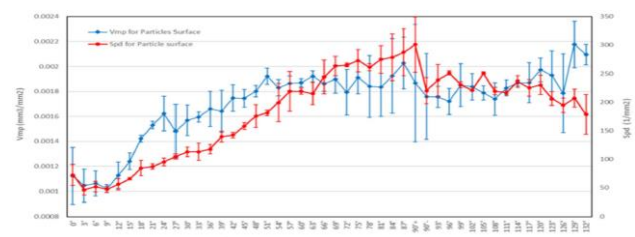


Figure 13. Vmp and Spd of particles surface.

3.5 Feature parameters

Spd, signifying the density of peaks, is based on the watershed segmentation of surface topography with 5% Wolf pruning. Spd and Vmp of particle surface with respect to varying inclination angles is shown in Fig. 13. Spd decreases between 0°-3° which is related to the spatters. Down-skin surface presents a steady decrease of Spd, which forms a certain reflection symmetry to the up-skin surfaces but showing more variations due to the random nature of the down-skin surface topography. By comparing the trend of down-skin surface Spd and Vmp: Spd decreases as the down-skin inclination increases, whereas it is the polar opposite in the case of Vmp. This implies as the down-skin tilt angle increases, the number of large particles or large protrusions on the bottom surface increases.

3.6 Particle analysis

Complimentary to Spd, height threshold segmentation approach is applied to the particle surface (staircase effect has been excluded). The cut-off is set to Smr1 by presuming the peak zone stands for the particle features [17]. The number of particles, the particle coverage, and the particle density are calculated respectively to provide quantitative characterization of particles, which displayed similar trends (see Fig. 14 & 15). These three particle characterization parameters of the up-skin surfaces increased slowly, while those for down-skin surfaces demonstrated a flatter pattern.

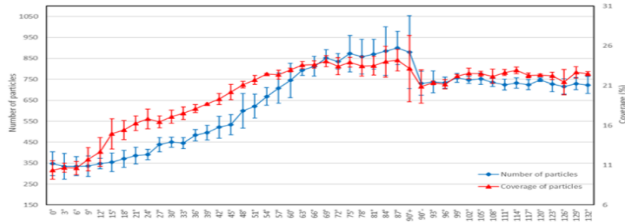


Figure 14. Number of particles, particle coverage of the particle surface

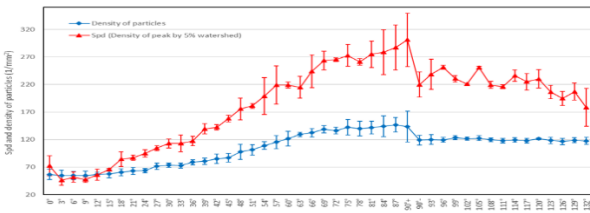


Figure 15. Particle density and Spd of the particle surface

Six examples of features-based particle identification and associated particle coverage ratio and numbers are illustrated in Fig. 16. On the up-skin surface, the number of stair steps increases as the inclination goes up, while the corresponding width of these steps gradually decreases. This causes a rising number of particles to adhere to the edges of the steps. The number of particles and the particle coverage rate on the down-skin surfaces remain relatively steady, which is attributed to the intermittent heat transfer and the gravity effects.

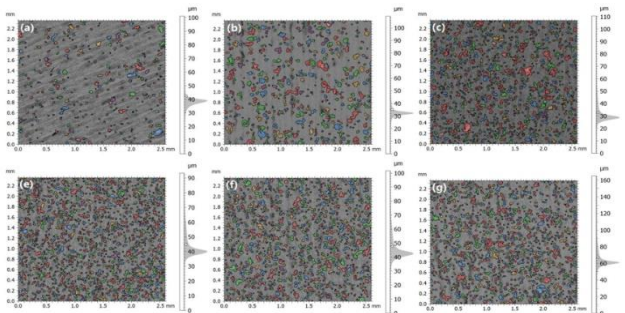


Figure 16. Particles identification for six inclined surfaces: (a) 0 deg, 314 particles, 10.20% coverage; (b) 30 deg, 394 particles;18.34% coverage; (c) 60 deg, 685 particles, 24.36% coverage; (d) 90 deg+, 848 particles, 27.28% coverage; (e) 114 deg, 717 particles,24.65% coverage; and (f) 132 deg, 707 particles, 24.33% coverage

4. Conclusions

The correlation between the various surface irregularities and different build inclination angles of a SLM built artefact was investigated. Appropriate surface texture parameters were used to characterize and quantify the various surface irregularities:

Sa and Sq values of inclined surfaces are mainly governed by the staircase effect, whilst the influence of adhered particles is less significant. Additionally, Sa and Sq of the down-skin surfaces were higher as compared to the up-skin surfaces due to the intermittent heat transfer. Sa and Sq trends for all cases tend to

closely follow the prediction model. Ssk values tend to be mostly positive, signifying the surface is dominated by peak features and displayed similar pattern for up-skin and down-skin surfaces. Recorded Sku was marginally above the nominal value 3, indicating the surface height distribution was basically spiky-natured normal distribution.

Sal is predominantly influenced by the staircase effect; the staircase width decreases with the increase of inclination angle. However, Sal could also be affected by the residue traces of particles on the staircase surface.

Sdr and Sdq of the primary surface and the particle surface displayed strong increasing trend as the inclination angles increased, implying that particle features are responsible for the increase in surface area and general surface slope. The impact of the staircase effect is insignificant.

Vmp (threshold ratio set to Smr1), exhibited strong upward trend with increasing inclination angles, denoting surfaces with higher inclinations showed larger total volume of particles.

Spd for particles surface showed the upward trend for the up-skin surfaces, signifying growth of particle features, whereas down-surfaces displayed an opposite trend.

The particle analysis descriptors of particles surface revealed steady rising trend for the up-skin surfaces, and relatively stable trend for the down-skin surfaces. Overall, the descriptors exhibited consistent trends.

Acknowledgements

S. Lou would like to acknowledge the support of EPSRC via New Investigator Award (EP/S000453/1) Catapult RiR (EP/R513520/1), and the support of the 3M Buckley Innovation Centre via 3M BIC Fellowship. The authors from the University of Huddersfield gratefully acknowledge EPSRC funding of the Future Advanced Metrology Hub (EP/P006930/1).

References

- [1] Mehrpouya, M., Dehghanghadikolaei, A., Fotovvati, B., Vosooghnia, A., Emamian, S.S. and Gisario, A., 2019. *9*(18), p.3865.
- [2] Brooks, W.K., Tsopanos, S., Stamp, R., Sutcliffe, C.J., Cantwell, W.J., Fox, P. and Todd, J., 2005, June. University, Lancaster, UK (Vol. 10).
- [3] Li, X., Tan, Y.H., Willy, H.J., Wang, P., Lu, W., Cagirici, M., Ong, C.Y.A., Herg, T.S., Wei, J. and Ding, J., 2019. *Materials & Design*, **178**, p.107881
- [4] Kannan, G.B. and Rajendran, D.K., 2017. (pp. 95-100). Springer, Singapore.
- [5] R. Leach, "Optical Measurement of Surface Topography" 2011 Springer-Verlag Berlin Heidelberg. DOI 10.1007/978-3-642-12012-1
- [6] Grimm, T., Wiora, G. and Witt, G., 2015. *metrology and properties*, **3**(1), p.014001.
- [7] Triantaphyllou, A., Giusca, C.L., Macaulay, G.D., Roerig, F., Hoebel, M., Leach, R.K., Tomita, B. and Milne, K.A., 2015 *Surface topography: metrology and properties*, **3**(2), p.024002.
- [8] Watson, D.A., 1999. (Doctoral dissertation, University of Texas at Austin).
- [9] Tang, P., Wang, S., Duan, H., Long, M., Li, Y., Fan, S. and Chen, D., 2020. *JOM*, **72**(3), pp.1128-1137.
- [10] Yasa, E., Deckers, J. and Kruth, J.P., 2011. *Rapid Prototyping Journal*.
- [11] Song, B., Dong, S.J., Liao, H.L. and Coddet, C., 2012. *Materials Research Innovations*, **16**(5), pp.321-325.
- [12] Yadroitsev, I., Krakhmalev, P., Yadroitsava, I., Johansson, S. and Smurov, I., 2013 *Journal of Materials Processing Technology*, **213**(4), pp.606-613.
- [13] Galicki, D., List, F., Babu, S.S., Plotkowski, A., Meyer, H.M., Seals, R. and Hayes, C., 2019. *Metallurgical and Materials Transactions A*, **50**(3), pp.1582-1605.
- [14] Lou, S., Jiang, X., Sun, W., Zeng, W., Pagani, L., and Scott, P. J., 2019, *Precis. Eng.*, **57**, pp. 1–15.
- [15] Ramadurga Narasimharaju, S., Liu, W., Zeng, W., See, T. L., Scott, P., Jiang, X., & Lou, S. *Journal of Tribology*, 1-37
- [16] Reeves, P. E., and Cobb, R. C., 1995, *Proceedings of Fifth European Conference on Rapid Prototyping and Manufacturing*.
- [17] Lou, S., Zhu, Z., Zeng, W., Majewski, C., Scott, P. J., & Jiang, X. (2021). *Surface Topography: Metrology and Properties*, **9**(1), 015029.

Topology optimization for additive manufacturing

Kazybek Kassym¹, Konstantinos Kostas¹, Didier Talamona¹

Nazarbayev University, MAE – School of Engineering and Digital Sciences, Nur-Sultan, Kazakhstan¹

Corresponding author: didier.talamona@nu.edu.kz

Abstract

The main aim of this project is to assess the use of topology optimization (TO) methods in additive manufacturing in conjunction with the effect of 3D-printing parameters on the resulting strength of the printed parts. The two most common topology optimization methods, i.e., Density-based and Level-Set methods, were used with the aim of minimizing the mass of a given prototype solid entity while maintaining, to the extent possible, its tensile strength. A family of designs was produced for different levels of retained mass. Specifically, topologically optimized designs were generated for mass levels ranging from 50% to 100% of the original entity's mass with a 10% step. These designs were experimentally assessed in conjunction with varying infill patterns and infill density parameters of the employed Fused Deposition Modeling (FDM) printer (Ultimaker S3). The assessment was carried out systematically via tensile testing of the 126 printed specimens (using at least 3 samples for each model) and generation of the corresponding stress-strain graphs. In summary, the non-optimized entities and the 10%-mass-reduced designs exhibited practically identical strengths, whereas the 30% and 50%-mass-reduced ones exhibited slightly lower values for the maximum load at specimen's failure. The general trend of maximum stress was almost the same with slight deviations in average values, while standard deviation for some of the models was high. Furthermore, the employed density-based TO method appeared to produce parts that are better suited for 3D printing as it was computationally inexpensive, and it consistently generated designs that outperformed the ones generated by the Level-Set method. Regarding 3D-printing parameters, it was observed that the 'triangle', 'line' and 'grid' patterns produce printouts with practically equivalent strength. Finally, for parts produced with low values of infill density unexpected results and break points were observed. This can be explained by the introduction of large gaps in the interior of the printed model that negatively affect the strength of the part. Further investigation is needed to assess, qualitatively and quantitatively, the effect of infill density on the strength of printed parts.

Keywords: Optimization, Design method, Algorithm, Additive Manufacturing

1. Introduction

The current development of additive manufacturing has contributed to increased production of complex mechanical parts with minimum material waste [1, 2]. At the same time manufacturers are implementing additive manufacturing approaches with the aim of producing complex shapes that can reduce the weight of products and/or components of interest without compromising their mechanical properties [3]. Topology optimization in this context is commonly implemented via appropriate methods (and corresponding software packages) that modify the component's material distribution by mainly removing material from the considered solid entity [4-5]. The modified topological structure, within the constrained design space determined by the application, will make the optimized component lighter while ideally maintaining the same strength. Obviously, additional performance criteria may be used and therefore the topology optimization result will generally satisfy the design constraints of the initial design and at the same time provide identical performance with reduced weight.

The most popular approaches used in relevant industries are Solid Isotropic Material with Penalization (SIMP) and Level-Set topology optimization methods [6]. The SIMP or Density-based approach performs optimization via a voxelization approach that is commonly computationally inexpensive. The approach results in a material density scalar field considering the corresponding

Young's modulus. The value of the penalty factor manipulates the addition of elements with intermediate densities to the total stiffness. Numerical experiments show that the penalty factor that is equal to 3 is the most suitable. [7]. The Level-Set Method (LSM) for topology optimization uses iso-contours of Level-set function to implicitly determine the interfaces between entity boundaries [8]. This approach, contrary to most density-based approaches, allows boundaries to be smoothly defined.

2. Methodology

Our approach in this work consists of the following major steps: static structural setup for each model instance, topology optimization, 3d printing of resulting optimized component (3 identical components printed for each case), tensile testing and extraction of load-elongation graph and analysis of the results. The details of each step are described in the following sections.

2.1. Static Structural Setup

Firstly, the geometry of the employed object should be determined and designed for further processing. There are essential conditions that our model needs to satisfy, e.g., the dimensions of the specimen should fit into the tensile test machine which has a maximum width of 25mm.

After reviewing pertinent publications [15,18,23] which included tensile tests on 3D printed plastic materials, the model shown in Figure 1 has been selected. The design of the model is

symmetric with respect to two planes (x-y and y-z; see Fig. 1). The geometry of the model is split into three parts, two side parts of identical shape and the middle part which is a quadrangular prism. Smooth transitions have been created between these parts to avoid stress concentrations. The model was drawn in SpaceClaim¹ software for further static structural analysis in Ansys².

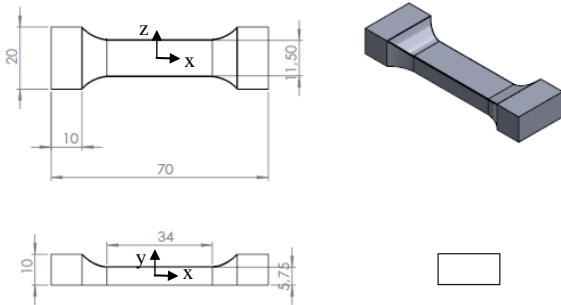


Figure 1. Sketch of the model

The two main modules for performing topology optimization in ANSYS Workbench are Static Structural and Topology Optimization [16]; see also Fig 2. Firstly, it is necessary to draw or import the geometry of the object into Static Structural, where the initial setup and meshing take place. To perform numerical solution of maximum stress, elongation at break or rigidity, the static structural analysis within the corresponding ANSYS workbench should be carried out. In Fig. 3 we see that one boundary face was selected for applying fixed support while the opposite face is subject to a normal force (100N) pulling the specimen. This is done to calculate the equivalent stress distribution along the model during the tensile test. After completion of structural analysis, all relevant information (engineering data, geometry, model setup, and solution) are transferred to the topology optimization module. In this module, we configure the optimization problem by specifying the objective function, optimization constraints, satisfaction tolerances, max iterations, percent of retain and other relevant algorithmic parameters. The module offers various topology optimization algorithms including the ones we have identified, i.e., density based and level-set methods [16]. In both cases, at each iteration of the topology optimization algorithm, the modified geometry is transferred again to a new Static Structural module, for analysis of its new structural characteristics. The second structural module is linked to the initial one and retrieves all relevant information, as needed, for analysis [17].

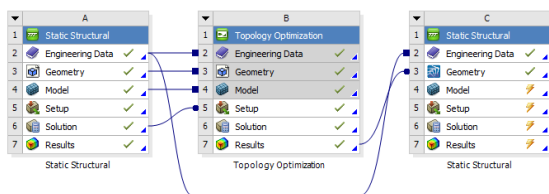


Figure 2. The Ansys modules connection

2.2. Mesh refinement and convergence

To produce accurate results, it is necessary to refine and optimize the mesh of the selected geometry. Identifying the optimum element and mesh sizes saves processing time while producing highly quality outcomes. Initially, the default ANSYS mesh settings were used followed by refinement and adjustments needed for sensitivity analysis and mesh convergence.

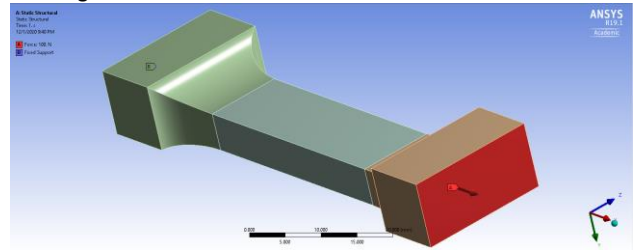


Figure 3. Model in Ansys

The maximum equivalent stress has been selected for checking the mesh quality of the model. ANSYS has a built-in mesh convergence tool, that was used in this work. The maximum level of mesh refinement was set to 5 with each level generating a finer mesh when compared to the previous one. Mesh converges when the change of RMS error of equivalent stress is less than 1%. Table 1 shows mesh refinement results for 3 different meshes that were produced by the mesh convergence tool. The initial mesh has 25985 nodes, 10659 elements and has an element size (maximum edge size) of 1mm with the maximum equivalent stress of 7.68 MPa, while the second mesh has significantly more nodes and elements resulting in an equivalent stress value of 7.82 MPa. The RMS error for the equivalent stress, calculated between the first two meshes, was slightly above 2.3%. However, the RMS error between the second and third mesh went down to 0.16%, which is below the set threshold. Hence, convergence stops at the third iteration, and this third mesh with 640581 nodes, 263626 elements and an element size of approximately 0.3 mm is used in analysis; see also Fig. 4.

Table 1 Mesh refinement results (Ansys generated table)

	Equivalent stress (MPa)	Change, %	Nodes	Elements
1	7.6853		25985	10659
2	7.8295	2.324812	278424	112851
3	7.8305	0.161422	640581	263626

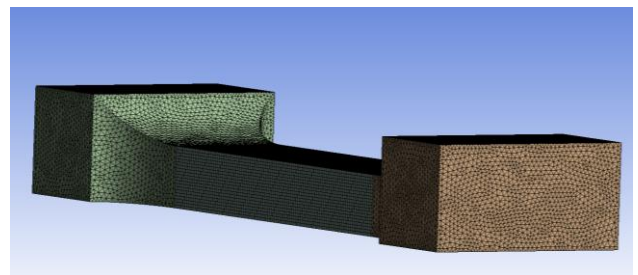


Figure 4. The final mesh of the model with 0.3mm element size

Figure 5 shows the distribution of equivalent stress during pull. Red regions correspond to higher values of stress and blue hues correspond to regions with low stress values. It can be clearly seen that comparatively high stress values are exhibited at the middle region.

¹ "SpaceClaim is a solid modeling CAD software developed by SpaceClaim Corporation."

² "Ansys engineering simulation and 3D design software delivers product modeling solutions with unmatched scalability and a comprehensive Multiphysics."

As mentioned previously, to efficiently perform topology optimization, the model was split into three parts with the middle part being the only part considered for design optimization [19]. Theoretically, the model is expected to break, during tensile testing, at the middle since the cross section there is thinner [18].

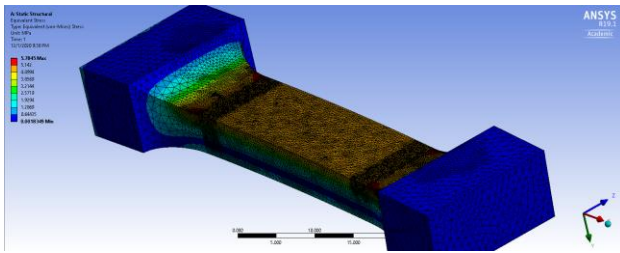


Figure 5. Distribution of equivalent stresses

Tables 2 and 3 record the volumes/material mass for the complete body and the middle part after optimization for various levels of material reduction. The difference between the two tables relates to the different infill density values. Specifically, Table 2 corresponds to an infill density of 100% that produces savings between 2.9% and 14.6%, whereas for the 60% infill density case (Table 3) savings go up to 50%.

Table 2 The volume of the model and reduction percent using 100% infill density.

Percent of retain, %	Volume of middle body, cm ³	Total volume, cm ³	Material reduction of middle body, g
100	2,25	7,70	0
90	2,02	7,47	0,55
80	1,80	7,25	1,11
70	1,57	7,02	1,67
60	1,35	6,80	2,22
50	1,12	6,57	2,78

Table 3 The volume of the model and material reduction percent using 60% infill density

Percent of retain, %	Volume of optimized body, cm ³	Total volume, cm ³	Material reduction of middle body, g
100	2,25	4,62	0,33
90	2,02	4,48	0,666
80	1,80	4,35	1,002
70	1,57	4,21	1,332
60	1,35	4,08	1,668
50	1,12	3,94	0,33

The topology optimization setup is shown in Fig. 6 which presents analysis and corresponding constraint settings. The convergence accuracy is set to be 0.1% while the maximum number of iterations is equal to 500 by default. The 'response constraint' category has an adjustable parameter corresponding to the "percent of retain" that needs to be preserved. Topology optimization in Ansys can be performed with respect to mass, volume, center of gravity, moment of inertia, global/local von-Mises stress, displacement, reaction force, compliance, and many others [19]. The results presented in this work correspond to mass usage optimization.

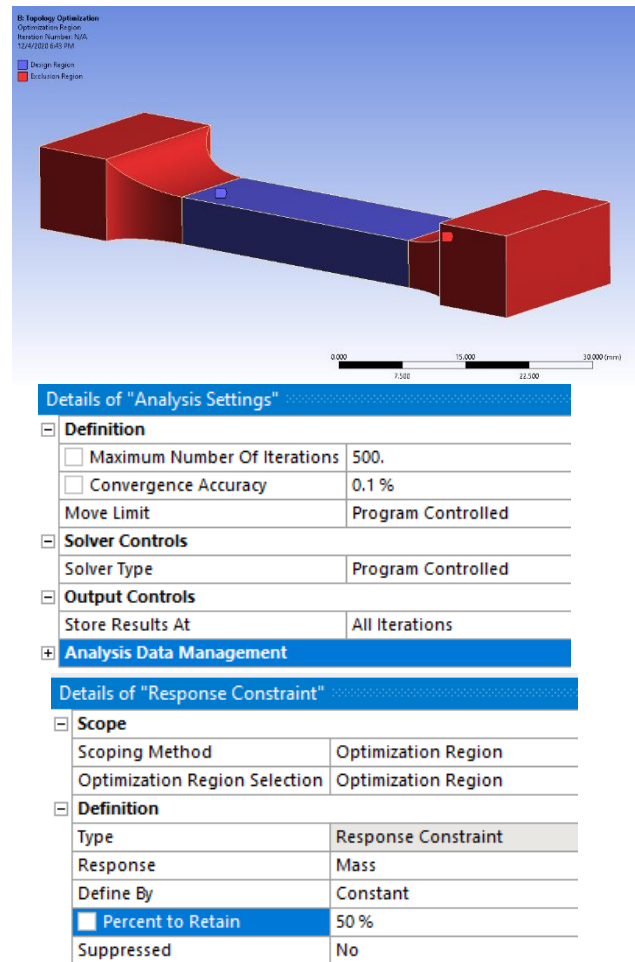


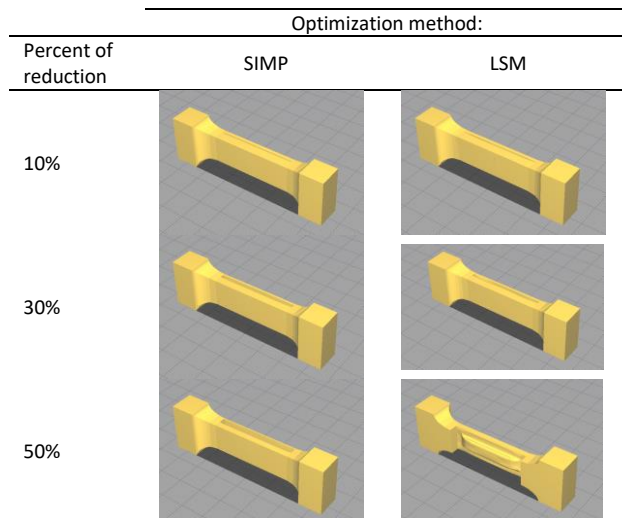
Figure 6. Region optimization and setup

3. Results

Tables 4 and 5 record the optimized designs for percent of retain. The resulting designs of the middle body part use less material in regions where stress concentration was low for both methods. The two methods exhibit variations for the cases of 90% and 50% of retain, while 70% of retain has almost similar results for both of them.

Table 4 Optimized body of the specimen

Optimization type: →	Optimization Method	
	SIMP	LSM
Percent of retain: ↓		
90%		
70%		
50%		

Table 5 Structurally evolved design of the specimen

The next step consists of manufacturing the optimized models using a FDM 3D-printer and test them in tension to failure. A speed rate of 5mm/min was used, based on pertinent literature. Table 6 contains tensile test results for SIMP-optimized specimens with triangular infill pattern, 100% infill density and 50%, 70% and 90% of retain. By averaging the load at break for the three specimens it can be seen that a 10% reduction of weight with TO results in an increase of load capacity per unit area of 5%, a small reduction of 1% for 30% and an increase of 8% for 50%.

Table 6 SIMP, 100% infill, triangle

Specimen #	Percent of retain	Optimization time, min	Printing time, min	Max stress, MPa	Yield stress, MPa	Young's M, MPa	Elong. at break, mm	Load at break point, N
1	50%	11	152	52,75	52,70	1687	2,50	1654
2	50%	11	152	49,81	49,80	2119	2,23	1548
3	50%	11	152	49,03	49,00	2556	1,66	1621
4	70%	10	163	53,38	53,38	2055	1,98	2471
5	70%	10	163	49,46	49,42	2214	1,79	1964
6	70%	10	163	41,07	41,07	2244	1,57	1740
7	90%	15	171	45,54	45,51	1742	2,07	2710
8	90%	15	171	41,55	41,53	1649	2,01	2473
9	90%	15	171	54,26	54,25	1417	2,66	3229
10	100%	0	146	44,91	44,91	1785	2,21	2969
11	100%	0	146	45,61	45,61	1668	2,30	3016
12	100%	0	146	43,98	43,95	1661	2,20	2908

4. Conclusion

In conclusion, topology optimization of simple 3D model has been successfully performed with interesting results. An initial investigation of printing parameters, such infill pattern shape and density, has been also performed. From tensile testing results, we observe that a slight increase of load carrying capacity per unit area can be achieved. At the same time, we have observed failures for some topologically optimized specimens that can be attributed to several reasons, including stress concentrations at abrupt cross-section changes, gaps introduced by low infill density along with the position the starting/ending deposition point of each printed layer that generates weak points. Further investigation is needed to such cases.

Acknowledgement:

This research was funded by Nazarbayev University under the Faculty Development Competitive Research Grant Program No 240919FD3923, "Cost effective hybrid casting methods for cellular structures".

References

- [1] Ngo, T.D., Kashani, A., Imbalzano, G., Nguyen, K.T. and Hui, D., 2018. Additive manufacturing (3D printing): A review of materials, methods, applications and challenges. *Composites Part B: Engineering*, 143, pp.172-196.
- [2] Clausen, A., 2016. Topology optimization for additive manufacturing. *DTU Mechanical Engineering*.
- [3] Ranjan, R., Samant, R. and Anand, S., 2017. Integration of design for manufacturing methods with topology optimization in additive manufacturing. *Journal of Manufacturing Science and Engineering*, 139(6).
- [4] Pedersen, C.B. and Allinger, P., 2006. Industrial implementation and applications of topology optimization and future needs. In *IUTAM Symposium on Topological Design Optimization of Structures, Machines and Materials* (pp. 229-238). Springer, Dordrecht.
- [5] Saadlaoui, Y., Milan, J.L., Rossi, J.M. and Chabrand, P., 2017. Topology optimization and additive manufacturing: Comparison of conception methods using industrial codes. *Journal of Manufacturing Systems*, 43, pp.178-186.
- [6] Kentli, A., 2020. Topology optimization applications on engineering structures. *Truss and Frames—Recent Advances and New Perspectives*, pp.1-23.
- [7] Erdelyi, H., Herz, M., Lemaire, E., Paffrath, M. and Wever, U., *Aspects of Industrial Topology Optimization*.
- [8] Sethian, J.A. and Wiegmann, A., 2000. Structural boundary design via level set and immersed interface methods. *Journal of computational physics*, 163(2), pp.489-528.
- [9] Liu, J., Gaynor, A.T., Chen, S., Kang, Z., Suresh, K., Takezawa, A., Li, L., Kato, J., Tang, J., Wang, C.C. and Cheng, L., 2018. Current and future trends in topology optimization for additive manufacturing. *Structural and Multidisciplinary Optimization*, 57(6), pp.2457-2483.
- [10] Langelaar, M., 2017. An additive manufacturing filter for topology optimization of print-ready designs. *Structural and multidisciplinary optimization*, 55(3), pp.871-883.
- [11] Stavropoulos, P. and Foteinopoulos, P., 2018. Modelling of additive manufacturing processes: a review and classification. *Manufacturing Review*, 5, p.2.
- [12] Li, N., Huang, S., Zhang, G., Qin, R., Liu, W., Xiong, H., Shi, G. and Blackburn, J., 2019. Progress in additive manufacturing on new materials: A review. *Journal of Materials Science & Technology*, 35(2), pp.242-269.
- [13] Grinde, S., 2018. Topology Optimization for Additive Manufacturing Using SIMP Method.
- [14] Peirce, C.S. and De Waal, C., 2014. *Illustrations of the Logic of Science*.
- [15] Beshimbay, D. and Kereyeva, A., 2018. 3D-PLA-plastics.
- [16] Lee, H.H., 2018. Finite element simulations with ANSYS Workbench 18. SDC publications.
- [17] Thompson, M.K. and Thompson, J.M., 2017. ANSYS mechanical APDL for finite element analysis. Butterworth-Heinemann.
- [18] Hosford, W.F., 1992. Overview of tensile testing. *ASM International, Tensile Testing (USA)*, 1992, pp.1-24.
- [19] Li, X.P., Zhao, L.Y. and Liu, Z.Z., 2017. Topological optimization of continuum structure based on ANSYS. In *MATEC Web of Conferences* (Vol. 95, p. 07020). EDP Sciences.

Prediction of dimensional accuracy and warpage of additive manufactured parts using finite element model

D. Syrlybayev¹, A. Seisekulova¹, M. Akhmetov¹, A. Perveen¹, D. Talamona¹

¹Department of Mechanical & Aerospace Engineering, School of Engineering and Digital Sciences, Nazarbayev University, Kabanbay Batyr Ave. 53, Nur-Sultan 010000 Kazakhstan

daniyar.syrlybayev@nu.edu.kz

Abstract

Fused Deposition Modelling (FDM) is one of the most affordable additive manufacturing technologies available. Although FDM printers are easy to use, the process itself is complex with nonuniform rapid heating and cooling. For this reason, complex residual stresses and part deformations are generated during the production process. Recently, the usage of simulations of the FDM process using Finite Element Analysis (FEA) to predict geometrical accuracy and residual stresses within the part has gained attention from the research community. Hence, the main objective of this study is to develop and validate a new model of the FDM process to predict dimensional deviations (length, width, and thickness), warpage, and residual stresses using FEA. To achieve the objective, thermo-mechanical analysis of a simple standard tensile test part was modelled and solved using ANSYS. To reduce the complexity of the numerical model and computational time, several important assumptions were made. The validation of the model was done against physical parts, which were manufactured using an Ultimaker S3 printer. The results have shown that with a given set of assumptions, the error between FEA predicted and experimentally measured warpage was 14.6%, while for dimensional accuracy it was found that the thickness deviation error was about 23%. Unfortunately, the current FEM model is unable to predict the length and width deviations. One of the reasons might be that the FEA model neglects the viscoelastic and viscoplastic effects. Also, the printer probably uses a compensation algorithm that is not included in the FEA model too. The possible improvements of the model, such as the inclusion of the viscoelastic and viscoplastic effects, will be discussed.

Accuracy, 3D printing, Finite Element Method (FEM), Simulation

1. Introduction

Fused deposition modelling (FDM) is the additive manufacturing process in which a filament or rod polymer is extruded through a nozzle that moves according to the programmed path. In comparison to other AM processes, it has a relatively low cost of machine and consumables and hence it is attractive for rapid prototyping.

Its process parameters determine the mechanical properties and accuracy of the manufactured part. That is why the current FDM research focused mostly on the optimization of the process parameters to achieve the best accuracy and mechanical properties.

Nowadays, numerous publications are found to focus on optimization of the strength and accuracy using Taguchi methods [1] Grey Taguchi [2] and Bayesian networks [3]. In addition, several studies were conducted to determine how each individual parameter affects a specific type of geometrical deviations. For example, [4] studied how warpage is affected by different process parameters.

As literature suggests, most of the research projects involve experimental testing, which is time consuming and provides only limited end-data. On the other hand, analytical and numerical results can help to understand how exactly deviations vary with respect to selected process parameters. Previously, few attempts were made to model the FDM process using the Finite

Element Method (FEM) [5, 6]. However, in both works each element was activated individually, which needed a fine time discretization in transient analysis and as a result significant computational effort. Hence the objective of this research is to develop a new methodology for modelling the FDM process using FEM and several simplifications described in later sections. The model was used for prediction of the dimensional deviations and warpage of standard part for tensile test. The effectiveness of the proposed method was assessed through its validation with experimental results.

The Finite Element (FE) model setup and how the experiments were conducted is also described. Then a summary of the results obtained numerically and experimentally are reported. Finally, the main trend of results is discussed, and numerical results are compared with the experimental ones. The main findings are summarized in the conclusions.

2. Methodology

To achieve the aim of the study a finite element model of the FDM process was built and validated against experimental results. The procedures for modelling and validation are described in this section.

2.1. Computational modelling

In this study, the following assumptions were used:

- The phase change, viscoelastic and viscoplastic effects were neglected
- Each layer is deposited instantly
- The manufactured part has isotropic properties with flawless microstructure
- Chamber and plate temperatures have time and space invariant values.
- Perfect bounding between the built platform and the part (no slippage)

The physical model used for simulations is shown in Figure 1. It is a dog-bone specimen for tensile test placed on the glass build platform. The specimen consists of ten layers. Each layer is 0.3 mm in thickness.

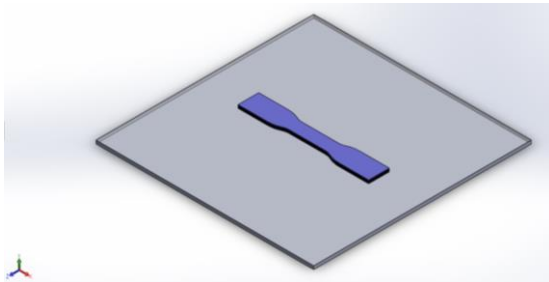


Figure 1. The model used for the simulation.

The model was meshed using ANSYS build-in automatic meshing tools. The meshing was done using 1x1x0.3 mm second-order hexahedral elements. Each element had mid-side nodes for improved accuracy. As each layer is deposited instantaneously, the model has two symmetry planes allowing to model only one quarter of the part as shown in Figure 2, which significantly reduces the computational time.

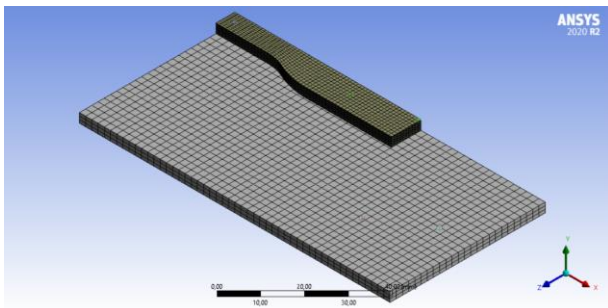


Figure 2. Model discretization.

To simulate the FDM process the thermomechanical model using the layer activation and deactivation technique was built. Its working principle is the following. When a new layer is activated the topology of the part updated and the transient thermomechanical simulation is performed on the part and the current temperature and stress distributions are used as the initial conditions [5]. This process repeats itself several times until the whole part is deposited within the simulation. Afterwards, the part is left to reach the thermal equilibrium. Finally, the constraints between the specimen and the build platform were deactivated and deformations of the part in the released conditions were obtained.

The boundary conditions for the following analysis are shown in Figure 3. The 3 mm glass platform was set at a constant temperature of 95 °C as in the real set up. The specimen and the top surface of the platform are subjected to convective heat transfer with a heat transfer coefficient of 80 W/m²K. Because

the glass platform is much stiffer than the part made of ABS it was assumed that it is rigid, and no structural analysis was conducted on it. To simulate the adhesion of the part to the glass the nodes on the lower surface of the specimen were fully constrained. This boundary condition was turned off during the detachment phase and only one node at the centre (indicated as E in Figure 3) remained constrained to prevent the rigid body motion.

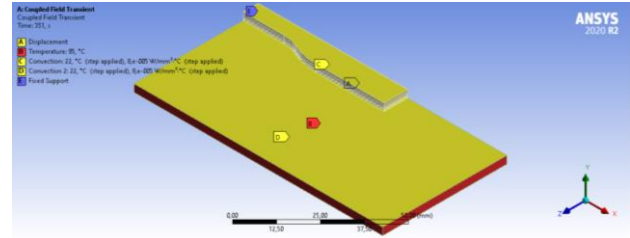


Figure 3. Boundary conditions.

As it was mentioned, the material utilized for this study is ABS. The temperature-dependent material properties were taken from [6]. In addition, a bilinear plastic model was used for this study. The validity of this model for ABS plastic was shown by [7].

2.2. Experimental Procedure

To validate the model, specimens were printed using an Ultimaker S3 (Figure 4). The key parameters used for printing are as follows: nozzle diameter was \varnothing 0.4 mm, temperature of extrusion was 220°C, temperature of the platform was 95°C and the ABS filament diameter was 2.85 mm. The remaining printing parameters are shown in Table 1. Three specimens were printed simultaneously to check the influence of the position. The middle position was denoted as “0” and the other two positions were denoted as “-1” and “1” respectively. Before printing, the platform was thoroughly cleaned with 80% of ethanol solution. To avoid severe warping that can lead to printing failure and nozzle damage, brims were added to the samples. After cooling and detachment, the brims were carefully cut off. The samples were measured at three different points using a digital caliper with an accuracy of 10µm.

Table 1 Default parameters during printing

Factor	Value	Unit
Layer thickness	0.3	mm
Wall thickness	1.3	mm
Infill density	100	%
Infill pattern	Rectilinear	-
Print speed	55	mm/s
Fan speed	2	%

The warpage was denoted as “H” and was measured from the horizontal surface at which the sample is located to the bottom side of the sample’s warped edge (Figure 5).

3. Results

In the following study, the numerical analysis was conducted and validated as described. The results of simulations and experiments are summarized in the subsections 3.1 and 3.2.

3.1. Numerical results

Using the simulation procedure described in section 2.1 the finite element analysis of the FDM was performed to find the dimensional deviations and warpage. The displacements of the part along the x, y and z axes are shown in Figures 6, 7 and 8, respectively.



Figure 4. Ultimaker S3 printer.



Figure 5. Warped sample edge

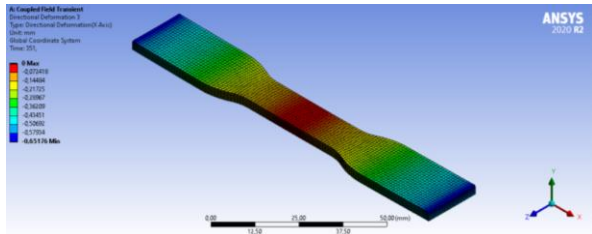


Figure 6. Deformation of the part along the x-axis

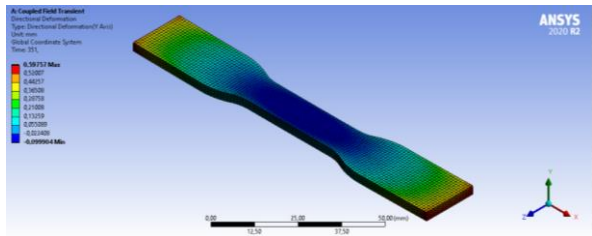


Figure 7. Deformation of the part along the y-axis

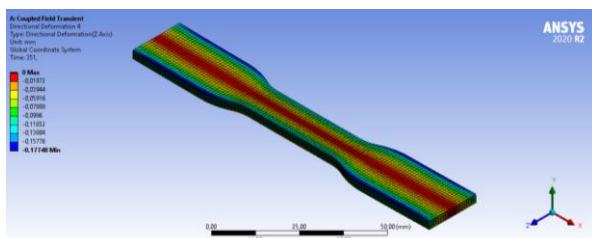


Figure 8. Deformation of the part along the z-axis

Note that the values represented in Figures 6-8 do not represent a dimensional deviation. Due to the usage of the quarter symmetry, it is necessary to multiply the values shown in Figure 6 and 8 by two to find length and width deviations (ΔL and ΔW , respectively).

The deformation along the vertical y-axis is the superposition of warpage (H) and dimensional deviation along the thickness of the part (ΔT). To find the thickness deviation following procedure was used: the corresponding deformations of the bottom and top surfaces along x-axis from $x = 0$ to $x = 60$ mm (central half-length) and along z-axis from $z = 0$ to $z = 9.5$ mm (utmost half-width) were sampled and subtracted from each

other. To find the warpage the deformation of the bottom surface was isolated. Using this procedure, the warpage and thickness deviations along the central half-length and utmost half-width were obtained and are shown in Figures 9 and 10.

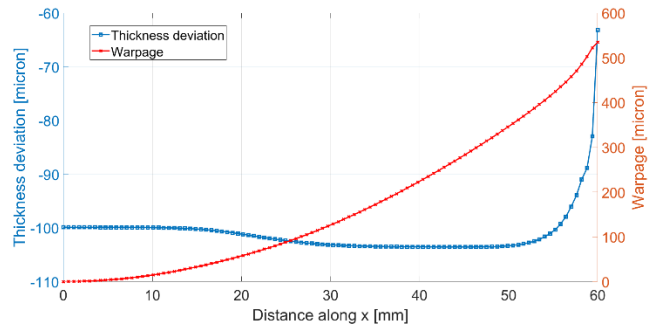


Figure 9. Warpage and thickness deviation of the part central half-length

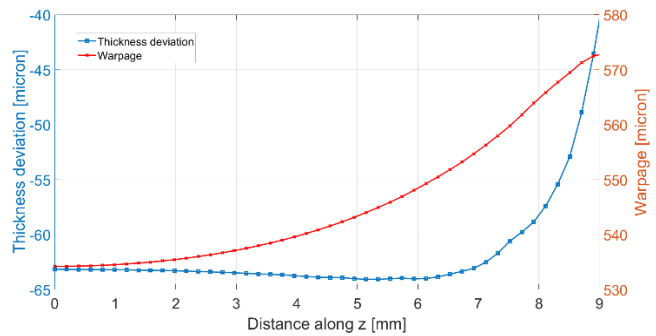


Figure 10. Warpage and thickness deviation of the part utmost half-width

From Figures 6, 7 and 8 and plots 9 and 10, the FE predicted maximum values of deviations in terms of length (ΔL), width (ΔW), thickness (ΔT), and warpage (H) have been summarized in Table 2.

Table 2 FE predicted maximum values of deviations (in μm)

ΔL	ΔW	ΔT	H
-1303	-355	-101	573

3.2. Experimental results

The influence of the position was minor. Hence, after measuring the samples and calculating the difference between the measured values and the nominal values, the resultant values were averaged and can be viewed in Table 3. The positive values of ΔL and ΔW indicate that the specimens were printed larger in length and width than the initial design. On the other hand, the negative value of thickness deviation implies that the printed samples are thinner than the digital model.

Table 3 Experimentally measured values of deviations (in μm)

ΔL	ΔW	ΔT	H
70	151	-133	501

4. Discussion

From Figures 6 and 8, both length and width deviations are negative. This happens because of the shrinkage that the part experiences while cooling.

Furthermore, Figure 7 shows that the part deforms in the vertical direction as well. The vertical deformation is associated with the shrinkage along the thickness, of each layer, and with the warpage of the part. It can be noticed that the corners of the part have the larger vertical deformation, while the centre remains relatively undeformed. Thus, the part attains the shape

of the bowl when it is detached from the built platform. This is known as warpage and its cause was described by [8]. When the material is deposited, it shrinks as it cools down. The shrinkage strain causes stress and resulting moments around the platform, which are blocked due to the constraints between the part and platform. When the part is detached, these moments cause the part to deform into a bowl shape.

Furthermore, Figures 9 and 10 show that the warpage increases with the increase in length. The shorter the dimension the smaller is the warpage. While comparing the warpage along the length and along the width, the warpage is more significant for the length direction. This phenomenon was also observed by [8]

It should be also mentioned that the thickness deviation along the length is relatively constant and is approximately $-100\ \mu\text{m}$. However, the FE model predicts that at the outer edges the thickness deviation will reduce and approach zero. This is especially true if the thickness deviation along the utmost half-width is considered. This happens because the elements located in the outer region has more faces exposed to the convective surroundings and hence FE model predicts that they will cool faster.

Considering the numerical and experimental results shown in Tables 2 and 3 it can be noticed that the planar deviations ΔL and ΔW predicted by FEM and experiment are not in agreement with each other. The experiment predicts positive deviations, while simulations results are negative ones. This might be due to the pressure from the nozzle that flattens the part and causes its dimensions to increase in size during extrusion process. In addition, it is possible that within the printer program, there might be shrinkage compensation algorithms. None of these assumptions were incorporated into the current model as it was out of the scope of this project.

The thickness deviation (ΔT) and warpage (H) predicted by the model are in good agreement with the experimental results. The errors between the values are 23% and 14.6% respectively. Experiments show larger values of the thickness deviation than the FE predictions. This might also be due to pressure acting from the extruder which flattens the molten part. Sources of errors might also include the calibration of the FDM machine and possible errors during the measurements as well as the assumptions employed during the modelling.

The Finite Element model can be improved by the inclusion of viscoelastic and viscoplastic effects and accounting for pressure acting from the nozzle to improve its planar deviation prediction.

5. Conclusion

In summary, a novel Finite Element Simulation of a ASTM part was created and the conditions of the FDM process were simulated to analyse and predict the deformation of the sample. It was found that the deviations in length and width are negative according to the FEM model and positive according to the measurements from the experimental results. The first possible explanation for such contradictions is the pressure imposed by the nozzle that leads to the flattening of the samples. Besides, the possibility of a shrinkage compensation mechanism can be another possible reason. However, the simulated and experimental results were in good agreement for thickness deviation and warpage such that the error values are 23% and 14.6% respectively.

To conclude, the model can predict thickness deformation and how much the sample can warp. The model can be improved to consider the factors that significantly affect dimensional accuracy. Thus, it will improve the ability of the model to predict planar dimensional deviations (ΔL and ΔW). This can help predict

the inaccuracies and errors reducing the wastage of material during the actual printing.

For future work, the effect of the process parameters can be considered by changing the respective values in the model to find more appropriate parameters that can mitigate the warping. The effect of nozzle pressure and shrinkage compensation mechanism can also be included in the model.

Acknowledgement:

This research was funded by Nazarbayev University under the Faculty Development Competitive Research Grant Program No 240919FD3923, "Cost effective hybrid casting methods for cellular structures".

References

- [1] Xinhua, L., Shengpeng, L., Zhou, L., Xianhua, Z., Xiaohu, C., & Zhongbin, W. (2015). An investigation on distortion of PLA thin-plate part in the FDM process. *The International Journal of Advanced Manufacturing Technology*, **79**(5) 1117-1126.
- [2] Sood, A. K., Ohdar, R. K., & Mahapatra, S. S. (2009). Improving dimensional accuracy of fused deposition modelling processed part using grey Taguchi method. *Materials & Design*, **30**(10) 4243-4252.
- [3] Mahapatra, S. S., & Sood, A. K. (2012). Bayesian regularization-based Levenberg–Marquardt neural model combined with BFOA for improving surface finish of FDM processed part. *The International Journal of Advanced Manufacturing Technology*, **60**(9-12) 1223-1235.
- [4] Panda, B. N., Shankwar, K., Garg, A., & Jian, Z. (2017). Performance evaluation of warping characteristic of fused deposition modelling process. *The International Journal of Advanced Manufacturing Technology*, **88**(5-8) 1799-1811.
- [5] Zhang, Y., & Chou, Y. K. (2006). Three-dimensional finite element analysis simulations of the fused deposition modelling process. *Proceedings of the Institution of Mechanical Engineers, Part B: Journal of Engineering Manufacture*, **220**(10) 1663-1671.
- [6] Cattenone, A., Morganti, S., Alaimo, G., & Auricchio, F. (2019). Finite element analysis of additive manufacturing based on fused deposition modeling: distortions prediction and comparison with experimental data. *Journal of Manufacturing Science and Engineering*, **141**(1).
- [7] Rodríguez-Panes, A., Claver, J., & Camacho, A. M. (2018). The influence of manufacturing parameters on the mechanical behaviour of PLA and ABS pieces manufactured by FDM: A comparative analysis. *Materials*, **11**(8) 1333.
- [8] Armillotta, A., Bellotti, M., & Cavallaro, M. (2018). Warpage of FDM parts: Experimental tests and analytic model. *Robotics and Computer-Integrated Manufacturing*, **50** 140-152.

Micro-replication of high precision optically enhanced moulds fabricated by multiphoton polymerization.

Sara Vidal¹, Félix Ares¹, Ivette Coto¹, Francisco Gontad¹, Tamara Delgado¹, Pablo Romero¹, Nerea Otero¹

¹AIMEN Technology Centre, Spain

sara.vidal@aimen.es

Abstract

Glass moulds with microstructures manufactured by Multiphoton Polymerization (MPP) are replicated using two different approaches. On the one hand, by means of an automatic Injection Moulding process; and on the other hand, by a manual approach using a high-resolution replication silicone. The main differences between the obtained replicas are evaluated in terms of their replication quality, the influence of the moulds' fabrication method on the replication process, and the impact on the optical characteristics of the final product. The results of this work indicate that high resolution and resistant moulds can be fabricated through MPP, favouring the fabrication of high-quality replicas.

Glass moulds, Replication, Injection Moulding, Femtosecond Laser, Multiphoton polymerization.

1. Introduction

MPP is a well known technique [1]-[3] for the fabrication of high resolution and complex 3D microstructures for many different applications as biomedicine [4] or microelectronics [5]. This methodology leads the way for the direct fabrication in the nanometric scale although its fabrication speed has been already pointed out as the most relevant limitation.

The work presented here is focused on the replication of diffraction gratings, fabricated by MPP technology over glass substrates, using different replication processes as promising technologies for mass production of high-quality micro-components. More in detail, Injection Moulding (IM) [6] and silicone cast moulding (CM) [7] methodologies were tested. Masters and replicas were then characterized in terms of their topographical features and optical properties such as the surface quality or the grade of transparency.

2. Methodology

MPP masters were fabricated by combining an Amplitude Satsuma HP2 laser (280 fs, 515 nm) with a micromachining workstation from OPTEC. Maximum power achievable was limited with a set of a half-wave plate and a linear polarizer. The laser radiation was focused inside the resin through a microscope objective (Olympus 60x, NA 1.42). The 3D characterization of the masters and the replicas was performed with an optical profilometer (SensoFar S-Neox).

Diffraction gratings were created applying a thin layer of resin of less than 10 μm over a microscope glass slide, and the same over sapphire round glasses. Laser processing parameters were a pulse energy between 20 and 60 μJ , a 500kHz frequency and a scan speed of 5mm/s. A diffractive optical element (DOE) of 1x25 points was used to create more homogenous lines. The photosensitive resin used for the MPP process (Ormostamp[®], from Microresist) contained a specific photoinitiator (Irgacure

to make the resin sensitive to the laser wavelength. After the fabrication, the samples were rinsed with Methyl Isobutyl Ketone and Isopropanol until all the non-polymerized resin was eliminated. The IM process was performed with a VICTORY 40 (ENGEL) injection moulding machine, using Zylar[®] 960, which is a high flow transparent styrene acrylic copolymer for low temperature IM processes (200°C). The alternative replication materials employed were two rubber silicones for CM process. One was the transparent PDMS-Sylgard 184 (Dow Corning) and the other the translucent XTX45-DRY (Zhermack). Those silicones were prepared following the instructions of each supplier and degassed with vacuum before being poured over the masters. The PDMS silicone curing time was reduced by heating the sample. This thermal treatment cannot be applied to the XTX45-Dry silicone because its curing agent is based in Platinum and heat would make the silicone darker, losing its grade of transparency.

3. Results and discussion

Previous results on the fabrication of diffraction gratings by MPP on Stainless Steel covered with a thin layer of cured resin [8] showed a good quality of the replicas obtained by injection moulding with Zylar, but these also revealed some of the limitations of this material. Further studies showed that the thin layer of cured resin between the metal and the structures breaks after several replication iterations. This was the reason to change the fabrication methodology to directly fabricate by MPP over glass samples, which need no pre-deposited layer of resin and neither any special treatment for a good adhesion apart from a surface cleaning with Ketone and Isopropanol.

Initial fabrication tests were performed on common microscopic glass slides. Despite the good results on adhesion and resolution achieved, the physical properties of the microscope slides are not compatible with this IM process, and most of the samples break during the replication.

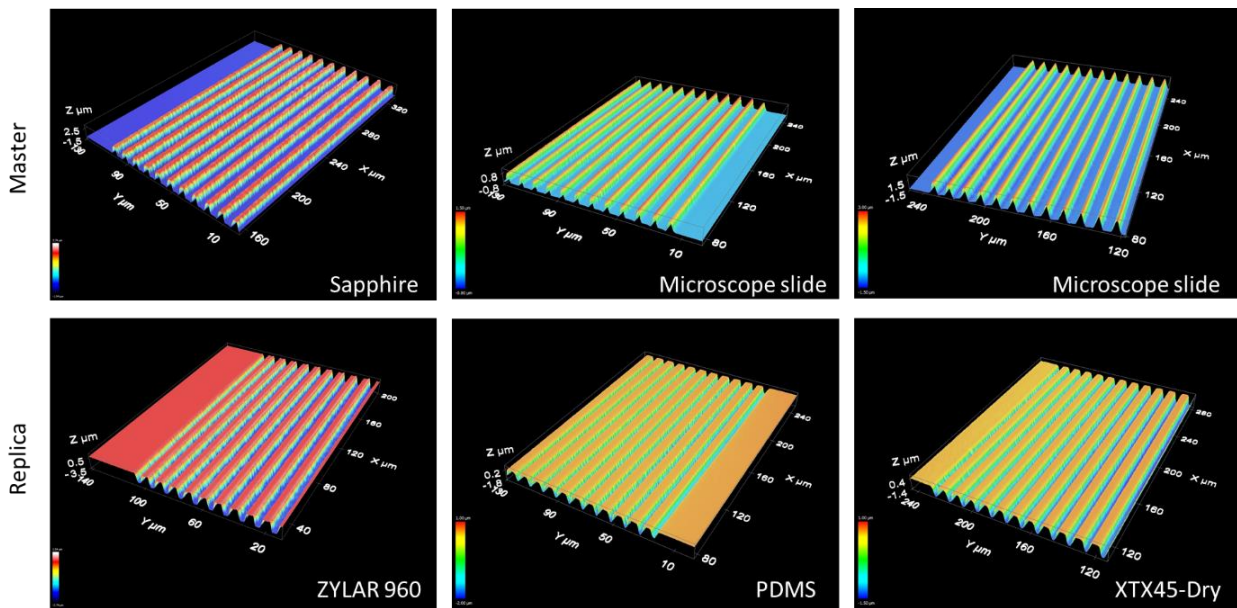


Figure 1. 3D Topographies of the masters fabricated by MPP and replicas, indicating each glass and replication material used (images obtained with the optical profilometer S-Neox). C

The usage of sapphire glasses was then proposed as a more resistant material for the injection process because of its higher resistance to thermal and physical shocks. Only gratings fabricated over sapphire were replicated by IM while structures fabricated on microscope slides were replicated by CM, as no specific physical requirement of the glasses was needed for this replication method.

The measurement of the topographies of the masters before and after the replications showed that none of the replication methods damaged or modified the samples, even after several replication iterations.

Regarding the measurement of the topographies of the replicas, all the three materials used showed very good behaviour allowing the perfect replication of the height, width and period of the gratings fabricated. Figure 1 shows the 3D topographical reconstruction of masters and replicas, where the high grade of similarity can be appreciated. Also, all the replicated structures show the same visual diffraction effect as the masters when illuminated with ambient white light.

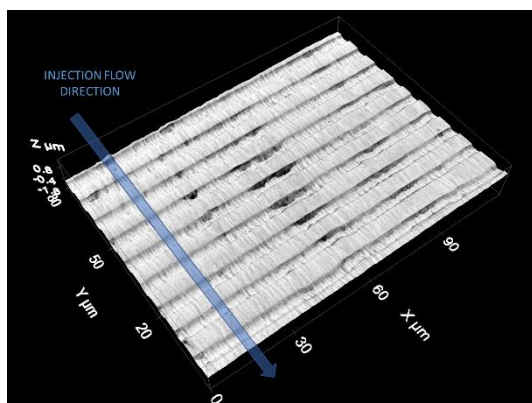


Figure 2. 3D topography of an IM replica where the Zylar polymer was not properly melted showing flow grooves all over the grating lines.

Some replicas made by IM showed certain random defects, even though the immediately previous and later injections were perfectly executed. Figure 2 shows an example of the failure of the IM process with Zylar in a replica of the same structure measured as the one showed in Figure 1. These defects were related with a failure in the melting temperature of the Zylar

polymer that reduced its flow rate and many flow lines appeared all over the surface. In consequence, a bad-quality replica is created where the depth of the gratings was almost 50% smaller than expected and the appearance reveals the flow direction of the injection. More effort will be done over this concern to find a solution for these thermal instabilities of the IM process.

Talking about the productivity of the replication processes, none of the methods used seem to be as fast as industrial typical processes that can fabricate over hundreds of units per minute. Nevertheless, the IM is the fastest procedure employed, with 2.5minutes needed for each injection at 200°C, while PDMS is only cured after 10 minutes at 150°C, and XTX45-Dry needs 12hours for curing at 23°C.

Physical properties of the replication materials, as surface roughness (Ra) and optical transmittance (Tr) and reflectance (Re), are summarized in Table 1.

Table 1. Surface and optical properties of the masters and replication materials. Ra= surface roughness; Re= reflectance; Tr=Transmittance.

	Ra (nm)	Tr (%)	Re (%)
Mic. slide	2.9	91.54	8.59
Sapphire	3.1	85.43	15.28
PDMS-front	3.2	93.31	5.47
PDMS-back	3.2	93.30	4.59
XTX-front	5.5	87.66	3.06
XTX-back	13.4	88.07	1.10
Zylar-front	4.3	70.41	5.07
Zylar-back	106.1	75.97	1.54
Std. Deviation	± 0.3	± 0.02	± 0.02

The roughness of the replicas was measured on both sides of the material. This means on the side where structures and glass surface are replicated (front side), and also on the opposite side (back side). In the case of the IM process, the opposite side of the replica has very poor quality because the injection mould assembly was not adequate for replicating high-optical-grade samples due to the usual industrial use of the equipment. Better results could be achieved in the IM process if a polished surface was used as back-side of the injection mould assembly. In the case of the silicone materials, replicas were cured with the back

side free to open air to evaluate the properties of the material itself. The optical properties were measured with a green laser diode of 5mW and a thermal power sensor S120C (both from Thorlabs). Reflectance was measured with an incident angle of 45° while transmittance is measured at 180° regarding the diode device.

As expected, transmittance of the XTX45-Dry silicone and the Zylar polymer are smaller than that of the PDMS because they are translucent instead of transparent materials. Zylar back-side high roughness covered up the results of transmittance and reflectance. Although the good quality of the replicas created with the XTX45-Dry silicone, roughness is higher in the back side because it was cured to open air.

4. Conclusions

Multiphoton polymerization technology was used for the direct fabrication of diffraction gratings on glass samples with no specific surface pre-treatment for adhesion promotion. This fabrication process is confirmed as an effective method for the creation of high-resolution optical micro-structures. Diffraction structures were fabricated on sapphire glass for later replication by injection moulding with Zylar 960 polymer, and over common microscope glass slides for cast moulding with Sylgard 184 and XTX45-Dry rubber silicones.

All replication processes provided high-quality replicas in terms of the exact reproduction of the dimensions of the structures in width, height and period. Nevertheless, some of the IM replicas presented several defects related to an inadequate melting of the Zylar polymer during the injection process.

Replicas obtained with Zylar 960 and XTX45-Dry materials need polished back-side surfaces during the moulding processes to ensure the optical quality of the replicas.

The results obtained along this work showed Sylgard 184 rubber silicone as a promising material for the replication of high-quality optical structures because of its replication achievable resolution and also because of its high transmission rate, even though its usual curing time is not compatible with common industrial applications.

Further work should be done for the evaluation of the replicated gratings in order to analyse the efficiency related to each material transparency. Also, more effort will be done for the selection of new transparent materials for the IM and CM processes, paying particular attention to the physical characteristics that lead these replications techniques to the industrial requirements of the FLOIM project.

Acknowledgements

This work has received funding from the Europeans Union's Horizon 2020 research and innovation programme under grant agreement n° 820661.

The authors would like to thank the FLOIM consortium for their collaboration in the project: UPC, PROMOLDING, HYBRONICS, MONDRAGON ASSEMBLY, FAGOR AUTOMATION, ADAMA INNOVATIONS, FLEXENABLE, RECENDT, FRAUNHOFER IWU, CEIT-IK4 and SNELL OPTIQUES.

References

- [1] Sun H.B. and Kawata S. 2004 NMR.3D Analysis - Photopolymerization *Adv. Polym. Sci.* **170** (Springer, Berlin, Heidelberg) 169-273
- [2] Gontad F. Vidal S. Otero N. Romero, P. 2019 *Proceedings of Lasers in Manufacturing Conference-LIM*

- [3] Serbin J. Ovsianikov A. Chichkov B. 2004 *Opt. Express* **12** 21 5221-5228
- [4] Buchroithner B. et al. 2004 *Nat. Mater.* **3** 444-447
- [5] Deubel M. von Freymann G. Wegener M. Pereira S. Busch K. Soukoulis C.M. 2004 *Nat. Mater.* **3** 444-447
- [6] Rytka C. Kristiansen P.M. Neyer A. 2015 *J. Micromech. Microeng.* **25** 065008
- [7] Ye X. Liu H. Ding Y. Li H. Lu B. 2009 *J. Micromech. Microeng.* **86** 310-313
- [8] Otero N. Vidal S. Ares F. Coto I. Gontad F. Delgado T. Romero, P. 2020 *Proc. SPIE 11271 - Laser 3D Manufacturing VII*, 112710X

High-resolution X-ray computed tomography for additive manufacturing: Towards traceable porosity defect measurements using digital twins

B. A. Bircher¹, S. Wyss¹, D. Gage², A. Küng¹, C. Körner², F. Meli¹

¹Laboratory for Length, Nano- and Microtechnology, Federal Institute of Metrology METAS, Bern-Wabern, Switzerland

²Chair of Materials Science and Engineering for Metals, Friedrich-Alexander University Erlangen-Nürnberg, Erlangen, Germany

benjamin.bircher@metas.ch, felix.meli@metas.ch

Abstract

Metal additively manufactured (AM) parts pose new challenges for dimensional metrology due to their high surface roughness, buried structures and internal defects. X-ray computed tomography (XCT) is a powerful volumetric measurement method providing resolutions down to the micrometre level that enables us to address several quality assurance requirements simultaneously. It can accompany the entire AM process by being employed for AM powder characterisation, as a non-destructive testing (NDT) tool to characterise defects, such as porosity and unfused layers, and to assess the part geometry, for example by comparison to the nominal CAD model.

We will discuss the potential and limitations of XCT for metal AM and present a new approach to render classical NDT analyses, such as porosity, metrologically traceable by assigning a measurement uncertainty to them. The approach uses dedicated simulations of digital porosity representations, i.e. digital twins, as a route towards estimating the measurement uncertainty (MU) of the pore parameters, such as size and shape factors, and the probability of detection (POD) with respect to defect size.

X-ray computed tomography (XCT), additive manufacturing (AM), defects, porosity, dimensional metrology, measurement uncertainty (MU), probability of detection (POD), electron beam melting (EBM)

1. Introduction

Additive manufacturing (AM) is becoming increasingly important because of its key advantage for rapid prototyping, freedom of design, and sustainability. Due to the complex manufacturing process, metrology tools for quality assurance and dimensional analyses are essential [1]. X-ray computed tomography (XCT) is a promising modality thanks to its ability to map the complete inner and outer structure of parts [2]. However, there is still limited comparability for certain analyses, such internal defects [3] and surface texture [4].

Traceability that enables comparability entails introducing a reference scale and assigning a task specific measurement uncertainty. Whereas, the former was addressed for high-magnification measurements [5,6], uncertainty estimations for porosity measurements were only established using the substitution method [7]. This method is time consuming due to the required reference measurements and difficult to implement for internal features. Further, the strict similarity requirement between the reference object and the workpiece, according to VDI/VDE 2630-2.1 [8], prevents generalisability. Digital representations, i.e. virtual reference samples [9], are a promising approach to estimate uncertainties and in a future step correct for systematic deviations introduced by the measurement system itself.

In this paper, we present a route to render XCT porosity measurements traceable using dedicated simulations of digital porosity representations. According to references [10,11], a digital representation that feeds back information to the measurement result is referred to as "digital twin". This definition applies to the digital porosity representation here, since it aids the estimation of the measurement uncertainty.

2. Porosity simulations

Since traceability in XCT is still not fully established, it is of paramount importance to understand the complex nature of the measurement process to estimate a feature specific measurement uncertainty (MU) as well as a probability of detection (POD) in dependence of defect size. Simulations are a promising method to fully describe the XCT measurement process [12] and evaluate different analysis algorithms.

2.1. Digital porosity representation

Virtual reference samples were previously used to evaluate the performance of XCT for surface texture measurements [9] or to determine the probability of detection (POD) of defects in radiography [13].

We used the Python API in FreeCAD (Version 0.17.13522, www.freecadweb.org) to generate a cylindrical sample that was filled with spherical pore defects as follows (Figure 1): The radii

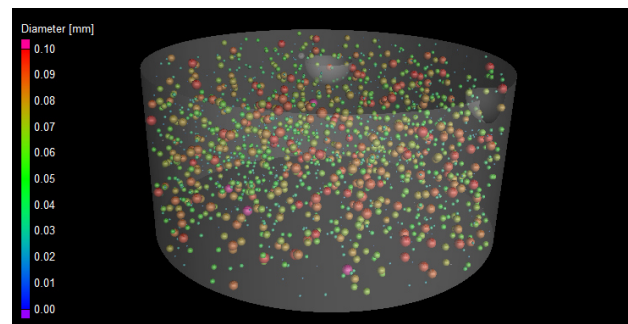


Figure 1. Digital porosity twin: \varnothing 3.8 mm, 1% porosity.

of the pores were drawn from a log-normal distribution (random.lognormvariate, $\mu = -2.2$, $\sigma = 1.5$ output in mm) within the limits $[0.2, 50] \mu\text{m}$, which was derived from high-resolution experimental data, until a porosity of 1% was reached. The porosity was defined higher than experimentally observed to increase the number of defects, i.e. improve statistics. The pore positions were sampled uniformly inside the cylindrical volume and redrawn in case of overlap.

2.2. XCT simulation and analysis

The radiographic simulator aRTist 2.0 (BAM [14]) was used to model the employed XCT system [15]. Different levels of simplification, shown in Table 1, were used to model a range from ideal (#1) to realistic (#4). The detector model (#3-#4) was created using the DetectorCalc module that incorporates experimentally determined image noise and information about the scintillator. The pixel matrix consisted of 2048 px x 1440 px with a pitch of 0.2 mm. The finite focal spot (#4) was modelled as a 2D-Gaussian intensity distribution with a FWHM = 4.0 μm . 10 points were randomly sampled from this distribution and used for ray tracing. 1500 radiographs were simulated on an ideal circular trajectory and reconstructed with a voxel size of 2 μm using CERA 5.1 (Siemens).

Data analysis was performed in VG Studio MAX 3.4 (Volume Graphics). The object was segmented using the advanced surface determination algorithm and registered using the cylinder axis and the two calottes to create a datum system. Furthermore, a 3x3x3 median filter was applied to the volume data of simulation #4 (referred to as #4f). Subsequently, a porosity analysis was performed using the VGEasyPore module with sub-voxel accuracy, a relative threshold of 50% and an area size of 10 voxel to determine the local contrast. To render the algorithm less prone to noise, defects were filtered with a probability threshold (non-disclosed quality metric) of 1% and minimum defect size of 4 voxel, representing an equivalent radius of 2 μm . The following parameters were derived from the pore volume and surface area. The equivalent radius

$$r_{eq} = \left(\frac{3}{4\pi} V_{\text{defect}} \right)^{\frac{1}{3}}$$

and the sphericity that indicates the ratio between the surface area of an ideal sphere with the same volume as the defect and the surface area of the defect:

$$S = \frac{(36\pi V_{\text{defect}})^{\frac{1}{3}}}{A_{\text{defect}}}$$

2.3. Simulation results and discussion

Figure 2 shows simulated XCT slices under the four scenarios described in Table 1: (a) shows a very homogeneous grey value distribution with weak cone beam artefacts. In (b) the polychromatic X-ray spectrum causes beam hardening that results in a grey value gradient across the sample. For (c) detector noise was added that mainly results in form deviations of the defects (as indicated by the arrow). For scenario (d), a finite X-ray focal spot was simulated that causes blur due to the penumbra effect, which renders the contrast of small pores too weak to be detected using a threshold method. The arrow indicates a pore that was not detected by the algorithm.

To quantify the results, tables of the defects were exported from VG Studio MAX and compared to the reference file, which was used to create the digital porosity representation. By assigning the reference defects to the ones detected, comparisons can be made for each defect. As shown in Table 2, adding more error sources to the XCT simulation lowered the

Table 1. Simulated scenarios.

#	Focal spot	X-ray spectrum	Detector
1	point source	monochromatic (55 kV)	Ideal
2	point source	polychromatic, (100 kV, 0.1 mm Cu)	Ideal
3	point source	polychromatic, (100 kV, 0.1 mm Cu)	noise, energy sensitive
4	Gaussian, FWHM = 4 μm	polychromatic, (100 kV, 0.1 mm Cu)	noise, energy sensitive

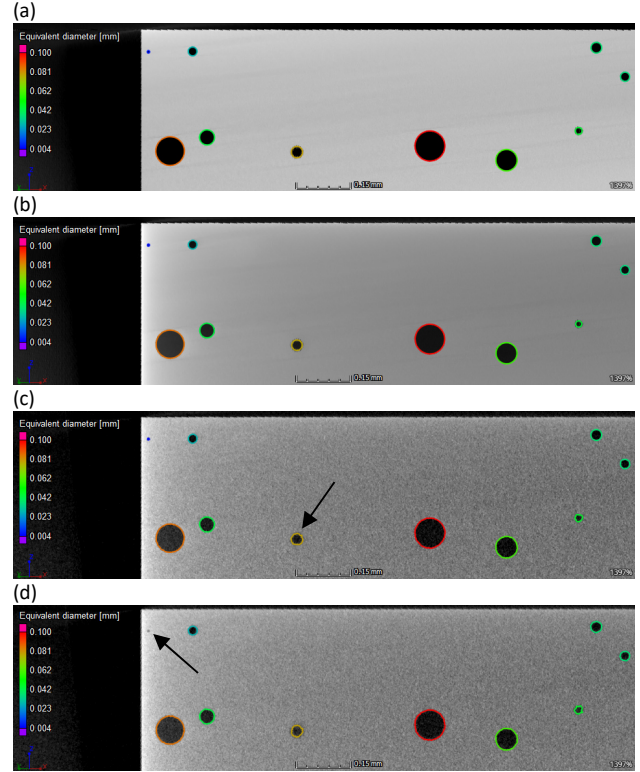


Figure 2. Simulated XCT slices for the different scenarios #1 (a) - #4 (d) shown in Table 1. Detected pores are outlined and colour coded according to their equivalent diameter. The arrows in (c) and (d), respectively, indicate a pore with a distorted shape and a pore, which was not detected due to the limited resolution.

Table 2. Global porosity evaluation results. The different simulation conditions are shown in Table 1.

#	Number of pores detected	Relative error	Porosity (%)	Relative error
Ref.	1813	-	1.0013	-
1	1767	-2.5 %	1.0005	-0.1 %
2	1755	-3.2 %	0.9334	-6.8 %
3	1758	-3.0 %	0.9569	-4.4 %
4	1722	-5.0 %	0.9776	-2.4 %
4f	1622	-10.5 %	0.8876	-10.4 %

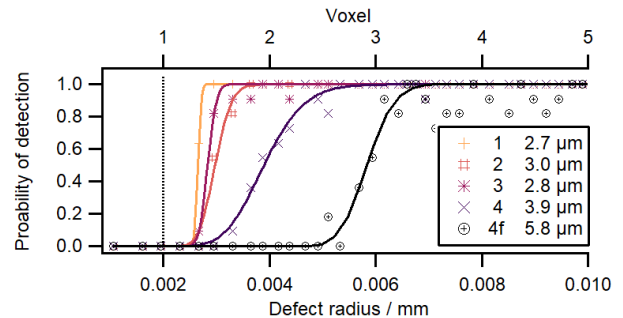


Figure 3. Simulated probability of detection (POD) for the scenarios described in Table 1. The dashed vertical line indicates the analysis threshold (#4f equal to #4 but data filtered with a 3x3x3 median filter).

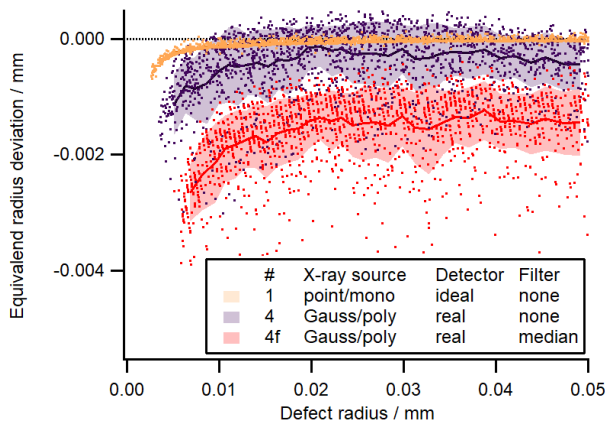


Figure 4. Simulated deviation of the equivalent radius.

number of detected pores and influenced the total porosity estimation. To investigate this effect further, a probability of detection (POD) analysis was performed [13], which is shown in Figure 3. With a point X-ray source (#1-#3) the minimum detectable defect radius was approximately 1.5 voxel (3 μm) and thus only slightly above the resolution limit. With a finite source size (#4), the minimum detectable defect radius increased to about the FWHM of the Gaussian X-ray source intensity distribution (4 μm). This was further increased to 3 voxel (6 μm) when applying a 3x3x3 median filter (#4f).

Next, the deviations of the equivalent radii of the defects were studied in dependence of defect size. In the ideal simulation (#1) the deviations showed a tendency to increase with smaller defect radii (Figure 4). This was also observed in the more realistic simulation (#4), however, the random scatter by the noise influence dominated. Filtering the XCT data (#4f) added a systematic deviation to the equivalent radii. For the shape factor sphericity (Figure 5), negligible deviations were observed for defects larger than 10 voxel in the ideal case (#1). Below, the shape of the defects was influenced by the finite voxel size. Adding noise and a finite X-ray focal spot (#4) led to a reduced sphericity, which was partially counteracted by median filtering (#4f). The deviations between reference and simulated values can be used as a basis for an uncertainty estimation [12].

3. Experimental porosity measurements

3.1. AM process

Small cylindrical Ti-6Al-4V samples with a diameter of 2 mm were manufactured using a custom-developed electron beam melting machine consisting of an Arcam S12 (vacuum chamber, powder management, build tank) retrofitted with an electron gun (pro beam AG & CO) with a maximum power of 6 kW and 60 kV accelerating voltage. To ensure occurrence of defects, the melting was performed using an electron beam power of 1.2 kW and a scanning speed of 8 ms^{-1} resulting in an energy input outside the optimal processing window.

3.2. XCT measurement and analysis

Measurements were performed on our custom metrology XCT system [15] at an acceleration voltage of 120 kV, a target power of 6 W using a 0.1 mm copper filter. The nominal focal spot size was 3 μm . 2000 projections with an exposure time of 5.3 s were recorded on a circular scan trajectory at a magnification of 127 and reconstructed with a voxel size of 1.6 μm .

To evaluate the porosity of the test cylinder we adhered to the following procedure: First, to exclude any influence from surface roughness, a cylindrical region of interest with a height of 1 mm

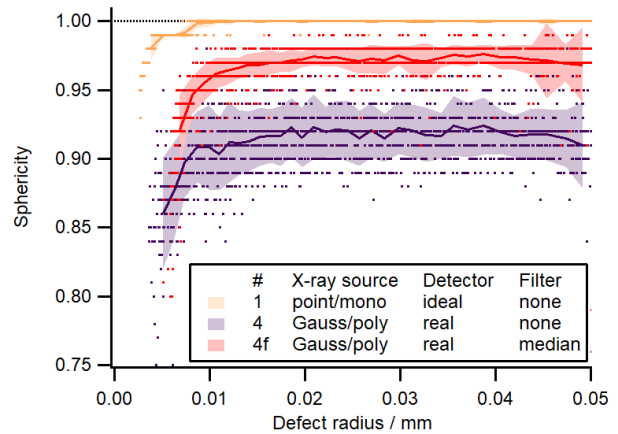


Figure 5. Simulated deviation of the sphericity (reference sphericity = 1).

and diameter of 1.1 mm was defined for analysis. Next, a 3x3x3 voxel median filter was applied to reduce noise. Subsequently, the porosity analysis described in section 2.2 was performed.

3.3. Experimental results and discussion

The results show a heterogeneous distribution of defects in terms of size (Figure 6) and shape (Figure 7). This suggests that the digital porosity twin requires refinement concerning the complexity of the defect shapes. In total, 476 defects were detected resulting in a porosity of 0.37 %. It can be seen that spherical air pores (Figure 7, red-orange) can be distinguished from high-aspect-ratio lack-of-fusion defects (Figure 7, green-blue) solely by their sphericity. As shown in Figure 8, a size dependent measurement uncertainty was assigned to each defect based on the simulation results in section 2.3. The presence of defects below the 50 % probability of detection (POD) threshold in Figure 8 is attributed to the uncorrected systematic underestimation of pore equivalent radii (Figure 4).

4. Conclusion

Digital porosity representations make it possible to study stochastic, e.g. detector noise, and local, e.g. beam hardening, influences on XCT porosity measurements.

Both the XCT simulation and the digital porosity twin require further refinement. The former by the introduction of e.g. machine geometry errors, in-line phase contrast and non-ideal detector pixels, the latter by better reflecting differently shaped defects, such as air pores and lack-of-fusion defects. This information could be deduced from higher resolution scan data.

The method enables benchmarking different segmentation and post-processing procedures to assess porosity against ground truth and deriving lower order models to predict the probability of detection solely based on a small number of parameters such as voxel size and focal spot. Next, the information gained from the digital representation can be fed back to correct the measured data for systematic errors, rendering it a full digital twin.

Acknowledgments

We thank Sylvain Hauser for XCT measurements and Federico Grasso Toro for fruitful discussions on digitalisation.

The project MANUELA has received funding from the European Union's Horizon 2020 research and innovation programme under grant agreement n°820774

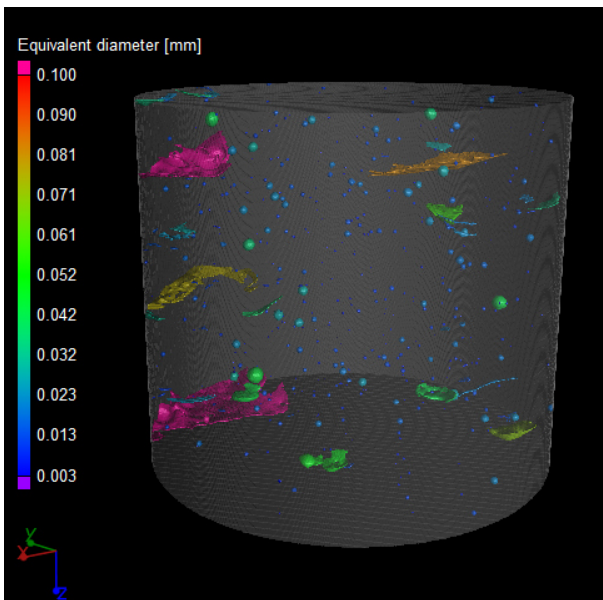


Figure 6. Experimentally determined defect equivalent diameter.

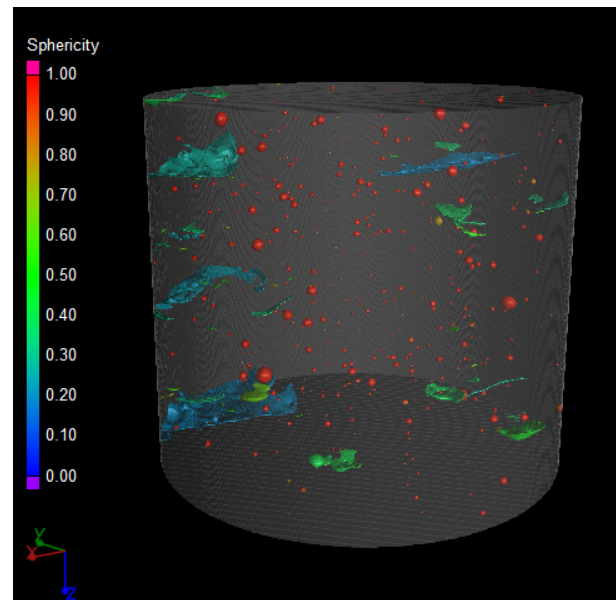


Figure 7. Experimentally determined defect sphericity.

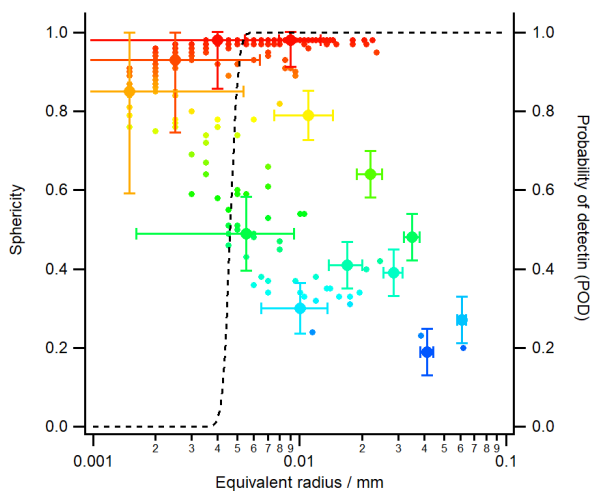


Figure 8. Experimentally determined defect sphericity versus equivalent radii. The error bars (only shown for a selection of markers) indicate the expanded measurement uncertainty ($k=2$) and the dashed line indicates the probability of detection derived from simulations.

References

- [1] Leach R K, Bourell D, Carmignato S, Donmez A, Senin N and Dewulf W 2019 Geometrical metrology for metal additive manufacturing *CIRP Ann.* **68** 677–700
- [2] Kruth J P, Bartscher M, Carmignato S, Schmitt R, De Chiffre L and Weckenmann A 2011 Computed tomography for dimensional metrology *CIRP Ann. - Manuf. Technol.* **60** 821–42
- [3] du Plessis A, le Roux S G, Waller J, Sperling P, Achilles N, Beerlink A, Métayer J F, Sinico M, Probst G, Dewulf W, Bittner F, Endres H J, Willner M, Drégelyi-Kiss Á, Zikmund T, Laznovsky J, Kaiser J, Pinter P, Dietrich S, Lopez E, Fitzek O and Konrad P 2019 Laboratory X-ray tomography for metal additive manufacturing: Round robin test *Addit. Manuf.* **30** 100837
- [4] Townsend A, Racasan R, Leach R, Senin N, Thompson A, Ramsey A, Bate D, Woolliams P, Brown S and Blunt L 2018 An interlaboratory comparison of X-ray computed tomography measurement for texture and dimensional characterisation of additively manufactured parts *Addit. Manuf.* **23** 422–32
- [5] Sinico M, Ametova E, Witvrouw A and Dewulf W 2018 Characterization of Am Metal Powder With an Industrial Microfocus CT: Potential and Limitations *ASPE and euspen Summer Topical Meeting - Advancing Precision in Additive Manufacturing* (Lawrence Berkeley National Laboratory, Berkeley, California, USA) pp 1–6
- [6] Bircher B A, Meli F, Küng A and Thalmann R 2018 A geometry measurement system for a dimensional cone-beam CT *8th Conference on Industrial Computed Tomography, Wels, Austria (iCT 2018)*
- [7] Hermanek P, Zanini F and Carmignato S 2019 Traceable Porosity Measurements in Industrial Components Using X-Ray Computed Tomography *J. Manuf. Sci. Eng. Trans. ASME* **141**
- [8] Verein Deutscher Ingenieure 2013 *VDI/VDE 2630 - 2.1 Coputertomografie in der dimensionellen Messtechnik: Bestimmung der Messunsicherheit und der Prüfprozesseignung von Koordinatenmessgeräten mit CT-Sensoren*
- [9] Chen X, Zhang Q, Sun W, Zeng W, Jin X, Scott P J, Jiang X and Lou S 2020 Development of virtual reference samples for XCT measurements of additively manufactured surface texture Development of virtual reference samples for XCT measurements of additively manufactured surface texture *10th Conference on Industrial Computed Tomography (Wels, Austria (iCT 2020))*
- [10] Yildiz E, Møller C and Bilberg A 2020 Virtual factory: Digital twin based integrated factory simulations *Procedia CIRP* **93** 216–21
- [11] Riesener M, Schuh G, Dölle C and Tönnies C 2019 The digital shadow as enabler for data analytics in product life cycle management *Procedia CIRP* **80** 729–34
- [12] Wohlgemuth F, Müller A M and Hausotte T 2018 Development of a virtual metrological CT for numerical measurement uncertainty determination using aRTist 2 *tm - Tech. Mess.* **85** 728–37
- [13] Gollwitzer C, Bellon C, Deresch A, Baron H-U and Ewert U 2012 Reliability Investigations of Radiographic Testing Using aRTist as a Simulation Tool aRTist and SimuPOD *18th World Conference on Nondestructive Testing (Durban, South Africa)* pp 16–20
- [14] Bellon C, Deresch A, Gollwitzer C and Jaenisch G-R 2012 Radiographic Simulator aRTist : Version 2 *18th World Conference on Nondestructive Testing (Durban, South Africa)*
- [15] Bircher B A, Meli F, Küng A and Thalmann R 2020 METAS-CT: Metrological X-ray computed tomography at sub-micrometre precision *euspen's 20th International Conference & Exhibition (Geneva, Switzerland (virtual))*

Impulse excitation technique for improved inspection in additive manufacturing

Juan Jose Bustos¹, Alex Van den Bossche¹

¹GrindoSonic bvba
Esperantolaan 4, Leuven 3001, Belgium
Juanjose.bustos@grindosonic.com

Abstract

The determination of mechanical properties is key when characterizing a material. In additive manufacturing, monitoring and validating printed materials is fundamental to confirm the adoption of this technology, aiming to improve the uniformity during a printing process. By using a non-destructive-testing method such as the Impulse Excitation Technique (IET), printed materials can be easily and accurately inspected to improve the printing process validation. Six lattice cubes, divided into two groups, were printed and tested using the Archimedes' method, gas pycnometry and impedance measurement by eddy current. These methods confirmed the identical values in volume, density and current resistance among the printed parts. Only by the use of IET we were able to detect differences among their elastic properties and internal friction. These results represent a highly valuable finding which indicates the possibility to improve the stability of the printing process by correlating these results with the printing parameters.

Additive Manufacturing, NDT, Impulse Excitation Technique, Material characterization, Quality Control, Quality assurance, LPBF

1. Introduction

Additive manufacturing (AM), also known as 3D printing, is an innovative technology that enables the construction of objects layer-by-layer starting from a 3D file that includes process parameters specifically dedicated to AM. Special attention from different branches of industry is dedicated to Laser Powder Bed Fusion (LPBF), which is an AM process consisting of a high-energy intensity laser beam that scans over the powder bed and fuses particles together according to the shape of that object [1], [2]. LPBF allows to manufacture complex geometries such as lattices and parts containing internal structures like cavities and channels, as well as mass-production of custom parts.

More and more manufacturers are using AM beyond prototyping and research. Nevertheless, there remain still some big challenges, particularly related to scalability, costs and materials, that need to be tackled in order to help for the acceptance of AM [3]. Therefore, quality assurance methods are necessary to bring bigger confidence in the adoption of this innovative technology as they, together with quality control methods, facilitate production of high-quality printed parts [4].

Material properties play an important role when characterizing a material. Moreover, the inspection of these properties, as well as the inspection of defects, could be performed by using different methods, either destructive or non-destructive.

The Impulse Excitation Technique (IET) is a known non-destructive testing method in industry, broadly known in refractory, cement and friction materials industry. This method is commonly used to determine mechanical properties such as Young's Modulus, Shear Modulus, Poisson's Ratio and internal friction.

The goal of this investigation is to apply the IET method into the inspection process of additive manufacturing to contribute for a more sustainable and accurate quality assurance and quality control.

2. Material and methods

The work involves the study of six Ti lattice cubes printed by LPBF. These cubes were divided into two groups of three cubes each, based on their cell sizes (77% and 79%). Figure 1 shows these components on a foam bed, ready to be tested by IET.

In order to guarantee the integrity of the printed parts, it is necessary to investigate, evaluate and validate existing volume non-destructive testing methods with complex parts as well as utilizing these methods for routine control of printed parts [5].

Previous to this study, the six lattice cubes were tested on the following methods [5]:

- Archimedes' method and gas pycnometry (volume and density)
- Eddy-current testing (impedance)



Figure 1. Six lattice cubes under study. Group 1 (in front) and group 2 (back).

The Archimedes' method and gas pycnometry allow the density measurement of the Ti cubes with different cell size structure. These methods were used due to the advantage on having independence on shape and size, surface condition and it is also an accredited method [6].

The Eddy-current testing enables to differentiate two specimens with different lattice sizes on the surface, with a certified and fast method [6].

2.1. Impulse Excitation Technique (IET)

The impulse Excitation Technique is based on the analysis of the resonance frequencies of a sample after it has been excited by a mechanical impulse. The vibration of the sample is detected by a piezoelectric accelerometer contact transducer or an acoustic vibration detector.

Three fundamental ground vibration modes are of interest when determining elastic properties: flexural, torsional and longitudinal modes. This method allows therefore to determine the dynamic elastic properties of elastic materials if the geometry, mass, and mechanical resonant frequencies of a suitable (rectangular or cylindrical geometry) test specimen of that material can be measured. Dynamic Young's modulus is calculated using the resonant frequency in either the flexural or longitudinal mode of vibration. The dynamic Shear modulus, is calculated by using the torsional mode. Dynamic Young's modulus and dynamic shear modulus are used to calculate Poisson's ratio [7].

For example, for the fundamental flexural frequency of a rectangular bar [7, eq. (2)]:

$$E = 0.9465 \times (m \times f_f^2 / b) \times (L^3 / t^3) \times T_1$$

where:

- E = Young's modulus, Pa,
- m = mass of the bar, g,
- b = width of the bar, mm,
- L = length of the bar, mm,
- t = thickness of the bar, mm,
- f_f = fundamental resonant frequency of bar in flexure, Hz, and
- T_1 = correction factor for fundamental flexural mode to account for finite thickness of bar, Poisson's ratio, and so forth.

Moreover, the measurement of damping results of great importance when characterizing a material. The damping, or attenuation value, is an indication of the amount of internal friction of a material, and it is independent of shape or size, for which a high damping value results on a clear indication of internal defects, such as microcracks [7], [8].

The frequency analysis for all six cubes was performed and analysed with GRINDOSONIC® MK7. All cubes were tapped twice to guarantee repeatability in the longitudinal mode. The set-up of the measurements can be seen in Figure 2.

The software GRINDOSONIC® Waterfall Spectrogram was then used for data visualization.



Figure 2. Set-up of lattice cube in order to perform IET.

3. Results and discussion

3.1. Volumetric testing

The results provided by the Laboratoire National de Métrologie et d'Essais (LNE) showed a consistency on volume and electrical conductivity for the 3 cubes in both groups as well as equal density among all six cubes. Gas pycnometry and Archimedes' methods give coherent density measurements. The repeatability in impedance shows a repeatability on surface for this AM process [5]. These results show no clear difference among the cubes on each group as seen in Figure 3, 4, 5.

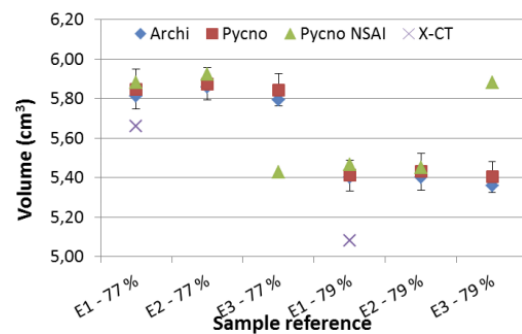


Figure 3. Volume of the six lattice cubes [5].

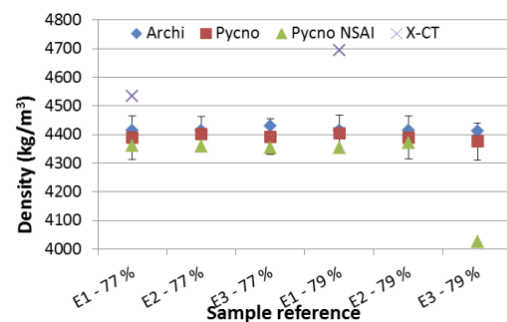


Figure 4. Density of the six lattice cubes [5].

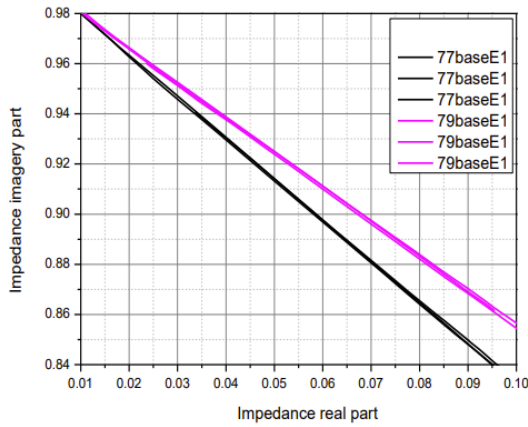


Figure 5. Impedance of the six lattice cubes [5].

It results then challenging to find a significant difference between the printed parts by the use of these non-destructive methods, leading into an initial idea that the process is stable and consistent in terms of volume, density and electrical impedance.

3.2. Frequency analysis

Impulse Excitation technique showed, by the frequency of the cubes, on the contrary difference between both groups and among each component. These values are described in table 1. Frequency values show that the first group has a big spread among them but higher frequencies with respect to the second group, which are proportional to the Young's modulus and therefore are stronger parts. On the other hand, although the second group has lower frequency values, their spread is smaller, showing that the overall process of printing these cubes is more consistent, considering the mechanical behaviour.

Table 1 Frequency and damping values for six lattice cubes

	Component	Frequency (Hz)	Damping (Hz)
Group 1	Cube 1	20728	18.91
	Cube 1	20726	10.58
	Cube 2	20997	10.58
	Cube 2	21005	10.58
	Cube 3	21175	22.00
	Cube 3	21175	18.50
Group 2	Cube 1	20532	10.58
	Cube 1	20535	16.83
	Cube 2	20553	10.58
	Cube 2	20552	10.58
	Cube 3	20620	23.31
	Cube 3	20620	26.25

The frequencies were plotted into the Waterfall Spectrogram Software for a clearer visualization of the results, as shown in Figure 6. In this plot, the first group is presented in the front and the second group in the back. Here, the difference on damping is more visible. Damping can be measured as the width at half height of the frequency peak [8]. By looking into the plot, the last cube of the second group is clearly the one with the highest value of damping, as also showed in table 1.

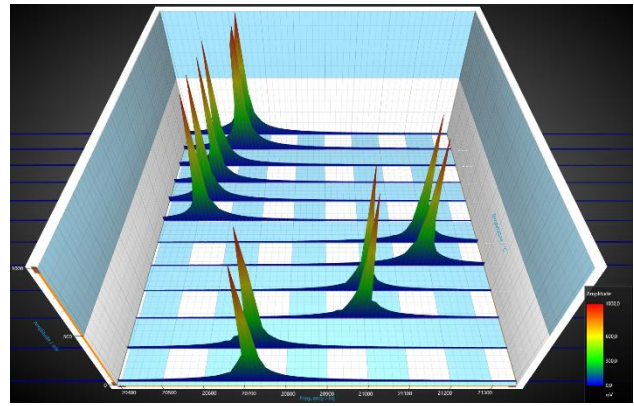


Figure 6. Waterfall Spectrogram of the six Ti lattice cubes.

These results create special attention to the quality consistency of the printing process, revealing that there exists a difference on mechanical properties among parts printed on the same machine with the same process parameters. One possible explanation could be related to the position of the parts on the chamber, as well as the sinter quality that it's achieved during the build.

By testing only one part (e.g. in a tensile testing procedure), one could draw wrong conclusions if the part that was chosen is the one presenting the higher frequency, resulting in a higher Young's modulus. Ergo, it is evident the importance to guarantee first a stable process to achieve equal mechanical properties among all printed parts.

Special attention should be given to the energy deposition of the printing process among the whole build plate, which would explain better the sinter quality of the parts. Improving the distribution of energy during printing could lead to a higher quality consistency of the AM process, which becomes very important when printing high-end parts that need to meet specific standards as well as when printing a big part that occupies most of the build platform.

Furthermore, this certainly grows of higher importance when dealing with multi-optics machines, where other considerations come into place such as calibration and alignment.

Finally, the IET method is useful not only for quality control, where parts can be checked and classified based on their frequency response, but also on a quality assurance approach. By controlling every step of your AM process, IET can lead into easy detection of where the process is failing or improve the whole process itself.

4. Conclusion

Volumetric NDT methods were performed to prove the integrity of the Titanium lattice cubes. These tests showed no clear difference among the printed parts.

By utilizing the IET method it was possible to detect a difference on frequency and damping for all six cubes, which are strictly correlated to the elasticity and internal friction of the material. The first group (77%) showed a bigger spread in terms of frequency whilst the second (79%) showed a lower spread. The last cube of the second group showed though a higher value of damping with respect to the other five cubes, resulting on higher internal friction due to possible microcracks.

Although this method was used for a specific technology within the AM field, it can be applied to any material that vibrates. This means, that in the context of AM, the same

approach could be followed in order to improve the inspection of printed parts, regardless of their process methodology.

In order to bring these results to a more conclusive interpretations, future work include the tomographic analysis of all 6 cubes in collaboration with the KU Leuven university.

Acknowledgements

The authors acknowledge the Laboratoire National de Métrologie et d'Essais (LNE) for the comparative measurements in terms of density, volume and electrical resistance.

References

- [1] T. DebRoy et al., "Additive manufacturing of metallic components – Process, structure and properties," *Prog. Mater. Sci.*, vol. **92**, pp. 112–224, 2018.
- [2] Thijs L, Verhaeghe F, Craeghs T, Van Humbeeck J, and Kruth J.P., "A study of the microstructural evolution during selective laser melting of Ti-6Al-4V," *Acta Mater.*, vol. **58**, no. 9, pp. 3303–3312, 2010
- [3] Jabil, "3D printing technology trends - A survey of Additive Manufacturing Decision-Makers," dimensional research, 2021.
- [4] EMPIR Project- JRP Protocol – Annex I v2, Metrology for Additively Manufactured Medical Implants (15HLT09 MetAMMI), 2016.
- [5] Obaton A-F, "Contrôle volumique des pièces réalisées en fabrication additive fusion laser sur lit de poudre", presented to JT Membres, Institut de Soudure, Paris, France, Oct. 10, 2020. [PowerPoint slides].
- [6] Wilbig J, Borges de Oliveira F, Obaton A-F, Schwentenwein M, Rübner K, and Günster J, 'Defect detection in additively manufactured lattices', *Open Ceramics*, p. 100020, Aug. 2020, doi: 10.1016/j.oceram.2020.100020.
- [7] Standard Test Method for Dynamic Young's Modulus, Shear Modulus, and Poisson's Ratio by Impulse Excitation of Vibration¹, ASTM-E1876-01, 2002.
- [8] Gade S, Herlufsen H, "Digital Filter vs FFT Techniques for Damping Measurements", *Brüel & Kjær, Sound and Vibration, Nærum, Denmark*, 1990.

Dimensional accuracy of an artifact for rapid casting

Muslim Mukhtarkhanov¹, Didier Talamona¹, Asma Perveen¹

¹*Department of Mechanical and Aerospace Engineering, Nazarbayev University, Nur-Sultan 010000, Kazakhstan*

muslim.mukhtarkhanov@nu.edu.kz

Abstract

Stereolithography based Additive Manufacturing (AM) technology has seen ever-increasing popularity in numerous modern applications. High dimensional accuracy, fine detail, high quality surface finish and availability of a wide range of materials makes this technology stand out from the other AM technologies. With decreasing cost, consumer grade printers can even be used at home set up. In addition, recently developed new materials such as castable resins generates greater interest for those involved in the casting production of small parts. Therefore, there is a need among the manufacturers to access qualitatively the innovations, whether it is a hardware improvement or new materials. As the dimensional accuracy of parts has been recognized as one of the most important parameters among the manufacturers, the aim of this paper is to evaluate the dimensional accuracy of SLA manufactured parts printed on the Formlabs Form 2 3D printer (3D Systems). For this evaluation, a benchmark with the external dimension of 60x60x25 mm has been designed which allows to assess the effect of the part position on the build platform, as well as the dimensional accuracy in X, Y and Z axes. To assess the quality of printed parts, the rectangular shape benchmarks have been printed on four locations of the build platform with sides parallel to X/Y axes and measures of several dimensions of the parts were collected. The results of the study show that both the location of the part on the build platform and orientation affect the dimensional accuracy. For instance, it was found that the accuracy in z vertical direction was the lowest, which confirmed the findings from other publications. Additionally, the findings have shown that the accuracy of the part might vary depending on the size of the part. In summary, SLA based AM technology continues to be a great tool for manufacturers in many fields. However, it is important to identify the limits and potential pitfalls that might be encountered during the manufacturing process and this study has attempted to reveal few controllable factors affecting the accuracy. These factors include position of the part on the build platform, build direction and size of the feature.

Dimensional accuracy, Additive manufacturing, Stereolithography, Benchmark

1. Introduction

Since its first appearance in the market, Stereolithography (SLA) based AM has shown great potential for the application in Rapid Casting (RC) industry. However, due to excessively expensive equipment and materials, AM machines were not considered as relevant to the Casting industries. Nevertheless, with the continuous development and innovations, nowadays, it is possible to find different machine configurations with more affordable price and high accuracy on the market. This has created an immense opportunity for small and large companies that are using RC, Investment Casting (IC) and Rapid Prototyping (RP). SLA based AM technology allows manufacturing of parts with complicated shapes and forms directly from a CAD model rapidly and with ease. Moreover, the market offers special types of polymers such as castable resins, making it possible to directly create investment patterns and eliminating the need of tools and reducing lead time and costs.

Among many properties of printed parts, the dimensional accuracy is one of the most important. Failing to produce a part within required dimensional tolerance renders the production process as ineffective. Therefore, it is crucial to identify the capabilities of the SLA technology in terms of accuracy at the earliest stage of designing or planning. By identifying the dimensional accuracy of parts, this research study aims to establish the accuracy level of Formlabs Form 2.

The established practise of identifying the dimensional accuracy of any given AM technology include benchmark/artifact design, manufacturing the benchmark and measuring the accuracy with the available instruments. By evaluating the errors of dimensional and geometric nature, one can identify the accuracy level of the technology concerned. The benchmark designed for this research is of the size of 60x60x25 mm (L*W*H) which allows to place four benchmarks at the four corners of the build platform to assess whether the position of the part on the platform effects the quality of the print or not. Although it is recommended to design an artifact which is large enough to cover the whole build area [1], producing smaller parts also minimizes the possibility of warpage occurrence [2].

It has been reported by several researchers that the build direction has an effect on the accuracy too [3-6]. It is noteworthy to mention that there is a level of contradictory information on whether the vertical Z build direction is better in terms of accuracy or worse. For instance, while Ji et al [4] and Islam et al [5] stated that the Z build direction is more accurate compared to X-Y plane orientation, the findings of Alexey et al [6] has shown the opposite. The present work aims to clarify this contradiction.

It appears that very limited information is available concerning the issue of part's location on the build platform and its effect on the accuracy. In general, literature conclude that the parts printed close to the center of the platform show higher accuracy

compared to those printed in the periphery. Previous literature mainly compared the dimensional accuracy of parts manufactured throughout the whole area of a build plate. However, the present work aims to make comparisons among benchmarks printed on the four corners of the build plate. In this case, an equal portion of each benchmark is located on both periphery and on the middle part of the build platform as shown in Figure 1. Thus, if the findings reveal a significant difference in accuracy among the four parts, it can be concluded that other locations of the build area might be preferable too in terms of accuracy. Moreover, the study finds it necessary to identify how features differ in accuracy depending on the distance they have from the center of the platform.

It is well known that depending on the size of the part, the accuracy level might change too. For example, as the size of the part increases, the shrinkage value increases proportionally. Therefore, several feature sizes have been introduced in this study for comparison purpose.

By collecting a meaningful measured set of data, this study provides preliminary results to establish whether the printing position on the build platform affects the accuracy of features or not. In addition, this study attempts to find the build directions that might produce higher accuracy and, finally, address the issue of feature size's influence on the accuracy.

2. Benchmark design

As can be seen from Figure 2, the benchmark represents a collection of simple geometrical features positioned on the surface of a base plate. These types of features are

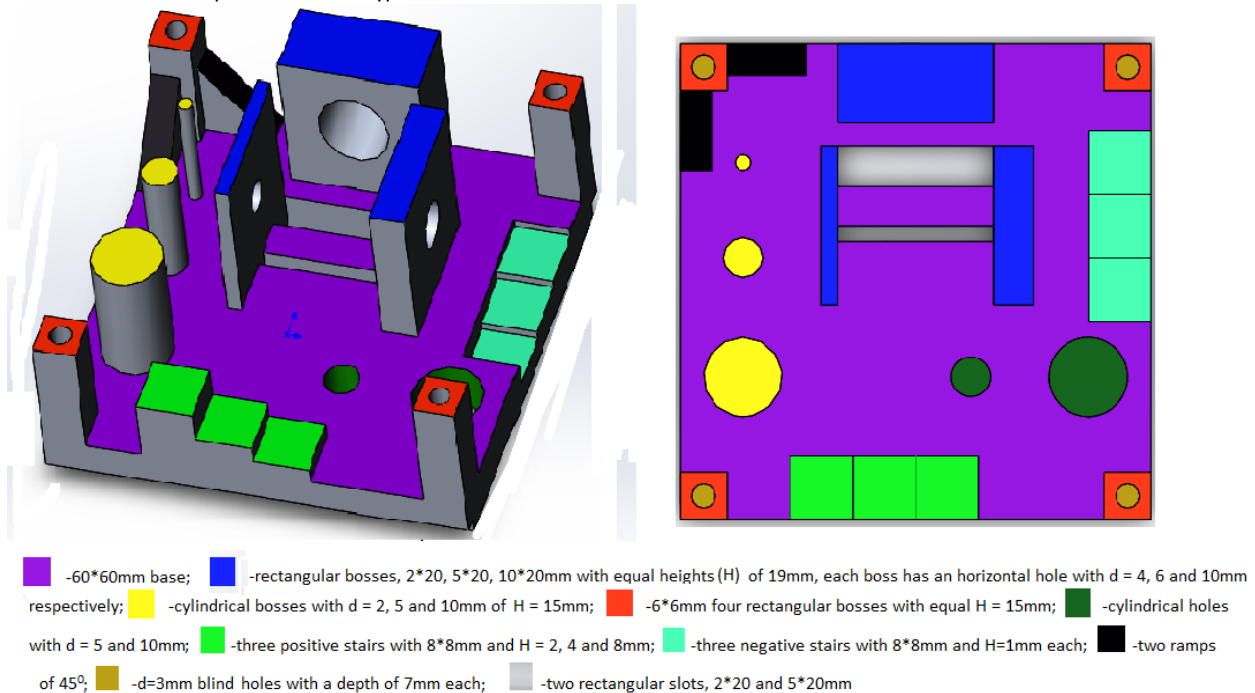


Figure 2. CAD model of the benchmark showing top view (right) and oblique view (left).

3. Experimental details

This section describes experimental procedures and methodology pertained to three main aspects of the study. Namely, the effects of part's position, orientation, and size on the accuracy.

3.1 The effect of part's position on the build platform

To identify the effect of part's position on the build plate using ANOVA (Analysis of Variance), the sixteen benchmark samples

representative of the most relevant objects produced by RP processes. The geometrical features are aligned with either X or Y axis of the SLA machine to evaluate the accuracy along those axes. In addition, the sizes and locations of all features are designed to be accessible to a digital calliper's jaws. The number and types of controlled elements are as follows: linear lengths (49), diameters of holes (9) and diameters of cylinders (3).

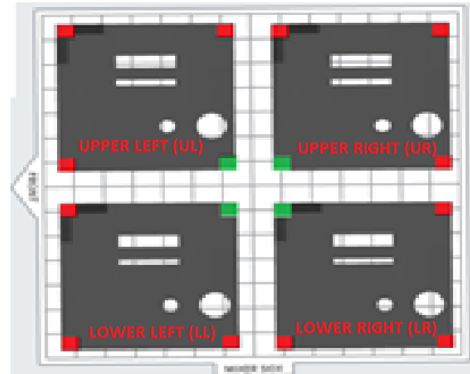


Figure 1. Benchmark's location and orientation on the build plate.

have been printed with 4 of 16 parts at each corner of the built platform as shown in Figure 1. Individual samples were labelled as Lower Left (LL1), Lower Right (LR1), Upper Left (UL1) or Upper Right (UR1). The number after two capital letters corresponds to an order the sample was printed within its group. For example, if the LL1 was printed first among LL group, an LL4 was printed last.

General purpose resin from Formlabs was used. The layer thickness was 0.1 mm, and all samples were printed one at a time with minimum support structures. After printing process, the samples were washed in Isopropyl alcohol for ten minutes and cured by the exposure to sunlight for eight hours. The

measurements were performed using a digital calliper with resolution = 0.01 mm, accuracy = 0.02 mm, and repeatability = 0.01 mm.

The confidence level α for One-Way ANOVA test was taken as 0.05. The Null hypothesis states that the mean values of absolute average deviations between groups of LL, LR, UL and UR are equal. In other words, if we assume that the absolute average deviation values of four benchmarks printed on lower left corner of the build platform are labelled as LL1....LL4, the Null hypothesis is accepted if the total variance within the group LL is equal to the total variance between the rest of the groups (LR, UL and UR). The average deviation values in the test were taken as absolute i.e., the negative values corresponding to undersized features were treated as positive.

The measured dimensions for which the deviation values have been recorded are listed in table 2.

To find the difference in accuracies between features printed close to the center and those on the periphery, the identical features have been chosen for the comparison as shown in Figure 1.

The features in Figure 1 are 6×6×15 mm (L×W×H) rectangular bosses located at four corners of the benchmark. In total, the average of deviations in heights (15 mm) of 48 periphery red bosses, representing 16 samples, were compared to corresponding 16 central green bosses' average deviation values.

3.2 Effect of build direction on the accuracy

For this type of study, certain features of the benchmark have been chosen for comparison purpose as highlighted in Figure 3.

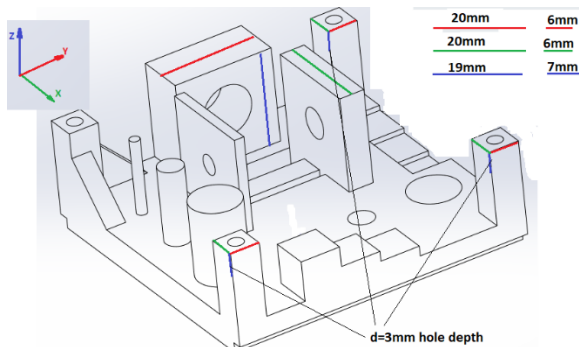


Figure 3. The dimensions of selected features for comparison (shown as red, green, and blue)

The values to be compared are chosen to be deviations of dimensions along XYZ axes corresponding to features indicated as red, green, and blue in Figure 3. In other words, the deviation values of dimensions that are similar in colour were compared to those of different colour. The main requirement for the features subject to comparison is the size compatibility. In addition, it was decided to not include features with dimensions over 20 mm for comparison as the maximum height of the features in Z build direction is 19 mm.

3.3 Effect of Feature's size on accuracy

In order to make comparison among features of varying sizes, it was necessary to divide features subject to analysis according to their sizes. For this purpose, table 1 was prepared that shows the classification of features for the analysis. It should be noted that the classification was according to the Standard tolerance grades gradation of sizes. The measured values are the linear dimensions along XYZ axes. The share of measured features along XYZ axes are almost equal.

Table 1. Features classified according to their sizes.

Feature type	Size range, mm	Number of measured values
Small	≤6	17(×16)
Medium	6<...<18	13(×16)
Large	>18	9(×16)

4. Results and discussion

The P values for One-Way ANOVA test have been found and listed in table 2.

Table 2. P values found for all measured deviations.

Measured dimensions	P value
Linear length of features measured along X axis (17*)	0.027
Linear length of features measured along Y axis (14)	0.025
Linear length of features measured along Z axis (20)	0.817
Diameters of holes and cylinders (12)	0.468

* - the numbers in brackets correspond to a number of measured values for one benchmark

As can be seen from table 2, a half of P values favour the alternative hypothesis. Therefore, dimensional comparison supports the notion that the position of the part on the build platform does influence the accuracy.

There are numerous explanations that have been reported by others regarding how the position might affect the accuracy. They include the localized wear of silicon layer that covers the resin tank, angulation of the laser beam, material properties and even position with regards to the wiper location. As for the following research, it is difficult to draw any solid conclusion on the source of the errors and it is beyond the scope of the study. Another important observation was noticed when comparing accuracies of identical features such as four 6×6 mm rectangular bosses located at corners of the benchmarks (see Figure 1). The differences among deviations in Z axis corresponding to features printed close to the center and peripheries were very small. For instance, it was found that the absolute average deviation values in heights of 6×6 mm rectangular bosses were 60 μm for features located close to the center and 70 μm for those in periphery. Thus, the findings support the view that the features printed at the periphery are not inferior to ones printed at the center with respect to accuracy.

As far as the build orientation is concerned, the boxplot in Figure 4 clearly shows the presence of its influence on the accuracy. According to the results of the comparison, the least accurate build orientation appears to be along Z axis. As for the remaining two axes, the highest accuracy was achieved in Y axis direction. Another significant observation to notice from Figure 4 is the ratio between oversized and undersized values. For instance, in the case of Y build direction, there is an almost equal share between oversized and undersized values. If we look at the remaining axes, Z build direction values are nearly all undersized. As for X axis, approximately 2/3 of the data is undersized. Two main causes can explain the prevalence of undersized features. One is the effect of shrinkage due to polymer cure. The other cause is the vertical pressure exerted from the build plate on the resin layer surface during laser scanning. Especially it is true for the parts printed flat on the platform[6]. Due to absence of supports, the pressure exerted from the build plate is applied directly to first polymer layers on the flat bottom of the part. As for the accuracy for X axis direction, it is interesting to observe that the movement of the resin tank occurs in X axis. As was indicated by Alexey et al [6], a

“peel-force” might be a cause of discrepancies for those objects lined up in the direction of the tank movement.

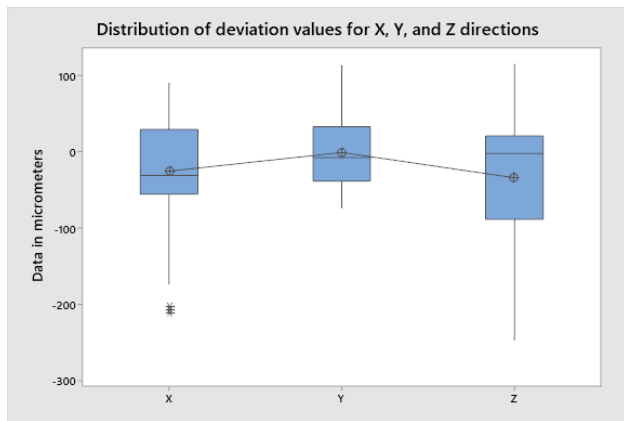


Figure 4. The boxplot of compared data.

A general trend observed in the size/accuracy analysis is the increase of errors with sizes of the features and it can be seen from the boxplot in Figure 5 and a graph in Figure 6. Important to note that the largest deviations were observed in features such as negative stair lengths, slots, and overall length of 60 mm base. Those highest deviations are shown as stars in Figure 6. According to the research conducted by Islam et al [5] in 2016, the volumetric shrinkage of parts is the main reason that explains the trend in Figure 6, where it is obvious that with the size increase the errors become more negative.

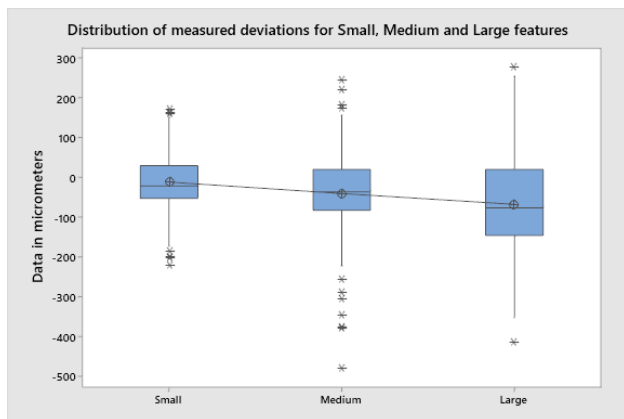


Figure 5. Measured deviation values for feature size effect analysis.

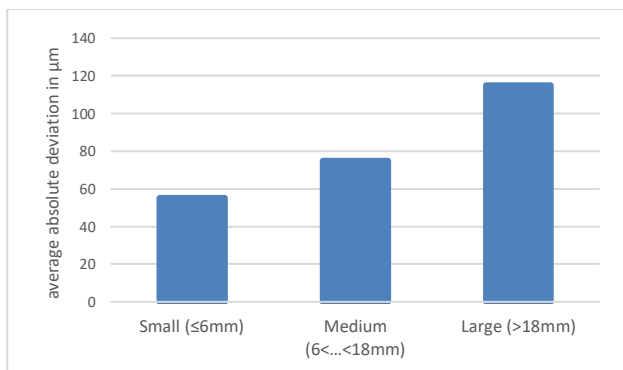


Figure 6. Comparison between absolute average deviation values for features of varied sizes.

5. Conclusion

This study has analyzed dimensional properties of a part manufactured using desktop SLA 3D printer. By measuring the

dimensional accuracy of the designed benchmark, the obtained data has helped to identify important parameters affecting the accuracy of printed samples. The preliminary findings show that part’s position on the build platform has an influence on the dimensional accuracy of features. P values identified for sizes along X and Y axes are 0.027 and 0.025 respectively, whereas differences between features in Z build direction have not been noticed. In addition, the research revealed that the orientation of the features along X, Y or Z direction affects the accuracy. The features of similar sizes aligned in three different axes showed the next range of deviations. For X axis {-210, 90} in μm, Y axis {-70, 110}, and Z axis {110, -250}. Therefore, features’ sizes along Y axes seems to be the most accurate while Z axis build direction was prone to show the highest values of error. Finally, it was found that the accuracy of the manufactured part might be high or low depending on its size.

Acknowledgement

This research study was funded by Nazarbayev University under the project “Cost effective hybrid casting methods for cellular structures”, grant No.: 240919FD3923. Authors would like to express their sincere gratitude to Nazarbayev University for the full support in accomplishing this research.

References

- [1] M. S. Moylan, J. Slotwinski, A. Cooke, K. Jurens, 2012 *Solid Free. Fabr. Symp.*, pp. 902–920.
- [2] L. Rebaioli and I. Fassi, 2017 *Int. J. Adv. Manuf. Technol.*, **93**, pp. 2571–2598.
- [3] J. G. Zhou, D. Herscovici, and C. C. Chen, 2000 *Int. J. Mach. Tools Manuf.*, **40**, pp. 363–379.
- [4] J. S. Shim, J. E. Kim, S. H. Jeong, Y. J. Choi, and J. J. Ryu, 2020 *J. Prosthet. Dent.*, **124**, pp. 468–475.
- [5] M. N. Islam, H. Gomer, and S. Sacks, 2017 *Int. J. Adv. Manuf. Technol.*, **88**, pp. 3077–3087.
- [6] A. Unkovskiy, P. H. B. Bui, C. Schille, J. Geis-Gerstorfer, F. Huettig, and S. Spintzyk, 2018 *Dent. Mater.*, **34**, pp. e324–e333.

Enhancing surface finish consistency by novel ECM process on SLM AM components

Ahmed Tawfik¹, Aaron Holt², Paul Bills¹, Neil Dickinson², Liam Blunt¹

¹Huddersfield University, UK

²Holtex group Ltd, UK

Ahmed.tawfik@hud.ac.uk

Abstract

Additive manufacturing (AM) is a process where the component is built layer-by-layer using powder or wire precursors. This novel technology offers advantages over conventional subtractive machining in terms of design optimization and weight reduction and enabling the creation of complex internal and external features that are impossible to achieve with conventional subtractive machining. AM component's surface finish is highly dependent on build orientation; thus, the surface finish is vastly different across the same component. Furthermore, the AM component's surface finish is relatively rougher than those manufactured by subtractive machining. Electrochemical polishing (ECM) is the process of removing the material from a component surface to optimise the finish. In the ECM process the part is placed in ionic solutions and material is removed by dissolution via a high electric current. In this experiment stainless steel 316 artefacts were made by an SLM Renishaw 400 AM machine, they were then polished by an AM optimised ECM method. The artefact surface was characterised by Alicona G5 focus variation before and after polishing. The impact of the ECM polishing on surface finish is reported. The data processing was carried out using Mountains digital surf software and focussed on ISO 25178 standard areal topography parameters. The focus of this study is identifying the impact of ECM on optimising the relatively AM surface resulting from the AM process.

Keywords: Additive manufacturing, ECM, powder bed fusion, selective laser melting, focus variation.

Application of metal additive manufacturing material extrusion in the production of tool inserts for polymer profile extrusion die surface roughness investigation

M. Kain^{1*}, P. Parenti², M. Calaan¹, D. B. Pedersen¹, M. Annoni², G. Tosello¹

¹*Department of Mechanical Engineering, Technical University of Denmark, Building 427A, Produktionstorvet, 2800 Kgs. Lyngby, Denmark*

²*Dipartimento di Meccanica, Politecnico di Milano, Via La Masa 1, Milan, Italy*

* mkain@mek.dtu.dk

Abstract

The ever increasing availability of different metal additive manufacturing (AM) technologies, enhanced process capabilities, and material variations results in an expanding area of application. With different AM variants challenging usability, timeline and costs, application tests of technological variants within certain manufacturing setups is of interest to determine new applications and developments of existing processes. In the current work, material extrusion based metal AM is investigated for the production of tool inserts for polymer profile extrusion. For this particular manufacturing process, the surface topography is of large interest as the internal surface roughness contributes toward the final external surface of the extrudate product. Conventionally manufactured benchmark inserts were compared to AM inserts. The internal surface roughness of inserts were evaluated using silicone replicate technology. The conventionally manufactured insert had a surface roughness of $Sa_{conv} = 374\text{nm}$ compared to a $Sa_{metalAM} = 5854\text{nm}$ for the AM insert. Extrusion of ABS was performed for each of the two inserts using water-cooling and constant extrusion process parameters. The subsequent surface roughness of the extrudates products were found to be $Sa_{convExtrudate} = 248\text{nm}$ and $Sa_{metalAMExtrudate} = 512\text{nm}$ respectively. This gives an indication that despite the high surface roughness of the AM insert, the influence on the final extrudates product is limited. However, additional post processing of the internal surface may provide a further reduction of the resulting extrudates surface roughness. In this work, successful testing and comparison of a conventionally manufactured tool insert and a metal AM tool insert has been performed, making it possible to determine the correlation between internal die surface roughness and resulting external extrudates surface roughness along with application feasibility of extrusion based metal AM for tooling on polymer profile extrusion. Future work will include an elaborate investigation of the correlation of internal die and external extrudates surface roughness.

Metal Additive Manufacturing, Tooling, Material Extrusion, Fused Filament Fabrication, Profile Extrusion, Surface Roughness

List of authors

Surname	Initial	Page			
A					
Akhmetov	M.	123			
Allen	A.	30			
Annoni	M.	143			
Ares	F.	127			
B					
Bayat	D.	19			
Becker	D.	42			
Bellens	S.	102, 110			
Bills	P.	68, 142			
Bircher	B.A.	130			
Blunt	L.	68, 142			
Bosler	E.	47			
Boudoire	F.	19			
Bouvet	P.	98			
Brummerloh	D.	82			
Bustos	J.J.	134			
Buzzacchera	N.	95			
C					
Calaon	M.	143			
Carmignato	S.	95			
Cayron	C.	64, 98			
Chahid	M.	68			
Chandrasekaran	S.	51			
Cherukuri	H.	26			
Cortes Gutierrez	J.	51			
Coto	I.	127			
Coutant	N.	98			
Craeghs	T.	102			
Cullinan	M.A.	15			
D					
Dardis	J.	86			
Davies	A.	26			
de Pastre	M-A.	56			
De Soete	A.	98			
Deisenroth	D.	26			
Delgado	T.	127			
Dewulf	W.	102, 110			
Dickinson	N.	142			
Donmez	A.	26			
Drossel	W-G.	60			
E					
Eastwood	J.	17			
Eiriksson	E.	39			
Emmelmann	C.	82			
Evans	C.	26, 30			
F					
Ferruci	M.	70			
			Fournet-Fayard	L.	64
			Fox	J.	26, 30, 70
G					
			Gage	D.	130
			Gaillard	Y.	98
			Godineau	K.	22
			Gontad	F.	127
			Gunenthiram	V,	64
H					
			Haahr-Lillevang	L.	39
			Hascoet	J-Y.	35
			Hjalmtysson	G.	39
			Holt	A.	142
			Holtzhausen	S.	60
			Hooper	P.	86
I					
			Isaac	R.	30
J					
			Janssens	M.	102
			Jiang	X.	106, 115
			Jones	N.	86
			Jutkuhn	D.	82
			Juzumas	V,	47
K					
			Kain	M.	143
			Kassym	K.	119
			Koch	P.	60
			Korn	H.	60
			Körner	C.	130
			Kostas	K.	119
			Koutiri	I.	64
			Kühne	S.	47
			Küng	A.	130
L					
			Lani	S.	19
			Lany	M.	91
			Lartigue	C.	56
			Lata	M.	30
			Lavernhe	S.	22
			Leach	R.	79, 86
			Liu	M.	79
			Liu	W.	115
			Lou	S.	106, 115
M					
			Majewski	C.	106
			Malcher	M.	47
			Mandloi	K.	26
			Meli	F.	130

Mettry	M.	51	Spierings	A.	91
Miller	J.	26	Spurek	M.	91
Moehring	H-C.	42	Syrlybayev	D.	123
Moretti	M.	75			
Morse	E.	30	T		
Mueller	B.	11	Talamona	D.	119, 123, 138
Mukhtarkhanov	M.	138	Tawfik	A.	142
Mullany	B.	30	Thielsch	J.	60
Müller	B.	60	Thompson	A.	86
			Tosello	G.	143
N			Tournier	C.	22
Nadimpalli	V.K.	39			
Nanjareddy	R.	98	U		
			Unterhofer	S.	19
O					
Obaton	A-F.	64, 98	V		
Oberschmidt	D.	47	Van den Bossche	A.	134
Otero	N.	127	Van Herreweghen	T.	110
			Vandewalle	P.	102
P			Vedel-Smith	N.	39
Paik	J.	19	Vidal Álvarez	S.M.	127
Panas	R.	51			
Parenti	P.	143	W		
Pedersen	D.B.	39, 143	Wegener	K.	91
Penn	A.	82	Williams	R.	86
Perveen	A.	123, 138	Wilm	J.	39
Praniewicz	M.	70	Worthington	M.	51
Probst	G.	110	Wyss	S.	130
Q			Y		
Quinsat	Y.	56	Yang	Z.	82
			Yardin	C.	98
R					
Racasan	R.	68	Z		
Ramadurga			Zanini	F.	95
Narasimharaju	S.	115	Zeng	W.	106, 115
Rauch	M.	35	Zhu	Z.	106
Remani	A.	16, 86			
Revaz	B.	91			
Romero	P.	127			
Rossi	A.	75			
S					
Saldana	C.	70			
Salvisberg	M.	12			
Sanchez	P.	64			
Santi	G.	91			
Schäfer	M.	13			
Scott	P.J.	106, 115			
See	T.L.	115			
Seidler	A.	60			
Seisekulova	A.	123			
Senin	N.	75, 79			
Sinico	M.	110			
Sonar	H.	19			
Sood	A.	30			
Sørensen	S.D.	39			

